ANUL XLIX **2004**

S T U D I A
UNIVERSITATIS BABEŞ-BOLYAI
PHYSICA
3

Papers presented at the 1st International Conference
Advanced Spectroscopies on Biomedical and Nanostructured Systems

2004 September 19-22, Cluj-Napoca, Romania

EDITORIAL OFFICE: Republicii no. 24, 400015 Cluj-Napoca ♦ Phone 0264-40.53.52

SUMAR - CONTENTS - INHALT

POSTER SESSION

Section 1: Biomedical applications

Section 2: Advanced and nanostructured materials

STUDIA UNIVERSITATIS BABEŞ-BOLYAI, PHYSICA, XLIX, 3, 2004

POSTER SESSION
Section 1: Biomedical applications

ATR-FTIR INVESTIGATIONS OF SECONDARY STRUCTURE OF LYOPHILIZED BLOOD PLASMA IN PREGNANCY INDUCED HYPERTENSION

LAVINIA SABĂU[1], G. DAMIAN[2], M. PUIA[2]

[1] "Babes-Bolyai" University, Faculty of Physics, Dept. Biomedical Physics, Cluj-Napoca,
[2] University of Medicine and Pharmacy "Iuliu Haţieganu", Faculty of Medicine, Dept. of Physiology, Cluj-Napoca, Romania, lavisabau@yahoo.com

Pregnancy-induced hypertension (PIH) knowns by many clinical names as toxaemia, gestational proteinuric hypertension and preeclampsia is not a simply high blood pressure, but is a pregnancy condition which must be taken seriously as it can pose a serious risk to health of both mother and baby. This is certainly one of the characteristic signs of the condition, the others being protein in the urine and fluid retention. These signs are not the disease itself but are symptoms of an underlying circulatory disorder. In order to study the effect of PIH on the changes in the secondary structure of blood plasma, we have investigated the changes in lyophilized blood plasma from 30 patients, healty and with different degree of diseases, by ATR-FTIR spectroscopy. Attenuated total re£ection Fourier transform infrared spectroscopy (ATR-FTIR) is one of the most powerful methods for recording infrared spectra of biological materials in general, and for proteins in particular. It is fast, yields a strong signal with only a few micrograms of sample, and most importantly, it allows information about the orientation of various parts of the molecule under study to be evaluated in an oriented system [1,2]. The environment of the molecules can be modulated so that their conformational changes in secondary structure, can be studied [3, 4]. Because a biomolecule is determined by its unique structure, each biomolecule will exhibit a unique FT-IR spectrum, representing the vibrations of its structural bonds. Furthermore, every biomolecule present in the sample will exhibit more or less specific FT-IR absorption peaks. Thus, a plasma FT-IR spectrum will exhibit absorption peaks related to its major components (mainly serum albumin). The changes in secondary structure refers to changes in ratio among three common structures, namely alpha helices, beta sheets, and turns. That which cannot be classified as one of the standard three classes is usually grouped into a category called "other", "random coil" or agregates. Protein aggregates play a large role in human diseases affecting human health. Structural information of lyophilized blood serum is obtained by analysis of the conformationally-sensitive amide I and amide III bands using Attenuated Total Reflectance FT-IR spectroscopy.

The second derivative spectrum was performed in order to overcome the bands overlapping due to the different C=O stretching vibrations of each type of secondary structure (i.e. α-helix, β-sheet, turns and unordered). The results of qualitative and quantitative analysis by curve fitting to the inverted second derivative spectra of amide I features [5,6] of proteins from blood plasma, reveal a decrease in α-helix and β-sheet content and and an increasing of aggregates content for patients affected dy PIH.

REFERENCES

[1] A. Dong, W.S. Caughey, *Methods Enzymol*. 232 (1994) 139–175.
[2] H.H. Mantsch, D. Chapman, *Infrared Spectroscopy of Biomolecules*, Wiley-Liss, New York, 1996
[3] Bandekar, J., *Biochim. Biophys. Acta* ,1120, 123-143 (1992)
[4] Fu, F.-D., DeOliveira, D.B., Trumble, W.R., Sarkar, H.K. and Singh, B.R. *Appl. Spectr*. 48, 1432-1441 (1994)
[5]Singh, B.R., Fuller, M.P., and Schiavo, G. , *Biophys. Chem*. 46, 155-166 (1990)
[6] Singh, B.R., DeOliveira, D.B., Fu, F.-N., and Fuller, M.P. *Biomol. Spectr*. III, 47-55 (1993)

STUDIA UNIVERSITATIS BABEŞ-BOLYAI, PHYSICA, XLIX, 3, 2004

CAFFEINE TEST BY GC-MS

MONICA CULEA[a,*], M. NANULESCU[b], O. COZAR[a]

[a]Babes Bolyai University, str.Kogalniceanu no.1, 400084 Cluj-Napoca, România, e-mail:mculea@phys.ubbcluj.ro;
[b]Pediatric Clinic III, Cluj-Napoca

ABSTRACT. A GC/MS method for caffeine levels determination in children suffering of liver diseases is described. Caffeine and ^{15}N-theophylline, the internal standard, were separated on a HP-5 capillary column 30mx 0.25mm diameter, 0,25µm film support in the temperature program: 200-250^{o}C, at 10^{o}C/min. The method was validated in the range 0-20µg/ml caffeine. A dose of 4mg/kg p.o. was followed by blood caffeine concentrations measurements at 1 and 9 h, for caffeine clearance and half live time measurements in children with liver disease and compared with control.

1. Introduction

Caffeine, 1,3,7 trimethylxanthine, has been introduced as a model compound for measuring the metabolic capacity of the liver [1]. Because it is metabolized by the hepatic P-450 cytochrome oxidase system, clearance of caffeine is a good quantitative test of hepatic function. Caffeine test consists in caffeine oral intake followed by measurements of blood caffeine concentration and pharmacokinetic parameters of caffeine as clearance and half-life time measured by gas chromatography-mass spectrometry (GC/MS).

The aim of the present investigation was to validate a rapid and precise GC/MS method for plasma caffeine level determination and the characterization of plasma clearance and half-life time of the drug in children by using ^{15}N-theophylline as internal standard.

2. Experimental

^{15}N-theophylline, 74,2 atom % ^{15}N, labeled at the nitrogen in the position 7, was synthesized in Cluj-Napoca [2] and used as internal standard [6]. Caffeine was administered p.o. in children with different hepatic dysfunctions. Caffeine sodium benzoate solution containing 125 mg of caffeine and 125 mg of sodium benzoate per 1 ml ampoule was used. All other reagents were from Comchim (Bucuresti, Romania). A Hewlett Packard (Palo Alto, CA, USA) 5989B mass spectrometer coupled to a 5890 gas chromatograph were used in the conditions: EI mode, electron energy 70 eV, electron emission 300µA and ion source temperature 200^{o}C, selected ion monitoring (SIM) mode. The GC/MS interface line was maintained to 280^{o}C, and quadrupol analyser at 100^{o}C. The GC/MS assay used a HP-5MS fused silica capillary column, 30m x 0.25mm, 0.25µm film-thickness, programmed from 200^{o}C to 250^{o}C at a rate of 10^{o}C/min, the flow rate 1ml/min, with helium as carrier gas. Injector temperature was 200 ^{o}C. Retention time for caffeine and ^{15}N-theophylline, the internal standard, were 3.5 min and 2.8 min. 3 µl of sample were injected. The molecular ions m/z 194 for caffeine and m/z 181 for the internal standard were monitored for quantitative analyses in the selected ion monitoring (SIM) mode.

Extraction procedure: 1ml of plasma containing caffeine was placed into a 5 ml screw-cap vial and 10µl of internal standard ^{15}N-theophylline, 2 ml of the extraction solvent, chloroform: isopropanol 20:1 v/v and 0,5 g NaCl were added. After mechanical mixing for 1 min, the sample was centrifuged for 3 min. 3 µl were injected.

Method validation: The method was validated in the range 0-20µg/ml caffeine. Aliquots containing known amounts of caffeine 3, 5, 10, 15, 20 µg ml^{-1} and 10 µg of ^{15}N-theophylline were taken through above procedure. Samples were prepared in duplicate and measured twice.

Table 1.

Precision and accuracy of the method

Concentration added (µg ml^{-1})	n	Concentration measured (µg ml^{-1}))	RSD (%)	Accuracy (%)
3	5	3.1	2.96	3.36
5	7	5.5	5.06	10

The regression curve, plotted as peak-area ratio of m/z 194 to m/z181 versus caffeine concentration, gave the following linearity parameters: slope 0.5207, intercept 0.1058, r = 0.97. Precision gave R.S.D values lower than 5% for 5µg/ml (n=7) and lower than 3% for 3µg/ml (n=5). Accuracy showed values lower than 10% (Table 1). L.O.D. was 0.1µg ml^{-1}caffeine in blood sample, signal to noise ratio 4:1.

Population: Caffeine concentration measurements were performed in 31 hospitalized children suffering of hepatic dysfuctions and controls: 19 children with hepatitis aged 3-19 years old, 4 children with cirrhosis, aged between 5-12 years old, and 8 children as control aged between 5-15 years old. The dose was 4mg/kg, p.o.. Blood samples were taken at 0, 30 min, 1, 3, 6, 9 and 12 h. Blood samples were drawn into heparinized plastic tubes and immediately centrifuged. Plasma was stored at -20^{o}C. Written informed consents were obtained from each subject parent prior to this study.

Calculation: Caffeine elimination constant was calculated as: $k_{el}=(\ln C_1-\ln C_2)/\Delta t$, where C_1=higher caffeine blood concentration; C_2=lower caffeine blood concentration; Δt= the time elapsed between venous blood samples. Two points (1 and 9 h) caffeine clearance was calculated: $Cl = k_{el} \times V_d$ and caffeine half-life as $t_{1/2} = \ln 2/k_{el}$, using a volume of distribution (V_d) of 0.6 liters per kg body weight.

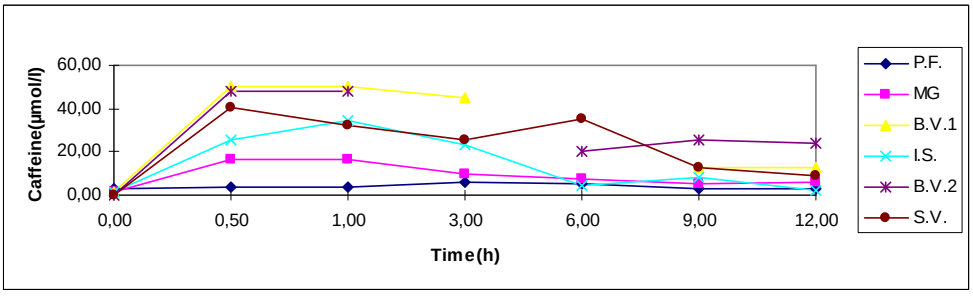

Fig. 1 Blood caffeine concentrations over a period following P.O. caffeine (4mg/kg body weight) for 1health (MG) and hepatitis children

3. Results and discussion

Caffeine clearance, measured in patients with cirrhosis and chronic hepatitis, was reduced and half live time was increased in children with liver disease as compared with control.

The method is simple, precise and rapid, useful in the analysis of xanthines. Isotopic labeled internal standard avoids metabolites overlapping. Good linearity, precision, accuracy and sensitivity were obtained in the range 0-20µg/ml of drug. Significant changes (Student's paired t-test $p<0.01$) were observed in caffeine metabolism in children with decompensate cirrhosis. The control values for clearance and half-life time were 1.36±0.23 ml min^{-1} kg^{-1} and $t_{1/2}$=5.23±0.85 h (n=8). In cirrhosis the clearance values of 0.55±0.41 ml min^{-1} kg^{-1} and half-life times of 19.11±14.9h are changed because of the reduction in “functioning hepatocyte mass”. Patients with noncirrhotic liver disease showed intermediate values (Cl=1.19±0.45 ml min^{-1} kg^{-1} and $t_{1/2}$=6.62±2.37 h) but higher values of caffeine plasma concentrations especially in the first hour after dose. The correlations of total body clearance between two-point study (sampling times 1h and 9 h) and seven-point study (sampling times 0, 0.5, 1, 3, 6, 9, 12 h) were significantly correlated (r = 0.94, p less than 0.001). The results suggest that caffeine pharmacokinetic parameters can be estimated *using two-point blood sampling* procedure and *GC/MS*. The higher *concentrations of caffeine observed in the first hour after caffeine* loading in hepatitis compared with controls could be *a possible test for hepatitis* when very precise and accurate methods are used.

REFERENCES

[1] J. Jodynis-Liebert, J. Flieger, A. Matuszewska, J. Juszczyk, *Serum metabolite/caffeine ratios as a test for liver function*. J Clin Pharmacol. 2004 44:338-47.

[2] M. Culea, N. Palibroda, P. Panta Chereches, M. Nanulescu, *Comparative of isotopic dilution methods for determination of theophylline in the plasma and saliva of infants and children*, Chromatographia, 2001, 53: S387-S-390.

STUDIA UNIVERSITATIS BABEŞ-BOLYAI, PHYSICA, XLIX, 3, 2004

MICROWAVE EXTRACTION OF BIOACTIVE COMPOUNDS FROM *GERANIUM HERBA*

SIMONA COBZAC[1], MIHAELA MOLDOVAN[1], ILDIKO BROŞ[2], EMANOIL SURDUCAN[2], SIMION GOCAN[1]

[1] *Faculty of Chemistry and Engineering Chemistry, Babes- Bolyai University, Avram Iancu Street, nr 43, Romania, csimona@chem.ubbcluj.ro*
[2] *National Institute of R&D for Isotopic and Molecular Technologies, 75-103 Donath street, POB 700, Cluj Napoca, Romania, manu@L30.itim-cj.ro*

ABSTRACT. The aim of this study was to use the microwave extraction instead the reflux extraction. TLC qualitative and VIS spectrophotometry quantitative analyses were performed. It were compared the results obtained in case of reflux and microwave extraction. Extraction is an important step in plant analysis because it must assure quantitative extraction of the compound from different classes with different polarities avoiding degradation processes. The first conclusion of this study is that the microwave extraction can by use for extraction of bioactive compounds from plant material. It has been also observed that the solvent composition has a great influence on the quantities of extracted compound.

I. Introduction

Geranium macrorrhizum is known as an ornamental plant but it is used in traditional medicine to cure the digestive disease. The important bioactive compounds are tannins that confer it the astringent proprieties. It contained also some flavonoids and anthocyans with antioxidant effects. Due its content in volatile oils it is used in fragrance industries and in aromatherapy [1-3]. The bioactive compound can be extracted using different techniques, like classical methods - maceration, reflux, Soxhlet [4, 5] and modern methods - superfluid extraction (SFE), microwave assisted solvent extraction (MASE) and sonication [6-9]. Microwave extraction is a very attractive method because of the energy, solvents and time saving [10-12].

II. Experimental

Plant material

The plant material investigated was *Geranium macrorrhizum herba* collected in May 2004. The powdered dried material was extracted with $CHCl_3$ for lipophylic compounds and chlorophyll extraction.

Extraction procedures

Bioactive compounds from 0.5 g prepared plant material were extracted using different techniques and conditions, as presented in table 1. Each extraction was performed for three times. The crude extract was concentrated at 5 mL and analyzed.

Spectrophotometric analysis

The total content of flavonoids was determined spectrophotometric, as indicated in the official method from Romanian Pharmacopoeias X for Cynarae folium, using $AlCl_3$ as colorimetric reagent [13]. The absorbance was measured at 430nm. As reference solution was used a similar sample without coloring reagent. The calibration curve was performed in the same condition using a methanolic solution of rutine (0.108 mg/mL) with volumes varying from 0.5 mL to 7 mL.

TLC Analysis

Thin layer chromatography was performed on Silica gel G F254 plate (Merck). The samples were applied manual, using a Hamilton microseringe as 20µL bands. Methanolic standard solution of rutine (1mg/mL), quercetine (1mg/mL), hyperozide (1.8mg/mL) and kaempferol (1.2mg/mL) were used for compound identification. The plates were developed in a normal development chamber with: etil acetate – formic acid – water, 90:5:5 (v/v), as mobile phase. Chromatographic plate was visualised at 366nm with an UV lamp after spraying with NTS reagent (diphenylboryloxyethylamin) [14].

Table1

Techniques, solvents and conditions used for extraction.

Sample	Extraction techniques/ Solvent extraction (v/v)	Extraction conditions				
		V (mL)	Time	Frequency (GHz)	Duty cycle (%)	Absorbed power (W)
Microwave extraction						
E 1	MeOH	25	90s	2.45	60	28.05
E2	MeOH-H_2O (85:15)	25	90s			41.03
E3	MeOH-H_2O (70:30)	25	90s			48.28
E4	MeOH-H_2O (50:50)	25	90s			60.27
E5	MeOH-H_2O (30:70)	25	90s			74.55
E6	MeOH-H_2O (15:85)	25	90s			95.62
Reflux extraction						
E7	MeOH	25	30min			
E8	MeOH-H_2O (70:30)	25	30min			
Maceration						
E9	MeOH	25	10 days			
E10	MeOH-H_2O (70:30)	25	10 days			
Soxhlet extraction						
E11	MeOH	25	8h			

III. Results and discussions

Figure 1 show typical chromatogram of *Geranium* extracts obtained in studied condition, visualized at 366nm after pulverization with NTS reagent. It were identified kaempferol (R_f=0.90), quercetin (R_f=0.86), hyperosid (R_f=0.23) and rutine (R_f=0.07).

Total content of flavonoids was determined based on calibration curve (fig.2.) and absorbance at 430nm (table 2).

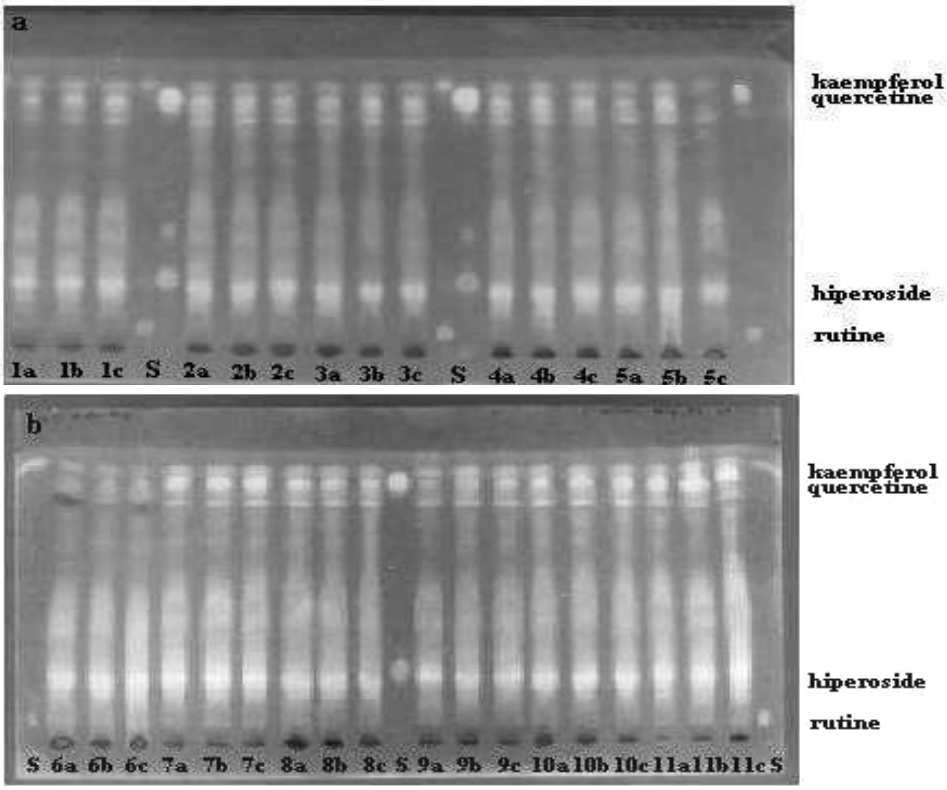

Fig.1 The typical chromatogram obtain for different Geranium extracts a) E1-E5; b) E6-E11 and standard solutions S (rutine, kaempferol, quercetine and hyperozide).

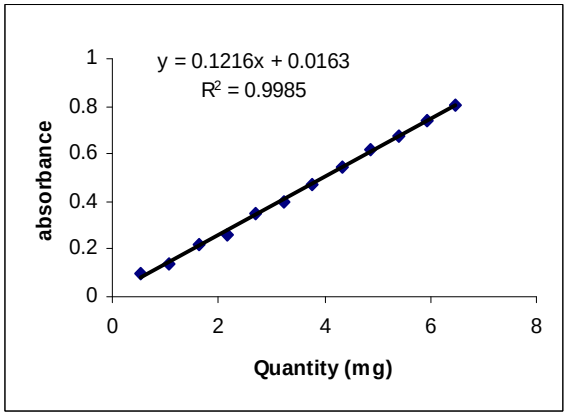

Fig.2 Calibration curve for rutine.

Table 2.

Experimental data and total flavonoids content in studied extracts.

Sample		Absorbance	Quantity (mg rutin /100g plant)	Quantity ± RSD(%) (g rutin /100g plant)
E 1	a	0.206	7.780	
	b	0.216	8.211	
	c	0.196	7.389	0.747±9.88
E2	a	0.602	24.083	
	b	0.605	24.206	
	c	0.580	23.220	2.154±2.26
E3	a	0.617	24.710	
	b	0.608	24.340	
	c	0.619	24.771	2.375±6.67
E4	a	0.459	18.203	
	b	0.481	19.108	
	c	0.427	16.887	1.807±6.18
E5	a	0.555	22.150	
	b	0.587	23.466	
	c	0.583	23.302	2.297±3.12
E6	a	0.328	12.817	
	b	0.352	13.803	
	c	0.334	13.063	1.323±3.88
E7	a	0.419	16.558	
	b	0.403	15.900	
	c	0.413	16.311	1.626±2.04
E8	a	0.582	23.261	
	b	0.587	23.466	
	c	0.603	24.124	2.362±1.91
E9	a	0.357	14.009	
	b	0.378	14.873	
	c	0.365	14.338	1.441±3.03
E10	a	0.601	24.042	
	b	0.629	25.193	
	c	0.598	23.918	2.438±2.88
E11	a	0.319	12.447	
	b	0.326	12.734	
	c	0.346	13.557	1.291±4.46

IV. Conclusions

The aim of this study was to use the microwave extraction instead classical techniques.

The first step of this study is to examine the qualitative composition of extracts obtained with the same extraction agent. Comparing the chromatograms of classical extracts (E8 and E10) with the microwave extract (E3), it can be observed a similar fingerprint (fig.1.). This is a proof for no chemical interaction between the microwave radiation and bioactive compound.

It can be also observed that the best extraction agent, for all techniques, is the mixture methanol-water (70:30, v/v). This solvent assures the greatest quantity of extracted flavonoids: microwave-2.37%, reflux-2.36% and maceration-2.44% (table 2).

Consider the time and solvent saving, we can conclude that microwave extraction is a quantitative fast techniques for extraction of bioactive compound from vegetal matrix.

REFERENCES

1. M.Tămaş, G.Neamţu, A.Mărculescu, Plante medicinale şi aromatice *Chrysanthenum balsamita L.*, Ed. Lux Libris, Braşov, 1996, 61.
2. V.Istudor, Farmacognozie, fitochimie, fitoterapia, vol.II, Ed. Medicală, Bucureşti, 2001, 167.
3. I.Ciulei, E.Grigorescu, U.Stănescu, Plante Medicinale, Fitochimie şi Fitoterapie, vol.I, Ed. Medicală, Bucureşti, 1993, 238.
4. M.Schuhmacher, J.L.Domingo, A.Xifro, S.Granero, J.L.Llobet, *J.Environ.Sci.Health,* **33**(1998), 195.
5. A.M.Kipopoulou, E.Manoli, C.Samara, *Environ.Pollut.,* **106**(1999), 369.
6. L.E.Garcia, M.Sanchez, F. de Alba, M.D.Luque de Castro, *Anal.Chem*., **70**(1998), 2426.
7. V.Camel, *Trends Anal. Chem*., **19**(2000), 229.
8. C.S.Eskilsson, E.Björklund*, J. Chromatogr. A.*, **902**(2000), 227
9. J.Namiesnik, T.Gorecki, *J.Planar Chromatogr.-Mod.TLC,* **13**(2000), 404.
10. K.Ganzler, A.Salgo, K.Valko, *J.Chromatogr*., **371**(1986), 299.
11. K.Li, J.R. Bélanger, M.P.Llompart, R.Turpin, R.Singhvi, J.R.Paré., *J.Int. Spectroscopy,* **13**(1997), 1.
12. J.R.Paré, J.M.Bélanger, S.Stafford, *Trends Anal.Chem.,* **13**(1994), 176.
13. ***, *Farmacopeea Română*, Ed.X, Ed.Medicală, Bucureşti, 1993, 781.
14. H. Wagner, S. Bladt, E.M. Zgainski, Drogenanalyse, Dunnschicht- chromatographische Analyse von Arzneidrogen, Springer Verlag, Berlin, Heidelberg, New York, 1983, 272.

STUDIA UNIVERSITATIS BABEŞ-BOLYAI, PHYSICA, XLIX, 3, 2004

ANALYSIS OF AMIDE I AND III BANDS OF BOVINE SERUM ALBUMIN BY ATR-FTIR AND RAMAN SPECTROSCOPY

S.CAVALU[1*], G.DAMIAN[2], S.CINTA PINZARU[2] , T.JURCA[1]

[1] University of Oradea, Faculty of Medicine and Pharmacy, Biophysics dept, P-ta 1 Decembrie 10, Oradea, ROMANIA scavalu@rdslink.ro
[2] "Babes-Bolyai" University, Faculty of Physics, Kogalniceanu 1, Cluj-Napoca, Romania

ABSTRACT. The amide I and III bands are sensitive to small variations in molecular geometry and hydrogen bonding patterns within proteins. In this paper we present ATR-FTIR and Raman spectroscopy investigations on lyophilized bovine serum albumin, at various pH values in the range 6.5-11. By analyzing both amides I and amide III we found that the decrease of α helix content is accompanied by an increase of the β sheet content in the studied pH range.

INTRODUCTION. The amide vibrational bands can be described in terms of five in-plane (C=O stretching, C-N stretching, N-H stretching, OCN bending and CNH bending) and three out of plane (C-N torsion and C=O and N-H bending) displacement coordinates. Specially, the amide I band is sensitive to small variations in molecular geometry and hydrogen bonding patterns within proteins. This band is due primarily to the C=O stretching vibrations of the peptide linkages that constitute the backbone structure of proteins, combined with small contributions from out of phase C-N stretching and C-C-N bending vibrations. The amide I band has been extensively used in studies of secondary structural compositions and conformational changes of proteins [1-3]. However, a major problem in the IR and Raman study of protein conformations is the intrinsically broad bandwidth of the amide I components that arise from the various secondary structures. The bandwidths of these overlapping components are often greater then the separation between the absorbance maxima of adjacent bands. To overcome this problem, the second derivative methods are successfully used. In this paper we present ATR-FTIR and Raman spectroscopy investigations on lyophilized bovine serum albumin, at various pH values in the range 6.5-11, in order to compare the conformational changes reflected in the vibrational spectra, through the amide I and III bands.

MATERIALS AND METHODS. The powder proteins were obtained from Sigma and rehydrated in phosphate buffer physiological saline at a final concentration of 10^{-3} mol/l. The pH range was adjusted and a small amount of 5 ml from each sample was lyophilized for 30 hours at -5^0 C and than used as powder sample. The FT-IR spectra were recorded in the region 4000-800 cm^{-1} by a Bruker EQUINOX 55 spectrometer OPUS software, using an Attenuated Total Reflectance accessory with a scanning speed of 32 cm^{-1} min^{-1} and the spectral width 2.0 cm^{-1}. The internal reflection element was a ZnSe ATR plate (50 x 20 x 2 mm) with an aperture angle of 45°.

The second derivative spectral analysis was applied to locate positions and assign them to different functional groups [3]. All second-derivative spectra, calculated with the derivative function of Opus software, were baseline-corrected, based on the method of Dong and Caughey [4]. Curve fitting was performed by setting the number of component bands found by second-derivative analysis with fixed bandwidth (12 cm^{-1} for amide I and 14 cm^{-1} for amide III) and Gaussian profile. A micro-Raman setup was employed in order to record the Raman spectra of lyophilized powder samples. The 514.5 nm line of an argon ion laser (Spectra Physics, Model 166) was applied for excitation. The scattered light was collected in back–scattering geometry by focusing an x50 objective (Olympus ULWD MSPlan50) on the entrance slit of a spectrometer LabRam, Dilor with 1800 grooves/mm diffractive grating. The detection system consisted of a charge–coupled multichannel detector (CCD, SDS 9000 Photometrics).

RESULTS AND DISCUSSION. Raman spectra of native BSA and at different pH values, in the spectral range 500-1800 cm^{-1}, are presented in Fig. 1.

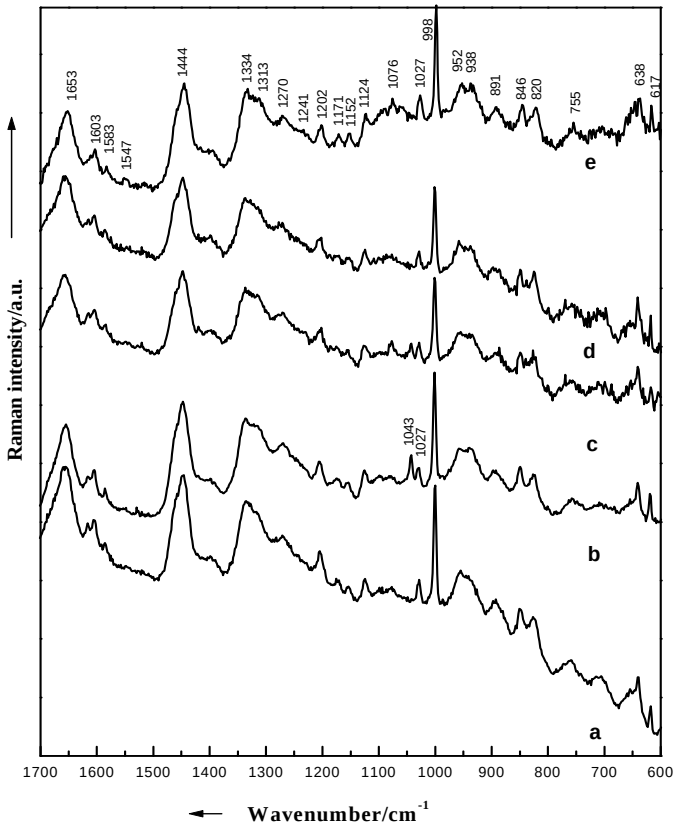

Fig.1. Raman spectra of native BSA (a) and BSA at different pH values: b) 6.7; c) 8.1; d) 9.5; e) 11. Laser line 514.5 nm, power 100 mW.

On comparing with previous Raman reports on BSA [5], the spectral region between 1200-1300 cm $^{-1}$ is poorly represented, indicating the dominant presence of alpha-helix content. The secondary structure (α-helix,β-pleated sheet and random coil) is observed in the Raman spectra through the contribution of the strong amide I band (1653 cm^{-1}) and weak amide III band (1270 cm^{-1}). The phenyl stretching bands at 998, 1027 and 1603 cm^{-1} are present in the Raman spectra indicating the aromatic amino acids residues. The CH_2 and CH_3 scissoring modes are located at 1444 and 1461 cm^{-1} respectively. In addition, bands from the side chains of some of the amino acids residues (Tyr, Trp, Phe, etc.) are present. Besides the common amide bands, the supplementary 17 disulphide bridges are characteristic for the BSA. The characteristic frequencies of C-S and S-S groups are present as weak-medium bands in the 500-750 cm^{-1} spectral region. Comparing the spectra from Fig.1 (a, b, c, d, e), the only one major difference observed is the presence of a new band at 1042 cm^{-1}, for the 6.7 and 8.1 pH values.

In order to study lyophilization-induced structural transitions, calculations of the second derivative FTIR spectrum is recommended [3]. This method is objective and alterations in component band widths, heights and positions, which are due to protein unfolding, are preserved in the second derivative spectrum. Structural information were obtained by analysis of the conformationally-sensitive amide I band located between 1600 and 1700 cm^{-1} and amide III located in the spectral region 1215-1335 cm^{-1}. Each type of secondary structure (i.e. α-helix, β-sheet, β-turn and unordered) gives rise to different C=O stretching frequencies [6, 7], and, hence, results in characteristic band positions. The relative band areas (determined by curve fitting) can then be used to quantitate the relative amount of each structural component. Figure 2 show the inverted second derivative amide I of the bovine serum albumin lyophilized from different pH. Assignments of the bands in Table I are made on the basis of previous reported studies together with the quantitative analysis. Fourier deconvolution, used to determine the component band positions, reveals that the protein exhibits a major band in range 1650-1653 cm^{-1} characteristic of α-helical structures [3, 8]. The bands in the region 1638-1640 cm^{-1} are expected to be characteristic for native β-sheet structures, while the bands in the ranges 1660-1667 cm^{-1} and 1682-1687 cm^{-1} may possibly be attributed to β-turns. On the basis of earlier IR studies [3,8], the bands from 1626-1628 cm^{-1} are indicative of intermolecular (antiparallel) β̃ sheet and, according with literature, is a common IR spectral features for both lyophilization and temperature-induced protein aggregation. Qualitative and quantitative analysis of amide I features reveal a decrease in α-helix content and an increasing β-sheet content with pH values.

The amide III is a more complex vibrational mode. It mainly is the in-phase combination of NH in-plane-bending and CN stretching with contributions from CC stretching and CO in-plane-bending [9] depending on the details of the force field, the nature of side chains and hydrogen bonding. The band position is very sensitive to the secondary structure, thus α-helix is reflected in the region 1298–1315 cm^{-1}, β-sheet in 1227–1240 cm^{-1} and unordered structures in 1260–1286 cm^{-1}. The inverted second derivative spectra of bovine serum albumin lyophilized from different pH values are given in the Figure 3 and the assignments of spectral bands, in the Table II. Quantitative analysis of amide III in the studied pH region, revealed that α-helix content decrease from 48.4 % to 42.3%, while β-sheet content increase between 36.6% and 39.7%. The results are in agreement with the qualitative and quantitative analysis of amide I region.

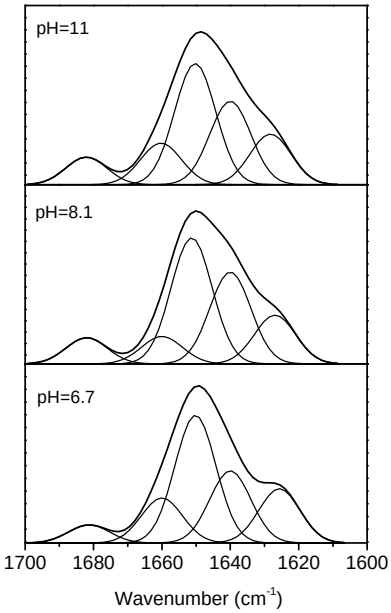

Fig.2. Curve fitted inverted second derivative spectra amide I of lyophilized Bovine Serum Albumin.

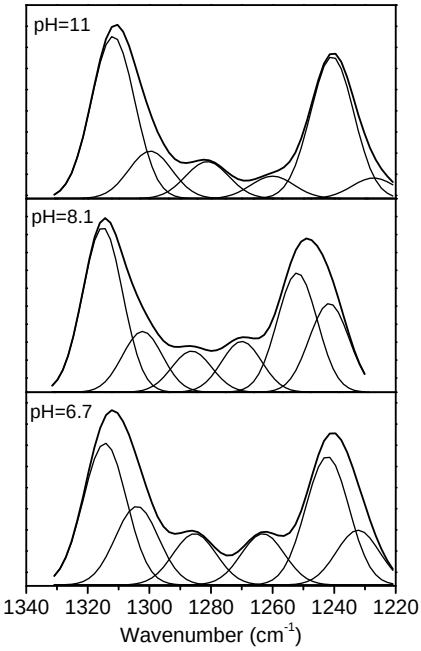

Fig.3. Curve fitted inverted second derivative spectra amide III of lyophilized Bovine Serum Albumin.

Table I.

Relative Areas and Assignments of Infrared Second Derivative Amide I Band of lyophilized Bovine Serum Albumin at different pH values

pH=6.7		pH=8.1		pH=11		
v (cm^{-1})	Area (%)	v (cm^{-1})	Area (%)	v (cm^{-1})	Area (%)	Assignment
1681	5.7	1682	8.2	1681	8.5	β -turn
1660	14.2	1660	10.6	1660	12.8	β -turn
1650	40.3	1651	39.4	1650	36.4	α-helix
1640	22.7	1640	26.7	1640	26.8	β-sheet
1626	17.1	1627	15.2	1628	15.6	β-sheet (aggregates)

Table II.

Relative Areas and Assignments of Infrared Second Derivative Amide III Band of lyophilized Bovine Serum Albumin at different pH values

pH=6.7		pH=8.1		pH=11		
v (cm^{-1})	Area (%)	v (cm^{-1})	Area (%)	v (cm^{-1})	Area (%)	Assignment
1311	37.6	1314	30.3	1313	31.3	α-helix
1300	10.8	1304	15.5	1299	11.5	α-helix
1281	6.2	1285	7.5	1281	7.8	unordered
1260	8.6	1263	9.2	1264	9.6	unordered
1240	31.8	1242	25.4	1244	22.7	β-sheet
1227	4.8	1232	11.7	1233	17	β-sheet

CONCLUSIONS. The Raman active amide I and amide III mode for the alpha-helix and beta sheet conformation appeared at the same frequency as in the FTIR spectra. The second derivative spectral analysis and curve fitting was used to quantitate the relative amount of each structural component. Qualitative and quantitative analysis reveal a decrease in α-helix content and increasing β-sheet content with pH values.

REFERENCES

[1]. Prestrelski, S.J., Arakawa, T., Carpenter, J.F. *Arch. Biochem. Biophys*. 303, 465-473 (1993).

[2].Van de Weert, M., Haris, P.I., Hennink, W.E., Crommelin, D.J.A., *Anal. Biochemistry,* 297, 160-169 (2001).

[3] A. Dong, S.J. Prestrelski, S.D. Allison, J.F. Carpenter, *J. Pharm. Sci*. 84, 415–424 (1995).

[4] Dong, A. and Caughey, W. S. *Methods Enzymol.* 232, 139–175(1994)

[5]. P. C. Painter and J. L. Koenig, (Eds), Handbook of Biochemistry and Molecular Biology, Proteins, Vol. III, 1976, Raman Spectroscopy of Polypeptides and Proteins, 575-587.

[6] A. Dong, W.S. Caughey, *Methods Enzymol*. 232 (1994) 139–175.
[7] H.H. Mantsch, D. Chapman, *Infrared Spectroscopy of Biomolecules*, Wiley-Liss, New York.
[8] Dong, A., Meyer, J.D., Brown, J.L., Manning, M.C., Carpenter, J.F., *Arch. Biochem. Biophys.* 383,148-155(2000).
[9] Bandekar, J., *Biochim. Biophys. Acta* ,1120, 123-143 (1992)

STUDIA UNIVERSITATIS BABES-BOLYAI, PHYSICA, XLIX, 3, 2004

EPR STUDY OF RADICALS KINETICS IN SOME γ –IRRADIATED BETA-BLOCKER DRUGS

DINA PETRIŞOR[1], G. DAMIAN[1], MARIA IONILA[3], FELICIA DRAGAN[2], S. SIMON[1]

[1]*"Babeş-Bolyai" University, Faculty of Physics, Cluj-Napoca, Romania, dsitar@phys.ubbcluj.ro*
[2]*University of Oradea, Faculty of Medicine and Pharmacy, Oradea, Romania*
[3]*Institute for Nuclear Research, Piteşti, Romania*

ABSTRACT. The aim of the present work is to study by EPR spectroscopy the behaviours of the γ-radiation-induced radicals in the four beta-blockers drugs (Pindolol, Verapamil, Atenolol and Metroprolol), to characterise the specific features of these radicals and stability of molecular compounds, on the absorbed dose. Powder samples of drugs irradiated to deferent doses and dose-flow until sterilisation limit (25KGy), were used to generate dose-response curve for the radicals associated with the integral of the EPR absorption spectrum. The effects of radiation on studied drugs are characterised by the same processes but with different parameters of generation and destroying of free radicals. This deference can be attributed to a much higher stability of Atenolol and Metoprolol than Pindolol and Verapamil.

KEYWORDS: EPR, free radicals, beta-blocker drug

1. INTRODUCTION

The use of ionising radiations is one of the most promising methods for the sterilization of solid pharmaceuticals. Therefore, the studies of effects of the high-energy ionising radiation (gamma rays, electron beams) on the medical devices and drugs or on foods, are increasing due to applications in the medical sterilization and hygienic quality of foods [1,2].

The main advantage of these methods is due to high penetrating power and the very small temperature rise induced. Radiation sterilization is used mainly for the sterilization of heat sensitive materials and products. In that many medicinal products and packaging materials are radiation-sensitive, this method is permissible only when the absence of deleterious effects on the material/product has been confirmed prior to use [3]. However, the radiosterilization produces new products, which can induce a modification of odour and colour, to produce the chemical and physical alterations leading to a loss of their biological activity and, even to be potentially toxic.

These products are formed in so low concentration that the usual analytical techniques and toxicity tests are not sensitive enough to detect them. During irradiation of solid drugs, free radicals are formed and trapped in the matrix.

One of the most used methods to study these effects is Elctron Paramagnetic Resonance (EPR) spectroscopy. In the study of free radicals generated by γ-irradiation in drugs, the hyperfine structure of the EPR spectrum (when it is well resolved) provides more important information about the radical than g-value, because most radicals detected are carbon- or nitrogen- centered radicals and the spectra positions are almost in the same magnetic field range [4].

This paper describes the results of experiments on beta-blocker drugs (Atenolol and Metroprolol than Pindolol and Verapamil) by EPR, in order to detect if they contain or can easily form stable paramagnetic species following sterilisation by ionising radiation. The beta blockers (ex: atenolol, metroprolol, propranolol, pindolol, verapamil) act as competitive antagonists at the adrenergic beta receptors. The newer agents tend to be more selective for the cardiac (beta-1) receptors, which allows for decreased systemic side effects. Most of the generic names for beta blockers end with "olol". Besides being used primarily for their cardiovascular effects to treat hypertension and postmyocardial infarction, beta-blockers are used to treat migraine headaches, essential tremors, thyrotoxicosis, glaucoma, anxiety, and various other disorders [5].

This drugs work by blocking beta-adrenergic substances, helping relieve stress on the heart, slowing the heart beat, lessening the force with which the heart muscle contracts and reducing blood vessel contraction in the heart, brain, and throughout the body. They are commonly used to treat high blood pressure and angina and to prevent a recurrence of heart attack. Beta-blockers block the stimulatory effects of the neurohormones epinephrine and norepinephrine, the so-called "fight-or-flight" hormones. By blocking these hormones, beta-blockers reduce the stress on the heart and reverse myocardial remodeling [5].

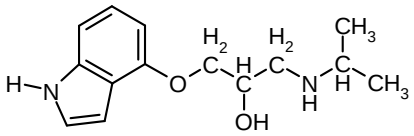

Pindolol

2. EXPERIMENTAL

The beta-blocker drugs (drugs (Atenolol, Metroprolol, Pindolol and Verapamil) were exposed to γ-irradiation from a ^{60}Co source (SIGMA gamma source from Institute of Nuclear Research, Piteşti) give a compact and uniform density of radiations and a different dose rates (2.48 kGy/h – 4.56 kGy/h).

Powder samples of drugs irradiated to deferent doses and dose-flow until sterilisation limit (25KGy), were used to generate dose-response curve for the radicals associated with the integral of the EPR absorption spectrum. EPR spectra were RECORDED WITH A “ADANI PORTABLE EPR Spectrometer PS8400”, operating in the X-band (9.1GHz – 9.6GHz) equipped with a computer acquisition system. The computer simulation analysis of the spectra was made by using POWFIT program that is available to the public through the internet (http://alfred.neihs.nih/LMB) for obtaining the magnetic characteristic parameters. The structural formulas of studied samples are presented in Fig.1.

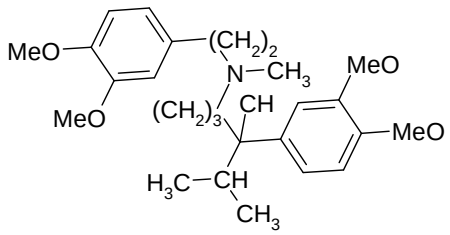

Verapamil

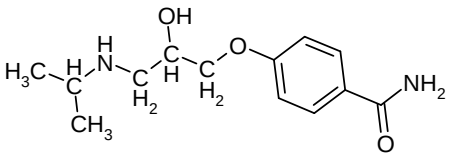

Atenolol

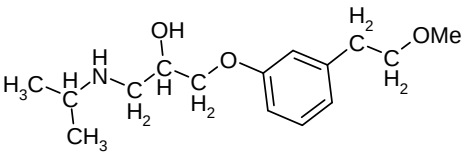

Metroprolol

Fig. 1. Chemical structures of irradiated samples

3. RESULTS AND DISCUSSIONS

Non-irradiated and irradiated samples were analysed by EPR spectroscopy. Only non-irradiated polycrystalline sample of Atenolol and Metroprolol exhibit some weak and unresolved EPR signals By γ-irradiation were generates free radicals detectable for all examined samples.

The singlet character spectra of Pindolol and Verapamil cannot be interpreted, due to low resolution. They exhibit a linewidth of 14.5 G which reflect the random orientations of the radicals with regard to the magnetic and a broadening mechanisms contribution by dipolar and spin-spin interactions. The total spectrum represents a sum of spectra corresponding to all free radicals simultaneously present in the sample, dominated by a broad central line. However, the broad signal observed is characteristic for free radical trapped in a solid matrix [6]. The value of the isotropic g-factor of g_0=2.0051, is characteristic for carbon- or nitrogen-centered radicals [7]. Moreover, a good agreement between experimental and simulated spectrum was obtained assuming the existence a two radical species (Fig. 2a, 2b). For Pindolol the magnetic parameters obtained by simulation was one free radical with a_N=25.9G couplated with three protons with a_H=14.6 G (radical centered on nitrogen) and another radical due to a unpaired electron unlocated on the aromatic ring with hyperfine constant a=17G couplated with three protons having a_H=3.8 G.

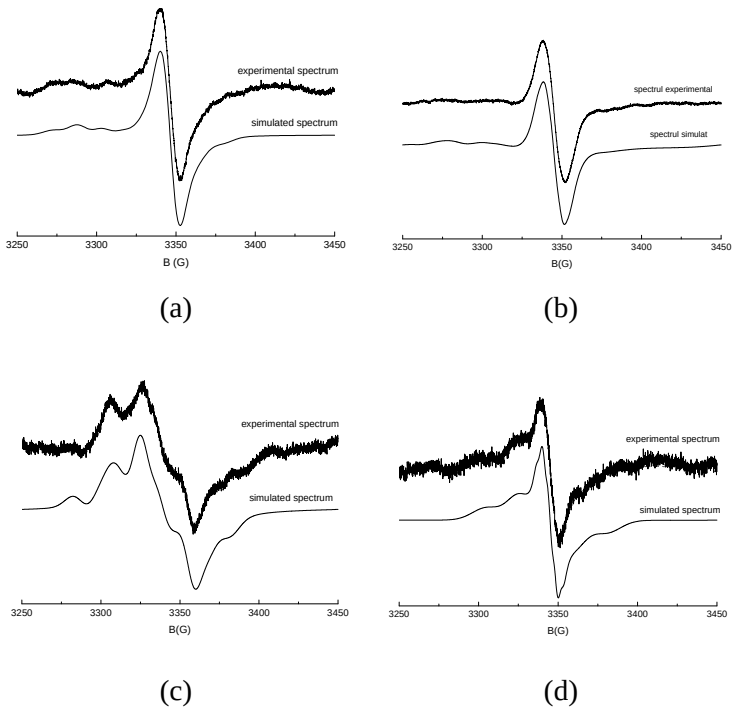

Fig. 2. Experimental and simulated EPR spectra: (a). Pindolol, (b) Verapamil, (c) Atenolol, (d) Metroprolol

The presence of hyperfine structure of EPR spectra of γ-irradiaed Atenolol (especially) and Metroprolol (Fig.2c and 2d) is due to the most probable changes in the reorientation of imidazolic group versus carbazolic group and breaking the bond between carbon and nitrogen. Such, the free radicals generated by irradiations, can be localized in different local conformations of molecular structures giving rise to nonequivalent magnetic species. The EPR spectrum of Atenolol has been attributed to the superposition of spectra of two radicals The first radical gives rise a triplet centered at g=2.0031 with 9.8 G peak-to-peak line width and is due to two equivalent protons with hyperfine coupling $a_1(H)=a_2(H)=16.3$ G. This radical, in very good agreement with the isotropic coupling generally found for carbon centered π-radicals, is of the form $R-\dot{C}H_2$ and can be produced by removal of hydrogen from methyl group. For the second radical assumed, the unpaired electron can be located on nitrogen atom from imidiazolic group, giving rise a characteristic hyperfine splitting with a(N)=16-18G and g=2.009 [8].

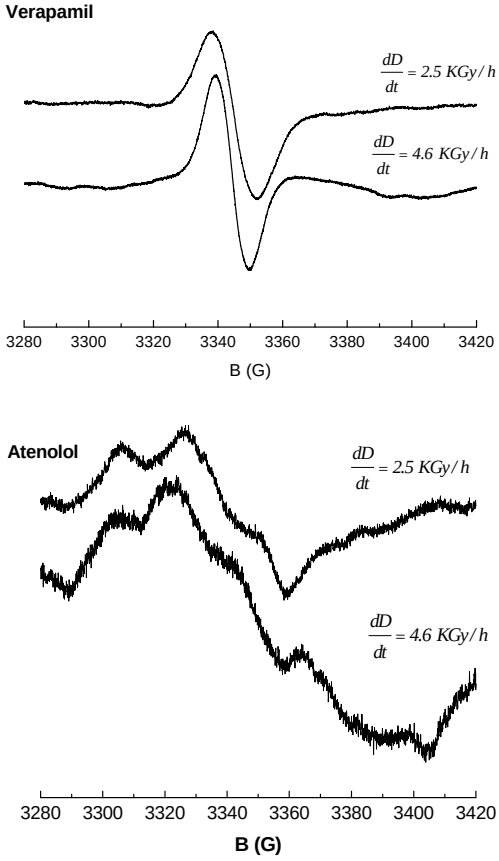

Fig.3. EPR spectra of γ-irradiated verapamil and atenolol at different dose rates

Due to the large values of line-widths it is very difficult to obtain the g and A parameters from experimental spectrum of Metroprolol. By computer simulation assuming two radical species the almost same characteristics like Atenolol, was observed. Their magnetic characteristics are situated in the same range as Metroprolol.

With the aim of study the influence of free radicals production with the different gamma dose rates of irradiation, we analysed the relative quantity of free radicals at absorbed dose of 25 kGy, but at two dose rates: 2.5 kGy/h and 4.6 kGy/h. The response factor to quantify the radicals is the normalised double integration of the whole first-derivative EPR spectrum. The radical concentration is proportional to the area of the double integrated curve. In figure 3 we show a comparison between EPR signals intensity of irradiated Verapamil and Atenolol (the most significant drugs) at two dose rates. We observed, that an larger dose rates gives an increases of the signal intensity.

4. CONCLUSIONS

The magnetic parameters corresponding to each radical were obtained by simulation of the spectrum. A good agreement between experimental and simulated spectrum was obtained by simulation with two radical species.

From the analysis of the EPR signal dependence on the dose rate, it can be concluded that γ-irradiation causes an increase in the amount of this radical in samples. We suggest that dose-rate irradiation could be an informative tool for the study of kinetics of formation and recombination of the free radicals generated by high-energy ionising radiation

The effects of radiation on studied drugs are characterised by the same processes but with different parameters of generation and destroying of free radicals depending on the radiosensitivity and on the dose rates. This deference can be attributed to a much higher stability of Pindolol and Verapamil than Atenolol and Metoprolol (more radiosensitive).

REFERENCES

1. Saint-Lebe, L., Raffi, J., *Cah. Nutri. Diete*., Paris 30 (2), 117-123, 1995.
2. Farkas, J., *Int. J.Microbiol*. 9, 1-45, 1989.
3. Engalytcheff, A., Deridder, V., Debuyst, R. and Tilquin, B. *Radiat. Res*. 160, 103–109, 2003.
4. A-S. Crucq, Chim. Nouv. 12, (1994)1356-1359.
5. Clyde W. Yancy, *Rev Cardiovasc Med;3, Suppl* 3, 527–535, 2002
6. J. Raffi, S. Gelly, L. Barral, F. Burger, P. Piccerelle, P. Prinderre, M. Baron, A. Chamayou, *Spectrochimica Acta Part A* 58, 1313–1320, 2002
7. H. Ambroz, E. Kornacka, B. Marciniec, M.Ogrodowczyk, G. Przybytniak, *Radiat. Phys. Chem*. 58 357–366, 2000
8. G.Damian, *Talanta*, 60, 923-927, 2003.

STUDIA UNIVERSITATIS BABEŞ-BOLYAI, PHYSICA, XLIX, 3, 2004

DENSITY FUNCTIONAL CALCULATIONS OF HYPERFINE COUPLING CONSTANTS IN GLYCINE-DERIVED RADICALS

RALUCA MARCU[1], VASILE CHIŞ[1]

[1]*Babeş-Bolyai University, Faculty of Physics, Kogălniceanu 1, RO-400084 Cluj-Napoca, Romania*

ABSTRACT. The geometries and proton hyperfine coupling constants of several glycine radicals have been determined using the density functional theory. All calculations were performed with the B3LYP hybrid functional in combination with various basis sets. Theoretical results have been compared with the experimental available data from EPR/ENDOR studies. In this paper we have investigated the structures of the five α-glycine radicals proposed in a recent paper by A. Sanderud et al. (*J. Phys*. *Chem*. **1998**, 102, 9353): NH_3^+-ĊH-COO^- (radical I), ĊH$_2$–COO^- (radical II), H_2 N-ĊH-COOH (radicals III and IV), H_3^+N-CH$_2$ –CO-ĊH-COO^- (radical V), the structure of the nitrogen centered π radical detected by J. Sinclair: $H_2\dot{N}^+ - CH_2 - COO^-$ (Sinclair, J.; *J. Chem. Phys*., 55, 1, **1971**) and the structure of the new radical reported previously by M. Brustolon et al. : NH_2 –ĊH$_2$ (*J. Phys. Chem*. **1997**, 101, 4887). Our calculations do not confirm the structure proposed by these later authors but support the structures proposed by Sanderud et al. for radicals I, II, III and IV. Also, the calculated couplings do not match those assigned for radical V .

1. Introduction

The ab initio methods for hyperfine couplings calculations have proven to be unpractical and expensive for large molecules because of the extensive CPU time. Lately, the development of DFT methods offered an excellent alternative for calculation of hyperfine parameters. Many recent papers confirmed an improved accuracy and agreement with the experimental data, especially when using Becke's exchange and Lee-Yang-Parr's correlation functionals [1-3]. Also DFT techniques require less computational time then ab initio methods.

α-glycine is the simplest amino acid from the series of 20 amino acids that enter the structure of proteins and therefore the study of its properties and behavior after irradiation is both of theoretical and practical importance. Ab Initio studies on the glycine molecule itself have been performed by Vishveshwara and Pople [4] and by Jensen and Gordon [5], aiming the complete analysis of the conformational potential energy surface of this molecule. Some theoretical investigations were carried upon glycine radicals in gas an liquid phase [6-9] and recently also in crystal phase [10]. Despite its simplicity, this amino acid gives rise to a variety of radicals, depending upon the temperature at which the irradiation was performed (low temperature or room temperature). In 1964, from ESR experiments on α-glycine crystals γ-ray irradiated at room temperature, two radicals have been identified [11]: the oxidation product NH_3^+-ĊH-COO^-(radical I) formed by net hydrogen abstraction

from the central carbon atom and the reduction product $\dot{C}H_2$–COO^-(radical II) formed by net deamination. The existence of these two radicals has been confirmed by subsequent studies [12-15] In 1997, the presence of a new radical stable at room temperature was detected from HF-EPR spectra (radical III). Brustolon et al. [14] identified radical III with the decarboxylation product of the primary radical anion: NH_2 –$\dot{C}H_2$. In 1998, Sanderud et al.[15] also observed the resonance due to this species but assigned a different structure for radical III: H_2 N-$\dot{C}$H-COOH. In addition they characterized two new-detected radicals, suggested to be a geometrical conformer of radical III (radical IV) and a dimer product: H_3^+N-CH_2–CO-$\dot{C}$H-COO^- (radical V).

2. Computational methods

All calculations were performed using the GAUSSIAN 98 program [16]. Both geometry optimization and hfcc's calculations were performed using B3LYP hybrid functional combining Becke's three parameter exchange functional and Lee, Yang and Parr's correlation functional. As it was ascertained by several previous papers regarding radicals investigation through DFT [17], the best agreement between calculated and experimental hfcc's values was achieved when using B3LYP hybrid functional in combination with 6-31+G(d) or 6-311+G(d) basis sets.

3. Results and Discussion

3.1. Radical I

The presence of radical I, NH_3^+-$\dot{C}$H-COO^-, was reported both in low-temperature [18] and room-temperature irradiated glycine crystals [15]. Earlier studies [19] established that, at room temperature, the amino protons are rotating freely and therefore the associated couplings are rotationally averaged. At low temperature, when the amino protons are locked into one position, another two couplings were measured and they were associated with two of the three β-protons. Being very small, the coupling due to the third proton couldn't be identified in these spectra.

Both geometry optimization and hfcc's calculations were performed using the B3LYP hybrid functional in combination with several basis sets.. During the optimization procedure, a proton transfer occurs from the amino group (H8) to the O1 oxygen atom. Consequently, we have performed a full optimization upon the original structure of the radical in the presence of a solvent (water) using the Onsager solvent model. The optimized radical displays a planar structure, excepting the H6 and H7 amino protons. The dihedral angle between H8-N5-C3-C2 equals 0.1˚ meanwhile the dihedral angles for the two others amino protons are 121.4˚ and –121.3˚. In this case, the bond lengths of the H6 and H7 amino protons are 1.035 Å and 1.027 for the H8 proton.. Figure 1. shows the optimized structure of radical I at B3LYP/6-311+G(d) level of calculation.

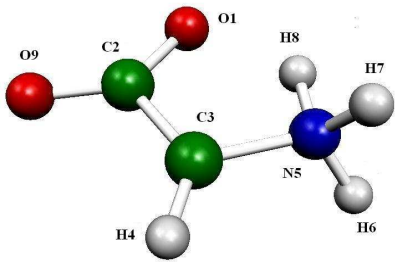

Fig.1. Optimized structure of α-glycine radical I at B3LYP/6-311+G(d) level of calculation

The best theoretical results, in agreement with the hfcc's experimental values determined by Sanderud et al., are those obtained at the B3LYP/6-311+G(d) level of calculation. In this case, the standard deviation from the experimental data is less than 3% for the α-proton coupling and about 5% for the averaged amino protons couplings. The calculated and available experimental values for the hyperfine coupling constants of the α-proton H4 and amino protons H6 and H7 are shown in table 1.

For the third amino proton's isotropic coupling we found a small value of 2.09 MHz, in accordance to the fact that, because its small value, this coupling couldn't be identified from EPR/ENDOR spectra. We have also observed that the averaged value for the isotropic couplings of the amino protons, 51.88 MHz, is very close to the experimental value of 49.07 MHz measured at room temperature. Therefore we suppose that both at low and room temperature the radical keeps the same conformation.

Table 1.

Experimental and calculated hyperfine coupling tensors in α-glycine radical I at B3LYP/6-311+G(d) level of calculation*. All values are in MHz (a) [15]; * solvent model; n.a.-not available)

	Calculated			*Experimental* [a)]		
	A_{iso}	B_{11} B_{22} B_{33}	A_{11} A_{22} A_{33}	A_{iso}	B_{11} B_{22} B_{33}	A_{11} A_{22} A_{33}
C2	-30.58	5.29 3.26 -8.55	-25.29 -27.32 -39.13	n.a.	n.a.	n.a.
C3	96.54	154.46 -75.75 -78.71	251 20.79 17.83	n.a.	n.a.	n.a.
H4	-61.85	40.19 -4.44 -35.74	-21.66 -66.29 -97.59	-63.72	31.94 1.85 -33.80	-31.94 -61.87 -97.52
N5	-8.65	0.44 0.09 -0.53	-8.21 8.56 -9.18	n.a.	n.a.	n.a.
H6	76.71	10.6 -4.71 -5.89	87.31 72.0 70.82	62.91	10.66 -4.07 -6.60	73.57 58.84 56.31
H7	76.84	10.59 -4.70 -5.89	87.43 72.14 70.95	83.05	10.65 -4.80 -5.86	93.70 78.25 77.19
H8	2.09	9.90 -4.37 -5.54	11.99 -2.28 -3.45	n.a	n.a	n.a

After the geometry optimization, single point hfcc's calculations were performed using the 6.311+G(d) basis set, by rotating the amino group around the N5-C3 bound axis over 180˚, in steps of 18˚. The angular variation of the amino protons hfcc's upon rotation is shown in figure 2. which proves the typical β character of these protons: the isotropic couplings of the β-protons may vary considerably between 10 MHz and 140 MH.

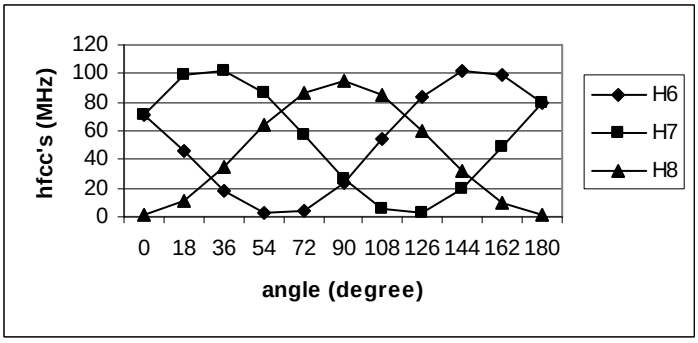

Fig.2. Angular variation of the H6, H7 and H8 hfcc's upon rotation of the amino group around N5-C3 bond axis in α-glycine radical I

3.2 Radical II

Radical II, $\dot{C}H_2$–COO^-, was detected as a stable species only in room-temperature irradiated crystals of α-glycine. The provenience of this radical is related to the deamination reaction of the glycine anion radical, probably followed by deprotonation. As this species was not detected in low-temperature irradiated crystals, it was assumed that, in this case, the radical decomposes at room temperature [18]. From ENDOR spectra of α-glycine crystals measured at 100 K two hyperfine couplings were assigned to radical II, due to the interactions of the methylen protons [15]. At room temperature, because of the methylen's fast rotation, these two protons are equivalent. The hfc tensors were previously calculated by Teslenko et. al. [20].

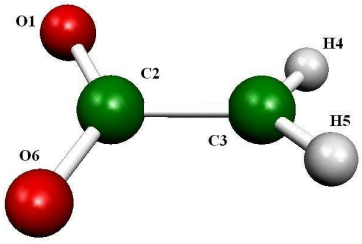

Fig.3. Optimized structure of α-glycine radical II at B3LYP/6-31+G(d) level of calculation

The optimized structure of radical II is shown in figure 3. The two α-protons are slightly twisted from the radical plane: the dihedral angles between H5 and O1 and H4

and O1 are about –18.6° and 161.1°. As can be seen from table 3, 6-31+G(d) basis set gives excellent agreement with the experimental average value of -59.05 MHz for the isotropic part of the hfc tensor. The calculated (B3LYP/6-31+G(d) level of calculation) and available experimental values of the hyperfine coupling constants for the two α-protons are displayed in Table 2. Adding a set of diffuse functions to the 6-31G(d) basis set improves the result but additional polarization functions do not lead to further improvements.

Table 2.

Experimental and calculated hyperfine coupling tensors in α-glycine radical II at B3LYP/6-31+G(d) level of calculation (all values are in MHz) (a)[20]; n.a.-not available)

	Calculated			Experimental [a)]		
	A_{iso}	B_{11} B_{22} B_{33}	A_{11} A_{22} A_{33}	A_{iso}	B_{11} B_{22} B_{33}	A_{11} A_{22} A_{33}
C2	-29.97	4.34 2.41 -6.75	-25.63 -27.56 -36.72	n.a.	n.a.	n.a.
C3	109.68	127.65 -63.58 -64.07	237.33 46.1 45.61	n.a.	n.a.	n.a.
H4	-57.27	35.51 -2.62 -32.89	-21.76 -59.89 -90.16	-58.6	32.2 1.7 -33.9	-26.4 -56.9 -92.5
H5	-57.43	35.51 -2.61 -32.9	-21.92 -60.04 -93.33	-59.5	33.5 0.4 -34	-26.0 -59.1 -93.5

3.3. Radicals III and IV

In this paper we investigate both the structures proposed for radical III by Brustolon et al. (NH_2 –$\dot{C}H_2$) and by Sanderud et al. (H_2 N-$\dot{C}$H-COOH). The geometry optimization and hfcc's calculations were performed at B3LYP/6-311+G(d) level. The isotropic couplings calculated for the first structure are significantly different from those reported by the authors: -31.32 MHz for the CH2 protons instead of -20.2 MHz or –18.8 MHz, and 6.35 MHz for the NH2 protons instead of 25 MHz.

Sanderud et al. correlated the resonance due to this radical in EPR/ENDOR spectra with a different structure: H_2 N-$\dot{C}$H-COOH. They proposed the existence of two geometrical conformers for this product: radical III and radical IV which have the same structure, but different conformations. The optimized structure of radicals

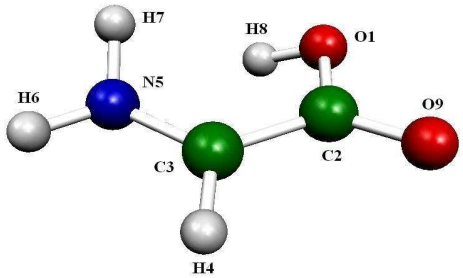

Fig. 4. Optimized structure of α-glycine radical III at B3LYP/6-311+G(d) level of calculation

III is shown in figure 4. The hyperfine couplings corresponding to the α and amino protons of the optimized structure are considerable different from the experimental ones. Yet, Sanderud et al. reported nonplanar conformations for both radical III and IV. Rotating the C-H_α bond around the C3-C2 bond axis, we found suitable values for the isotropic coupling of the α-proton corresponding to a dihedral angle between H4, C3, C2 and O1 atoms of 120° for radical III and of 127° for radical IV. The isotropic values calculated in this case are about –24.39 MHz instead of –24.62 MHz for radical III and –30.29 MHz instead of –30.15 MHz for radical IV. However, the isotropic couplings for the amino protons are far from being adequate.

Single point calculations were performed by modifying the corresponding dihedral angles. The best fits were obtained for dihedral angles between H6-N5-C3-C2 of 175° and between H7-N5-C3-C2 of -30° (radical III) respectively 177° and -8° (radical IV). The corresponding isotropic couplings are: -13.34 MHz and –17.87 MHz for radical III (-15.46 MHz and –16.87 MHz experimental values) and –10.18 MHz and –13.34 MHz for radical IV (-16.79 MHz and –18.05 MHz experimental values).

3.4. Radical V

In their paper, Sanderud et al. also reported the detection of another new radical, radical V, suggested to be a dimer product: H_3^+N-CH_2 –CO-ĊH-COO^- , formed by water elimination between radical II and a neighboring glycine molecule.

For this species, the authors have determined one hyperfine coupling tensor corresponding to the α-proton of C10, with an isotropic coupling of –47.99 MHz.

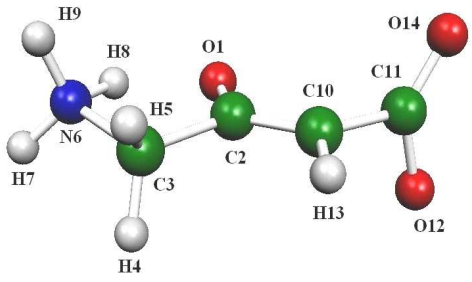

Fig. 5. Optimized structure of α-glycine radical V at B3LYP/6-311+G(d) level of calculation

Yet, our calculations at B3LYP/6-311+G(d) level do not agree with the experimental results. The isotropic coupling value of –19.99 MHz is significantly different from the reported value of –47.99 MHz. Single point calculations upon rotation of the α-proton around C10-C11 bond axis did not lead to any considerable improvement. The optimized structure of radical V is shown in Figure 5.

3.5. The nitrogen centered π radical

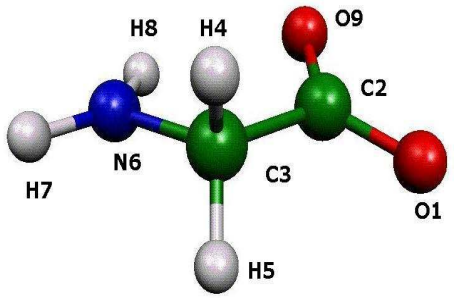

Fig. 6. The X-ray diffraction obtained structure of the α-glycine nitrogen centered π radical (NH_2 group planar)

The presence of this radical was first reported by Sinclair in 1971 in 77 K α-glycine spectra, warmed to 110 K and measured at 100 K [18]. Nunome et al. [21] reinvestigated the presence of this radical in the spectrum of α-glycine irradiated and measured at 77 K and they established that, at this temperature, the radical preserves the framework of the undamaged molecule, excepting the planarity of the NH_2 group. Because it was suggested that the radical preserves the structure of the undamaged molecule, all calculations were performed upon the X-ray diffraction obtained geometry of the α-glycine molecule. The NH_2 group was made planar by imposing the dihedral angles between H_7, N_6, C_3, C_2 and H_8, N_6, C_3, C_2 at the values of 180° and respectively 0° (figure 6). Single point calculations at B3LYP/6-31+G(d) level were performed by rotating the NH_2 group around the C_3-N_6 bond axis in steps of 18°, from 0° to 180°.

Table 3.

Calculated and available experimental values for the hyperfine coupling constants in α-glycine nitrogen centered π radical at B3LYP/6-31+G(d) level of calculation.

Atom	Calculated (G)		Experimental (G)	
	a_{iso}	B	a_{iso}	B
H_4	41.21	3.76 -1.58 -2.17	23.2	4.6 -1.7 -2.9
H_5	32.32	3.53 -0.87 -2.66	8-14	-
N_6	13.68	22.25 -11.25 -11.00	14.8	23.0 -11.2 -11.8
H_7	-18.88	-13.27 -4.35 17.62	-21.2	-8.6 -1.1 9.6
H_8	-17.84	-13.16 -4.32 17.48	-21.1	4.7 -1.7 -2.9

The best agreement with the experimental data for the CH_2 protons (24.36 G and 17.78 G) was achieved when the amino group was rotate with 8° around the C_3-N_6 bond axis; yet the hyperfine coupling values for the amino protons differ significantly from the experimental ones (-11.28 G and -10.77 G), probably due to the influence of the neighbouring intact molecules via the hydrogen bonds. Therefore we have considered 2 glycine molecules corresponding to the hydrogen bond of 1.83 A and 2,12 A between the oxygen atoms of the glycine molecule and the amino protons of the radical (H_7 and H_8). Single point calculations upon this system proved a significant

improvement in the isotropic hyperfine values for the amino protons but the corresponding values for the CH_2 protons deteriorated (Table 3).

Conclusions

In the present study, we have calculated the hyperfine coupling constants through the use of density functional theory for some of the radiation products of α-glycine irradiated at room temperature.

On the basis of the excellent agreement obtained between the calculated hfcc's and the available experimental values we confirm the structures proposed for α-glycine radicals I and II: NH_3^+-ĊH-COO^- and respectively $ĊH_2$–COO^-. Regarding the structure of radical III, relying on our results, we support the structure proposed by Sanderud et al. H_2 N-ĊH-COOH instead of that proposed by Brustolon et al.: NH_2 –$ĊH_2$. Anyway, we suppose that the slightly different values for the amino couplings are related to the matrix effects and to the reorientation of the radical molecule in the crystal matrix. Regarding the nitrogen centered π radical our results indicate that its structure does not change significantly from the undamaged glycine molecule, except the planarity of the amino group which slightly rotates around the C_3-N_6 bond axis. Yet, the hfcc's of the α and β protons are extremly sensitive to the matrix effects and therefore more complex calculations are required. Finally, the calculated isotropic couplings of the radical V do not match the experimental results assigned to this dimeric structure by Sanderud et al., H_3^+N-CH_2 –CO-ĊH-COO^- , the difference between calculated and isotropic values being considerable. Yet, recently, Ban et al. [10] have also investigated the radiation products of α-glycine and their results indicate that the radical V is more likely in nonzwitterionic form.

REFERENCES

[1] De Proft, F.; Martin, J.M.L.; Geerlings, P *Chem.Phys*. *Lett*, **1996**, 250, 393.
[2] Batra, R.; Giese, B.; Spichty, M.; Gescheidt, G.; Houk, K. N. *J. Phys. Chem*. **1996**, 100, 18371
[3] Adamo, C.; Barone, V.; Fortunelli, A. *J. Chem. Phys*. **1995**, 102 (1), 384.
[4] S.Vishveshwara, J.A.Pople, *J.Am.Chem.Soc*., **1977**, 99, 2422
[5] J.H.Jensen, M.S.Gordon, *J.Am.Chem.Soc*., **1991**, 113, 7917
[6] Barone, V. *Recent Advances in Density Functional Methods*, World Scientific Publishing, Singapore, **1995**, Chapter 8, p.287-334.; V. Barone, C.Adamo, F.Lelj, *J.Chem.Phys*., **1995,** 102, 364
[7] L.Rodriguez-Santiago, M.Sodupe, A.Oliva, J.Bertran, *J.Phys.Chem*. A, **2000**, 104, 1256
[8] Rega, N.; Cossi, M; Barone, V. *J. Am. Chem. Soc*. **1998**, 120, 5723;
[9] Tureček, F.; Carpenter, F. H. *J. Chem. Soc*., **1999**, 2315;
[10] Ban, F.; Gauld, W.J.; Boyd, J.R. *J. Phys. Chem*. A **2000**, 104, 5080-5086.
[11] Morton, J. R. *J. Am. Chem. Soc*. **1964**, 86, 2325.
[12] Hedberg, A.; Ehrenberg, A. *J. Chem. Phys*. **1968,** 49, 11, 4822.
[13] Syutkin, V. M.; Tolkatchev, V. A. *Chem. Phys. Lett*. **1985**, 122, 3, 201.
[14] Brustolon, M.; Chis, V.; Maniero, A. L. *J. Phys. Chem*. A **1997**, 101, 4887.
[15] Sanderud, A.; Sagstuen, E. *J. Phys. Chem* B **1998**, 102, 9353.

[16] M. J. Frisch, G. W. Trucks, H. B. Schlegel, G. E. Scuseria, M. A. Robb, J. R. Cheeseman, V. G. Zakrzewski, J. A. Montgomery, Jr., R. E. Stratmann, J. C. Burant, S. Dapprich, J. M. Millam, A. D. Daniels, K. N. Kudin, M. C. Strain, O. Farkas, J. Tomasi, V. Barone, M. Cossi, R. Cammi, B. Mennucci, C. Pomelli, C. Adamo, S. Clifford, J. Ochterski, G. A. Petersson, P. Y. Ayala, Q. Cui, K. Morokuma, D. K. Malick, A. D. Rabuck, K. Raghavachari, J. B. Foresman, J. Cioslowski, J. V. Ortiz, B. B. Stefanov, G. Liu, A. Liashenko, P. Piskorz, I. Komaromi, R. Gomperts, R. L. Martin, D. J. Fox, T. Keith, M. A. Al-Laham, C. Y. Peng, A. Nanayakkara, C. Gonzalez, M. Challacombe, P. M. W. Gill, B. Johnson, W. Chen, M. W. Wong, J. L. Andres, C. Gonzalez, M. Head-Gordon, E. S. Replogle, and J. A. Pople, *Gaussian 98*, Revision A.6Gaussian, Inc., Pittsburgh PA, 1998.
[17] Raiti, M. J.; Sevilla, M. D. *J. Phys. Chem. A* **1999**, 103, 1619.
[18] Sinclair, J. *J. Chem. Phys*. **1971**, 55, 245.
[19] Collins, M.A.; Whiffen D. H. *Mol. Phys*. **1966**, 10, 317.
[20] Teslenko, V.V.; Gromovoi, Yu.S.; Krivenko, V.G. *Mol. Phys*. **1975**, 30, 425.
[21] Nunome, K.; Muto, H.; Toriyama, K.; Iwasaki, M. *J. Chem. Phys*. **1976**, 65, 10, 3805;

STUDIA UNIVERSITATIS BABEŞ-BOLYAI, PHYSICA, XLIX, 3, 2004

EPR SPIN TRAPPING INVESTIGATION OF RADICALS GENERATED IN THE COMPLEX FENTON REACTION

G. DAMIAN[1], V. MICLĂUŞ[2], DINA SITAR[1], S.SIMON[1]

[1]*"Babes-Bolyai" University, Department of Physics, Cluj-Napoca, Romania*
E-mail: dgrig@phys.ubbcluj.ro
[2]*"Babes-Bolyai" University, Department of Chemistry, Cluj-Napoca, Romania*

ABSTRACT. The study of formation and reaction of some radicals generated via Fenton reaction in the presence of cetearyl alcohol and lauric acid, using a commonly encountered nitrone spin trap, N-t-Butyl-α-phenylnitrone (PBN) releave that HO radicals are not the dominant reactant at all. Possibly hydroxyalchyl radicals were generated in situ due to attack of hydroxyl radical on the long chains alcohols and/or from acetone. A relatively stable PBN-trapped species with spin label characteristics, was observed after seven days.

Introduction

Free radicals are chemical species that possess an unpaired electron in the outer shell of the molecule. In principle, they can be generated both in-vivo and in-vitro by three main mechanisms: (i) homolytic cleavage of a covalent bond, in which a normal molecule fragments in two, each fragment retaining one of the paired electrons [1, 2]. This mechanism occurs less commonly in biological systems, because it requires high-energy input from ultra-violet light, heat or ionising radiation, (ii) loss of a single electron from a normal molecule and (iii) addition of an electron to a normal molecule.

The fact that they have open shell configuration are unstable, short-lived, and highly reactive with low chemical specificity; i.e. they can react with most molecules or atoms in its vicinity and new radicals are created beginning a chain reaction. Reactions involving free radicals are usually divided into three categories: initiation, propagation, and termination. Initiation reactions are those which result in a net increase in the number of free radicals. They may involve the formation of free radicals from stable species or they may involve reactions of free radicals with stable species to form more free radicals . Propagation reactions are those reactions involving free radicals in which the total number of free radicals remains the same. Termination reactions are those reactions resulting in a net decrease in the number of free radicals. Typically two free radicals combine to form a more stable species.

A fundamental fact about free radicals is that the unpaired electrons in their outer shells do not affect the charge on the resultant molecule [3,4]. Thus, free radicals can be negatively charged, positively charged or electrically neutral. This is because charge is concerned with the number of negatively charged electrons in relation to the positively charged protons whereas free radicals are related only to the spatial arrangement of the outer electron. The unpaired electron may have

been gained on top of a neutral molecule making it negative; alternatively, it may have resulted from the loss of an electron from the same molecule resulting in a positive charge. Likewise, if the original molecule were not neutral to begin with the addition or removal of an unpaired electron would result in a neutral charge.

The increase of interest in the role of free radicals in the chemical proceses and pathogenesis of disease had led to an increased need for techniques to measure free radicals and their reactions in vivo [5, 6]. The fact that in free radicals, the unpaired electron is involved, these species are paramagnetic, thus the most used method for detecting free radicals is electron paramagnetic resonance spectroscopy (EPR). When an unpaired electron in a magnetic field interacts with a nuclear spin, the spectrum splits into two or more lines, which produce hyperfine structure in the spectrum. The splitting of the spectrum is expressed in terms of a hyperfine coupling constant (A value in G or mT units), and the relative position of the spectrum is expressed by the spectroscopic spliting factor (*g* value, dimensionless).

There exist two posibilities to use EPR spectroscopy in detection of the free radicals, depending on the they mobility and on the phase of the system in which are generated. In case of solid systems, free radicals can be detected directly due to low capacity to combine [7].

In the liquid or gas phase two several problems arise when considering measurement of free radicals: First the ultra-short half-life of these radicals (usually measured in microseconds). Second any free radicals produced in vivo react at or close to their source of formation. Therefore it is necessray to use a diamagnetic reagent named “spin trap” and to produce, a relatively persistent product radical “spin adduct” which can be studied by conventional EPR (indirect detection) [8-10]. The intensity of the spin adduct EPR signal corresponds to the amount of short-lived radicals trapped, and the hyperfine splittings of the spin adduct are generally characteristic of the original, short-lived, trapped radical. A third problem is that many of these end products are in themselves reactive although to a lesser degree. Free radicals attack aromatic compounds and therefore the nitrones can be used to react with transient radicals to form longer-lived nitroxides (spin trapping). The nitrone spin trap is widely used to provide evidence for the involvement of free radicals in many biological and chemical reactions.

One of the most studied free radical species is hydroxil radical. The hydroxyl radical is an extremely reactive oxidising radical that will react to most biomolecules at diffusion controlled rates, which means that reactions will occur immediately with biomolecules [11]. The hydroxyl free radical is important in radiobiological damage and is several orders of magnitude more reactive towards cellular constituents than superoxide radicals (and many orders more reactive than hydrogen peroxide).

Materials and Methods

A solution of 1 mM ferrous sulfate in water with molar extinction coefficient of 43.6 M^{-1} cm^{-1} at 240 nm, has been deoxygenated using nitrogen bubbling. The hydroxyl radical was generated by addition of 1 mM Fe^{2+} to the reaction mixture. (Fenton reaction). The spin trap N-t-Butyl- α-phenylnitrone (PBN) was solved in acetone. The hydrogen peroxide was conditioned as a 6% oxi cream with EDTA,

cetearyl alcohol and lauric acid ($CH_3(CH_2)_{10}COOH$). Cetearyl alcohol is a mixture of fatty alcohols consisting predominantly of cetyl alcohol ($CH_3(CH_2)_{14}CH_2OH$) and stearyl alcohol ($CH_3(CH_2)_{16}CH_2OH$).

Samples were measured using 20 mm length, 1 mm inside diameter quartz capillary.

EPR spectra were recorded at room temperature with a PORTABLE EPR SPECTROMETER, PS 8400, Resonance Instruments Inc., operating in the X-band (~9.5 MHz) and equipped with a computer acquisition system. The spectrometer settings used for the experiments were as follows: modulation frequency, 100 kHz; modulation amplitude $2x10^3$; sweep width, 100 G; sweep time, 300 s; receiver gain $5x10^2$; number of data points, 4096.

Results and Discussion

We have investigated the formation and reaction of some radicals generated via Fenton reaction (Scheme 1) in the presence of cetearyl alcohol and lauric acid, using a commonly encountered nitrone spin trap, N-t-Butyl- α-phenylnitrone (PBN). The classical Fenton mechanism predicts that hydrogen peroxide is reduced at the iron center with generation of free hydroxyl radical [3]. The reaction has the same pattern when even ligands are included:

$$Fe^{+2} + H_2O_2 \longrightarrow Fe^{+3} + OH^- + {}^{\bullet}OH$$

$$Fe(H_2O)_6^{+2} + H_2O_2 \longrightarrow [Fe(H_2O)_5OH]^{+2} + OH^- + {}^{\bullet}OH$$

Scheme 1.

The nitrones used as spin traps, N-t-Butyl- α-phenylnitrone (PBN) is a stable compound and forms relatively long-lived spin adducts with various types of radicals as in Scheme 2.

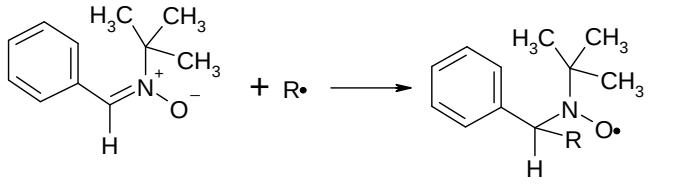

PBN PBN/R•

Scheme 2. Formation of spin aduct with PBN

Experiments in the presence of the spin trap gave complex results (Fig. 1). From spectra analysis by computer simulation, it can be concluded that HO radicals are not the dominant reactant at all (Fig. 1). Possibly hydroxyalchyl radicals were generated in situ from acetone. We assume that an attack of hydroxyl radical on the long chains alcohols was also employed. One of the most important drawbacks of this nitrone is that the EPR spectra of the various amin-oxyl spin adducts are not very characteristic of the radical trapped [4]. The difference in the EPR signal total width of methyl, hydroxyethyl and acetyl radical spin adducts of PBN (PBN-CH_3, PBN-$CH(OH)CH_3$•, PBN-$COCH_3$• respectively) can be evaluated only by computer

simulation. A direct evidence of characteristic different spin adducts can be, probably, observed by NMR spectroscopy after the reduction of the species to the corresponding hydroxylamines.

The $Fe^{2+}/EDTA/H_20_2$ hydroxyl radical generating system produced the hydroxyl radical spin trap PBN-OH (A_N = 15.2 G, a_H = 3.2 G). The PBN-OH adduct signal was less intense after few days (Fig. 2). A relatively stable PBN-trapped species PBN-R, where R denotes an unknown radical, was observed. The EPR signal from PBN- R decays slowly over the course of several days. The adduct had hyperfine splitting constants of A_N = 15.8 G and a_H = 2.9 G corresponding to neither PBN-OOH nor PBN-OH most probably due to PBN-CH_3 trapped in the solid matrix. During evaporation of the acetone the EPR spectra resambles more to a spectra of stable nitroxide radicals (where R=CH_3 in the scheme 2).

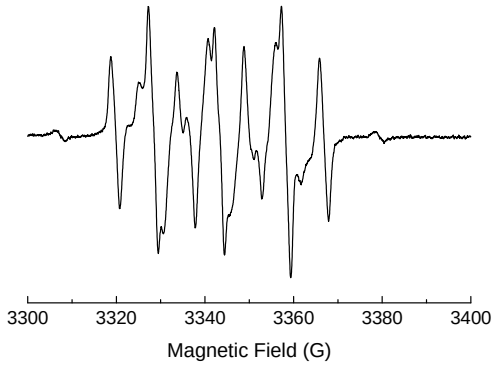

Fig. 1. EPR spectrum of. spin-aduct-PBN in Fenton reaction was solved in acetone and conditioned with 6% oxi cream with EDTA, cetearyl alcohol and lauric acid

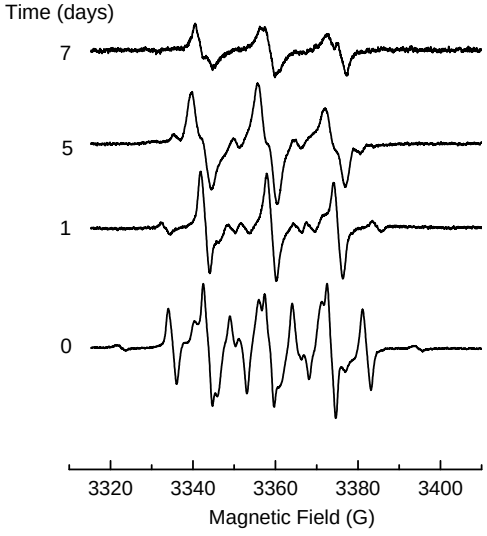

Fig. 2. EPR spectra of free radicals generated in complex Fenton reaction using spin trapping PBN during acetone evaporation

Conclusion

The Fenton reaction in complex systems generates different radicalic species.

The nonspecific spin trap N-t-Butyl- α-phenylnitrone (PBN) is able to trap some species. Beside the well-known OH• radical, EPR spectra shown the existence of some carbon centered radicals, such CH_3•, $CH(OH)CH_3$•, $COCH_3$• giving the related spin adducts. The obtained spin adducts have specific features expressed by different living-times. Thus, during the EPR measurements, we observed a time dependence of the spectral characteristics and signal intensities. We assumed that the longest life time spin adduct, has the structure PBN/CH_3•, due to similar structure and magnetic parameters with a stable spin label.

REFERENCES

1. Leigh GJ. Ed. (1990), *Nomenclature of inorganic chemistry. Recommendations 1990.* Oxford:, Blackwell Scientific Publications.
2. Koppenol WH. (1990), What is in a name? Rules for radicals. *Free Radic. Biol. Med.* 9:225-227.
3. Trynham JG. (1986), A short guide to nomenclature of radicals, radical ions, iron-oxygen complexes and polycyclic aromatic hydrocarbons. *Adv. Free Radic. Biol. Med.* 2:191-209.
4. OLINESCU R., Œ Radicali liberi in fiziopatologia umana. Seria ieMedicinalg. Editura Tehnica, Bucuresti, 1994.
5. George V. Buxton, Clive L. Greenstock, W. Phillip Helman, and Alberta B. Ross, *J. Phys. Chem. Ref. Data*, 17(2):513-886, 1988. Reprint No 343.
6. Halliwell, B. and Gutteridge, J. M. C. (1989), Free Radicals in Biology and Medicine, 2nd edn, Clarendon Press, Oxford.
7. G.Damian, *Talanta, 60(2003) 923-927.*
8. P. Bilsky, K.Reszka, M. Bilska, C.F. Chignell J. Am. Chem. Soc., 1996, 118, 1330-1338.
9. R.V.Lloyd, P.M. Hanna, R.P. Mason Free Radical Biology & Medicine, 1997, 22, 885-888.
10. J.M.Coxon, B.C.Gilbert, R.O.C. Norman J. C. S. Perkin II, 1981, 379 –381.
11. Walee Charnulitrat, Sandra J. Jordan, Ronald P. Mason, Kieko Saitoy, and Richard G. Cutlery, The Journal of Biological Chemistry, 268,16, (1993) 5, 11520-11527.

STUDIA UNIVERSITATIS BABEŞ-BOLYAI, PHYSICA, XLIX, 3, 2004

ELECTRON PARAMAGNETIC RESONANCE AND SPECTRO-PHOTOMETRIC DETERMINATION OF THE CD-TEMPOL FREE RADICAL IN REACTION WITH ASCORBIC ACID

V. MICLĂUŞ[1], G. DAMIAN[2], ANAMARIA HOSU[1] AND L. GIURGIU[3]

[1]"Babeş-Bolyai" University, Department of Chemistry, Cluj-Napoca, miclaus@chem.ubbcluj.ro
[2]"Babeş-Bolyai" University, Department of Physics, Cluj-Napoca
[3]National R&D Institute of Isotopic and Molecular Technologies, Cluj-Napoca

ABSTRACT. β-Cyclodextrin (β-CD) was used as a "host" molecule in molecular incapsulation of Tempol (4-hydroxy-2,2,6,6-tetramethylpiperidin-N-oxyl). The inclusion complex tempol: β-CD was prepared in ethanol, using the slurry method. The complex was separated and monitored in reaction with ascorbic acid through EPR spectroscopy. The changes of the paramagnetic centers from the mixture, in the EPR spectra, depend on the disposition of Tempol's molecules related to cyclodextrin's cavity. An estimation of the stable free radical Tempol simultaneously performed by electron paramagnetic resonance (EPR) and visible spectrophotometric reduction is also reported.

Keywords: β-Cyclodextrin, ascorbic acid, EPR spectroscopy, Tempol

1. Introduction

Cyclodextrins (CD) are chemically and physically stable molecules formed by the enzymatic modification of starch with empirical formula $(C_6H_{10}O_5)_7$ and is basically a carbohydrate. There exist three main types of the cyclodextrins, namely: α-CD, β-CD and γ-CD, with different inner cavity size 5.7 Å, 7.8 Å and 9.5 Å respectively.

β-CD's are oligosaccharide consisting of seven α(1-4)-linked D-(+)-glucopyranose units. It is cyclic compound obtained by enzymatic fermentation of starch. It has the form of short truncated con with the wide and the narrow rims occupied by the secondary (2- and 3-OH groups) and primary (6-OH groups) hydroxyls groups, respectively. The central cavities of these molecules are hydrophobic in nature, but the external faces are hydrophilic [1]. β-CD is known because of their ability to form inclusion complexes with a wide variety of molecules, based on physical fit and chemical affinity [2]. We prepared inclusion complexes β-CD – Tempol.

In this paper we studied if the complex cyclodextrine-nitroxide radicals are formed and what are the rate of antioxiding of inclusion complex using EPR spectroscopy. As antioxidant agent we have used ascorbic acid. Ascorbic acid, or ascorbate, is an antioxidant because of the high reducing potential of its carbon-carbon double bond, which readily donates one or two hydrogenous and electrons to a variety of oxidants, including oxygen free radicals, peroxides, and superoxide. It has been known that nitroxides strongly react with ascorbic acid giving raise to unparamagnetic species [3-5]. By EPR spectroscopy we monitoring the changes of the EPR spectra in the reduction with ascorbic acid of the paramagnetic center.

2. Experimental

Tempol (2,2,6,6-tetramethyl-4-hydroxypiperidine- oxyl) obtained from Fluka (p > 97%), β-CD and ascorbic acid were used without any treatment in advance. The ethanol used as solvent was analytically pure. Inclusion complexes were prepared in ethanol with excess of Tempol by slurry method [1]. The compounds were precipitated and then they were collected by filtration. The filtration was performed into a quartz tube in which it was fixed a frit disc.

To avoid sedimentation, the suspension obtained was rapidly injected into the tube. The precipitate from the disc was washed with ethanol and then it was analyzed by EPR Spectroscopy.

EPR spectra were registrated at room temperature with the aid of a X band (~9.5MHz) RADIOPAN ESR spectrometer (National R&D Institute of Isotopic and Molecular Technologies, Cluj-Napoca*)* with a field modulation of 100 KHz. Plotted data stored in graphics spectra, were digitized using freely distributed TRACER 1.2 program written by Marcus Karolewski (karolewski@alum.mit.edu).

The computer simulation analysis of the spectra was made by using WINSIM2002 program that is available to the public through the internet (http://alfred.neihs.nih/LMB) for obtaining the magnetic characteristic parameters. The variation of the relative concentration of radical species were obtained through double integration of the experimental spectra.

The spectrophotometric measurements in the region 12 500–30 000 cm^{-1} were performed with a SPECORD UV-VIS (Carl-Zeiss, Jena) spectrophotometer using standard 5 cm quartz cells.

3. Results and Discussions

We suppose that there are many possibilities for attach the radical: with oxyl group into the cavity of β-CD, with hydroxyl group into the cavity of β-CD and the third case when Tempol's molecules don't penetrate the cavity so they are adsorbed at/on the surface of β-CD molecules.

To evaluate the ability of β-CD to bind Tempol's molecules the solution obtained after the filtration was analyzed. The quantity of Tempol that was bind was determinate using the UV calibration curve for Tempol (λ=244nm) The electronic spectrum of TEMPOL in the visible region is characterized by an absorption maximum and its intensity was chosen as a measure of the free radical concentration (Fig.1.).

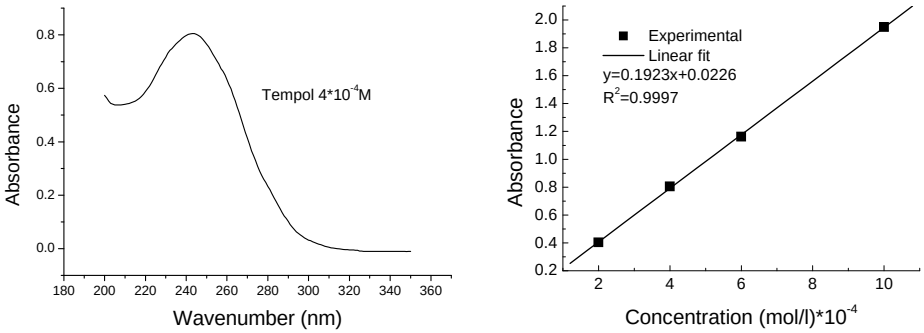

a) b)

Fig. 1. Tempol's UV spectrum (a) and calibration curve (b)

We obtained that the molar ratio β-CD: binded Tempol is 1:2.25 (the initial molar ratio β-CD: Tempol was 1:4,2; this sustains the supposition that there are many possibilities to attach Tempol.

For the reaction between Tempol and ascorbic acid the following mechanism (Scheme 1) is accepted [6, 7].

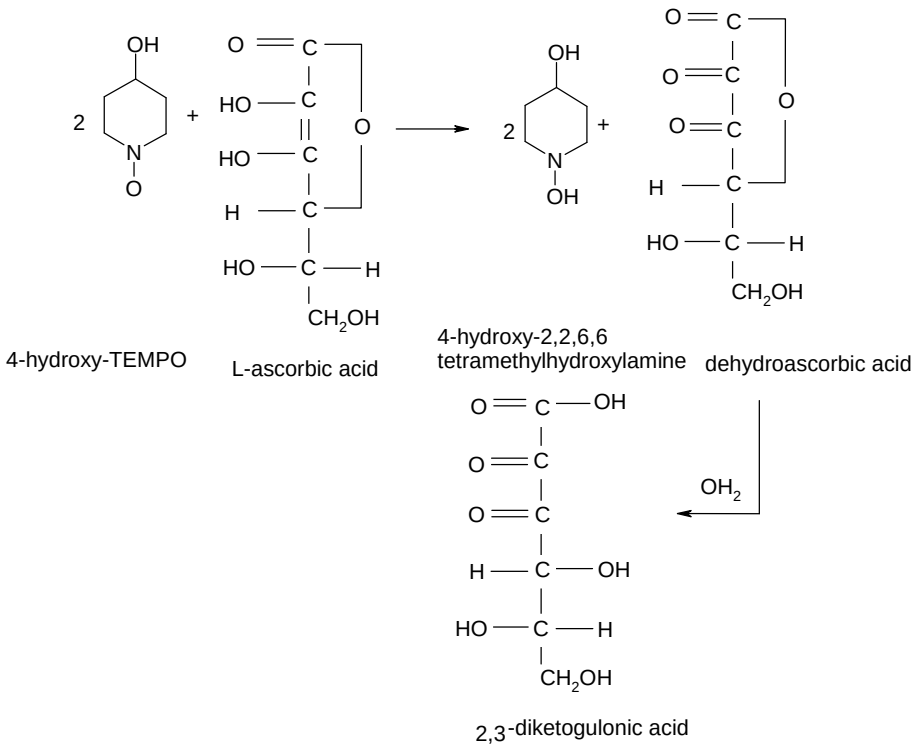

Scheme 1. Reaction mechanism between 4-hydroxy-Tempo and ascorbic acid

The reaction is quantitatively completed to the products. The reaction proceeds with the consumption of two moles of nitroxide per mole ascorbic acid [8]. The final products are 4-hydroxy-2,2,6,6-tetramethylhydroxylamine from the nitroxide and dehydroascorbic acid. The obtained dehydroascorbic acid cannot be converted back under these conditions.

The precipitate from the disc will react with ascorbic acid. The solution of the ascorbic acid in ethanol was injected into the tube in small portion (1mL). Part of a portion was injected over the precipitate and the rest was injected under the precipitate.

The EPR spectrum of Tempol consists of three hyperfine lines due to the interaction of the unpaired electron with the nitrogen nucleus and the changes of their intensity in the course of reaction were monitored.

The EPR spectra of nitroxide spin label starting after ascorbic acid titration, consist of two spectral parts; the part has a line shape, resembling the powder spectrum of the rigid matrix and is typical for slow isotropic rotational motion asumed to inclusion complex[9,10]. The part of the spin label spectrum (marked with an asterisk) is typical for faster isotropic rotational fluctuations atributed to free radical nitroxide in solution (Fig 2).

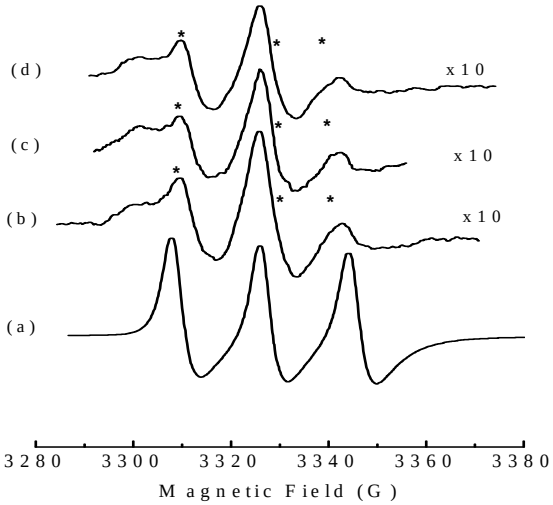

Fig. 2. EPR spectra of ethanolic spin label Tempol-βCD complex (a) before ascorbic acid titration, (b) after 15 minutes, (c) after 30 minutes and (d) after 35 minutes

The changes in the concentration of the spin label due reaction with ascorbic acid at different time intervals were obtained by double integration of the EPR signal and represented in Fig. 3. It was found that the rate of the reaction between ascorbic acid andthe nitroxide radical is very fast.

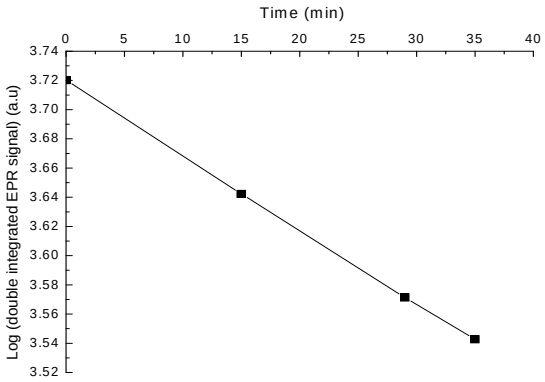

Fig. 3. The plot of the dependence between double integrated EPR spectrum of β-CD-Tempol complex in presence of ascorbic acid at differents time intervals

The spectrophotometric data showed gradually decreasing absorbance of Tempol at 22 900 cm^{-1} with the appearance of one isosbestic point at 27 180 cm^{-1} upon addition of ascorbic acid suggesting a neat conversion of Tempol to ist hydroxylamine derivative (Fig. 3). Similar, for the first part of reaction between ascorbic acid and β-CD -Tempol, a linear decrease of the EPR intensity of Tempol was found. In the second part, the reaction rate was much lower probably due to the limitative equilibrium constant of disociation of the complex β-CD - Tempol.

3. Conclusion

It may be concluded that estimations performed by both methods are in good agreement and may be used as a future criterium about the degree of complexation guest molecule–β-cyclodextrine. The EPR spectroscopy can give informations about degree of hydrophobicity of inner cyclodextrins and UV spectrophotometry degree of complexation.

REFERENCES

1. O 'Souza V.T., Lipkowitz K.B.,(Eds.).*Chem.Rev*., 98,1741, 1998.
2. Bender M.L., Komiyama M., *Cyclodextrin Chemistry* Springer Verlag:Berlin,1978.
3. Graziella Vecchio, Diego La Mendola and Enrico Rizzarelli, *Journal of Supramolecular Chemistry* 1, 87 –95, 2001.
4. C. Ebel, K.U. Ingold, J. Michon, A. Rassat, *Nouv. J.Chim*. 9, 479-487, 1985.
5. N. D. Yordanov , K. Ranguelova, *Spectrochimica Acta Part A* 56,373–37, 2000.
6. C.M. Paleos, P. Dais, *J. Chem. Soc. Chem. Commun*. 345, 1977.
7. Bors W, Buettner GR., The vitamin C radical and its reactions in *Vitamin C in Health and Disease*, ed. by L. Packer and J. Fuchs, Marcel Dekker, Inc, New York, Chapt. 4, 75-94, 1997.
8. M. Okazaki, K. Kuwata, *J. Phys. Chem*. 89, 4437, 1985.
9. L.J. Berliner (Ed.), *Spin Labeling: Theory and Applica-tions*, Academic Press, New York, 507, 1976.
10. Lucien Marx, Robert Chiarelli, Thierry Guiberteau, André Rassat *J. Chem. Soc*., *Perkin Trans.* 1, 1181, 2000.

STUDIA UNIVERSITATIS BABEŞ-BOLYAI, PHYSICA, XLIX, 3, 2004

β-CYCLODEXTRIN AND THE ANIONIC A-DNBP IN DMSO SOLUTION

C. FLOARE[1,3], S. ASTILEAN[2], M. BOGDAN[1] and O. COZAR

[1]National Institute for Research and Development of Isotopic and Molecular Technologies, P.O. Box 700, RO-3400, Cluj-Napoca, Romania.
[2]Babeş-Bolyai University, Faculty of Physics, Kogălniceanu 1, RO-3400 Cluj-Napoca, Romania.

ABSTRACT. 2-(2',4'-Dinitrobenzyl)-pyridine is a photochromic molecule presenting a proton transfer reaction from the methylene group to the nitrogen of the pyridine, both in solution and in the crystalline state. Its photochromism in solution depend on the solvent characteristics as: his polarity, his protic character (tendency of liberating a proton), or on his hydroxylic properties (aptitude of creating hydrogen bonds solute-solvent). In this report, the disappearing of the stable anion of α-DNBP in dimethyl sulfoxyde solution is investigated at the addition of β-cyclodextrin. This comportment is compared with the similar effect observed in the presence of water.

Key words: α-DNBP anion, DMSO, β-cyclodextrin.

1. INTRODUCTION

2-(2',4'-Dinitrobenzyl)-pyridine (αDNBP) is known to show photochromism since 1925 [1]. This phenomenon results from a photoinduced intramolecular proton transfer (PIPT) reaction from the methylene group to the nitrogen of the pyridine, after irradiation in the near-UV spectral region, and takes place both in the crystalline state and in solution. Scheme 1a shows the proposed reaction mechanism in solution and the tautomers of α-DNBP: the thermodynamically stable 'CH_2' form, the 'NH' quinoid and the 'OH' aci-nitro forms, and the anion. The metastable NH tautomer is relatively long-lived (4.7 s in ethanol [2] at 298 K and about 4.6 h in the crystal [3,4]) and absorbs in the visible (λ_{max}=550 nm). Systems of this kind have attracted renewed attention in recent years [2-6], because they represent the basis of optical switches in optical data processing and data-storage applications.

In solid state, the tautomerization process can take a direct path, $CH_2 \rightarrow NH$, or an indirect path through OH intermediate states, $NH \rightarrow OH \rightarrow CH_2$ [6]. Previous semi-empirical and DFT calculations have shown that in both cases, the *o*-nitro group, play an essential role either as an active intermediate, OH, or as a chaperon that escorts the moving proton along a hydrogen bond, thus lowering the barrier along the direct path [7-8]. In solution, another way for the proton transfer becomes possible, as we can see in Scheme 1, via the anion. For solvated γ-DNBP, where the nitrogen of the pyridine ring is in the *para* position, this will remain the only way by which the NH quinoid form is produced [9].

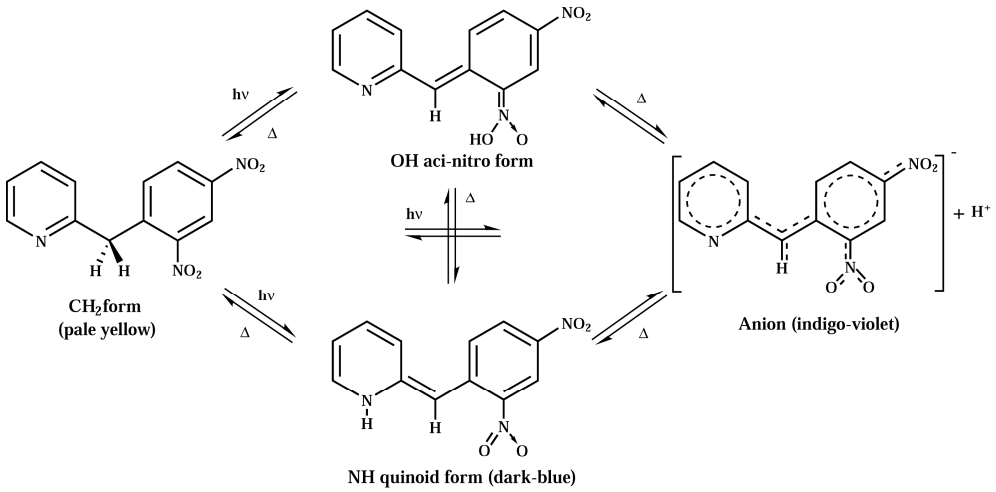

Scheme 1. – Photochromic mechanism for α-DNBP in solution.

The cyclodextrins are the well known cyclic oligosaccharides composed of 6, 7 or 8, α-1,4-linked, glucopyranose units (α-, β- and γ-cyclodextrines), having a toroidal shape, which can form inclusion compounds encapsulating a wide variety of molecules.

In this article we report the disappearing of the anionic form of αDNBP existing in dimethyl sulfoxyde (DMSO) solution at the addition of β-cyclodextrin (βCD). This comportment is compared with a similar effect observed in the presence of water.

2. EXPERIMENTAL

αDNBP (Lancaster Synthesis) was purified by repeated crystallization from ethanol. DMSO (Fluka) was spectrophotometric grade containing a maximum of 0.3 % water. βCD (ACROS ORGANICS) was used as received. The water was simply distilled. At the beginning we have prepared a 3.86 mM stock solution, dissolving 1mg α-DNBP per ml DMSO. The equilibrated solution had a stable indigo-violet colour, due to the presence of the anionic α-DNBP. At this solution we added increasing amounts of water or of β-cyclodextrin.

The total concentration of the anion was determined by absorbance measurements with a SPECORD UV VIS spectrophotometer (Carl-Zeiss, Jena).

3. RESULTS AND DISCUSSION

The equilibrium between the photochemically produced αDNBP tautomers in solution [10-11] is known to be solvent dependent, shifting toward the aci-nitro and/or quinoid forms in non-polar solvents and toward anion form in polar solvents. The anionic form of αDNBP, the subject of this article, has been also produced chemically in basic media [12].

Even if we couldn't found any reference dealing with αDNBP in DMSO solution, due to the similarity of its absorption spectrum, having two bands with maxima centered at 498 nm and 665 nm, with that of the anion found in literature [10-12],

and because it was stable during two hours in the dark, we have concluded that, in this solvent, αDNBP is mainly deprotonated. We think that this behavior is a consequence of the fact that, DMSO is a highly polar molecule (dipole moment 3.9 debye), being known to have a great affinity for cations, and especially for protons (H^+). For comparison, we mention that the life-time of the αDNBP anion photochemically produced in acetonitrile, aprotic solvent which have a dipole moment of 3.5 debye, is 15 s [5].

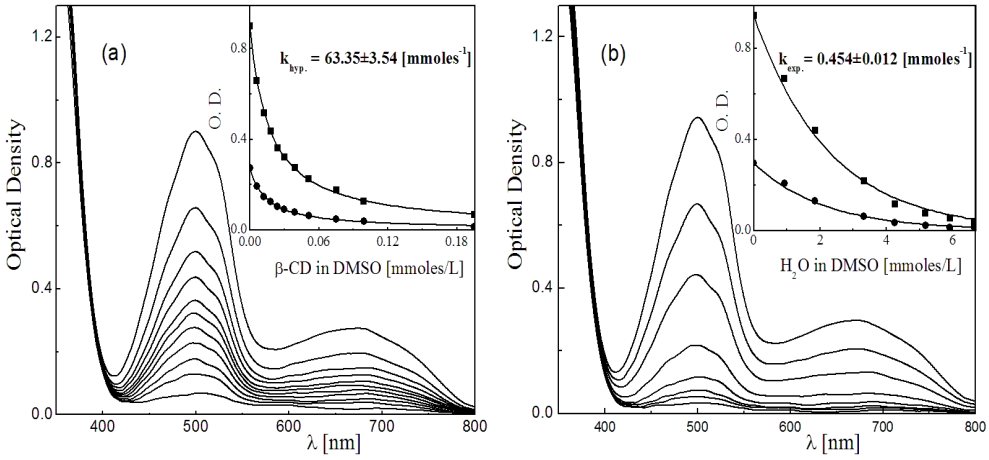

Fig. 2. The disappearance of the αDNBP anion in DMSO solution at the addition of βCD (a) or water (b). The inset contains the variation of the optical density at the maximums of the absorption bands situated at 498 and 667 nm. The reaction rate constants obtained form the fit of these values using a hyperbolic dependence (a) or an exponential one (b), are also presented.

Because DMSO dissolves βCD up to 40 g/100 mL at 25℃ [13], the starting idea was to investigate a possible formation of an inclusion complex between αDNBP anion and βCD. We added, gradually, increasing amounts of βCD, and after each solubilization and equilibration, one spectrum was acquired. In Figure 2a we present the spectra obtained. As we can see, the solution fades gradually until it becomes transparent. No visible shift of the two absorption bands is observed, only the progressive disappearing of the anion. This effect is clearly due to the fact that, when βCD appear, the DMSO molecules will preferentially form hydrogen bonds with βCD hydroxyl groups and with the water with which βCD is normally crystallized [14], leaving the engine proton of the photochromic mechanism of αDNBP to this molecule. However, this effect turn to be interesting if we look at the molar ratios between the molecules involved, αDNBP, DMSO, βCD and water, which varied in the range 1:3572:(1.5-25.6):(18.4-307), where we have also considered the water of crystallization of βCD. At the beginning, when the first quantity of βCD was added, even if we had approximately 50 DMSO molecules for every hydroxyl group, counting all 21 of βCD and 2 for water, the concentration of the αDNBP anion decreased. Moreover, as we can see in the small window inserted in Figure 2 (a), where we represent the

evolution of the optical density corresponding to the two absorption maximums, function of the quantity of βCD added per liter DMSO, the disappearing of the anion is more accentuated at small concentrations of βCD and diminishes at high concentrations. To understand this behavior, we remember that, at room temperature where all these spectra were taken, the energy of molecules (k_BT=0.6 kcal/mol) is sufficient to break hydrogen bonds, which range between 3 and 7 kcal/mol [15]. Consequently, water and βCD molecules are diffusing in this environment, decreasing to some extent the capacity of the DMSO molecules to keep the proton taken from αDNBP. Additionally, at small concentrations theirs mobility is greater than when the solution becomes saturated.

The recombination of the anion being essentially a bimolecular process between the anion and the protonated DMSO, influenced by the quantity and the diffusivity of water and βCD molecules, was found to follow a hyperbolic law:

$$c_{anion}(c_{\beta CD}) = c_{anion}(0)/(1+k_{hyp.}c_{\beta CD}), \quad (1)$$

where $c_{anion}(c_{\beta CD})$ is the concentration of the anion, $c_{\beta CD}$ the concentration of βCD and $k_{hyp.}$ the reaction rate constant.

Since βCD contains water as mentioned, subsequently we performed a similar analysis adding only water at the initial stock solution. As we can see in the Figure 2 (b), the αDNBP anion disappeared as well but in this case, the kinetics of reaction is different. Even if primarily we used also a hyperbolic function to fit the experimental values of optical densities of both bands maximums obtained for different concentrations of water, this function didn't performed well, the dependence being in this case exponential:

$$c_{anion}(c_{H_2O}) = c_{anion}(0)\exp(-k_{\exp.}c_{H_2O}) \quad (2)$$

The coefficient of determination describing the goodness of fit was greater than 0.995, the two reaction rate constants obtained being also presented in Figure 2.

The fact that the stoichiometric ratio water/DMSO at which the anion disappeared entirely, was determined to be just about 1:2, tell us that this effect occur when every DMSO molecule will be 'hydrogen bonded' with water, two of them for every water molecule, being a logical and intuitive result.

Because, as mentioned, no visible shift of the absorption maxima is observed, we can't say anything about a probable supramolecular complex between αDNBP and β-CD.

Finally, as applicability, we suppose that this method can be used in a general manner to determine the reaction rate constants corresponding to a broad range of other molecules containing hydroxyl groups or which are soluble in DMSO. The temperature dependence of this parameter can be other interesting domain to examine.

4. CONCLUSIONS

The decrease of the αDNBP anion concentration in dimethyl sulfoxyde solution was investigated at the addition of βCD and water, using absorption spectroscopy. The dependence of the optical densities at the wavelengths 498 and 667 nm function of the concentration of βCD or water has been adjusted using a hyperbolic and respectively an exponential law and the reaction rate constants have been determined to be: $k_{hyp.} = 63.35 \pm 3.5$ mmoles^{-1} et $k_{exp.} = 0.45 \pm 0.01$ mmoles^{-1}.

We suggested that this method can be used to determine the reaction rate constants for broad range of other molecules containing hydroxyl groups or which are soluble in DMSO.

Acknowledgements. The financial support received from 'Laboratoire de Spectrométrie Physique', Joseph-Fourier University, Grenoble, France, and that received as a MIRA scholarship (Rhones-Alpes, France) is gratefully acknowledged. C.F. would like to thank to Professor H.P. Trommsdorff for his helpful advice.

REFERENCES

1. Tschitschibabin, A. E.; Kuindshi, B. M.; Benewolenskaja, S. W. *Ber. Dtsch. Chem. Ges.* 58, 1580 (1925).
2. Eichen, Y.; Lehn, J.-M.; Scherl, M.; Haarer, D.; Casalegno, R.; Corval, A.; Kuldova, K.; Trommsdorff, H. P. *J. Chem. Soc., Chem. Commun.* 7,713 (1995).
3. Scherl, M.; Haarer, D.; Fischer, J.; DeCian, A.; Lehn, J-M.; Eichen, Y. *J. Phys. Chem.* 100, 16175 (1996).
4. Corval, A.; Kuldova, K.; Eichen, Y.; Pikramenou, Z.; Lehn, J. M.; Trommsdorff, H. P. *J. Phys. Chem.* 100, 19315 (1996).
5. Kuldova, K. *PhD. Thesis* 1997, Laboratoire de Spectromètrie Physique, Univeristé Joseph Fourier, Grenoble 1, France.
6. K. Kuldová, A. Corval, H.P. Trommsdorff, *J. Phys. Chem. A* 101(37), 6850 (1997).
7. Frank, I.; Grimme, S.; Peyerimhoff, S.D. *J. Phys. Chem.* 100, 16187, (1996).
8. Frank, I.; Marx, D.; Parinello, M. *J. Phys. Chem. A* 103, 7341 (1999).
9. Suzuki, S.; Isaka, H.; Ito, .S.; Hirukawa, S.; Matsubara, S.; Takahashi, H. *J. of Raman Spectrosc.* 18, 105 (1987).
10. Klemm, D.; Klemm, E.; Graness, A.; Kleinschmidt, J. *J. Z. Phys. Chem.* 260(3), 555 (1979).
11. Klemm, E.; Klemm, D. *J. Prakt. Chem.* 321(3), 407, (1979).
12. Mosher, H. S.; Hardwick, E. R.; Ben Hur, D. *J. Chem. Phys.* 37, 904, (1962).
13. Shieh, W.; Hedges A. *J.M.S. – Pure Appl. Chem.* A33(5), 637 (1996).
14. Steiner, T.; Koellner, G. *J. Am. Chem. Soc.* 116, 5122 (1994).
15. Watson J. D. and col. *Molecular Biology of the Gene* 4th Edition, Benjamin/Cummings, 1987.

STUDIA UNIVERSITATIS BABEŞ-BOLYAI, PHYSICA, XLIX, 3, 2004

BUFFERED *VERSUS* UNBUFFERED ASPIRIN SPECIES MONITORED BY RAMAN AND SURFACE-ENHANCED RAMAN SPECTROSCOPY

N. PEICA[1], L. M. ANDRONIE[2], S. CÎNTĂ PÎNZARU[2] and W. KIEFER[1*]

[1]Institut für Physikalische Chemie, Universität Würzburg, Am Hubland, D-97074 Würzburg, Germany
[2]Babeş-Bolyai University, Physics Department, Kogălniceanu 1, 400084 Cluj-Napoca, Romania

ABSTRACT. Aspirin, pharmaceutically available in two forms, buffered and unbuffered, was found to be detectable by the micro-Raman spectroscopy of the tablet, in spite of the different excipients, which are used in drugs preparation. A strong chemical interaction of the both aspirin species with the silver colloidal particles was observed at micromole concentrations. Different adsorption behaviors of these molecular species are discussed.

Keywords: Buffered aspirin; unbuffered aspirin; Raman; SERS.

INTRODUCTION

Aspirin, as well as related derivatives of salicylic acid belongs to the analgesics class, being frequently used on top of non-steroidal anti-inflammatory drugs. Belonging to the peripheral analgesics class, aspirin like other non-steroidal anti-inflammatory drugs acts for reducing inflammation caused by injury or arthritis. Aspirin presents low acidity (pKa 3) and by oral administrating, almost all salicylate is found in the unionized form in the stomach [1]. This is poorly soluble in the acid media of the stomach and the precipitate products concentrate, thereby delaying its absorption up to 24 hours. However, aspirin absorption following overdose commonly occurs more slowly in the blood concentrations, which continue to rise for up to 24 hours after ingestion [2]. Absorption of salicylate can be further delayed if an enteric-coated preparation has been ingested [3].

In spite of its largely pharmaceutical and medical interest, the spectroscopic data available are limited to recent theoretical and experimental IR and Raman data [4], where the differences between the calculated and experimental wavenumbers are partly due to anharmonicity and to the intermolecular interactions and also correlation effects [4]. In addition, previous IR and *ab initio* studies were reported by Binev et al. [5], and the interaction of aspirin with RNA [6] or DNA [7] was studied using FTIR and laser Raman difference spectroscopy, respectively.

The potential polymorph of aspirin were also reported [8], an exploration of the potential conformers being presented. Further, a direct assay and monitoring of aspirin tablets using Raman spectroscopy was reported [9]. As a basis for assaying aspirin and analysis of the major degradation products, salicylic acid, the Raman technique was highlighted being feasible [9].

Moreover, the Raman and SERS spectra of aspirin were reported [10], where the adsorption was promoted by mixing aspirin/chloroform solution with silver sol. It was supposed that the aspirin species, like salicylic acid, adsorbs on silver particles via the carboxylate group. Having a larger substitution group than salicylic acid, at the ortho-position of carboxylate group, the surface adsorption was qualitatively appreciated as being not as easy as for the salicylic acid [10].

In the present study, we report the vibrational Raman characterization of buffered (ASA) and unbuffered aspirin (ANT) in order to get insight into their adsorption behavior on a given surface, ant to check the possibility to monitor the both pharmaceutical species using SERS spectroscopy.

EXPERIMENTAL

Pharmaceutical tablets of aspirin commercially available (Europharm) were employed in our study without further purification. The aspirin solutions were prepared by tablet dissolving in distilled water at 50℃, an d 15 minutes ultrasonicated.

As a SERS surface, a sodium citrate reduced silver colloid was employed, prepared according to the literature [11]. The SERS samples were obtained by adding 0.01 ml of aspirin solution of 10^{-5} mol l^{-1} to 3.5 ml of silver colloid, getting the final SERS concentration (5 and 8 μmol l^{-1} for ANT and ASA, respectively).

The micro-Raman and the SERS spectra of the aspirin on silver colloid were recorded with a Dilor Labram spectrometer by using 514.5 nm excitation line from a Spectra Physics argon ion laser. The spectra were collected in the back-scattering geometry with a resolution of 2 cm^{-1}. The detection of the Raman signal was carried out with a CCD camera (Photometric 9000 model). The laser power varied from 150 to 200 mW.

RESULTS AND DISCUSSIONS

The vibrational fundamentals from the micro-Raman spectra, presented in the Fig. 1 for unbuffered and buffered aspirin were analyzed by comparing the experimental vibrational modes with the previous published Raman data [4-10].

Comparing micro-Raman spectra of ASA and ANT (Fig. 1), we can observe many differences in band position and relative intensities.

Our Raman spectrum of ASA species is very similar with that reported by Wang et. al. [10]. Moreover, this similarity was found either by comparison with the Raman spectrum of pure aspirin from Sigma Aldrich (spectrum not given here). Distinctly from ASA, strong bands were observed for ANT at 1651, 1488, 1338, and 583 cm^{-1}, whereas other bands from ASA (1288, 1185, 1149, 746 cm^{-1}) are absent in the spectrum of ANT. Rather similar behavior of the ν(C=O) at 1622-1624 cm^{-1} was observed for the both species, whereas the $\nu_s(COO^-)$ spectral region is very different. According to the literature [12], the characteristic $\nu_s(COO^-)$ mode could be present in the 1380-1420 cm^{-1} spectral range, whereas the asymmetric mode of the COO^- could exhibit a weak Raman band in the 1561-1552 cm^{-1} spectral range. Taking a closer examination of these spectral regions, one can observe weak to medium different bands in the spectra of ANT and ASA. These differences could be tentatively explained by the presence of the buffering agent, responsible for the given acidity of the species.

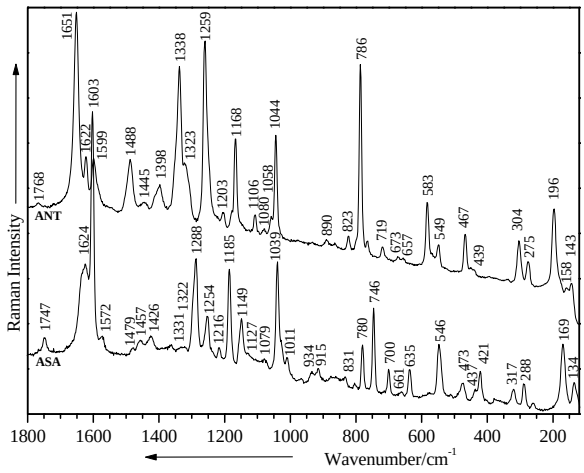

Figure 1. Micro-Raman spectra of ASA and ANT (Excitation 514.5 nm, 150 mW).

They could be also responsible for the supplementary observed bands of ASA (1288, 1185 and 1149 cm^{-1}). Further the deformation modes of the COO^- group were also found at different positions (786 and 780 cm^{-1} for ANT and ASA, respectively). The ester C=O stretching mode was observed in both species at 1747 cm^{-1} for ASA and 1768 cm^{-1} for ANT, respectively.

In conclusion, the Raman spectra of the different aspirin tablets can be employed for differentiating the buffered and unbuffered pharmaceutical species.

On passing from Raman to SERS spectra of each corresponding species, large differences in band positions and relative intensities can be observed (Fig. 2), allowing the supposition of chemisorbed species.

The strongest SERS bands of ANT are observed at 1387, 1635, 1262, 825, and 239 cm^{-1}, whereas for the ASA, the main bands are located at 1614, 1367, 1302, 1239, 1026, 802, and 218 cm^{-1}, respectively.

According to the surface selection rules [13] the vibrational modes that are preponderant enhanced should have such an orientation on the metal surface for which the polarizability Raman tensor component has a perpendicular orientation with respect to the surface. Based on the previous Raman assignments the bands at 1387 cm^{-1} (for ANT) and at 1367 cm^{-1} (for ASA) are due to the enhanced symmetrical stretching mode of COO^- group. Moreover the close presence of this group with respect to the surface provides the specific enhancement of the C=O mode observed at 1635 cm^{-1} (for ANT) and 1614 cm^{-1} (for ASA), respectively, both of them being shifted for their Raman corresponding positions due to the interaction with the metal surface. However the manner of interaction seems to be different since in the low wavenumber spectral region different strong bands assigned to ASA-Ag and ANT-Ag modes were observed in both cases. These differencies suggest a double interaction in the case of ANT through the both C=O

functional groups, one from the carboxylate and the other from the ester, whereas in the case of ASA an interaction through only one of these functional would be more probable since only one well resolved band was observed at 218 cm^{-1} (Fig 2, (a)), assigned to the Ag-O stretching mode [14,15]. This supposition was further confirmed by the presence of the 1778 cm^{-1} SERS band of ANT.

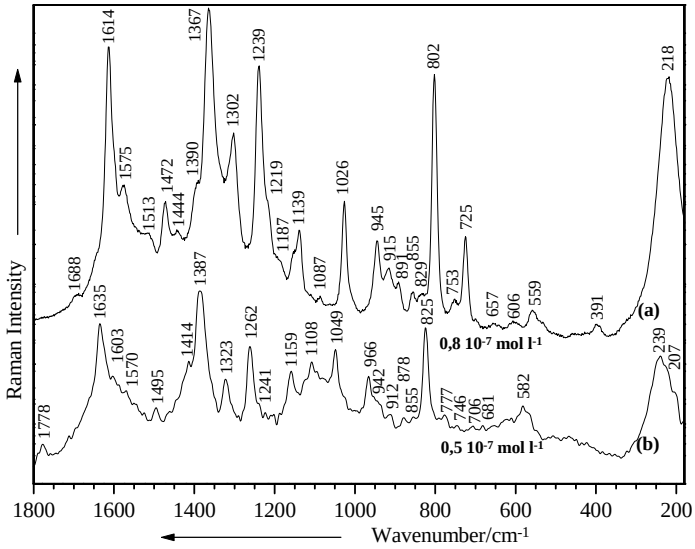

Figure 2. SERS spectra of ASA (a) and ANT (b)
(Excitation: 514.5 nm, 200 mW).

As a concluding remark, the two distinct species were found to be slightly different chemisorbed on the silver surface. At the presence stage of the work the both pharmaceutical compounds, buffered and unbuffered aspirin, could be detected from powder tablets up to micromolar level.

Acknowledgements

We gratefully acknowledge financial support from the German Science Foundation (Sonderforschungsbereich 630, Project C1) and as well from the Fonds der Chemischen Industrie.

REFERENCES

1. R. K. Ferguson, A. R. Boutros, Journal of the American Medical Association, *213*, 1186-1187 *(1970)*.
2. F. L. Kaufman, A. S. Dubanksy, *Pediatrics*, *49*, 610-611 *(1972)*.
3. G. Levy, *Pediatrics*, **62**, 867-872 *(1978)*.
4. M. Boczar, M. J. Wójcik, K. Szczeponek, D. Jamróz, A. Zięba, B. Kawałek, *Chem. Phys.*, *286*, 63-79 *(2003)*.

5. I. G. Binev, B. A. Stamboliyska, Y. I. Binev, *J. Molec. Str.*, *378*, 189-197 *(1996)*.
6. J. F. Neault, H. A. Tajmir-Riahi; *J. Phys. Chem.*; *101*; 114-116 *(1997)*.
7. J. F. Neault, M. Naoui, M. Manfait, H. A. Tajmir-Riahi, *FEBS Letters*, *382*, 26-30 *(1996)*.
8. R. S. Payne, R. C. Rowe, R. J. Roberts, M. H. Charlton, R. Docherty; *J. Computational Chemistry*; *20*; 262-273 *(1999)*.
9. C. Wang, T. J. Vickers, C. K. Mann, *J. Pharm. Biomed. Anal.*, *16*, 87-94 *(1997)*.
10. Y. Wang, Y. S. Li, Z. Zhang, D. An, *Spectr. Acta A*, *59*, 589-594 *(2003)*.
11. T. K. Lee, D. Meisel; *J. Phys. Chem.*; *87*; 3391 *(1982)*.
12. F. R. Dollish, W. G. Fateley, F. F. Bentley; *Characteristic Raman frequencies of organic compounds*; Eds. J. Wiley & Sons, USA, pp.110 *(1974)*.
13. J. A. Creighton; *Spectroscopy of Surface*; Eds. R. J. H. Clark, R. E. Hester; Wiley, New York, pp. 37 *(1988)*.
14. B. A. Sexton, R. J. Madix, *Chem. Phys. Lett.*, *76*, 294 *(1980)*.
15. E. Szlyk, I. Lakomska, *Polish J. Chem.*, *76*, 1399-1403 *(2002)*.

STUDIA UNIVERSITATIS BABEŞ-BOLYAI, PHYSICA, XLIX, 3, 2004

VIBRATIONAL FT-IR, FT-RAMAN AND EPR STUDIES OF PYRAZINAMIDE AND OF ITS COMPLEX COMBINATIONS WITH Cu(II)

T. JURCA[*], S. CAVALU[*], S. CÎNTA-PÎNZARU[**], V. SIMON[**], F. BĂNICĂ[*]

[*]*University of Oradea, Faculty of Medicine and Pharmacy, P-ta 1 Decembrie, 10, Oradea 3700, Romania*

[**]*Babes-Bolyai University, Faculty of Physics, Kogalniceanu, 10, Cluj-Napoca, 3400, Romania*

ABSTRACT. Three new mixed complexes combinations of pyrazinamide (PZA) have been prepared and analyzed by UV-VIS, FT-IR, FT-Raman and EPR spectroscopy. They correspond to:$[Cu(PZA)_nX_m]$, where X = $C_6H_5COO^-$, Cl^- and $[Hg(SCN)_4]^{2-}$.

PZA can coordinate through the pyrazine ring nitrogens, the >C=O and/or $-NH_2$ groups. When the aromatic ring nitrogen involves in complexes formation, certain ring modes, particularly the ring breathing mode and the two ring stretching modes around 1400-1600 cm^{-1} increase in value due to the coupling with Me-N(ligand) vibrations. On the other hand, when amino nitrogen is involved in coordination, drastic changes occur in amino groups vibrational wavenumbers, and if coordination occurs through the oxygen of the carbonyl group, a negative shift of the ν(C=O) mode of the coordinated molecule with respect to the free ligand is expected.

The given formula was confirmed by elemental analysis and the ligand to metal molar ratio is found to be 2:1 for $[Cu(PZA)_2(C_6H_5COO)_2 \cdot 4H_2O$, $Cu(PZA)_2]Cl_2$ and 1:1 for $[Cu(PZA)_2][Hg(SCN_4]$.

Complementary EPR investigation allowed the supposition that $[Cu(PZA)_2(C_6H_5COO)_2 \cdot 4H_2O$ complexes are hexacoordinated, while in the case of $[Cu(PZA)_2]Cl_2$ and $[Cu(PZA)_2][Hg(SCN_4]$ the corresponding complexes are tetra coordinated [8].

1. Introductions and Experimental

It is well known that the metalloelements play a significant role in the regulation and control of essential biological processes. Usually they perform the functions of participants, mediators and regulators bound in complexes with proper bioligands. Many substances introduced in the organism as food ingredients and especially as drugs or different biostimulators, represent mono or poly-dentate ligands, capable of coordinating to the biometals, and thus altering their homeostatis.

Pyrazinamide (Pyrazine-2-carboxamide $C_5H_5N_3O$, PZA) was obtained as reagent from Trans Medical Pharma GmbH, Germany.

The aim of this study is to investigate the coordination effects on pyrazinamide ligand using experimental methods.

The chemical structure of pyrazinamide is presented in Fig.1.

The synthesis of $Cu(PZA)][Hg(SCN_4$, $Cu(PZA)_2]Cl_2$ and $[Cu(PZA)_2](C_6H_5COO)_2$ complexes was early reported [1].

The C, H, N, S analysis results for the investigated complexes are shown in Table 1.

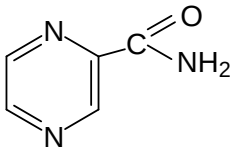

Fig.1. *The molecular structure of pyrazinamide.*

Table 1.

Elemental analysis of complexes

Nr	Formula	M	Color	C% Found/ Calc.	N% Found/ Calc.	S% Found/ Calc.	H% Found/ Calc.
1.	$[Cu(PZA)_2]$ $(C_6H_5COO)_2$ $4H_2O$	623,66	Light Blue	45,12/ 45,85	13,85/ 13,37	-	4,368/ 4,458
2.	$[Cu(PZA)_2]Cl_2$	398,66	Light Green	30,10/ 30,6	21,07/ 22,04	-	3,04/ 3,15
3.	[Cu(PZA)] $[Hg(SCN_4]$	656,6	Green	16,36/ 16,44	14,27/ 14,92	19,10/ 19,49	1,29/ 1,37

The FT-IR and FT-Raman spectra of pyrazinamide and their complexes with cooper (II) were recorded using a Bruker EQUINOX 55 spectrometer with an integrated FRA-106 S Raman module. The InGaAs detection was used and the 1064 nm line from a Nd:YAG laser was employed for the excitation of the Raman spectra. The spectral resolution was 4 cm^{-1}.

The electron paramagnetic resonance spectra were recorded at room temperature using an ADANI EPR spectrometer operating in the X-band (9,2 GHz), with a sensitivity of 5 x 10^{10} spin/10^{-4}T and a relative resolution of 2 x 10^{-5}.

2. Results and Discussion

Based on the elemental analysis the metal to ligand ratio is found to be 1:1 for $[Cu(PZA)][Hg(SCN_4]$ and 1:2 for $Cu(PZA)_2]Cl_2$ and $[Cu(PZA)_2](C_6H_5COO)_2 \cdot 4H_2O$.

PZA can coordinate through the pyrazine ring nitrogens, the –C=O and/or – NH_2 groups. IR technique is diagnostic of the coordination mode of PZA in complexes.

The assignment of most prominent IR bands is presented in the Table 2**.**

When the aromatic ring nitrogen involves in complex formation, certain ring modes, particularly the ring breathing mode and the two ring stretching modes around 1400-1600 cm^{-1} increase in value both due to the coupling with Me-N (ligand) [4,5] bond vibrations and due to alterations of the ring force field.[2] On the other hand when amino nitrogen is involved in coordination, drastic changes occur in amino group vibrational wavenumbers [7], and when coordination occurs through the oxygen of the carbonyl group, a negative shift of the $\nu_{c=o}$ mode of the coordinated molecule with respect to the free ligand is expected [2]. Therefore, in order to determine the coordination mode of PZA in Me-PZA complexes, the wavenumbers of PZA in complexes are compared with those of free PZA.

Table 2.

The main observed bands in the infrared spectra

Tent. Assig.	PZA	Me-PZA complexes		
		$Cu(C_6H_5\text{-}COOH)_2$	$CuHg(SCN)_4$	$CuCl_2$
ν_{as} NH_2	3410s	3610w	3440w	3430s
ν_s NH_2	3140m	3170m	3100s	3110m
ν_{CH}	3080	3065m	3080w	3070m
$\nu_{C=O}$(1)	1705s	1915w	1670m	1700s
δ_{NH2}(2)	1600m	1590m	1630m	1590m
ν_{ring}	1570	1585m	1580m	1585m
ν_{ring}	1530	1545s	1540w	1510w
ν_{CN}(III)	1375s	1380s	1370w	1385s
δ_{CH}	1150w	1180w	1180w	1170m
ΔNH_{2t}	1090m	1085w	1090w	1080w
δring	870w	850w	860w	870m
ΔNH_{2w}	665w	680m	675w	670w

In the IR spectra of the PZA complexes studied, the $\nu_a(NH_2)$ and $\nu_s(NH_2)$ modes are found to be higher in value than those of microcrystalline PZA. Since it is well known that a coordinated amino group shows a negative shift, Δ = 150-220 cm^{-1}, in the NH_2 stretching modes, in comparison to the free ligand [6,7], we can conclude that this group does not take part in coordination. On the other hand, the ν(C-NH_2) mode of aniline and aniline derivates shows a negative shift, Δ = 50-60 cm^{-1} , upon coordination, but we do not observe such a shift of this mode in Me-PZA complexes, which is a further proof of a non-coordinated amide nitrogen. In solid PZA, amide group hydrogens are involved inter and intra H-bonds [2]. We could not record IR spectrum of PZA dissolved in a non-polar solvent, due its poor solubility. Nevertheless, the slight up shift of $\nu(NH_2)$ of Me-PZA complexes indicates that the NH_2 group of PZA forms weaker H-bonds than in the pure solid. The IR data show that the amide NH_2 of PZA does not take part in coordination, but forms weak hydrogen bonds, probably with guest water molecules, for example Cd-PZA complex. In the IR spectra the ring-breathing mode of PZA is observed at 1015±10 cm^{-1} and around 1035 cm^{-1} for Me-PZA complexes. The lack of blue shift of ring breathing suggests that the PZA molecule does not coordinate to the metal (II) in Me-PZA complexes through the heterocyclic ring nitrogen. We also do not observe any blue shift in certain ring modes due to formation of Me-PZA complexes, which are known to be very sensitive to complex formation through the ring nitrogen [4,6]. According to theoretic studies of pyrazinamide two characteristic of symmetric and asymmetric stretching mode NH_2 bands could be clearly identified. The out of plane NH_2 wagging band appears at 3440-3100 cm^{-1}.

The amides, containing nitrogen atom having lone pair electron to donate, have absorption $\nu_{c=o}$ at 1640-1700 cm^{-1}. The IR spectra of the Me-PZA compounds show negative shifts of $\nu_{c=o}$.

The Raman spectra of studied complexes and ligand are presented in figures 2 - 4.

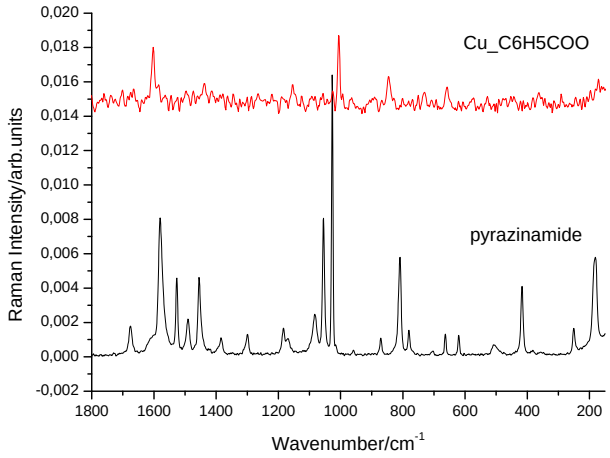

Fig.2. *FT-Raman spectra of $[Cu(PZA)_2](C_6H_5COO)_2\ 4H_2O$ and the pyrazinamide*

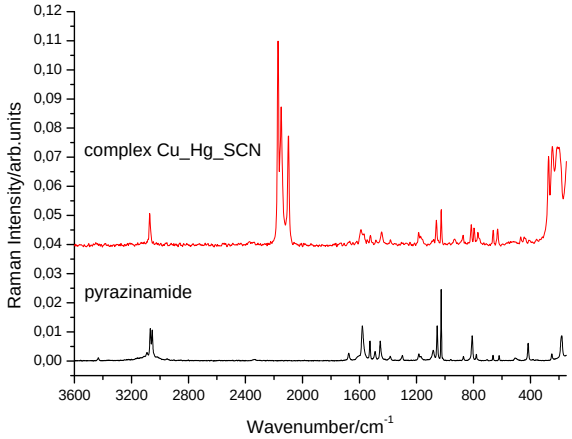

Fig.3. *FT-Raman spectra of $[Cu(PZA)][Hg(SCN_4]$ and pyrazinamide.*

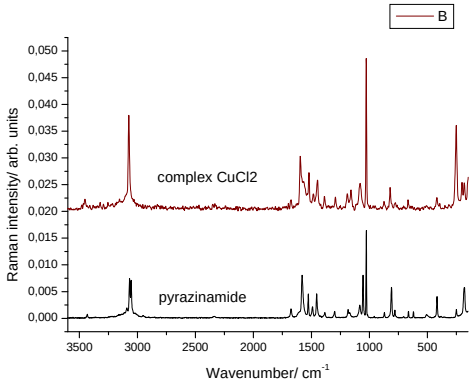

Fig.4. *FT-Raman spectrum of $Cu(PZA)_2]Cl_2$ and pyrazinamide.*

The observed frequencies in the FT-Raman spectra with the proposed assignments are summarized in Table 3.

Table 3.

Main observed bands in the FT-Raman spectra.

PZA	PZA + $CuCl_2$	PZA+ $Cu[Hg(SCN)_4]$	PZA+ $Cu(C_6H_5COO)_2$	Assignment
94m	88s	87s	87	Lattice
119m	139m	139m	-	Lattice
-	202m	213m	-	Cu-PZA
251w	252s	247m 274m	-	Twisting -ring, δ
417w	418w 420w	444vw 469vw	-	δ ring
620vw	-	631w	-	δNH_2
780m	-	769vw 796w	-	$\delta(O=C-NH_2)$
1027vs	1027vs	1026m	1006m	δCH ring breathing
1055s	-	1061w	-	νPZA trigonal ring stretching
1184w	1191w	1185w	1154w	νC-C ring
1384w	1388vw	1383vw	-	νC-N ring
1455m	1448w	1445w	1438w	νCN+νNH
1490m	1483w	-	-	ν ring quadr. Streching
1527m	1521w	1523vw	-	ν ring quadr. Stretching
1580s	1596m	1590w	1602m	δNH_2
-	-	2099m 2149s 2171vs	-	νSCN
1676w	1675vw 1673vw	-	-	νC=O
-	-	-	2752w	ν benzoat
3054m	3074s	-	-	νC-H

Because the trigonal and quadrant stretching modes are position modified and the ring breathing modes remain unshifted, we can conclude thus the coordination of carbonyl group. Analyzing in detail the spectral region of the low wavenumbers we observed the appearance of new band characteristics for the metal-ligand bonds. The specific modifications due to the Me- ligand bound are visible around 200 cm^{-1}.

The ESR spectrum of $[Cu(PZA)_2](C_6H_5COO)_2$ is anisotropic having a $g_\perp$ parameter value of 2.06 and a $g_\parallel$ value of 2.25.

The spectrum shown the Cu^{2+} ion occurs in a tetragonal field with axial symmetry.

The values of the spectroscopic splitting factor are: $g_\parallel = 2.25; g_\perp = 2.06$

$$g_{av} = 1/3(g_{\parallel} + 2g_{\perp}) = 2{,}12;\quad G = (g_{\parallel}-2)/(g_{\perp}-2) = 4{,}16$$

Because $g_{\parallel} > g_{\perp}$, and $G > 4$ is evident that the unpaired electron is localized in the $d_{x^2-y^2}$ orbital.

The ESR spectrum recorded from $[Cu(PZA)_2]Cl_2$, occurs from resonant centers disposed in an elongated octahedron vicinity, with rhombic symmetry, having different ligands along the three x, y, z axes.

The values of the spectroscopic splitting factor are: $g_1 = 2.22$; $g_2 = 2.02$; $g_3 = 2.00$. The ESR spectra of studied complex are presented in figure 5.

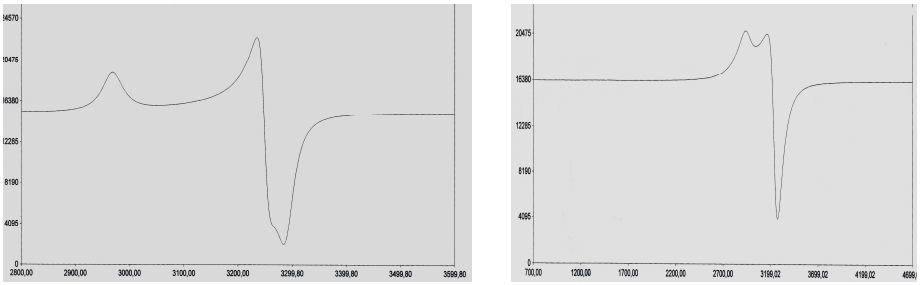

Fig. 5. *The ESR spectra of $Cu(PZA)_2]Cl_2$ and $[Cu(PZA)_2](C_6H_5COO)_2$*

Taking into account the spectroscopic results, the proposed structure for one of the investigated complexes, namely the $Cu(PZA)_2]Cl_2$ is presented in figure 6.

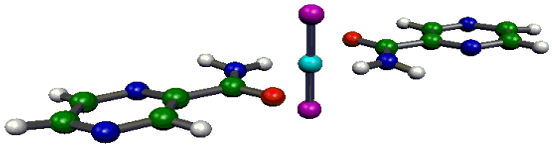

Fig.6. *The geometric structure of $[Cu(PZA)_2]Cl_2$*

Conclusions

We may conclude that the coordination through the – C=O and aromatic nitrogen ring groups in the Me-PZA complexes is evidenced by the FT-IR and FT-Raman spectra. A similar coordination mode of PZA was observed in lanthanide complexes and adsorbed species on metal surfaces. The complexes are crystalline, non-hygroscopic and insoluble in common organic solvents.

However, they are soluble to limited extent in DMF and DMSO.

The EPR investigation allowed to conclude that $[Cu(PZA)_2(C_6H_5COO)_2 \cdot 4H_2O$ complexes are hexacoordinated, while in the case of $[Cu(PZA)_2]Cl_2$ and $[Cu(PZA)_2][Hg(SCN_4]$ the corresponding complexes are tetra coordinated [8].

REFERENCES

1. T. Jurca, S. Cavalu, S. Cîntă Pînzaru, V. Simon, Studia, Physica, Special Issue 1, 457-460, (2003).
2. E. Akalin, S. Akyuz, J. Mol. Struct. 463-464 (2001), 579.
3. V. Lavini, A. S. Maia, I. S. Paulino, U. Schuchardt, W. Oliveira, J. Inorg. Chem. Commun. **4** (2001), 582.
4. Sevim Akyuz, J. Mol. Struct., 12754, 2002.
5. T. Jurca, Analele Univ. Oradea, Fascicula Stiinte farmaceutice, 10, Vol I (2002).
6. N. Ekici, Z. Kantarci, S. Akyuz, J. Inclusion Phenom. 10 (1991) 9.
7. M. Bakiler, I.V. Maslov, S, Akyuz, J. Mol.Struct. 476 (1999) 21.

STUDIA UNIVERSITATIS BABEŞ-BOLYAI, PHYSICA, XLIX, 3, 2004

SPECTROSCOPIC BEHAVIOR OF COPPER COMPLEXES OF TOLBUTAMIDE

E. MARIAN, T. JURCA, F. BANICA, S. CAVALU, T.S. NEMETH

University of Oradea, Faculty of Medicine and Pharmacy

ABSTRACT. Tolbutamide, N-Butylcarbamoyl-4-methylbenzen-sulfonamide, was the first hypoglycemic agent used in the treatment of diabetes.

In this present paper, crystalline complexes of Cu (II) with tolbutamide have been studied by means of infrared spectroscopy.

Adding an aqueous solution of Cu (II) to the basic solution of tolbutamide and obtaining a green or leaden precipitate obtained the complexes.

The conformational and structural changes due to the complexation have been studied by FT-IR spectrometry using an Attenuated Total Reflectance accessory.

INTRODUCTION

Due to the fact that the ion of Cu(II) is one of the essential microelements for the organism, the metallic complexes formed by it with ligands constituted from drug substances have been studied lately.

Tolbutamide has the following chemical formula:

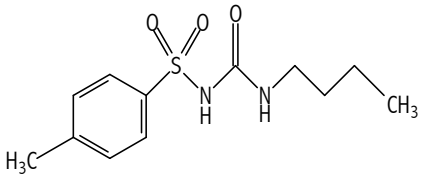

Figure 1. Structure of tolbutamide.

Its denomination is: N-(Butylcarbamoyl)-4-methylbenzensulfo-namide.

Tolbutamide is a white, crystalline with no smell or taste. It is easily soluble in acetone, soluble in alcohol and chlorophorm, and practically non-soluble in water. Its melting point is 126-130^{o}C. Its conservation is done in well-closed containers, safe of light. [1,2]

MATERIALS AND METHOD

Synthesis of tolbutamide complexes with ions of Cu(II)

a) $[Cu(TBA)_2]\ (SCN)_2$

1.25 g $CuSO_4$ x$5H_2O$ are dissolved in 50 mL distilled water and treated, while stirring, whit 80 mL low basic solution of NaOH that contains 2.7 g tolbutamide and 40 mL distilled water in whitch 1.5 g ammonium thiocyanate was dissolved. A grey precipitate which easily deposits it self, is separated. The precipitate is filtered, washed with washing water that contains 0.2% tolbutamide and 0.2% ammonium thiocyanate, then a few times with distilled water, alcohol and ether. It is dried at air or in vacuum.

b) $[Cu(TBA)_2]Cl_2$ x2 H_2O

1.35g $CuCl_2$ is dissolved in 50 mL distilled water and treated, while stirring, with 100mL low basic solution in which 5.4g tolbutamide was dissolved. While continuous stirring, a green-bluish precipitate, which easily deposits itself, appears. The precipitate is slowly filtered through a Buchner funnel, than it is washed several times with distilled water and then with alcohol.

c) $[Cu(TBA)_2][Hg(SCN)_4]$ x H_2O

1.36 g $HgCl_2$ is dissolved at heat in 100 mL distilled water, and after cooling, we add ammonium thiocyanate and 50 mL low basic solution of NaOH in which 2.7 g tolbutamide was dissolved. The solution thus obtained is treated with 1.0 g $Cu(CH_3COO)_2$ x H_2O dissolved in 60 mL distilled water. The obtained green precipitate is filtered through the Buchner funnel, and then washed several times with warm distilled water and then with alcohol.

The FT-IR spectra were recorded using a Bruker Equinox 55 spectrometer in the region 400 - 4000 cm^{-1}.

Table I.

Essential analysis of investigated complexes

Nr.	Compound	Color	C% Found/ Calculated	H% Found/ Calculated	N% Found/ Calculated	S% Found/ Calculated	Cu% Found/ Calculated
1.	$[Cu(TBA)_2](SCN)_2$ 720,390	Grey	42,496/ 43,33	5,12/ 5,00	11,28/ 11,67	17,69/ 17,78	8,72/ 8,89
2.	$[Cu(TBA)_2]Cl_2 \times 2H_2O$ 711,148	Green-Blue	40,32/ 40,51	5,21/ 5,63	7,56/ 7,88	9,12/ 9,00	8,88/ 9,00
3.	$[Cu(TBA)_2][Hg(SCN)_4] \times H_2O$ 1055, 158	Green	31,62/ 31,85	3,49/ 3,60	10,14/ 10,62	17,89/ 18,20	5,91/ 6,07

RESULTS

The elementary analysis has established that the combination ratio Cu: ligand is 2:1 and that at 2 of the 3 complexes crystallization water appears. This ratio must be confirmed by diffraction with X-rays, spectroscopy etc. The vibrating data in IR of tolbutamide and of synthesized complexes are given in Table II.

Table II.

Assignment of IR bands

Tent assign	TBA	$[Cu(TBA)_2](SCN)_2$	$[Cu(TBA)_2]Cl_2$	$[Cu(TBA)_2][Hg(SCN)_4]$
$\nu_{s\ NH}$	-	-	-	3351(w)
$\nu_{s\ NH}$	3324(m)	3325(w-m)	3327(m-s)	-
ν_{CH}	3091(w-m)	3092(s)	3097(w-m)	-
ν_{CH3}	2958(w-m)	2957(w)	2956(w)	-
H_2O	-	-	2930(w)	-
H_2O	-	-	2873(w)	-

Tent assign	TBA	$[Cu(TBA)_2](SCN)_2$	$[Cu(TBA)_2]Cl_2$	$[Cu(TBA)_2][Hg(SCN)_4]$
H_2O	-	-	-	2811(w)
ν_{SCN}	-	2177(s)	-	2066(s)
$\nu_{C=O}$	1702(w-m)	-	-	-
δ_{NH}	1659(s)	1659(s)	1658(s)	-
ν_{ring}	1549(s)	1548(s-m)	1547(s)	-
ν_{ring}	1458(s)	1460(m)	1462(m)	-
ν_{CN}	1335(s)	1336(m)	1336(m)	-
δ_{CH}	1246(m)	-	1246(m)	-
ν_{SO2N}	1155(s)	1157(s)	1158(s)	-
ν_{C-O}	-	1120(m)	1121(m)	-
ν_{SO2}	1090(s)	1091(s)	1091(m-s)	-
δ_{CH}	1000(m)	-	-	-
δ_{ring}	896(s-m)	896(s-m)	895(m-s)	916(w-m)
γ_{ring}	815(s-m)	815(s-m)	815(m-s)	-
γ_{ring}	724(s-m)	724(s)	724(m-s)	741(w-m)
ν_{CH}	-	703(s)	702(s)	-
Δ_{NH}	658(s-m)	661(s)	662(s)	-

DISCUSSION

Tolbutamide can coordinate through the two NH groups from the methyl-benzensulfonamide chain and through the carbonyl oxygen.

With the help of FT-IR spectra, the coordination pathway was supposed [3].

The valence vibrations of the benzene rings situated at 3091, 1549, 1458, 815, 724 cm^{-1} do not change significantly in comparison to those of the free ligand.

The valence vibrations of the NH groups situated at 3324, 1659 cm^{-1} present very small changes, thus we can conclude that these groups do not take part at the coordination.

It can also be observed that that the absorption of C=O group from 1702 cm^{-1} disappears, thus coming to the conclusion that the oxygen is involved in the coordination [4].

The elongation vibration of C-N link is found at 1335 cm^{-1} and does not change compared to the free ligand.

In the case of ammonium thiocyanate, the strip specific to the SCN group appears, proving the appearance of a complexes combination. It can also be observed the appearance of strips specific to the crystallization water at the complex with $CuCl_2$ at 2930 and 2873 cm^{-1} and at 2811 cm^{-1} at the complexes with thiocyanate.

CONCLUSION

FT-IR spectroscopic studies demonstrate that the three complexes synthesized from tolbutamide with Cu(II) are coordinated by means of the carbonyl group based on the elemental analysis the metal to ligand ratio is found to be 2:1

The structures of the complex combinations can be clarified after performing Raman spectra, X-rays, ESR and mass spectra.

REFERENCES

1. * * * - *FR X* p.940.
2. * * * - *USP 23* p.1565-1566.
3. C. Rao, *Chemical Applications of Infrared Spectroscopy*, Academic Press, London, 1963.
4. T. Jurca, S. Cavalu, S. Cântă Pînzaru, V. Simon, Studia Physica UBB, Special issue 1, 457-460 (2003).

STUDIA UNIVERSITATIS BABEŞ-BOLYAI, PHYSICA, XLIX, 3, 2004

MOLECULAR AND VIBRATIONAL STRUCTURE OF PYRAZINAMIDE; A COMBINED EXPERIMENTAL AND THEORETICAL STUDY

V. CHIŞ[1], A. PÎRNĂU[1], T. JURCĂ[2], M. VASILESCU[1], O. COZAR[1], L. DAVID[1]

[1]*Babeş-Bolyai University, Faculty of Physics, 1 Kogălniceanu, RO-400084 Cluj-Napoca, Romania*

[2]*University of Oradea, Faculty of Medicine and Pharmacy, Str. Armatei Romane 5, RO-410087 Oradea, Romania*

ABSTRACT. In this work we report a joint experimental and theoretical investigation on the pyrazinamide (PZA) molecule, with particular emphasize on its intra- and intermolecular hydrogen bonds (HB's). A value of 8.33Kcal/mol was estimated for the intramolecular H bond energy, at B3LYP/6-31G(d) level of theory. Intermolecular interactions effects on molecular properties of PZA have been considered by calculations performed on PZA dimer. The calculated geometrical parameters of the intermolecular HB are in excellent agreement with the experimental ones and suggest a moderate, mostly electrostatic interaction.

It is shown that a very good quantitative agreement between experimental NMR spectra and the calculated chemical shifts both for ^{1}H and ^{13}C nuclei can only be reached by modelling the intermolecular interactions. Moreover, theoretical and experimental NMR data suggest that only one of the two protons of NH_2 group can be involved in intermolecular hydrogen bonds.

Introduction

Pyrazinamide (PZA), an analogue of nicotinamide, is used in the medical field as anti-infective agent, esspecially in the treatment of tuberculosis.

For a proper understanding of the electronic structure of PZA, a reliable assignment of its NMR spectrum is essential. For this purpose, quantum mechanical methods, ranging from semiempirical to Density Functional Theory (DFT) approaches are very useful, each method having its own advantages. Semiempirical calculations are very fast and in some circumstances are able to provide good theoretical results, being also capable to deal with complex molecular systems. The Hartree – Fock methods give good results provided a flexible basis set is used and electron corellation is taken into account. DFT methods, esspecially those using hybrid functionals, have evolved to a powerful quantum chemical tool for the determination of the electronic structure of molecules.

In the framework of DFT approach, different exchange and correlation functionals are routinely used. Among these, the B3LYP hybrid functional [1, 2] is the most used since it proved its ability in reproducing various molecular properties, including vibrational, ESR and NMR spectra. The combined use of B3LYP functional and standard split valence basis set 6-31G(d) has been previously shown to provide an excellent compromise between accuracy and computational efficiency of vibrational spectra for large and medium-size molecules.

The molecular and crystal structure of PZA was obtained by Takaki *et al*. [3] from an X-ray diffraction study. It was shown that PZA is monoclinic, belonging to the space group $P2_1/a$, with four molecules in a unit cell of dimensions: a=23.07Å, b=6.73Å, c=3.73Å, β=101.0°. The pyrazine ring is completely planar while the amide group is about 5° out of this plane. The molecules are connected by NH…O hydrogen bonds of 2.90Å length, forming dimers which are linked by NH…N hydrogen bonds of 3.14Å into chains extended along [011] direction.

Experimental

PZA was purchased from Sigma and used without further purification. FT-IR/ATR spectra of PZA powder sample were recorded at room temperature on a conventional Equinox 55 FT-IR spectrometer equipped with an InGaAs detector, coupled with a Bruker Miracle ATR sampling device.

The ^{1}H and ^{13}C NMR spectra were recorded at room temperature on a Bruker AVANCE NMR spectrometer (400.13 MHz for ^{1}H and 100.63 MHz for ^{13}C, internal standard TMS). The samples were prepared by the dissolution of PZA in DMSO (signal for ^{1}H at 2.512 ppm and at 39.476 ppm for ^{13}C). The spectra were recorded using a single excitation pulse of 12 μs for ^{1}H and 9 μs for ^{13}C. The FID signal was acquired 100 times for ^{1}H and 400 times for ^{13}C.

Computational details

The molecular geometry optimizations were performed with the Gaussian 98W software package [4] by using DFT methods, with the hybrid functional B3LYP [1, 2]. The split-valence 6-31G(d) basis set of the Pople's group [5] has been generally used for the expansion of molecular orbitals. The correlation consistent cc-pVDZ basis set was also used with B3LYP method, in order to test the performance of the higher quality basis sets in predicting the NMR spectrum of PZA.

For the calculation of NMR spectrum (chemical shifts) of PZA and PZA dimmer we used the GIAO method (Gauge-Including Atomic Orbitals) [6, 7], implemented in the Gaussian package [4], using the exchange-correlation functional B3LYP with 6-31G(d) and cc-pVDZ basis sets.

Results and Discussions

The geometries of the two possible conformers of PZA were optimized: one with NH_2 group in *cis* position relative to the N1 nitrogen atom from the pyrazine ring and the other with the NH_2 group in *trans* position. The theoretical geometrical parameters are given in Fig.1. In order to test the effect of intermolecular interactions, the PZA dimer formed by N-H...O intermolecular hydrogen bonds was also investigated by theoretical method B3LYP/6-31G(d).

Comparing the energies of the two conformers it comes out that the *cis* conformer is 8.33Kcal/mol more stable than the *trans* conformer. This difference is comparable with the intramolecular hydrogen bond energies [8] so that we can conclude that the C1 conformer is stabilized by the NH…N intramolecular hydrogen bond.

The rotational barrier of the $CONH_2$ group in PZA, calculated with $CONH_2$ group perpendicular to the pyrazine ring is 10.2Kcal/mol. This rather small value, suggests that in gas or liquid phase, both conformers of PZA could contribute to the experimental derived properties of the PZA molecule.

A complete characterization of monomer and its isomers is possible only by taking the intermolecular interactions into account. These later interactions were considered in our study by modeling the PZA dimer, whose structure was obtained from the X-ray diffraction data [3].

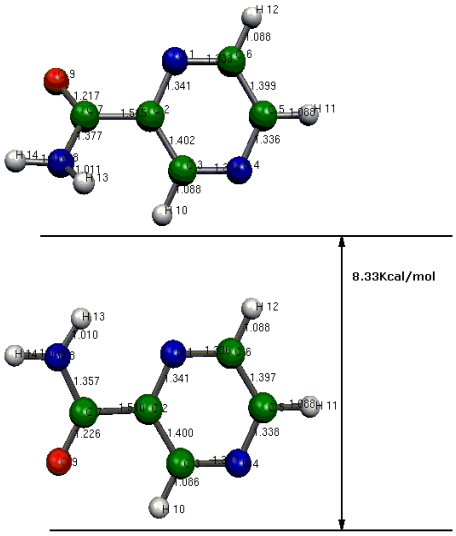

Fig.1. Optimized geometry (B3LYP/6-31G(d)) for the two PZA conformers (bottom C1, top C2)

The calculations performed on the PZA dimer shows that the bond lengths are similar with those from the monomer. Significant differences could be observed only for the C7-N8 bond (shorter in the dimer) and for the C7-O9 and N8-H14 lengths (both longer in the dimer). As compared to the experimental data, the greatest differences are observed for X-H (X=C, N) bonds lengths, obtained with the B3LYP/6-31G(d) method.

The best correlation with the experimental data for the PZA dimer is observed for the C7-O9 bond, which is significantly longer as compared to the monomer and, in the limits of experimental errors, it is equal to the experimental value. The discrepancies observed for C7-N8 and X-H (X=C, N) bonds is due probably to the packing effects in the crystal.

The bond angles are well reproduced by computation for both dimer and monomer, too. Significant differences were observed for the C2C3H10 and C7N8H13 angles, which are significantly greater than the experimental values.

The experimentally obtained X-ray diffraction data shows that the amide group is not in the same plane with the pyrazinic ring, the N8H13 bond forming a dihedral angle of 20.5^{o} with the plane containing the pyrazine ring, the theoretical data showing a planar PZA molecule.

An excellent agreement was obtained between the computed and the experimental value of the intramolecular hydrogen bond length: dimer: 2.895 Å - experimental, 2.905 Å - theoretical value.

According to the classification criteria for the strength of the hydrogen bonds as a function of geometrical parameters given by Jeffrey [9] our data suggest a moderate strength intermolecular hydrogen bond, with a predominant electrostatic character. The strength of this bond is also proved by the computed vibrational spectra,

especially by the frequencies associated with the NH_2 group in the monomer and dimer, observing and important decrease of these frequencies for the dimer.

The computed geometry for the second conformer is different from the first from one point of view, its geometry being not planar anymore. The N8H13 bond makes a dihedral angle of 25.6^o with the pyrazinic ring and the N-H bond with 6.5^o. Significant differences are noted for the bonds containing the C7 carbon atom, especially for the C7-O9 bond which is predicted to be 0.09 Å shorter.

For a reliable assignment of NMR spectra of organic molecules, the computation of the chemical shifts associated with their magnetic nuclei is essential [10].

The experimental ^{1}H and ^{13}C NMR spectra of PZA are given in Fig.2 and Fig.3, respectively. Table 1 shows the computed values for the chemical shifts for the pyrazinamide molecule, along with the experimental values.

The NMR spectrum of the pyrazinamide, along with other member of this drug-family, in DMSO solvent was investigated by Cox and Bothner-By [11]. They have found the following values for the chemical shift of protons H10-H14: 9.25, 8.9, 8.8, 7.9 and 8.3 ppm. As it is proved by Table 1 our values are in a very good agreement with this study, with minor differences for protons H11 and H12.

Chemical shifts corresponding to the two protons of the NH_2 group in the adenine-4-tiouracil complex are [12] 7.64 and 8.30 ppm, very close to those corresponding to the pyrazinamide.

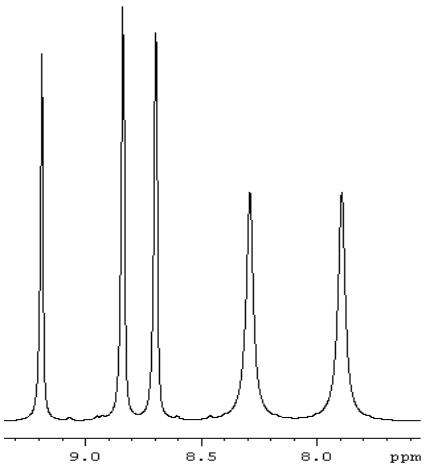

Fig.2. ^{1}H NMR spectrum of PZA in DMSO, at room temperature

We computed the ^{1}H and ^{13}C NMR spectra for the two monomers in conformations 1 and 2, respectively and for dimer. As shown in Table 1 the ^{13}C chemical shifts are essentially the same for C1 conformer and for dimer. Marked differences are noted between the two conformers, especially for C2 and C6 and in a smaller manner for the others carbon nuclei. On the other hand, a significant difference between conformer 1 and dimer is noted for C& nucleus: chemical shift increases from 151.6 ppm for the monomer to 155.6 ppm for the dimer.

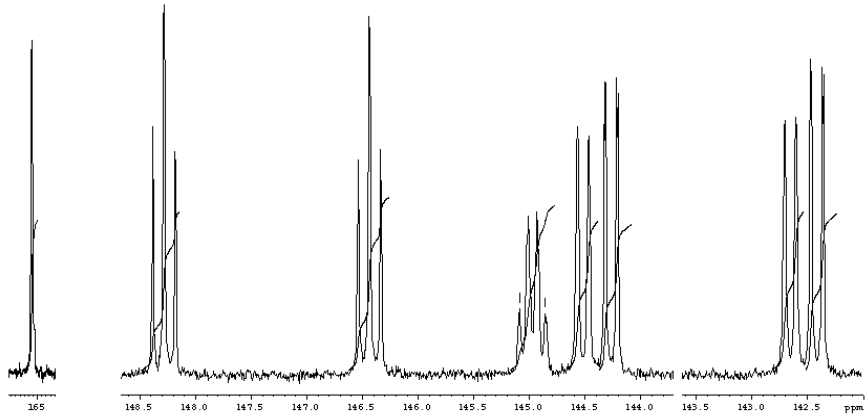

Fig.3. ^{13}C NMR spectrum of PZA in DMSO, at room temperature

Table 1.

Experimental and Theoretical Chemical Shifts for Pyrazinamide Molecule

Nucleus	Experimental	Calculated				
		B3LYP/6-31G(d)			B3LYP/cc-pVDZ	
		Monomer C1	Dimer	Monomer C2	Monomer C1	Dimer
C2	146.4	138.3	138.9	143.8	144.9	145.6
C3	145.0	140.7	140.5	137.3	145.2	145.1
C5	144.4	140.8	140.8	139.2	146.1	146.2
C6	148.2	135.4	135.6	139.4	140.8	141.0
C7	165.1	151.6	155.6	154.7	155.7	160.8
H10	9.2	9.4	9.4	8.7	9.3	9.4
H11	8.7	8.6	8.6	8.5	8.5	8.5
H12	8.5	8.3	8.3	8.6	8.2	8.3
H13	7.9	6.7	6.9	4.3	6.9	7.2
H14	8.3	4.0	8.9	4.1	4.1	10.2

The correlation between the computed and experimentally obtained chemical shifts was performed using the study of Barich et al. [13] about the ^{13}C NMR spectra of PZA powder. Their chemical shifts were: 143.9 ppm for C2, 143.4 ppm for C3 and C5, 148.3 ppm for C6 and 167.1 ppm for C7. The highest difference between our and their data was found for the C2 nucleus, which is with 2.5 ppm more shielded in solution than in solid phase. In the study of Barich et al. [13] the signals for C2 and C7 were identified non-ambiguously using a dipolar dephasing experiment, the other signals being correctly assigned by comparing the experimental and computed spectra. The disagreement for C7 nucleus between our experimental and computed data could be associated with the disagreement regarding the theoretical and experimental values of the C7N8 bond length (1.309 Å - experimental, theoretical: 1.357 Å for the monomer and 1.340 Å for the dimer).

Regarding the chemical shifts of the protons, our experimental data are similar to those reported by Cox and Bothner-By [11]. The theoretical data for the dimer suggests a qualitative and a quantitative agreement with the experimental data. There are qualitative differences between the values computed for the monomer and for the dimer of PZA. Thus, the ^{1}H NMR spectrum computed for the dimer suggests a higher degree of non-shielding for the H14 proton. This is the proton involved in the intermolecular hydrogen bonds, therefore the theoretical data sustains the fact that the protons involved in the intra and intermolecular hydrogen bonds [14] are less shielded with respect to the case when they are not involved in such type of interactions [15-17]. Thus, for H14 the computed chemical shift increases from 4.0 ppm for monomer to 8.9 ppm for the dimer, the latter value being in good agreement with the experimental value of 8.3 ppm.

The non-coplanarity of the $CONH_2$ group with the rest of PZA molecule is manifested in the ^{1}H NMR spectrum. Thus, the calculated proton chemical shifts for the C2 conformer are substantially different with respect to dimer but also to the C1 conformer.

It is clear from our NMR study that it is very important to take the intermolecular interactions into account. For PZA molecule this fact is manifested on the chemical shifts associated to H14 and C7 nuclei. Also, it is worth to mention that both vibrational and NMR spectra clearly show that only one from the two protons of NH_2 group is involved in intermolecular hydrogen bonds.

The highest discrepancies between the experimental and theoretical wavenumbers of PZA are observed for the modes corresponding to vibrations related to the NH_2 group which has a very important role in the biological activity and conformation of peptides or Watson-Crick type complexes, because this group intermediates the hydrogen bonds responsible for the stabilization of a certain conformation of the peptides. Regarding these frequencies, as compared to theoretical values of the monomer, the calculated values obtained for PZA dimer are in much better agreement with experimental data. Thus, the wavenumber corresponding to the $\nu_{as}(NH_2)$ vibration decreases from 3582 cm^{-1} for the monomer to 3503 cm^{-1} for the dimer. The wavenumber corresponding to the symmetric stretch of the NH_2 group is predicted to be higher than that obtained experimentally for the monomer (3453 instead of 3373 cm^{-1}). Theoretical vibrational spectrum gives a band at 3240 cm^{-1} and other one at 3196 cm^{-1} for the $\nu_s(NH_2)$ vibration, in agreement, both quantitatively and qualitatively, with the experimental data. The medium intensity bands from 3288 cm^{-1} and 3198 cm^{-1}, observed in the FT-IR/ATR spectrum are assigned to the symmetrical stretching of the NH_2 group. This assignment is well supported by the computed IR spectra of the dimer, where the corresponding wavenumbers are 3240 cm^{-1} and 3196 cm^{-1} respectively. In the study of Akyuz [18] the first of these bands appears at 3210 cm^{-1} and it was attributed to the overtone of the fundamental band corresponding to mode $\delta(NH_2)$. The intense band at 3150 cm^{-1} observed in the FT-IR/ATR spectrum is attributed also to $\nu_s(NH_2)$ type vibrations in agreement with other studies on some primary amides, with group NH_2 involved in hydrogen bonds [19].

Conclusions

An experimental and theoretical (DFT) study on the structure and vibrational properties of Pyrazinamide is reported in this study. Theoretical calculations at

B3LYP/6-31G(d) level of theory show that the intramolecular hydrogen bonded conformer of PZA is 8.33Kcal/mol more stable than non-intramolecular hydrogen bonded conformer. At the same level of theory we obtained a very good agreement between the experimental and theoretical geometrical parameters of PZA, especially in the case of dimer. According to calculations, the intermolecular hydrogen bond in PZA dimmer has a moderate, mostly electrostatic character.

It is shown that a very good quantitative agreement between experimental NMR spectra and the calculated chemical shifts both for ^{1}H and ^{13}C nuclei can only be reached by modelling the intermolecular interactions. The correlation consistent cc-pVDZ basis set provide significantly better theoretical chemical shifts for carbon nuclei, with respect to the standard 6-31G(d) basis set. Moreover, theoretical and experimental NMR data suggest that only one of the two protons of NH_2 group can be involved in intermolecular hydrogen bonds.

REFERENCES

1. A.D. Becke, J.Chem.Phys. 98 (1993) 5648.
2. C. Lee, W. Yang, R.G. Parr, Phys.Rev. B 37 (1988) 785.
3. Y.Takaki, Y.Sasada, T.Watanabe, Acta Cryst., 13,693(1960)
4. *Gaussian 98, Revision A.7*, M. J. Frisch, G. W. Trucks, H. B. Schlegel, G. E. Scuseria, M. A. Robb, J. R. Cheeseman, V. G. Zakrzewski, J. A. Montgomery, Jr., R. E. Stratmann, J. C. Burant, S. Dapprich, J. M. Millam, A. D. Daniels, K. N. Kudin, M. C. Strain, O. Farkas, J. Tomasi, V. Barone, M. Cossi, R. Cammi, B. Mennucci, C. Pomelli, C. Adamo, S. Clifford, J. Ochterski, G. A. Petersson, P. Y. Ayala, Q. Cui, K. Morokuma, D. K. Malick, A. D. Rabuck, K. Raghavachari, J. B. Foresman, J. Cioslowski, J. V. Ortiz, A. G. Baboul, B. B. Stefanov, G. Liu, A. Liashenko, P. Piskorz, I. Komaromi, R. Gomperts, R. L. Martin, D. J. Fox, T. Keith, M. A. Al-Laham, C. Y. Peng, A. Nanayakkara, C. Gonzalez, M. Challacombe, P. M. W. Gill, B. Johnson, W. Chen, M. W. Wong, J. L. Andres, C. Gonzalez, M. Head-Gordon, E. S. Replogle, and J. A. Pople, Gaussian, Inc., Pittsburgh PA, (1998)
5. W.J. Hehre, L. Radom, P.v.R. Schleyer, J.A. Pople, “Ab Initio Molecular Orbital Theory”, John Wiley & Sons, New York, 1986.
6. R. Ditchfield, Mol. Phys. 27, 789 (1974).
7. K. Wolinski, J. F. Hilton, P. Pulay, J. Am. Chem. Soc. 112, 8251 (1990).
8. H.G. Korth, M.I. de Heer, P. Mulder, J.Phys.Chem. 106 (2002) 8779.
9. G.A.Jeffrey, An Introduction to Hydrogen Bonding, Oxford University Press, New York, 1997
10. M.Kaupp, M.Buhl, V.G.Malkin (Eds.) *Calculation of NMR and EPR Parameters : Theory and Applications*, Wiley-VCH, Weinheim, 2004
11. R.H.Cox, A.A.Bothner-By, J.Phys.Chem., 72, 1646-1649(1968)
12. E.M.Janke, A.Dunger, H.H. Limbach, K.Weisz, Mang.Reson.Chem., 39, S177-S182 (2001)
13. D.H.Barich, J.S.Clawson, D.Stueber, M.Strohmeier, R.J.Pugmire, D.M.Grant, J.Phys.Chem. A, 106,11375(2002)
14. G.Chung, O.Kwon, Y.Kwon, J.Phys.Chem. A, 101, 9415-9420(1997)

15. B.Ishimoto, K.Tonan, S.Ikawa, Spectrocim. Acta A, 55 (1999) 2321-2327
16. G.-B.Liang, C.J.Rito, S.H.Gellman, J.Am.Chem.Soc. 114 (1992) 4440
17. K.Kim, J.P.Germanas, J.Org.Chem., 62 (1997) 2847
18. S.Akyuz, J.Mol.Struct., 651-653,541(2003)
19. D. Lin-Vien, N. B. Colthup, W. G. Fately, J. G. Grasselli, The handbook of Infrared and Raman Characteristic Frequencies of Organic Molecules", Academic Press Limited, London, 1991

STUDIA UNIVERSITATIS BABES-BOLYAI, PHYSICA, XLIX, 3, 2004

MOLECULAR AND VIBRATIONAL STRUCTURE OF 5-PARA-BROMO-BENZILIDEN–TIAZOLIDIN-2-TION-4-ONA. EXPERIMENTAL AND THEORETICAL INVESTIGATION

A. PÎRNĂU[1], M. BAIAS[1], O. ONIGA[2], V. CHIŞ[1], M. VASILESCU[1], O. COZAR[1]

[1]Babeş-Bolyai University, Faculty of Physics, Kogălniceanu 1, RO-400084 Cluj-Napoca, Romania
[2]Department of Pharmaceutical Chemistry, Faculty of Pharmacy, UMF "Iuliu Haţieganu", Cluj Napoca

ABSTRACT. The 5-para-bromo-benziliden-tiazolidin-2-tion-4-ona molecule was recently synthesized at the Department of Pharmaceutical Chemistry, UMF "Iuliu Hatieganu" Cluj-Napoca, and it was shown to be a very efficient antibiotic that has a superior activity to ampicilin on beta-hemolytic Streptococcus.

The molecular vibrations of 5pBBTT were investigated in polycrystalline sample, at room temperature, by Fourier Transform Infrared Spectroscopy (FT-IR), IR-ATR and FT-Raman spectroscopy. In parallel, quantum chemical calculations based on Density Functional Theory (DFT) are used to determine the geometrical, energetic and vibrational characteristics of the molecule. All the possible conformers and tautomers have been considered and analyzed by theoretical methods.

All the experimental vibrational bands of 5pBBTT were assigned to normal modes on the basis of DFT calculations at the B3LYP and BLYP levels of theory in conjunction with the standard 6-31G(d) basis set. Using a uniform scaling of calculated frequencies, a very good correlation was obtained between the experimental and theoretical vibrational data.

Introduction

DFT methods are increasingly applied to representative pharmacological compounds aiming to elucidate their molecular structures, electronic properties and bonds, the establishment of electronic and structural factors of selected reactions and their mechanisms. These studies contribute to the recognition of structure-activity relationships and to the understanding of the properties and system behavior. For a proper understanding of IR and Raman spectra, a reliable assignment of all vibrational bands is essential. For this purpose, the quantum chemical methods, ranging from semiempirical to DFT approaches, are invaluable tools [1-3], each method having its own advantages. The semiempirical calculations provide very fast, and in certain

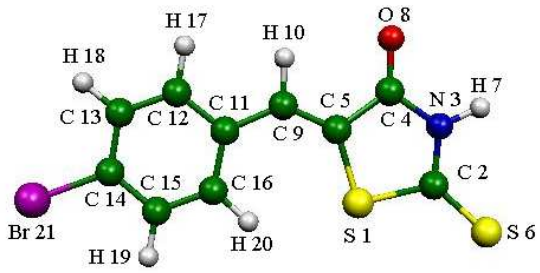

Fig.1. *Molecular structure and atom numbering scheme for 5-para-bromo-benziliden- tiazolidin-2-tion-4-ona molecule*

circumstances fairly good theoretical results, being applicable to large molecular systems. The Hartree-Fock *Ab Initio* methods are able to give good results provided a reasonable basis set and an appropriate correlation treatment is taken into account. On the other hand, DFT methods, particularly hybrid functional methods [4], have evolved to a powerful quantum chemical tool for the determination of the electronic structure of molecules. In the framework of DFT approach, different exchange and correlation functionals are routinely used. Among these, the B3LYP combination [5,6] is the most used since it proved its ability in reproducing various molecular properties, including vibrational spectra. The combined use of B3LYP functional and standard split valence basis set 6-31G(d) has been previously shown [7-9] to provide an excellent compromise between accuracy and computational efficiency of vibrational spectra for large and medium-size molecules.

Experimental

The experimental techniques used in the study of 5pBBTT molecule are: FT-IR/ATR and FT-RAMAN. FT-IR/ATR spectra for 5pBBTT powder sample were recorded at room temperature on a conventional Equinox 55 FT-IR spectrometer equipped with an InGaAs detector, coupled with a Bruker Miracle ATR sampling device. The FT-Raman spectra were recorded in a backscattering geometry with a Bruker FRA 106/S Raman accessory attached to the FT-IR spectrometer. The 1064 nm Nd:YAg laser was used as excitation source, and the laser power was set to 400 mW. All spectra were recorded with a resolution of 4 cm^{-1} by co-adding 32 scans.

Computational details

The molecular geometry optimizations and vibrational frequencies calculations were performed with the Gaussian 98W software package [10] by using DFT methods with B3LYP and BLYP functionals, which have been previously shown to perform very well for vibrational spectra calculations [11]. The basis sets used in these calculations are: 6-31G(d), 6-31+G(d,p) and 6-311+G(2df,p). The geometries were fully optimized without any constraint with the help of analytical gradient procedure implemented within Gaussian 98W program. Vibrational mode assignments were made by visual inspection of modes animated by using the Molekel program [12]. The calculated molecular properties are: equilibrium geometries and vibrational spectra (IR and Raman).

Results and discussion

Due to its complexity, a number of possible conformers are possible for this molecule. Moreover, each conformer may exist in two tautomeric forms as thion and thiol, respectively. First we optimized the geometries for all the possible conformers and tautomers for 5-pBBTT molecule. The optimized structures are given in Fig.2 and their absolute and relative energies are summarized in Fig.3. The geometries were fully optimized without any constraint at B3LYP/6-31G(d) level of theory. No imaginary frequencies were obtained for optimized geometries and thus, all the optimized structures represent true minima on the potential energy surface. Comparing the calculated energies for each conformer we found that the lowest energy conformer is C1 conformer in its thionic form, as shown in Fig.3.

The small difference between the energy of the two thionic conformers of 5-pBBTT (C1 and C2) suggest that very possible, the two conformers coexist in liquid phase, so that for a careful analysis of the solvent effects, the two contributions must be taken into account.

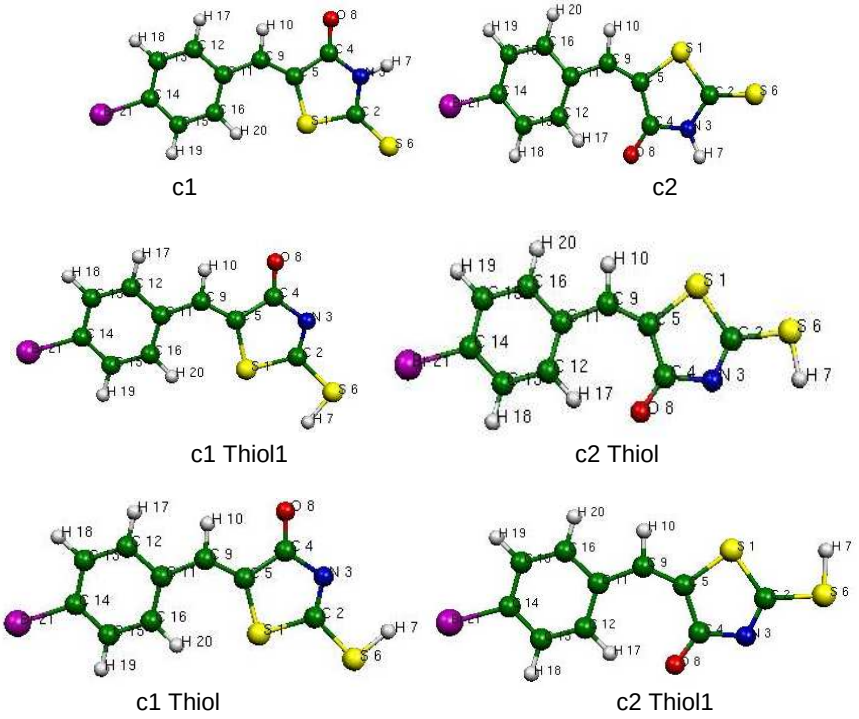

Fig.2. *Optimized geometries for the possible conformers and tautomers of 5pBBTT*

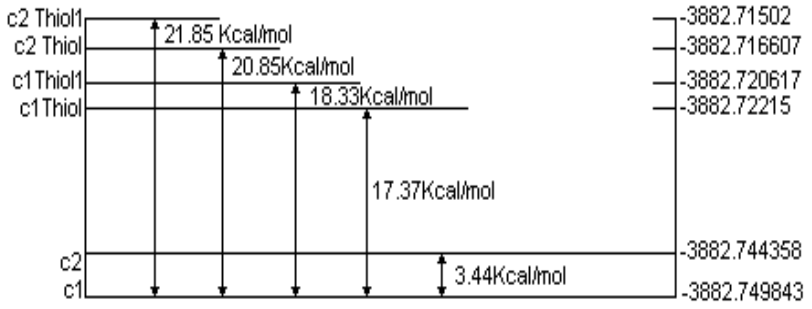

Fig.3. *Total and relative energies (not to scale) for the equilibrium geometries of the conformers and tautomers of 5-pBBTT molecule*

In Fig. 4 are given the experimental FT-Raman, FT-IR and ATR spectra. Normal mode frequencies have been calculated by using the Gaussian program [10] and the computed wave-numbers have been scaled by 0.9614 [13]. Theoretical values were obtained for the single 5-pBBTT molecule but also for a complex formed by 5-pBBTT molecule with two DMSO molecules, in order to test how these later molecules bind to the 5-pBBTT.

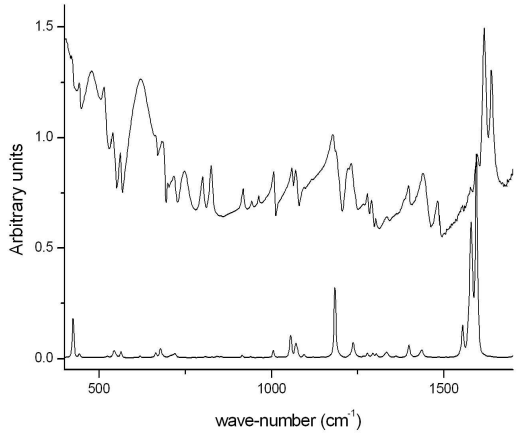

Fig.4. *Experimental vibrational spectra of 5-pBBTT. Top: FT-IR/ATR spectrum, bottom: Raman spectrum*

According to calculations, the experimental band at 3477cm^{-1} in IR spectrum corresponds to the ν(NH) stretching vibration. The corresponding theoretical value for the gas-phase molecule is 3460cm^{-1}, in very good agreement with experiment. However, as expected, for 5-pBBTT-DMSO complex, the calculated value is significantly lower in frequency, at 2930cm^{-1}. The ν(CH) vibrations are predicted by B3LYP/6-31G(d) calculations in very good agreement with experiment: theoretical values are between 3108cm^{-1} and 3044cm^{-1}, while the experimental counterpart is 3082cm^{-1}.

Another characteristic band is that due to the ν(CO) vibration which is seen in the infrared experimental spectrum at 1734cm^{-1}, the calculated value being 1743cm^{-1}. For the complex, this band is shifted to a lower value at 1715cm^{-1} and according to calculations, this mode is coupled with ν(CC), δ(NH) and δ(CH) vibrations. ν(CC) vibrations give rise to experimental bands at 1597, 1578, 1554 and 1398cm^{-1} with theoretical counterparts at 1599, 1576, 1543 and 1393cm^{-1}. Stretching vibrations of CN bond are seen in the experimental spectrum at 1441 and 1187cm^{-1}, the calculated values being 1404 and 1213cm^{-1}, respectively. The positions and infrared intensities of these bands are very well reproduced by B3LYP/6-31G(d) calculations. Out of plane vibrations of ring CH bonds give the experimental bands located at 1483, 1178 and 1094cm^{-1} in very good agreement with theory: 1477, 1178 and 1108cm^{-1}. Stretching vibration involving the heavy atoms Br and S give the experimental bands at: 1060cm^{-1} (ν(BrC)) and 1007cm^{-1} (ν(C2S6)).

The calculated values match again very well the experimental data in band positions (1055 and 1029cm^{-1}, respectively) and intensity pattern. However, the ν(C2S1) vibration has the calculated wave-number at 636cm^{-1} but it is not seen in the experimental spectrum. This could be an indicative for the involvement of this group in intermolecular interactions which could have as a result an important shift of this band.

The experimental vibrational bands for the δ(CCC) trigonal bending vibrations are located at 1279, 963, 686 and 663cm^{-1} with corresponding calculated values at 1283, 978, 693 and 663cm^{1}. As resulted from this analysis, a very good overall agreement is obtained between the experimental and theoretical infrared spectrum of 5-pBBTT molecule and this fact confirms the assignment of vibrational spectrum of this molecule.

Conclusions

The main conclusions of our work can be summarized as follows:

i) the most stable conformer of 5-pBBTT molecule is the thionic conformer with S1 atom in cis position with respect to C16 atom.

ii) the small energetic difference between the two thionic conformers suggest that in liquid or gas-phase both conformers could contribute to the vibrational and NMR spectrum of this molecule.

iii) the very good match between the experimental and calculated normal modes wave-numbers of 5-pBBTT molecule allow us to safely assign the vibrational spectrum of the molecule.

REFERENCES

1. M. Castella-Ventura, E. Kassab, G. Buntinx, O. Poizat, Phys.Chem.Chem.Phys. 2 (2000) 4682.
2. D.N. Shin, J.W. Hahn, K.H. Jung, T.K. Ha, J.Raman Spectroscop. 29 (1998) 245.
3. B. Giese, D. McNaughton, Phys.Chem.Chem.Phys. 4 (2002) 5161.
4. R.G. Parr, W. Yang, Density-Functional Theory of Atoms and Molecules, Oxford University Press, New York, 1989.
5. A.D. Becke, J.Chem.Phys. 98 (1993) 5648.
6. C. Lee, W. Yang, R.G. Parr, Phys.Rev. B 37 (1988) 785.
7. V. Chiş, Chem. Phys. 300 (2004) 1.
8. W. Zierkiewicz, D. Michalska, B. Czarnik-Matusewicz, M. Raspenk, J.Phys.Chem. A 107 (2003) 4547.
9. G. Korth, M.I. de Heer, P. Mulder, J.Phys.Chem. 106 (2002) 8779.
10. M.J. Frisch, G.W. Trucks, H.B. Schlegel, G.E. Scuseria, M.A. Robb, J.R. Cheeseman, V.G. Zakrewski, J.A. Montgomery Jr., R.E. Stratmann, J.C. Burant, S. Dapprich, J.M. Millam, A.D. Daniels, K.N. Kudin, M.C. Strain, O.Farkas, J. Tomasi, V. Barone, M. Cossi, R. Cammi, B. Mennucci, C. Pomelli, C. Adamo, S. Clifford, J. Ochterski, G.A. Petersson, P.Y. Ayala, Q. Cui, K. Morokuma, D.K. Malik, A.D. Rabuck, K.Raghavachari, J.B. Foresman, J. Cioslowski,

J.V. Ortiz, A.G. Baboul, B.B. Stefanov, G. Liu, A. Liashenko, P.Piskorz, I. Komaromi, R. Gomperts, R.L. Martin, D.J. Fox, T. Keith, M.A. Al-Laham, C.Y. Peng, A. Nanayakkara, C. Gonzalez, M. Challacombe, P.M.W. Gill, B. Johnson, W. Chen, M.W. Wong, J.L. Andres, C. Gonzalez, M. Head-Gordon, E.S. Replogle, J.A. Pople, Gaussian 98, Revision A.7, Gaussian, Inc., Pittsburg, PA, 1998.

11. F. Jensen, *Introduction to Computational Chemistry*, John Wiley, New York, 1999.
12. P. Flukiger, H.P. Luhti, S. Portmann, J. Weber, MOLEKEL 4.2, Swiss Center for Scientific Computing, Manno (Switzerland), 2000-2002; S. Portmann, H.P. Luhti, Chimia 54 (2000) 766.
13. A.P. Scott, L. Radom, J. Phys. Chem. 100 (1996) 16502.

STUDIA UNIVERSITATIS BABES-BOLYAI, PHYSICA, XLIX, 3, 2004

SELF-ASSEMBLED GOLD NANOPARTICLES ON SOLID SUBSTRATE

FELICIA TODERAS, ADRIANA M. MIHUT, M. BAIA, S. ASTILEAN*, S. SIMON

Faculty of Physics, Babes-Bolyai University, M. Kogalniceanu 1, 400084 Cluj-Napoca, Romania,

ABSTRACT. Gold colloids were prepared and self-assembled onto glass substrates by using an organic coupling agent as 3-aminopropyl-trimethoxysilane (APTMS). The size and spatial distribution of immobilized metal nanoparticles onto solid substrate were characterized by transmission electron microscopy (TEM). Optical extinction spectra of self-assembled gold monolayers exhibit well-defined surface plasmon resonance peaks located at 522 nm. Such noble-metal nanostructures are under current investigation for applications in the field of surface plasmon resonance (SPR) optical biosensing as well as in surface-enhanced Raman spectroscopy (SERS) studies.

Introduction

Noble-metal nanoparticles have been widely investigated due to their unique applications in diversified fields such as surface-enhanced spectroscopies, biosensors, bioprobes, chemical sensors, catalytic activity, and new optical devices [1-5]. In order to optimize their applications and provide materials with controllable optical properties, an important current challenge is to develop effective ways to build large, well-defined structures made of pre-synthesized noble-metal nanoparticles.

A simple method for building and controlling patterns on solid substrates [6,7] is through self-assembly of small, spherical, uniformly sized particles at an interface, imparting a repeating feature size that is dependent upon the particles used. Self-assembly is herein defined as the autonomous organization of nanoparticles into two-dimensional patterns without artificial intervention. Self-assembling particles in the nanometer size range are attracting increasing attention with the growth of interest in nanotechnological discipline. The dimensions of this nanoparticle make them ideal candidates for the nanoengineering of surface and the fabrication of functional nanostructures.

In the past few years, fabrication of noble-metal structures by self-assembling monodisperse populations of nanoparticles has attracted much attention due to their simplicity and flexibility [8]. In particular, gold nanoparticles exhibit a number of advantages, among them being easily to synthesize and tune their size from 3 to 150 nm and having well-understood optical properties [8] and high chemical stability.

In the present work gold colloids were chemically synthesized and self-assembled onto glass substrates by using an organic coupling agent as 3-amino-propyltrimethoxysilane (APTMS). The self-assembled structures were characterized by transmission electron microscopy (TEM) and UV-visible optical spectroscopy.

Experimental

The Au sol was prepared by the following procedure: 500 ml of 10^{-3} M $HAuCl_4$ is brought to a boil with vigorous stirring on a magnetic stirring hot plate. Ten milliliters of 38.8 mM Na_3citrate is add to the solution all at once with vigorous stirring. The yellow solution turns clear, dark blue and then a deep red-burgundy color within a few minutes. Stirring and boiling has been continued for 10-15 minutes after the burgundy color was observed. The solution has been removing from head and kept stirring until the solution is getting cold and then the volume is adjusted to 500 ml with water. Colloidal solutions were stored in clean brown glass bottles until used [8]. The Au nanoparticles diameter is determined by Transmission Electron Microscopy (TEM) with a JEM 1010 microscope.

One method for control of surface morphology is through assembly of small, spherical, uniformly sized particles at an interface. The construction protocol for Au colloid monolayer explains the simplicity of self-assembly from solution and the affinity of noble-metal surface for certain organic functional groups.

In the first step the glass slides were sonicated in CH_3CH_2OH and treating in *Piranha* solution for 24 h to remove organic groups. After that they were rinsed in CH_3OH and functionalized for a few minutes in 3-aminopropyltrimethoxysilane (APTMS) solution. The substrates were rinsed several times with CH_3OH and water before being placed into solution of Au colloid. The silanized substrate may be stored in water for 2-3 h before exposure to colloidal Au. The substrates were placed in solution of Au colloid and are observed surface evolutions in real times. At each time indicated the slides were removed from the Au colloid solution and optical spectra were recorded in water. The optical extinction spectra were recorded with a Jasco V-530 UV-VIS spectrophotometer.

Results and discussion

Figure 1 shows the transmission electron micrograph of the gold colloidal nanoparticles self-assembled on a glass surface. In this self-assembling process the colloidal gold particles were strongly immobilized upon the glass substrate due to the affinity of the amino groups to the gold nanoparticles. As one can see from Fig. 1 the gold particles are uniformly adsorbed on the glass substrate and are isolated one from another. The mean value of the particle diameters was found to be in the range of 16 to 18 nm.

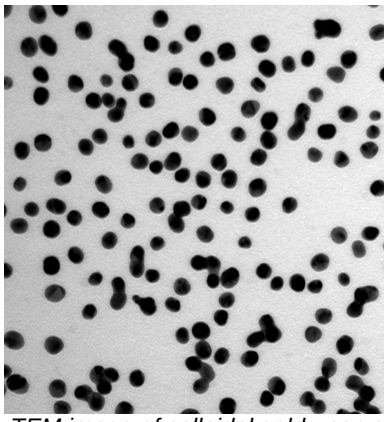

Figure 1. *TEM image of colloidal gold upon glass slide*

In order to monitor the surface evolutions in real time different self-assembled gold monolayers were prepared by varying the immersion time of the glass slide in the colloidal solution. The optical extinction spectra of the as obtained colloidal gold monolayers have been recorded in water and are illustrated in Fig. 2. For comparison purposes the absorption spectrum of pure gold colloid is also presented. As can be seen from Fig. 2 the self-assembled gold monolayers exhibit well-defined surface plasmon resonance peaks at 522 nm. By increasing the immersion time the peak intensity increases. The absorption peak of the sample maintained for 60 min into the colloidal solution presents a shoulder at longer wavelengths, which is most probably due to aggregated gold colloidal nanoparticles.

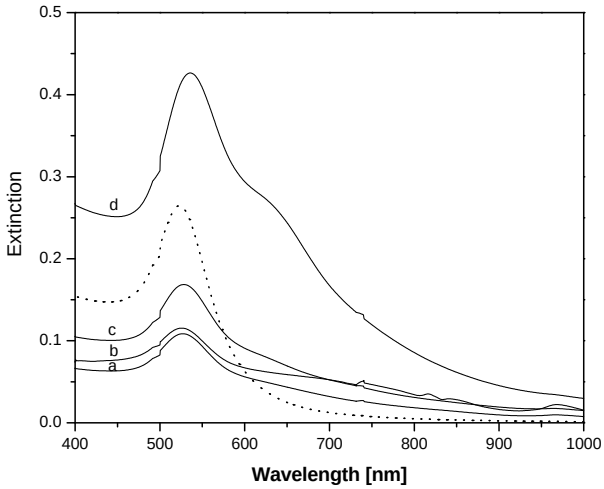

Figure 2. *Optical spectra (in H_2O) of an APTMS-derivatized glass slide after immersion in gold colloid for (a) 5min, (b) 10 min, (c) 20 min, (d) 60 min. The dotted line represents the absorption spectrum of pure gold colloid.*

We were also interested to study the influence of the drying conditions on the morphology and optical response of the as prepared gold substrates. Therefore, the samples were dried in different conditions, in nitrogen atmosphere and in air, and their optical extinction spectra have been measured. A first difference between the dried samples was observed with the naked eye. While the color of all the samples dried in air turned deep blue, among the samples dried in nitrogen atmosphere only the one kept in colloidal solution for 60 min changes its color.

The optical extinction spectra of the samples dried under nitrogen atmosphere are shown in Fig. 3. One can remark in all spectra the presence of the peak at 522 nm, due to isolated small Au particles oscillations, while a new feature corresponding to a collective particle surface plasmon oscillation grows at 650 nm as the particles coverage increases and the interparticle spacing becomes smaller compared with the incident wavelength (see Fig.3d). This feature is responsible for the pronounced SERS activity of the collective gold particles.

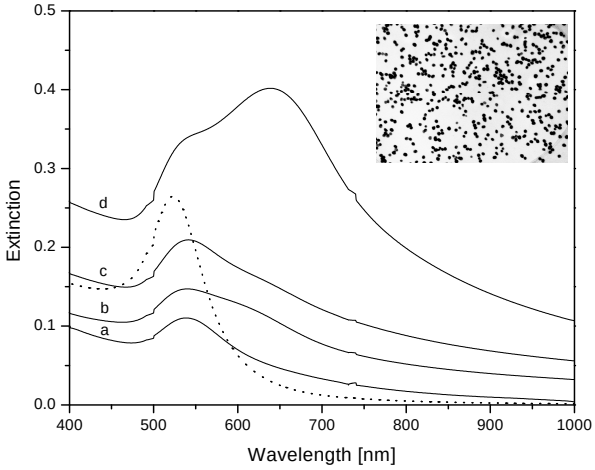

Figure 3. *Optical spectra of an APTMS-derivatized glass slide after immersion in gold colloid for (a) 5min, (b) 10 min, (c) 20 min, (d) 60 min and dried under nitrogen atmosphere.*

On the other hand, the existence of the absorption band around 650 nm in the optical extinction spectra of the samples dried in air, which are presented in Fig. 4, clearly reveals that the drying conditions influence the aggregation process. For colloidal particles of smaller dimensions, a slight blue shift (a few of nanometers) of the absorption band is expected, whereas for larger colloidal particles a red shift of this band is observed.

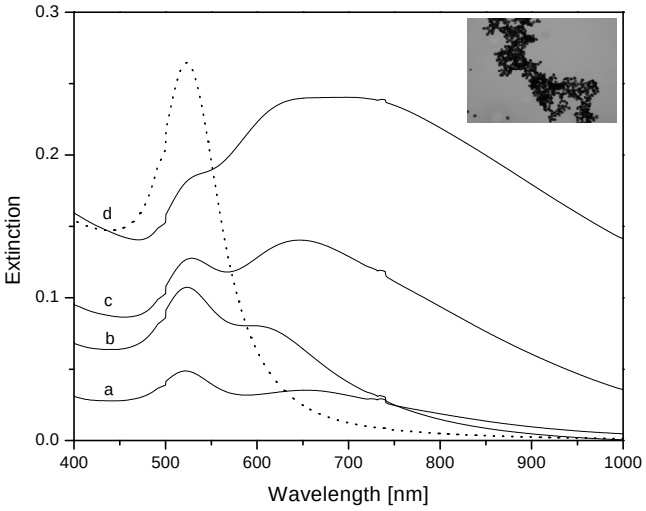

Figure 4. *Optical spectra of an APTMS-derivatized glass slide after immersion in gold colloid for (a) 5min, (b) 10 min, (c) 20 min, (d) 60 min and dried in air.*

Having in view this consideration and analyzing the optical extinction spectra of the dried self-assembled gold substrates we assume that the drying in nitrogen atmosphere prevent the aggregation process. This, assumption was supported by the transmission electron micrograph of the dried samples (see Fig. 5). As it can be observed most of the gold nanoparticles are aggregated and form clusters. Due to their presence the as obtained noble-metal nanostructures should be suitable substrates for applications in surface-enhanced Raman spectroscopy.

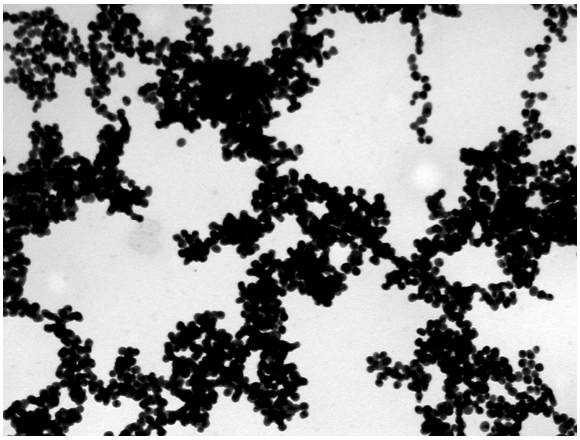

Figure 5. *TEM image of collective gold particles*

Conclusions

Gold colloids were prepared and self-assembled onto glass substrates by using an organic coupling agent as 3-aminopropyl-trimethoxysilane (APTMS). The size and spatial distribution of immobilized metal nanoparticles onto solid substrate were characterized by transmission electron microscopy (TEM).

The optical extinction spectra of the as prepared substrates show a well-defined peak at 522 nm, due to the surface plasmon resonance of the isolated gold particles, and a broad band around 650 nm, given by the collective particle surface plasmon oscillation. It was found that the immersion time in the colloidal solution and drying conditions influence the morphology and the optical response of the as prepared gold nanostructured substrates. The substrates are under current investigation for applications in the field of surface plasmon resonance (SPR), optical biosensing as well as in surface-enhanced Raman spectroscopy (SERS) studies.

REFERENCES

1. N. Felidj, J. Aubard, G. Levi, J. R. Krenn, A. Hohenau, G. Schider, A. Leitner, F. R. Aussenegg, Appl. Phys. Lett., 82, 3095, (2003).
2. J. B. Jackson, S. L. Westcott, L. R. Hirsch, J. L. West, N. J. Halas, Appl. Phys. Lett., 82, 257, (2003).

3. T. Okamoto, I. Yamaguchi, T. Kobayashi, Optical Letters, 25, 6, (2000).
4. C. L. Haynes and R. P. Van Duyne, J. Phys. Chem. B 105, 5599 (2001).
5. M. Baia, L. Baia, S. Astilean, Chem. Phys. Lett, in press 2005.
6. R. G. Freeman, K. C.Grabar, K. J. Alison, R. M. Bright, J. A. Davis, A. P. Guthrie, M. B. Hommer, M. A. Jackson, P. C. Smith, D. G. Walter, M. J. Natan, Science, vol. 267, 1629 (1995).
7. Y. Xia, B. Gates, Y. Yin, Y. Lu, Adv. Mater., 12, 693, (2000).
8. C. D. Keating, M. D. Musick, M. H. Keefe, M. J. Natan, J. Chem. Edu., 76(7), 949 (1999).

STUDIA UNIVERSITATIS BABES-BOLYAI, PHYSICA, XLIX, 3, 2004

XPS INVESTIGATIONS OF GLASS CERAMICS CONTAINING HYDROXYAPATITE

V. SIMON*[1], D. ENIU[2], M. NEUMANN[3], S. SIMON[1]

[1] Babes - Bolyai University, Faculty of Physics, 3400 Cluj-Napoca, Romania
[2] University of Medicine and Pharmacy, Faculty of Pharmacy, 3400 Cluj-Napoca, Romania
[3] University of Osnabrück, Physics Department, 49069 Osnabrück, Germany
**Corresponding author: viosimon@phys.ubbcluj.ro*

ABSTRACT. Glass and vitroceramic samples belonging to $CaO\text{-}SiO_2\text{-}P_2O_5\text{-}Fe_2O_3$ system were investigated by X-ray photospectroscopy (XPS). Glass ceramics were obtained by partial crystallisation of a precursor glass sample heat treated at different temperatures between 1000°C and 1200°C. It was evidenced the effect of partial crystallisation on the ratio of bridging (BO) to non-bridging (NBO) oxygens in the glass ceramic samples in function of heat treatment temperature.

Introduction

Hydroxyapatite, HA, is an important biomaterial and is the principal inorganic constituent of bones and teeth. It corresponds to $Ca_{10}(PO_4)_6(OH)_2$ compound and the calcium and phosphorous cations are in the ratio 1.67. There is a great demand of this material in odontology and traumatology [1], together with others materials of the same family, such as the tricalcium phosphate. Synthetic HA has high biocompatibility and is suited in the reconstruction of damaged bone or tooth zones. HA also finds applications in others fields of industrial or technological interest as catalyst, in chromatography or gas sensor, or its possible use in water purification, fertilizers production or manufacturing of biocompatible ceramics [2, 3].

Calcium phosphate ceramics and vitroceramics are intensely investigated due to their use as bone substitutes that became common in orthopedic surgery. The systems containing also iron oxide [4] present the advantage to reduce the recurrence of tumors by hyperthermic treatment because by hysteresis of ferrimagnetic phases developed in glass-ceramics the temperature can be sufficiently raised to induce significant delay of tumor growth.

The aim of this work is to investigate the effect of partial crystallisation of $CaO\text{-}SiO_2\text{-}P_2O_5\text{-}Fe_2O_3$ glass system on the ratio of bridging (BO) to non-bridging (NBO) oxygens, that affect the local structure and implicitly the surface properties of a potential biomaterial.

Experimental

The starting materials used to prepare $29.04(3.34CaO{\cdot}P_2O_5){\cdot}58.06SiO_2 \cdot \cdot 12.9Fe_2O_3$ (mol %) glass matrix were analytically pure reagents SiO_2, $CaHPO_4{\cdot}2H_2O$, $CaCO_3$ and Fe_2O_3. The suitable mixtures were melted in sintercorundum crucibles. The crucibles were introduced in furnace directly at 1200°C and then the temperature was increased up to 1500°C. As the temperature reached 1500°C the crucibles were taken out and quickly undercooled at the room temperature by pouring onto stainless steel plates.

Specimens of the glass samples were heat treated with a rate of 4°C/min from the room temperature to 1000, 1100 and 1200°C in air. They were maintained at the treatment temperature for 30 minutes and then were slowly cooled in the furnace down to the room temperature.

XPS measurements were performed using a PHI 5600ci Multi Technique system with monochromatised Al K_α radiation from a 250 W X-ray source ($h\nu$ = 1486,6 eV). During the measurements the pressure in the analysis chamber was in the 10^{-9} Torr range. A low energy electron beam was used to achieve charge neutrality at the sample surface. Thermal analysis measurements were carried out using a MOM derivatograph. The TG, DTG and DTA curves were recorded from powder samples, with a rate of 10°C/min. The X-ray diffraction (XRD) patterns were obtained by means of standard DRON-3M powder diffractometer.

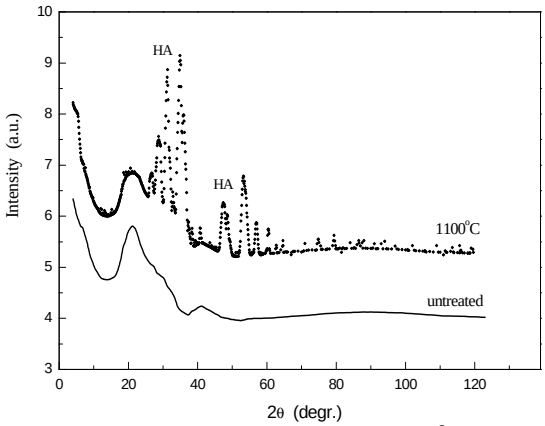

Fig. 1. *XRD patterns for as prepared and 1100°C heat treated samples.*

Results and discussion

The as prepared hydroxyapatite type sample obtained by melt undercooling is vitreous, as evidenced by the XRD pattern recorded from untreated sample (Fig.1). The differential thermal analysis traces (Fig. 2) do not show any thermal event up to 1000°C and consequently the thermal treatment applied to achieve a partial crystallisation was carried out starting from 1000°C. The XRD patterns of the treated samples point out structural changes and the development of hydroxyapatite (HA) crystals (Fig. 1). Other crystalline phases like $Ca_2P_2O_7$, Fe_3O_4, Fe_2O_3, FeO, SiO_2 were also identified [5, 6].

XPS survey spectra recorded from the fractured samples evidence differences in the elemental composition and implicitly in the ratio of the elements on the sample surface due to the crystalline phases developed after heat treatment. This is illustrated in Figure 3 for the untreated glass sample and for the partially crystalline sample resulting after 1100°C treatment. The O 1s core level spectra from all the samples studied are not symmetric (Fig. 4) and denote the presence of both bridging (BO) and non-bridging (NBO) oxygen atoms. The connection type of oxygen atoms is important for biomaterials due to the fact that the BO/NBO ratio

influences their structure and stability in biological media [7-9]. The BO photoelectron peak occurs at higher binding energy and NBO photoelectron peak at lower binding energy [10-13].

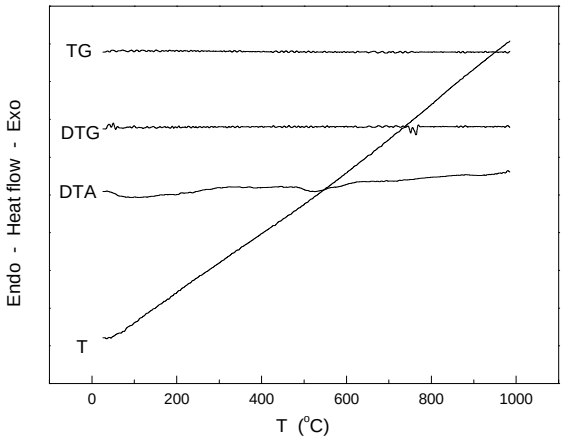

Fig. 2. *Thermogravimetric (TG) differential thermogravimetric (DTG), differential thermal analysis (DTA) and temperature (T) curves recorded from as prepared sample.*

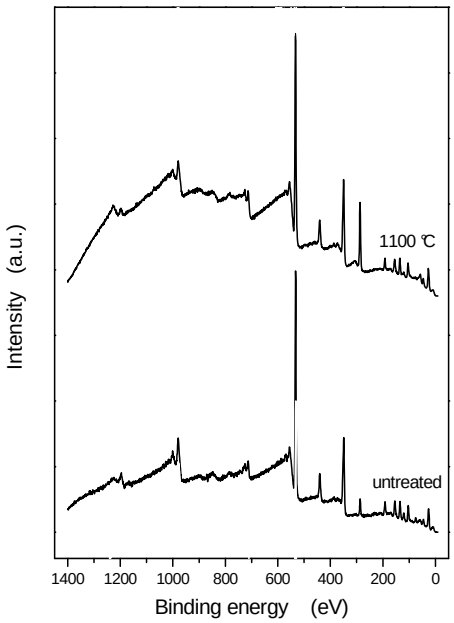

Fig. 3. *XPS survey spectra of as prepared and 1100°C heat treated samples.*

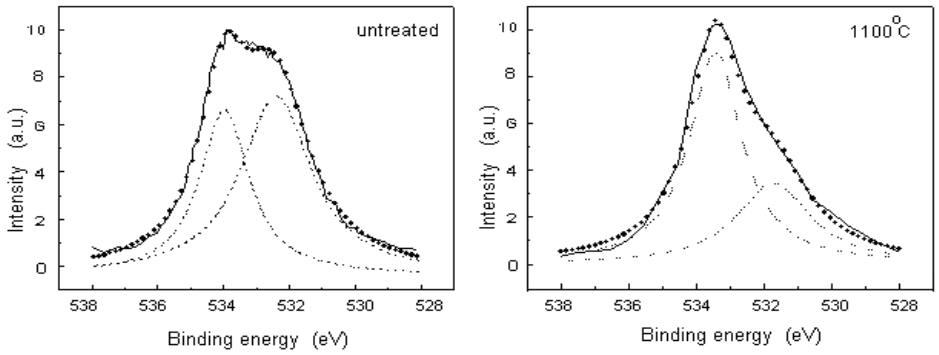

Fig. 4. *XPS O 1s core level spectra (experimental □ and fitted •• with two lorentzian components --) for as prepared and 1100°C heat treated samples.*

For the investigated range of heat treatment temperature, the O 1s binding energy, both for BO and BNO, linearly depends on the heat treatment temperature and lies in the range 531.5 - 533.5 eV. According to the model proposed by Dimitrov and Komatsu [14] regarding the oxide classification on the basis of correlation between electronic polarisabilities of the ions and their binding energies determined by XPS, the values obtained correspond to semicovalent oxides and the investigated samples could be considered semicovalent compounds.

In fact, X-ray photoelectron core lines are sensitive to the chemical environment of the element under examination. Consequently, the analysis of the binding energies of the spectral components offer information about the local structure. A two peaks fit to the O 1s photoelectron spectra (Fig. 4) was carried out for all samples. The number of BO and NBO is assumed proportional to the areas estimated from the BO and NBO peaks [12, 13, 15]. The relative number of BO and NBO is modified by the applied heat treatment as can be seen from the corresponding areas under BO and NBO fit peaks (Table 1). In relation to the glass sample, the first treatment carried out at 1000°C led to an decrease with 12 % in BO number, while for higher treatment temperatures, of 1100°C and 1200°C, the BO number increases up to twice. These data reveal that as a result of the heat treatment at 1000°C a part of BO from the vitreous network became NBO. The behaviour is changed as the samples are slowly cooled from heat treatment temperatures higher than 1000°C. In these cases the crystalline phases are better developed and contain a larger BO number that increases with the treatment temperature.

Table 1

T_t (°C)	A_{BO} (a.u.)	A_{NBO} (a.u.)	N_{BO}/N_t (%)
untreated	1,677	2,623	39
1000	1.085	2.934	27
1100	2.964	1,596	65
1200	3,776	0,944	80

Conclusions

XPS data show that O 1s binding energies both for glass and glass ceramic samples lie in the range 531.5 - 533.5 eV and denote that these compounds are semicovalent. After the heat treatment applied at 1000^{o}C the BO number diminishes with respect to the precursor glass sample, while for higher heat treatment temperatures, 1100^{o}C and 1200^{o}C, BO number increases. In the first case the result is due firstly to the perturbation of the local order from the glass sample at a temperature that evidenced no thermal event by differential thermal analysis, but leads to partial crystallisation as seen from XRD data. The higher treatment temperatures are more favourable for the crystallisation process and the increase of BO number in these samples also reflect a better long range order.

REFERENCES

1. R.Z.Legeros, in Calcium Phosphates in Oral Biology and Medicine, vol. 15, Ed. H.M. Myers, Karger Publ., Basel, 1991.
2. T.S.B. Narasaraju, D.E. Phebe, J. Mater. Sci., 31, 1 (1996).
3. J. Arends, J.L. Ruben, J. Chistoffersen, W.L. Jongleboed, T.G.M. Zuidgeest., Carier Res. 24, 432 (1990).
4. K.A. Gross, R. Jackson, J.D. Cashion, L.M.Rodriguez-Lorenzo, Eur. Cells and Mat., *3*, 2, 114 (2002).
5. Inorganic Index to the Powder Diffraction File, Published by Joint Committee on Powder Diffraction Standards Easton, Md., 1971.
6. V.Simon, S.G.Chizbaian, M.Neumann, D.Eniu, E.Indrea, A.Torok-Kiss, S.Simon, Mod. Phys. Lett. B, *14*, 21, 767 (2000).
7. Ahmed, M. Lewis, I. Olsen. J. C. Knowles, Biomaterials, *25*, 3, 491 (2004).
8. F. Branda, F. Arcobello-Varlese, A. Costantini, G. Luciani, Biomaterials, *23*, 3, 711 (2002)
9. E. De Barra and R. G. Hill, Biomaterials, *21*, 6, 563 (2000).
10. J. Jen, M. Kalonowski, J. Non-Cryst. Solids, 38-39, 21 (1980).
11. B.M. Smets, T.P.A. Lommen, Phys. Chem. Glasses, *22*, 6, 158 (1981).
12. I.A. Gee, D. Holland, C.F. McConville, A. Mekki, R. Hussin, Phys. Chem. Glasses, *41*, 4, 175 (2000).
13. V. Simon, H. Bako-Szilagyi, M. Neumann, S.G. Chizbaian, S. Simon, Mod. Phys. Lett. B, *17*, 7, 291 (2003).
14. V. Dimitrov, T. Komatsu, J. Solid State Chem., 163, 100 (2002).
15. G. Speranza, M.Ferrari, M. Bettinelli, Philosophical Magazine B, *79*, 11/12, 2145 (1999).

STUDIA UNIVERSITATIS BABES-BOLYAI, PHYSICA, XLIX, 3, 2004

IR AND RAMAN SPECTROSCOPIC INVESTIGATIONS OF THE IRON DOPING EFFECT ON THE STRUCTURE OF PHOSPHATE GLASSES

L. BAIA[1], D. MURESAN[1], E. BUREAN[1], V. SIMON[1], W. KIEFER[2] and S. SIMON[1]*

[1] *Faculty of Physics, Babes Bolyai University, 400084*
Cluj-Napoca, Romania
[2] *Institut für Physikalische Chemie, Universität Würzburg, D-97074*
Würzburg, Germany

ABSTRACT. Glasses belonging to (100-x)[$50P_2O_5 \cdot 30CaO \cdot 20Na_2O$]x$Fe_2O_3$ system, with $0 \le x \le 1.48$, have been investigated by means of infrared (IR) and Raman spectroscopy. Specific data regarding their local structure and structural changes induced by the iron oxide addition to soda-calcium-phosphate matrix were evidenced and analyzed.

Introduction

Calcium phosphate glasses have a great potential for use as bone and dental implants, since the chemical composition of these materials could be easily choose close to that of the replaced bodies [1, 2]. On the other hand, it was found that biological glasses based on calcium phosphate represent an interesting option as biodegradable materials for tissue engineering constructs [3, 4]. Recently a new type of phosphate glasses, of $50P_2O_5 \cdot 30CaO \cdot 20Na_2O$ composition, has been obtained and characterized, its possible use as biomaterial for tissue engineering being evidenced [4].

The basic building blocks of amorphous phosphate systems are the PO_4 tetrahedra. These structural units link through covalent bridging oxygens to form various phosphate anions. The tetrahedra are classified using the Q^i terminology, where "i" represents the number of bridging oxygens (BO) per tetrahedron [5]. The addition of a modifier oxide to the pure P_2O_5 glass network leads to non-bridging oxygens (NBO) in the glass, that result in a depolimerization of the phosphate network, with oxygen atoms breaking the P-O-P links [6].

The addition of iron to some phosphate glasses was found to increase the chemical durability and to suppress the tendency for crystallization on cooling or reheating [7]. Furthermore, it was evidenced that the change from BO to NBO with increasing Fe_2O_3 content affects various glass properties [8].

In this study our interest was to obtain by means of IR and Raman spectroscopic methods information concerning the structural changes in glasses belonging to the (100-x)[$50P_2O_5 \cdot 30CaO \cdot 20Na_2O$]$\cdot x Fe_2O_3$ system, with $0 \le x \le 1.48$, in order to determine the influence of small iron contents on the structure of a potential bioglass.

Experimental

Glass samples of compositions (100-x)[$50P_2O_5 \cdot 30CaO \cdot 20Na_2O$]$\cdot x Fe_2O_3$ with $0 \le x \le 1.48$ were prepared using as starting materials $NH_4H_2PO_4$, $CaCO_3$, $Na_2CO_3 \cdot 10H_2O$, and Fe_2O_3 of reagent purity grade. The mixtures corresponding to the

* *Corresponding author. E-mail address: simons@phys.ubbcluj.ro*

desired compositions were melted in air, in sintered corundum crucibles, in a Carbolite RF 1600 electric furnace at 1200 ℃ and maintained for 15 minutes at this temperature. The melts were quickly cooled at room temperature by pouring and pressing between two stainless steel plates. The samples have been analyzed by X-ray diffraction and no crystalline phase was evidenced.

The Raman measurements were performed on a Dilor Labram system equipped with an Olympus 0.90 X 100 microscope objective, an 1800 lines/mm grating and an external laser with an emission wavelength of 514.5 nm. In the recording of the micro-Raman spectra a power of 100 mW on the sample has been employed.

For IR measurements the glasses were powdered and mixed with KBr in order to obtain thin pellets with a thickness of about 0.3 mm. The IR spectra were recorded with a Bruker Equinox 55 spectrometer; the spectral resolution in this case was 2 cm^{-1}.

Results and discussion

The Raman spectra recorded on the investigated samples are displayed in Fig. 1. It can be observed that the addition of the iron oxide to the soda-calcium phosphate matrix leads to the increase in intensity of the bands and shoulders situated around 340, 755 and 1080 cm^{-1} and attributed mainly to the O-P-O bending, P-O-P stretching, $(PO_3)^{2-}$ (Q^1 species) asymmetric stretching and $(PO_2)^-$ and $(P_2O_7)^{4-}$ (Q^2 and Q^1 species) symmetric stretching vibrations, respectively [9 - 12].

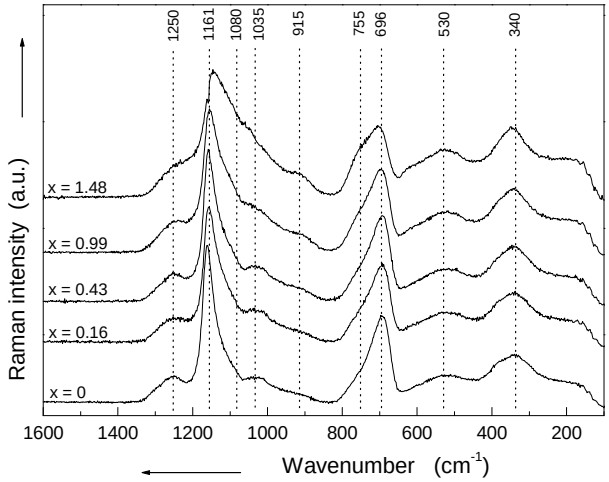

Fig. 1. *Raman spectra of (100-x)[50P_2O_5·30CaO·20Na_2O]·xFe_2O_3 glasses.*

These spectral changes shown that the addition of iron to the glass network matrix has as consequence both the appearance of a distortion of the phosphate structural units as well as the increase of the the NBO number in PO_4 tetrahedra. The last result indicates the progressive occurrence of a depolimerization process of the phosphate glass network. It was reported [13] that the increase in asymmetry on the high energy side of the band around 696 cm^{-1}, which is assigned to the P-O-P stretching vibrations of the long-chain species, is caused by the increase of the

number of very short phosphate units. A close analysis of the Raman spectra in this spectral range, by deconvolution of the bands under discussion (696 and 755 cm^{-1}), reveals (Fig. 2) that the addition of iron oxide has as effect the increase of the number of very short phosphate units. This result represents an supplimentary proof that accounts for the existence of the depolimerization process. By inspecting further the Raman spectra one can see that while the weak Raman signal recorded around 915 cm^{-1} and due to the P-O-P stretching vibrations slowly increase in intensity, a progressive shift towards smaller wavenumbers of the band recorded at 1161 cm^{-1}, for x = 0, and attributed to asymmetric stretching vibrations of $(PO_2)^-$ (Q^2 species) [9] takes place as the doping level increases. On the other hand, a slight broadening of the Raman bands at 1250 cm^{-1} assigned to asymmetric stretching vibrations of $(PO_2)^-$ (Q^2 species) occurs with the increase of the Fe_2O_3 content. The main cause of these spectral modifications is represented by the progressive distortion of the phosphate structural units.

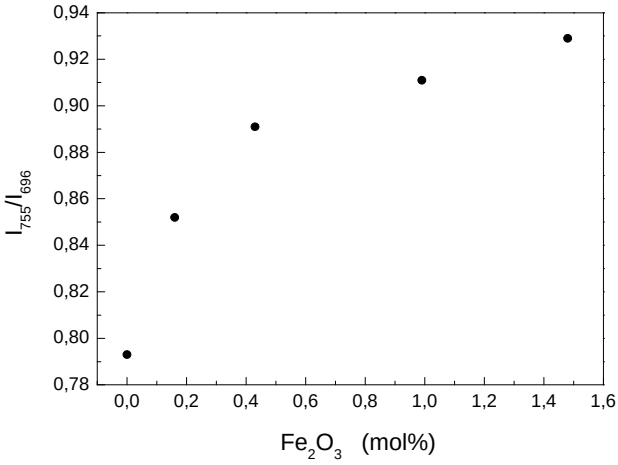

Fig. 2. *Iron doping influence on the ratio between intensities of the Raman deconvoluted bands assigned to very short (755 cm^{-1}) and long chain (696 cm^{-1}) phosphate species vibrations.*

By surveying the IR spectra depicted in Fig. 3 one can remark spectral features similar to those observed in the Raman spectra. Thus, it can be observed that the addition of iron leads both to the increase in intensity of the shoulders located around 540, 1050 and 1180 cm^{-1} and assigned to P-O-P bending, $(PO_3)^{2-}$ (Q^1 species) asymmetric and symmetric stretching vibrations, respectively, as well as to the shift to smaller wavenumber values of the band situated at 1120 cm^{-1} for x = 0 and attributed to $(PO_3)^{2-}$ (Q^1 species) asymmetric stretching vibrations [9, 14]. It can be also seen the decrease in intensity of the band at 1260 cm^{-1} due to $(PO_2)^-$ (Q^2 species) asymmetric stretching vibrations.

The absorption band at 920 cm^{-1} assigned to P-O-P stretching vibrations does not visibly change its intensity as iron content increases. These spectral changes in the IR spectra, like those observed in the Raman spectra, show the distortion of the phosphate units and the increase of the the NBO number in PO_4 tetrahedra as a result of the depolimerization process of phosphate glass network with the increase of the iron doping level.

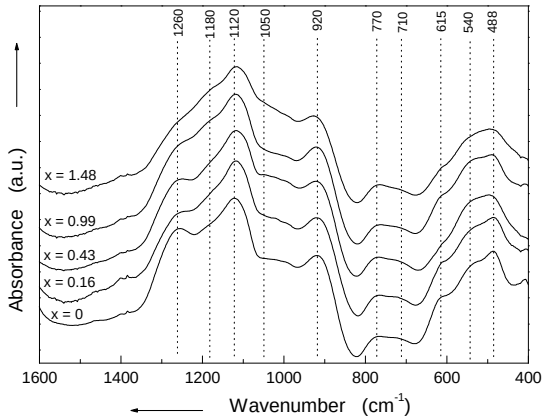

Fig. 3. *IR spectra of (100-x)[50P_2O_5·30CaO·20Na_2O]·xFe_2O_3 glasses.*

Conclusion

Glasses belonging to the (100-x)[50P_2O_5·30CaO·20Na_2O]·(1-x)Fe_2O_3 system, with $0 \leq x \leq 1.48$, have been characterized by means of IR and Raman spectroscopy. It was found that the glass network structure of the investigated samples is mainly formed by anionic Q^2 [$(PO_2)^-$] and Q^1 [$(PO_3)^{2-}$] species. Despite the fact that in all samples the iron oxide content is low, the spectral data reveal that by progressive addition of Fe_2O_3 a distortion of the PO_4 structural units and an increase of the NBO number occur. These results evidence the appearance of a depolimerization process with the increase of the Fe_2O_3 content.

REFERENCES

1. L. L. Hench, R. J. Splinter, W. C. Allen, T. C. Greenlee, *J. Biomed. Mater. Res. Symp.*, 2, 117 (1972).
2. M. Ogino, L. L. Hench, *J. Non-Cryst. Solids*, 38-39, 673 (1980).
3. M. Navarro, S. del Valle, S. Martinez, S. Zeppetelli, L. Ambrosio, J. A. Planell, M. P. Ginebra, *Biomaterials*, 256, 4233 (2004).
4. I. Ahmed, M. Lewis, I. Olsen and J. C. Knowles, *Biomaterials* 25, 491 (2004).
5. R. K. Brow, *J. Non-Cryst. Solids*, 263-264, 1 (2000).
6. A. G. Dias, M. A. Lopes, I. R. Gibson, J. D. Santos, *J. Non-Cryst. Solids*, 330, 81 (2003).
7. B. C. Sales, L. A. Boatner, *Science*, 226, 45 (1984).
8. M. G. Mesko, D. E. Day, *J. Non-Cryst. Solids*, 273, 27 (1999).
9. G. Le Saoüt, P. Simon, F. Fayon, A. Blinn, Y. Vaills, *J. Raman Spectr.*, 33, 740 (2002).
10. M. Hafid, T. Jermoumi, N. Niegisch, M. Mennig, *Mater. Res. Bulletin*, 36, 2375, (2001).
11. S. T. Reis, D. L. A. Faria, J. R. Martinelli, W. M. Pontuschka, D. E. Day, C. S. M. Partiti, *J. Non-Cryst. Solids*, 304, 188 (2002).
12. D. Ilieva, B. Jivov, G. Bogachev, C. Petkov, I. Penkov, Y. Dimitriev, *J. Non- Cryst. Solids*, 283, 195 (2001).
13. J. E. Pemberton, L. Latifzadeh, *Chem. Mater*, 3, 195 (1991).
14. C. Dayanand, G. Bhikshamaiah, V. J. Tyagaraju, M. Salagram, A. S. R. Krishna Murthy, *J. Mater. Science*, 31**,** 1945 (1996).

STUDIA UNIVERSITATIS BABES-BOLYAI, PHYSICA, XLIX, 3, 2004

THE INVESTIGATION OF EXCITED-STATE DYNAMICS OF BIOLOGICAL PHOTOSENSORS BY MEANS OF FEMTOSECOND TIME-RESOLVED FOUR-WAVE MIXING SPECTROSCOPY

[1]B. DIETZEK, [1]R. MAKSIMENKA,[2]G. HERMANN, [1]W. KIEFER, [3]J. POPP, [1,3] M. SCHMITT*

[1] *Institut für Physikalische Chemie, Bayerische Julius-Maximilians Universität Würzburg, Am Hubland, 97074 Würzburg, Germany*
[2] *Institut für Biochemie und Biophysik, Friedrich-Schiller-Universität Jena, Philosophenweg 12, 07743 Jena, Germany*
[3] *Institut für Physikalische Chemie, Friedrich-Schiller-Universität Jena, Helmholtzweg 4, 07743 Jena, Germany*
** Corresponding author. Tel.: (+49-3641) 948367. Fax: (+49-3641) 948300. email: m.schmitt@uni-jena.de*

ABSTRACT. Femtosecond-time-resolved four-wave-mixing spectroscopy was employed to study the primary light-induced processes of phycocyanobilin. The excitation wavelength was varied over the spectral region of the ground-state absorption. The results obtained, show that both the rate of the photoreaction in phycocyanobilin and the ratio of the decay of different excited-state species via two decay channels depend on the excitation wavelength. The data presented here support a recently established model for the primary photoprocesses in phycocyanobilin (J. Phys. Chem B ***2000***, *104*, 1810-1816).

Introduction

Phycocyanobilin belongs to a class of open-chain tetrapyrrole chromophores which play a functional and vital role in nature.[1] As a 2,3 dihydrobilindion chromophore (panel A of Fig. 1), phycocyanobilin constitutes the prosthetic group of the phycobiliproteins C-phycocyanin and allophycocyanin, both involved in the light harvesting and energy transfer processes within the photosynthetic antenna complexes of cyanobacteria or red algae.[2-4] Most likely, phycocyanobilin is also the main target in reactions of C-phycocyanin which result in an antioxidant, radical scavenging, anti-inflammatory and anti-cancer effect.[5,6] Furthermore, phycocyanobilin occurs slightly modified as the chromophore of the light sensor protein phytochrome. The latter chromophore, phytochromobilin, differs from phycocyanobilin only by substitution of a vinyl instead of an ethyl group at the terminal pyrrole ring D (Figure 1, panel A). In contrast to the phycobiliproteins, phytochromes function as the on-off switch for biological processes in plants, collectively termed photomorhogenesis. They control physiological responses such as germination, seedling development and flowering.[7,8] In the two functional systems, the phycobiliproteins and the phytochromes, the very similar bilin prosthetic groups are covalently bonded to a protein moiety which obviously influences the definite biological function of the whole chromoprotein through specific chromophore protein interactions. Thus, studies on the isolated tetrapyrrole chromophores in solution should provide very useful information in order to understand the more complex molecular mechanisms inside the protein cavity and to unravel the driving force of the highly selective photochemical events.[9 -15]

First femtosecond time-resolved transient absorption measurements on phycocyanobilin were reported together with a kinetic model for the excited-state reaction dynamics in a preceding paper.[16] In the present work, the validity of this model is tested by performing transient population grating (TG) experiments at excitation wavelengths throughout the spectral range of the steady state absorption spectrum. The coherent TG technique provides nearly background- and noise-free kinetic data and, therefore, highly accurate kinetic constants.[17] Concerning the details of our experimental setup, the isolation of phycocyanobilin (PCB) from the cyabobacterium *Spirulina geitleri* and the sample preparation the reader is referred to the references 18 and 19 as well as reference 16, respectively.

Kinetic model under discussion and consequences

The kinetic model proposed by Bischoff et al.[16] to account for the excited state processes in photoexcited PCB is based on pump probe experiments with excitation at a single wavelength of 610 nm only. It is summarized schematically in figure 1: Three different ground-state species of phycocyanobilin, PCB_A, PCB_B and PCB_C, can be identified in alcoholic solutions. PCB_A, adopting a cyclical-helical conformation,[12] is the predominat species at room-temperature. The structural features which distinguish PCB_B and PCB_C from PCB_A are still unknown, though recent semiempirical AM1 studies suggest that other minimum-energy conformations may coexist along with the most stable cyclic-helical structure[15].

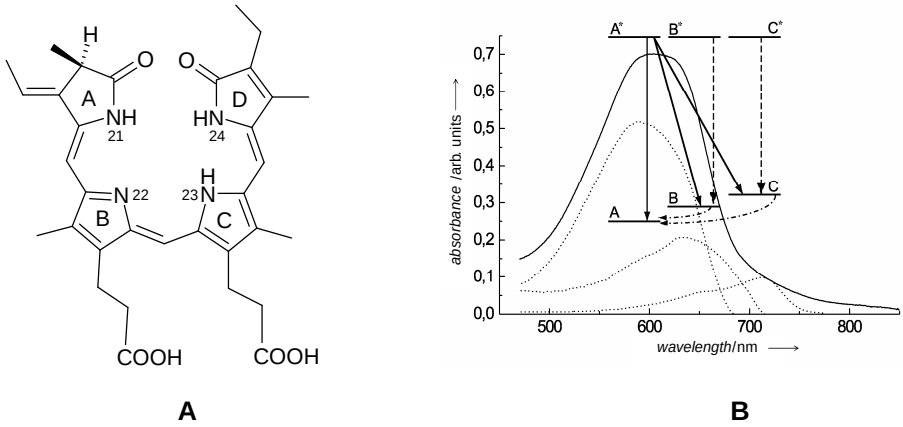

A **B**

Figure 1. Panel A *shows the structure of phycocyanobilin in the cyclic helical conformation. In the chromophore of phytochrome, the ethyl side chain at pyrrole ring D is substituted by a vinyl group.* ***Panel B*** *displays the steady-state absorption spectra of the individual species of phycocyanobilin and the kinetic model of the reaction dynamics in photo-excited phycocyanobilin. The individual absorption spectra of the species PCB_A, PCB_B and PCB_C (dotted lines) are shown vs the stationary absorption spectrum of phycocyanobilin (solid line).*

In the experiments of Bischoff et al.[16] PCB was excited at 610 nm leading to the species PCB_A and PCB_B in the corresponding excited states while the species PCB_C is not photoexcited due to its longwave absorption maximum. The population

in B* internally converts back into the corresponding ground state resulting in a lifetime of B* of τ_1 = (3.2 ± 1.0) ps (time constants referring to methanol as solvent). A* also returns back to its ground state, while however simultaneously undergoing a photoreaction into species PCB_B and PCB_C leading to a decay of the population in A* with a time constant of τ_2 = (30 ± 8) ps. As the photoinduced interconversion from PCB_A into PCB_B and PCB_C leads to a state that is not populated according to the thermal equilibrium any longer, a thermally driven back-reaction from PCB_B and PCB_C into PCB_A occurs until thermal equilibrium is reached again. This process can be described with a time constant τ_3 = (350 ± 100) ps. The model introduced by Bischoff et al.[16] implies that the ratio of the decay amplitudes associated with the different decay channels is dependent on the excitation wavelength.

Pump-wavelength-dependency of the excited-state processes

In order to verify the kinetic model described above, we have examined the excitation wavelength dependency of the decay processes in PCB by carrying out TG measurements. The excitation wavelength was varied between 600 and 670 nm, thus covering mainly the steady state absorptions of PCB. TG signals were recorded with the probe wavelength set to 500 nm, i.e. in a spectral region where a transient absorption of the species PCB_A and PCB_B can be observed.[16] Quantitative data analysis is done by normalizing each transient signal and fitting the experimental transients to a function, which includes the convolution of our experimental response function with the bi-exponential decay. (For details concerning the details of the fitting procedure the reader is referred to reference 18.)

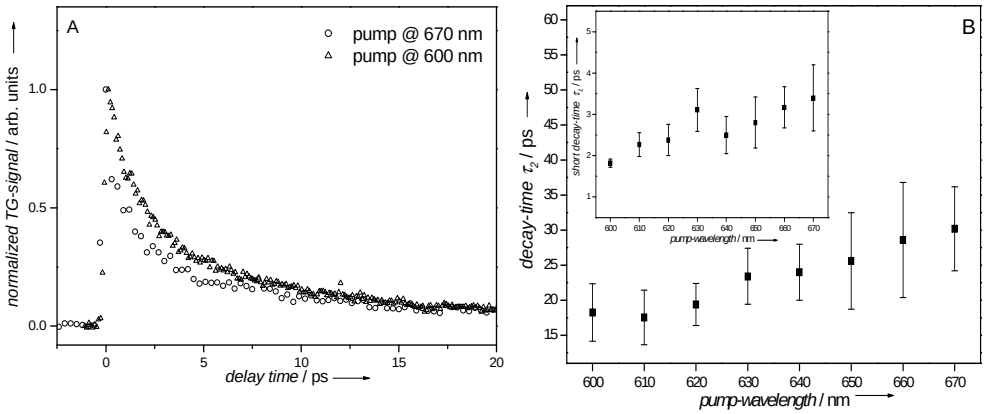

Figure 2. Panel A. *Kinetics of the absorption changes at 500 nm after excitation of phycocyanobilin at 670 nm (circles) and 600 nm (triangles).* ***Panel B****. Pump-wavelength dependency of the decay times and decay amplitudes in the kinetics of phycocyanobilin. The main panel shows the photoreaction time* τ_2 *as a function of pump-wavelength, the inset displays an analogous plot of the short decay time* τ_1*.*

Figure 2A shows two representative TG signals taken at different pump-wavelengths while panel B summarizes the estimates of the time constants τ_1 and τ_2 obtained from the fits of the data. The majority of estimates for the short decay

time τ_1 conform well with the value of τ_1 = (3.2 ± 1.0) ps as determined by Bischoff et al.,[16] an exception being the estimate of 1.8 ps for pumping at 600 nm. On the other hand a pronounced dependence on the pump wavelength can be observed for the long decay component τ_2; it clearly increases with an increased pump wavelength. The estimates of τ_2 reach from 18 ps for excitation at 600 nm to 30 ps for pumping at 670 nm. This finding is most likely due to an accelerated rate of the internal conversion process in the S_1 state, which occurs, when the pump photons deliver an excess vibrational energy to the molecular system.[20]

Figure 3 displays the amplitude ratio α/β associated with the two lifetime components τ_2 and τ_1, respectively, as a function of the excitation wavelengths. It can be seen clearly that the ratio α/β strongly depends on the pump color. The pronounced drop when tuning the pump laser to longer wavelength is explained in the context of the model suggested by Bischoff et al[16]. As only A* molecules (and not B* species) can undergo a photoreaction the amplitude of the photoreaction channel associated with the decay time τ_2 decreases as more B* molecules are excited. The corresponding species related absorption spectra for PCB dissolved in methanol are shown in figure 1. Pumping at longer wavelengths creates an increasing excitation into species PCB_B resulting in an increasing contribution of excited state PCB_B to the overall excited state population and thus in decreasing estimates for α/β.

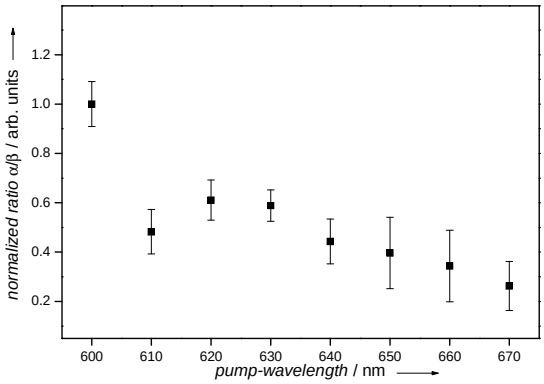

Figure 3. *Pump-wavelength dependency of the ratio of the decay amplitudes of the long- (τ_2) and short-component (τ_1) lifetimes α/β as a function of the pump-wavelength. The decay parameters are obtained from double exponential fits to the changes in the excited-state absorption at 500 nm*

Conclusions

The coherent technique of femtosecond-time-resolved four-wave-mixing was employed to provide further insight into the complex reaction dynamics in phycocyanobilin. Excitation wavelength dependent transient grating measurements of the excited-state kinetics clearly revealed the coexistence of three different ground-state species, PCB_A, PCB_B and PCB_C. When exciting the species PCB_A and PCB_B, two kinetic components with lifetimes of τ_1 ~ 2-3 ps for excited-state PCB_B and τ_2 ~ 18-

30 ps for excited-state PCB_A are identified. The relative contributions of these two components to the overall kinetic changes vary with the excitation wavelength. The 18-30 ps decay time of excited PCB_A, τ_2, matches the ground-state appearance time of the photoproducts PCB_B and PCB_C observed by Bischoff et al.[16] The decay-time τ_1, the excited-state lifetime of PCB_B and PCB_C, as well as τ_2 are significantly dependent on the excitation wavelength. They are remarkably shortened with decreasing pump wavelength. This effect is most likely due to an acceleration of the internal conversion process in case that the exciting photons deliver an excess vibrational energy to the molecular system, thus leading to an enhanced photoreaction rate $(\tau_2)^{-1}$.

These results are in accordance with the kinetic model suggested by Bischoff et al. for the excited-state processes of phycocyanobilin.[16] However, further insight is added due to the excitation wavelength dependent analysis of the excited-state dynamics.

Acknowledgment

One of the authors, B.D., gratefully acknowledges financial support from the *Fonds der Chemischen Industrie*.

REFERENCES

1. H. Falk, *The Chemistry of Linear Ologopyrroles and Bile Pigments,* Springer, Vienna, 1989.
2. M. Betz, *Biol. Chem*. **1997**, *378*, 167-176.
3. R. MacColl, *J. Struc. Biol.* **1998**, 311-334.
4. N.T. de Marsac, *Photosynth. Res.* **2003**, *76*, 197-205.
5. Ch. Romay, R. Gonzalez, N. Ledon, D. Remirez, *Curr. Prot. Pept. Res.* **2003**, *4*, 207-216.
6. M.C. Reddy, J. Subhashini, S.V.K. Mahipal, V.B. Bhat, P.S. Reddy, G.K. Kiranmai, K.M. Madyastha, P. Reddanna, *Biochem. Biophys. Res. Comm.* **2003**, *304*, 385-392.
7. H. Smith, *Nature*, **1999**, *400*, 710-713.
8. P.H. Quail, *Nature Reviews* **2002**, *3*, 85-93.
9. S.E. Braslavsky, D. Schneider, K. Heilhoff, S. Nonell, P.F. Aramendia, K. Schaffner, *J. Am. Chem. Soc.***1991**, *113*, 7322-7334.
10. R. Micura, K. Grubmayr, *Angew. Chem.* **1995**, *107,* 1896-1899.
11. B. Knipp, K. Kneipp, J. Matysek, W. Gärtner, P. Hildebrandt, S.E. Braslavsky, K. Schaffner, *Chem. Eur. J.* **1997**, *3,*363-367.
12. B. Knipp, M. Müller, N. Metzler-Nolte, T.S. Balaban, S.E. Braslavsky, K. Schaffner, *Helv. Chim. Acta* **1998**, *81,* 881-888.
13. Ch. Kneip, P. Hildebrandt, K. Nemeth, F. Mark, K. Schaffner, *Chem. Phys. Letters* **1999**, *311,* 479-484.
14. M. Stanek, K. Grubmayr, *Nonatsh. Chem.* **2000**, *131,* 879-888.
15. A.H. Göller, D. Strehlow, G. Hermann, *ChemPhysChem.* **2001**, 665-671.
16. M. Bischoff, G. Hermann, S. Rentsch, D. Strehlow, S. Winter, H. Chosrowjan, *J. Phys. Chem. B* **2000**, *104,* 1810-1816.

17. A. Materny, T. Chen, M. Schmitt, T. Siebert, A. Vierheilig, V. Engel, W. Kiefer, *Appl Phys B* **2000**, *71,* 299-317.
18. B. Dietzek, R. Maksimenka, G. Hermann, W. Kiefer, J. Popp, M. Schmitt, *ChemPhysChem* **2004** (in press).
19. T. Siebert, R. Maksimenka, A. Materny, V. Engel, W. Kiefer, M. Schmitt, *J. Raman Spectrosc.* **2002**, *33,* 844-855.
20. A.J. Wurzer, T. Wilhelm, J. Piel, E. Riedle, *Chem. Phys. Lett.* **1999**, *299,* 296-302.

STUDIA UNIVERSITATIS BABES-BOLYAI, PHYSICA, XLIX, 3, 2004

SOLUTION STRUCTURE AND BACKBONE DYNAMICS OF HUMAN CENTRIN 2, A PROTEIN IMPLIED IN NUCLEOTIDE EXCISION REPAIR

E. MATEI[*a], Y. BLOUQUIT[b], P. DUCHAMBON[b], C.T. CRAESCU[b], S. SIMON[c]

[a]Department of Physics, Florida Atlantic University, 777 Glades Rd. Boca Raton, Florida 33431, USA
[b]INSERM U350 & Institut Curie - Recherche, Centre Universitaire, Bâtiments 110-112, 91405 Orsay, France
[c]Babes-Bolyai University, Kogalniceanu 1, 3400 Cluj-Napoca, Romania

ABSTRACT. Global genom excision repair (NER) is carried out by *Xeroderma Pigmentasum* (XP) factors. *Human Centrine 2* (HCen2), a member of EF-hand superfamily of Ca^{2+}-binding proteins, interacts directly with XPC and in cooperation with HR23B stimulates XPC-NER activitry. However, Centrin 2 has been shown to play an important role in centrosome duplication. Therefore the XPC-HsCen2 interaction may reflects coupling of cell division and NER.

Nuclear magnetic resonance (NMR) measurements were used to characterize backbone dynamic behavior of longer C-terminal domain LC-HsCen2 by comparison with the complex formed by the C-terminal domain of HsCen2 with P1-XPC. The backbone dynamics of C-terminal fragments of HsCen2 was analyzed in relation with other well-characterized Ca^{2+}-binding proteins. Structural and Ca^{2+}-binding properties of two C-terminal fragments of this protein were investigated by NMR.

Introduction

Cellular Ca^{2+} signals are highly regulated, primarily by Ca^{2+}-binding proteins that belong to the EF-hand superfamily. Centrins are Ca^{2+} sensor proteins from the EF-hand superfamily involved in the cell cycle control [1, 2]. In upper eukaryotes they are partially associated with the centrosomes, as components of the centrioles and of the surrounding matrix. A significant fraction of HsCen2 is localized in the nucleus, where it was recently found associated with the xeroderma pigmentosum group C protein (XPC), a component of the nuclear excision repair pathway.

This study was focused on the characterization of solution structure and backbone dynamic behaviour of longer C-terminal domain LC-HsCen2 by comparison with the complex formed by the C-terminal domain of HsCen2 with P1-XPC using nuclear magnetic resonance. The backbone dynamics of C-terminal fragments of HsCen2 was analyzed in relation with other well-characterized Ca^{2+} -binding proteins.

Experimental

The samples for NMR spectroscopy (0.7–1.2 mM) were obtained by dissolving the lyophilized protein in deuterated Tris HCl buffer, pH 6.5 and 100 mM KCl (or NaCl). NMR spectra were recorded on a Varian Unity 500 NMR spectrometer, at 35°C. Standard homonuclear (COSY-DQF, TOCSY, NOESY) and heteronuclear (^{15}N-HSQC,

[*] *Corresponding author: ematei_1@yahoo.com*

^{15}N-NOESY-HSQC, T1, T2) spectra were used for resonance assignment and collection of distances and angle restraints, and calculation of relaxation parameters. Spectra analysis was done using Felix 230 software.

Results and discussion

Using NMR spectroscopy we investigated structural, dynamic and functional aspects of human centrin 2. The human centrin 2 (HsCen2) has only one of the four EF-hand motifs, localized in the C-terminal domain, with a relevant affinity for Ca^{2+} and discriminates against Mg^{2+} ions [3]. In order to avoid experimental difficulties related to the aggregation tendency of the integral protein, we concentrated our study on the isolated protein domains, we expressed and purified the full-length protein and two C-terminal fragments: SC-HsCen2 of 79 residues (T94-Y172, covering the two EF-hand sequence) and LC-HsCen2, possessing ten additional residues (the D-helix), on the N-terminal side.

Only the longer C-terminal domain, in the Ca^{2+}-saturated state and in the presence of Na^{+} ions, was amenable to structure determination by nuclear magnetic resonance [4]. The solution structure of LC-HsCen2 reveals an open two EF-hand structure with its D-helix segment (F86-T94) lying over the exposed hydrophobic groove (Fig. 1). This intramolecular interaction increases considerably the Ca^{2+} affinity and constitutes a useful model for the target binding.

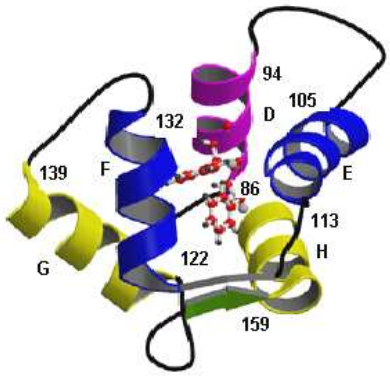

Fig.1. *Ribbon representation of the solution structure of Ca^{2+}-bound LC-HsCen2*

Recent studies have been proven the existence of two Hscen2- XPC binding sites: P1-XPC (high affinity) and P2-XPC with low affinity. The identified peptide, P1-XPC (N_{847}-R_{863}), interacts strongly (K_a= 2.2x10^8 M^{-1}) with HsCen2 as well as with its C-terminal [5].

Nuclear Magnetic Resonance relaxation measurements were used to characterize backbone dynamic behavior of longer C-terminal domain LC-HsCen2 by comparison with the complex formed by the C-terminal domain of HsCen2 with P1-XPC.

Uniform ^{15}N labeling of long C-terminal fragment (LC-HsCen2) and the complex formed by the short C-terminal with P1-XPC enabled us to perform highly sensitive heteronuclear (^{15}N-^{1}H) spectra. This opens the way towards a comprehensive relaxation analysis in terms of internal movements of the N-H groups of the polypeptide chain.

In the study of protein dynamics by ^{15}N relaxation measurements the Lipari–Szabo model free formalism are used in order to determine the motion parameters [6].

We measured ^{15}N relaxation rates and NOE effect of ^{15}N –labeled at a magnetic field of 11.74 T. Comparative analysis using a model-free procedure shows that in both fragments, EF-hand motifs behave like compact structural units with restrictive mobility, as reflected in the quite uniform order parameter. Motif IV, having a higher affinity for the metal ion, is more rigid. The linker fragment between EF –hand motifs is animated by larger amplitude of motion.

The measured relaxation parameters (R1, R2, and noe), are within the theoretically expected ranges for a molecule of this size in the absence of an important exchange contribution. The order parameter (S^2) reflects the amplitude of the fast internal motion of the H^N-N bond vectors in the picosecond to nanosecond time range. With a fixed value for the global correlation time (τc = 7.8 ns for LC-Hscen2 fragment and τc = 4.7 ns for SC-Hscen2+P1 complex) the dynamic parameters were estimated within the simple (S^2 and τe) Lipari-Szabo approach. The experimental data for 8 residues (115-122) within Ca^{2+} –binding loop of EF hand motif III could not be fitted to any model. This is in agreement with the low Ca-binding affinity of corresponding motif according to the solution structure information [3,4].

An increased flexibility is observed for the residues of the N terminal and C-terminal ends of the complex SC-Hscen2+P1(XPC). For instance, S^2 decreases progressively from 0.78 to 0.52 over the last residues of the C-terminal segment The S^2 values over the EF-hand motiv IV are quite homogeneous in both fragments, with an average of 0.85 nsec (Fig. 2), indicating that the backbone of this Ca^{2+}-binding motif behaves like a rigid unit, with highly restricted movements.

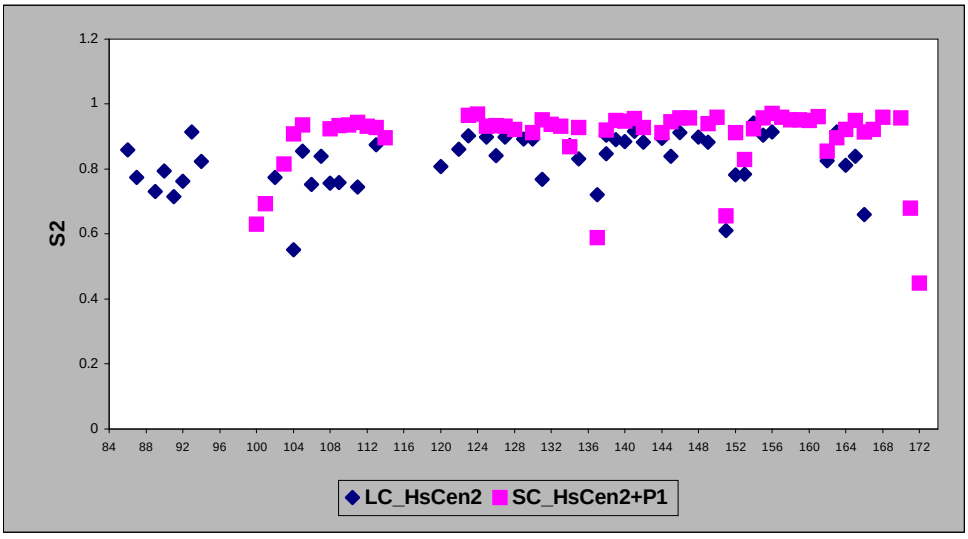

Fig 2. *Order parameters S^2 for the backbone H^N-H vectors of Ca^{2+} saturated of LC-HsCen2(blue) and Sc-Hscen2+P1(XPC) complex (magenta).*

Conclusions

Comparison of the S^2 profiles shows a relatively constant and high S^2 value (~0.8) of the N-terminal (D-helix) of the long fragment LC-Hscen2 and higher than N-terminal end of the complex SC-Hscen2+P1 (Fig.2). A limited flexibility is associated to D-helix region in LC-HsCen2 as a consequence of the interaction with hydrophobic core. Such interaction observed in solution structure study strongly confirmed the capacity of HsCen2 to recognize and bind its molecular target(s).

REFERENCES

1. Brinkley, B. R., Annu. Rev. Cell Biol. 1, 145-172, 1985.
2. Mazia, D., Int. Rev.. Cytol. 100, 49-92, 1987.
3. Durussel, Y. Blouquit, S. Middendorp, C.T. Craescu, J.A. Cox, FEBS Letters, 208-212, (2000).
4. Elena Matei, S. Miron, Yves Blouquit, Patricia Duchambon, Isabelle Durussel, Jos A. Cox, Constantin T. Craescu, Biochemistry, 42, 1439 – 1450, 2003.
5. Popescu A., Miron. S., Blouquit Y., Duchambon P., Christova P., Craescu C., *J.Biol. Chem*, 278(41), 40252-40261, (2003).
6. Clore, G.M., Szabo, A., Bax, A., Kay, L.E., Driscoll, P.C., and Gronenborn, A.M, *J. Amer. Chem. Soc.* ***112:*** 4989–4991, (1990).

STUDIA UNIVERSITATIS BABES-BOLYAI, PHYSICA, XLIX, 3, 2004

SPECTROSCOPIC APPROACH OF THE CATION SELECTIVE MOLECULE DESFERRIOXAMINE B AND ITS Fe(III) COMPLEX

O. COZAR[1*], N. LEOPOLD[1], M. TOMOAIA-COTIŞEL[2], A. MOCANU[2], C. JELIC[1], L. DAVID[1], V. CHIŞ[1], R. GRECU[3]

[1]Babeş-Bolyai University, Faculty of Physics, Kogălniceanu 1, RO-400084 Cluj-Napoca, Romania, cozar@phys.ubbcluj.ro
[2]Babeş-Bolyai University, Faculty of Chemistry, Arany Janos 11, RO-400028, Cluj-Napoca, Romania
[3]Raluca Râpan Institute of Chemistry, Fântânele 30, Cluj-Napoca, Romania

ABSTRACT. IR spectroscopy was used for the structural investigation of the chelator desferrioxamine B and its Fe(III) complex, ferrioxamine B. Comparing the FT-IR absorptions of desferrioxamine B and ferrioxamine B, the structural changes due to the Fe(III) chelation were clearly evidenced by the spectra. Despite the intense C=O stretching vibration (1629 cm^{-1}) from the spectrum of desferrioxamine B, in two bands at 1577 cm^{-1} and 1636 cm^{-1} in the IR spectrum of ferrioxamine B (DFO:Fe) suggests the appearance of a resonative process in the O=C-N bond by chelating the Fe(III). The new bands at 1577 cm^{-1} and 1043 cm^{-1} from DFO:Fe spectrum are due to the C=N and C-O bonds, respectively. This fact contributes to the homogenization of the electronic charge of oxygen environment around ferric ion in the octahedral Fe chelate.

Introduction

Iron is an essential element for the growth of almost all forms of life. Iron in its most common form, Fe(III) hydroxide, is not a readily available nutrient since its solubility is limited, typical concentrations at neutral pH are about 10^{-18} M. The low environmental concentration of soluble Fe(III) has forced the microorganisms and higher plants to synthesize and secrete siderophores, that can chelate Fe(III) and carry it into the cell via specific high-affinity uptake receptors [1] The mechanism for Fe acquisition by siderophores such as desferrioxamine B, (Fig. 1), relies on the selectivity of these ligands for Fe(III) to form very stable complexes. In order to improve the understanding of the mechanism by which siderophore-mediated iron transport occurs, the interaction of desferrioxamine B with iron was studied in detail[2-10].

Desferrioxamine B is a hydroxamate-based siderophore currently used for removal of iron from the body in treatment of patients suffering from β-thalassemia or acute iron poisoning. Iron chelators are also used as Fe fertilizers. To overcome the problems due to the easily leached beyond the depth of the root zone, the binding of chelates to solid phase was proposed. A recent study has investigated the desferrioxamine B and ferrioxamine B molecules, when sorbed on activated Sepharose gels[3].

According to the crystal structure of ferrioxamine B[2] the chelate molecule consists of two closed loops and an open chain containing a protonated amine (Fig. 1a). The six hydroxamate oxygen atoms coordinated to the Fe(III) center form a distorted octahedral geometry around the metal center (Fig. 1b).

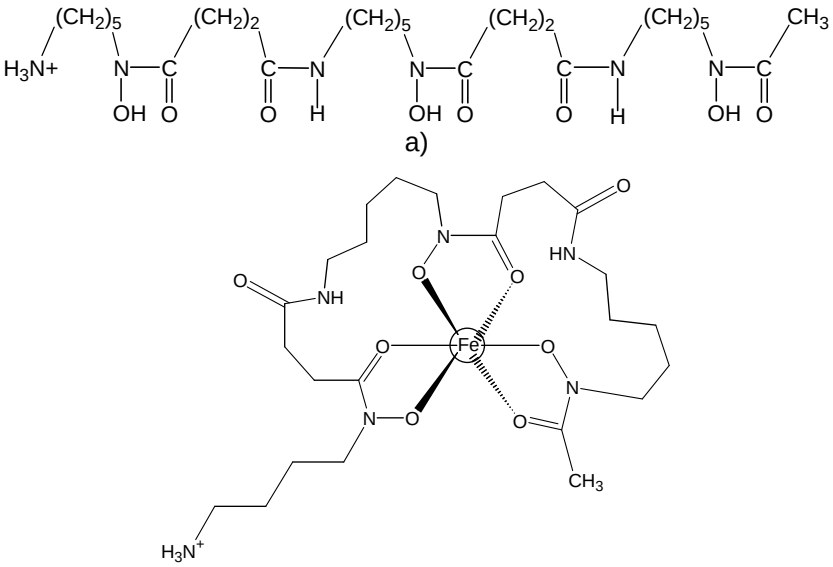

Fig. 1. *A schematic drawing of (a) desferrioxamine B and (b) ferrioxamine B.*

A recent review about calixarene-type macrocycles used for different metal cation recognition selectivity is given by Ludwig and Dzung [11].

The FT-IR spectra of desferrioxamine B and ferrioxamine B were obtained for a wavenumber range of 400-3500 cm^{-1} with a Bruker Equinox 55 spectrometer with a resolution of 2 cm^{-1}. Samples for analysis were prepared by mixing and pounding 300 mg potassium bromide with 0.8 mg of the tested material and then compressing the mixture into pellets. To obtain the FT-IR spectra 32 scans were collected.

All the employed chemicals were reagent grade or better. Desferrioxamine B methanesulphonate (Desferal) was purchased from Ciba Geigy, Basel, Switzerland.

Results and Discussion

The FT-IR absorption spectrum of desferrioxamine B and the FT-IR spectra of desferrioxamine B Fe(III) complexes, prepared at the stoichiometric ratios 1:1, 1:3, 1:4 are shown in Fig. 2.

The FT-IR spectrum of desferrioxamine B is dominated by the strong amide I band of the C=O stretching vibrations, observed at 1629 cm^{-1} due to the internal hydrogen bonding, that reduced the frequency of the carbonyl stretching. The absorption at 1569 cm^{-1} is an amide II band, due to the supposition of the N-H bending of the secondary amides and C-N stretching vibrations of the secondary amides and of the hydroxamate groups. The N-O stretching vibration of the hydroxamate groups is present as a medium peak at 1051 cm^{-1}. In the high wavenumber region, the N-H stretching vibrations at 3105 and 3312 cm^{-1} are overlapped by the broad O-H stretching band of the hydroxyl groups.

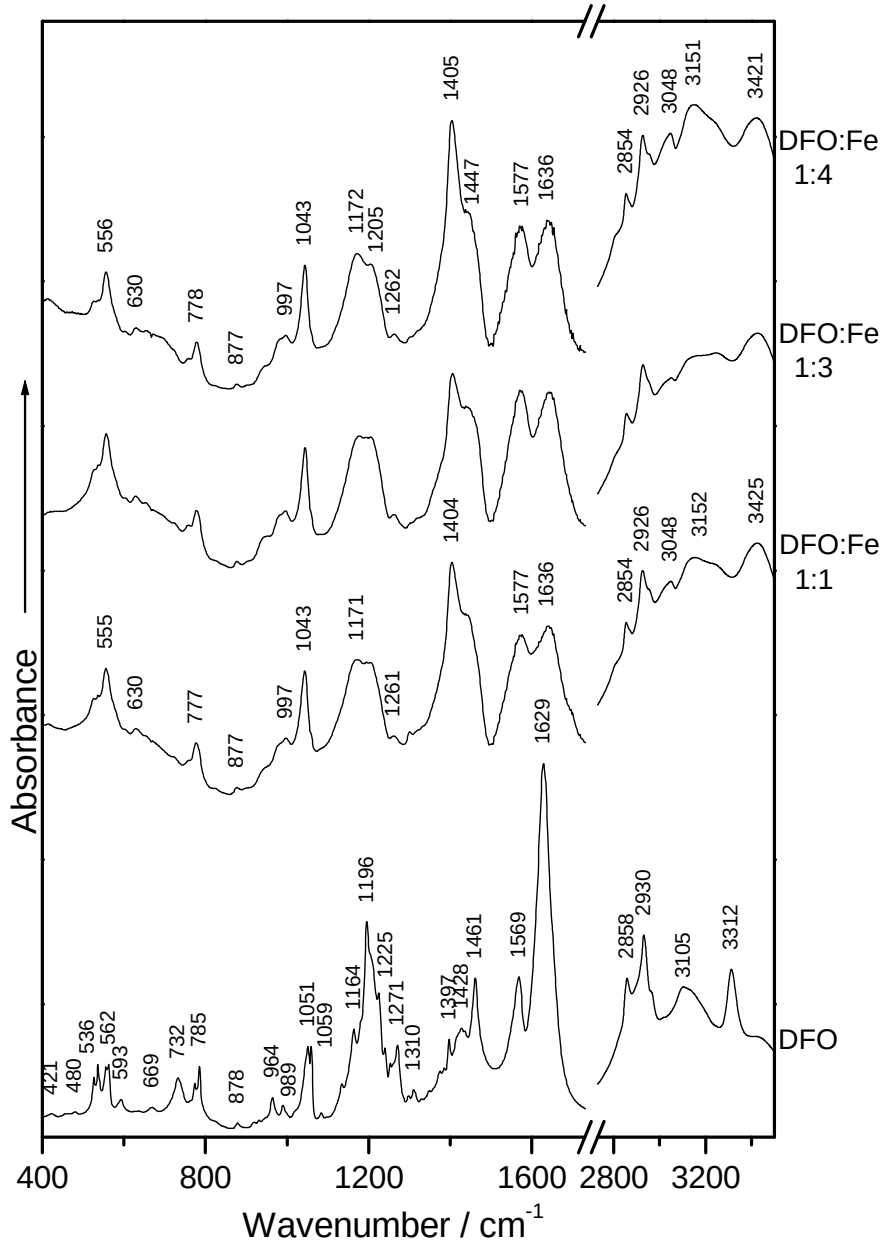

Fig. 2. *FT-IR spectra of desferrioxamine B (DFO) and ferrioxamine B (DFO:Fe) with the stochiometric ratios as indicated.*

The C-H bending vibrations of the ethane and pentane chains of the desferrioxamine B molecule display a broad band formed by the peaks at 1461, 1428 and 1397 cm^{-1}, whereas the C-C skeletal stretching vibrations are present in the range of 1133-1271 cm^{-1}. In the high wavenumber region, the symmetrical and the asymmetrical C-H stretching vibrations are shown by the peaks at 2858 cm^{-1} and 2930 cm^{-1}, respectively.

Desferrioxamine B is available as methanesulphonate salt. The symmetrical and asymmetrical SO_3 stretching vibrations are usually strong IR active and are therefore present in the spectrum at 1058 and 1164 cm^{-1}, respectively.

Comparing the ferrioxamine B FT-IR spectra from Fig. 2, the spectral shapes of these spectra present similar features, consequently, independently of the used Fe(III) ratios, desferrioxamine B chelates Fe(III) to a complex with a unique structure. The medium-strong band at 555 cm^{-1} in the FT-IR spectra of ferrioxamine B is attributed to the Fe-O stretching vibration. The amide I band of ferrioxamine B appears broadened and blue shifted at 1636 cm^{-1}, due to the overlapping of the C=O stretching vibrations of the secondary amides and the C=O stretching vibrations of the hydroxamate groups whose O atoms are involved in the Fe(III) bonding. Also, the intensity of the amide I band is significantly reduced due to a resonative O=C-N bond that arise after the Fe(III) chelation, as indicated by the X-ray diffraction.[2] The X-ray diffraction of crystallized ferrioxamine indicates an increase in the C-N double bond character on complexation to Fe(III), as shown by the resonance structure II in Scheme 1.

Consequently, new bands of C=N and C-O appear at wavenumbers of 1577 and at 1043 cm^{-1}, respectively.

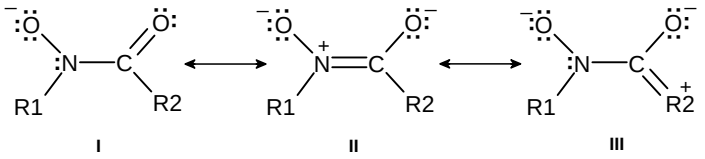

Scheme 1. *Major resonance structures for a hydroxamate anion*

An increase in C-N double bond character and the localization of a greater negative charge at the carbonyl oxygen results in a relatively strong Fe(III) complex [2]. The dissociation of the hydroxyl groups resulting from the coordinative bond to Fe(III) influences the N-H stretching vibrations at 3152 and 3425 cm^{-1}, being blue shifted. Bonding Fe(III), induces also modifications in the shape of the C-H deformation bands, the band at 1404 cm^{-1} with a shoulder at 1447 cm^{-1} appearing broadened, whereas the C-C skeletal stretching vibrations of the alkanes are shown by the intense bands, blue shifted at 1171 and 1205 cm^{-1}.

A tentative assignment of the bands of the FT-IR spectra of desferrioxamine B and ferrioxamine B is presented in Table 1.

DFOB coordinates with Fe(III) through its three hydroxamates groups forming an octahedral Fe chelate. The high stability of this complex is attributed to the high coordinative energy of hydroxamic acid for Fe(III) and also to the number and spacing of the coordinative groups [3,12].

Table 1.

Assignment of the main IR absorption bands of desferrioxamine B (DFO) and ferrioxamine B (DFO:Fe)

DFO	DFO:Fe	Assignment
	555s	ν(Fe-O)
785m	777m	rock(CH_2)
1051m		ν(C-C), ν(N-O)
	1043s	ν(C-O)*
1058m		$\nu_{sym}(SO_3)$
1133m		$\nu_{asym}(SO_3)$
1164m	1171s	ν(C-C)
1196s	1205s	ν(C-C)
1225s		ν(C-C)
1271m		ν(C-C)
1397m	1404vs	δ(C-H)
1428m	1447s	δ(C-H)
1461s		δ(C-H)
1569s		δ(NH)+ν(C-N) (amide II)
	1577s	ν(C=N)*+δ(NH)+ν(C-N)
1629vs	1636s	ν(C=O) (amide I)
2858m	2854m	$\nu_{sym}(CH_2)$
2930s	2926s	$\nu_{asym}(CH_2)$
	3048m	$\nu_{asym}(CH_3)$
3105m	3152m	$\nu(NH_3^+)$+ν(O-H)
3312s	3425m	ν(N-H)+ν(O-H)

Abbreviations: ν-stretching, δ-deformation, sym-symmetrical, asym-asymmetrical s-strong, vs- very strong, m-medium, *-resonative O=C-N bond.

Conclusions

The structural changes induced by the complex formation of desferrioxamine B with Fe(III) were evidenced by the FT-IR spectra, the Fe-O stretching absorption being observed at 555 cm^{-1}. Changing the ratio of Fe(III) in the desferrioxamine B Fe(III) complexes preparation, the FT-IR spectra displayed the same shapes, consequently desferrioxamine B chelates Fe(III) to a unique structure.

By chelating the Fe(III) ion, a resonative process in the O=C-N bond of DFOB molecule was evidenced. Thus the new bonds of C=N and C-O appear in the IR spectra at 1577 cm^{-1} and 1043 cm^{-1}, respectively. This fact leads to the homogenization of the electronic charge of oxygen environment around ferric ion in octahedral Fe chelate.

REFERENCES

1. G. Winkelmann, Handbook of microbial iron chelates, CRC Press, Boca Raton, 1991.
2. S. Dhunganga, P.S. White, A.L. Crumbliss, J. Biol. Inorg. Chem., 6, 810 (2001).
3. Z. Yehuda, Y. Hadar, Y. Chen, J. Agric. Food Chem., 51, 5996 (2003).
4. B. Borgias, A. D. Hugi, K.N. Raymond, Inorg Chem., 28, 3538 (1989).
5. J. Leong, K.N. Raymond, J. Am. Chem. Soc., 97, 293 (1975).
6. K.N. Raymond, G. Müller, B.F. Matzanke, in Topics in current chemistry, F.L. Boschke (Ed.), Vol. 123, Springer, Berlin, Heidelberg, New York, 1984, p 49-102.
7. F. Bickel, R. Bosshart, E. Gäumer, P. Reusser, E. Vischer, W. Voser, A. Wettstein, H. Zähner, Helv. Chim. Acta, 43, 2118 (1960).
8. W. Keller-Schierlein, V. Prelog, Helv. Chim. Acta, 45, 590 (1962).
9. W. Keller-Schierlein, P. Mertens, V. Prelog, A. Wasler, Helv. Chim. Acta, 48, 710 (1965).
10. V. Prelog, A. Walser, Helv. Chim. Acta, 45, 1732 (1962).
11. R. Ludwig, N.T.K. Dzung, Sensors, 2, 397 (2002).
12. A. Winston, D. Kirchner, Macromolecules, 11, 597 (1978).

STUDIA UNIVERSITATIS BABES-BOLYAI, PHYSICA, XLIX, 3, 2004

CARBON NANOFIBRES-SUPPORTS FOR ADSORPTION OF BIOLOGICALLY ACTIVE SUBSTANCES

LILIANA OLENIC, GH. MIHĂILESCU, D. LUPU, AL. BIRIŞ, P. MĂRGINEANU

National Institute of R&D for Isotopic and Molecular Technologies
PO Box 700, Cluj-Napoca, ROMANIA

ABSTRACT. Our paper is concerned with preliminary studies on carbon nanofibres (CNF) obtained by chemical vapour deposition (CVD) method, used for adsorption of some amino acids (alanine, aspartic acid, glutamic acid) and enzyme (glucose oxidase GOD). The effects of surface properties on amino acids and enzyme adsorption process were investigated. Surface properties of CNF have been characterized by the pH values, the concentration of acid/ base values and hydrophobic values. Adsorption isotherms of amino acids and enzyme were presented. The immobilized GOD on CNF was investigated as a biosensor for glucose.

INTRODUCTION

The first place among the adsorbents used in practice belongs to the different kinds of specially prepared carbons. These can have exceptionally high porosity and, hence, a huge surface area. Adsorption has a wide variety of applications. It is well known that carbon supports may be used in biotechnology and pharmaceutical industry for immobilized enzymes and bacterial cells, which exhibit desired enzymatic activity.

Enzyme immobilization is central to bioreactor and biosensor technologies. Looking for new materials with high sensitivity and efficiency for the immobilization and detection of enzyme is of great importance in different biochemical application.

Since their discovery in 1991, carbon nanotubes (nanofibres, single-wall nanotubes and multi-wall nanotubes) have been attractive and practical new materials.

In this paper we described the investigation of the adsorption properties of carbon nanofibres with respect to adsorbates of biological origin (amino acids: alanine, aspartic acid glutamic acid and enzyme: glucose oxidase).

EXPERIMENTAL

Carbon nanofibres (CNF) were prepared by CVD method on Fe:Ni:Cu catalyst (85:10:5). The CNF were purified in 37% HCl.

A. The **pH** of CNF[1] was measured according to the “Datronix” ionometer. About 0.1 g of dry CNF was added to 10 ml of distilled water and the suspension was shaken overnight to reach equilibrium. The sample was filtered and the pH of the solution was measured.

Hydrophilic and hydrophobic properties of CNF were characterized by the concentration of acid and basic sites of different strength on the surface of the support respectively by naphthalene adsorption from aqueous solution.

Acid and base values were determined by Boehms titration method [2]. In the case of acid values, about 0.01 g of the sample was added to the beakers containing 10 ml of 0.02N NaOH solution. The beakers were sealed and shaken for 24h with purging N_2 gas, then the excess of base was titrated with 0.02N HCl. The acid value was calculated from the amount of HCl that reacted with NaOH.

The base value was determined by converse titration.

Hydrophobicity of the support was expressed in nmol of adsorbed naphthalene/m^2 of accesible surface area [3]. 1 m^2 of CNF were desairated under vacuum and were contacted with 2 ml of 0.1 mM naphthalene at 18^0C under static conditions for 2h.

The concentration of naphthalene was determined by UV spectroscopy at λ= 225 nm.

B. Adsorption of amino acids was performed from 10^{-5}-10^{-3} M solutions (in distilled water) with izoelectric pH. The amino acids were adsorbed at ambient temperature and stirred for 24 h.

The ratio between the adsorbent weight (in g) and the solution volume (in ml) was equal to 1:10 (0.01g support/1ml amino acid solution). The amino acids concentration was determined by ninhydrin method and measured spectrophotometrically at λ= 575 nm.

The amount of adsorbed amino acids was calculated from the difference of its concentration in solution before and after adsorption and expressed in mg/g of support.

C. The glucose oxydase (GOD) (Fluka) **concentration** was determined by Bradford method (using Coomassie Blue G-250 as reagent) [4]. The adsorption of enzyme was performed under conditions similar to those used for amino acids but the pH of the enzyme solution was pH= 7.

The amount of adsorbed enzyme was calculated from the difference of its concentration in solution before and after adsorption and expressed in mg/g of support.

The enzyme activity of immobilized GOD was determined by amperometric method. The enzyme immobilized on CNF was used as an amperometric sensor. The enzymatic reaction was:

$$\text{Glucose} + \text{GOD}(FAD^+) \rightarrow \text{Gluconolactone} + \text{GOD}(FADH_2)$$
$$FADH_2 + O_2 \rightarrow FAD^+ + H_2O_2$$
$$H_2O_2 \rightarrow 2\,H^+ + O_2 + 2e^-$$

Carbon nanofibres materials show very good electrodic properties [5] and they can be used as support for enzymes immobilization.

EXPERIMENTAL RESULTS

A.

Table 1.

pH, hydrophilic and hydrophobic properties of CNF respectively active carbon (CA) sample.

Sample	BET surface m^2/g	pH	Acid values meq/g	Basic values meq/g	Naphtha-lene adsorption nmoli/m^2
CNF	170	6,20	0,15	0,6	51,17
CA	1400	6,52	0,04	0,28	27,8

B.

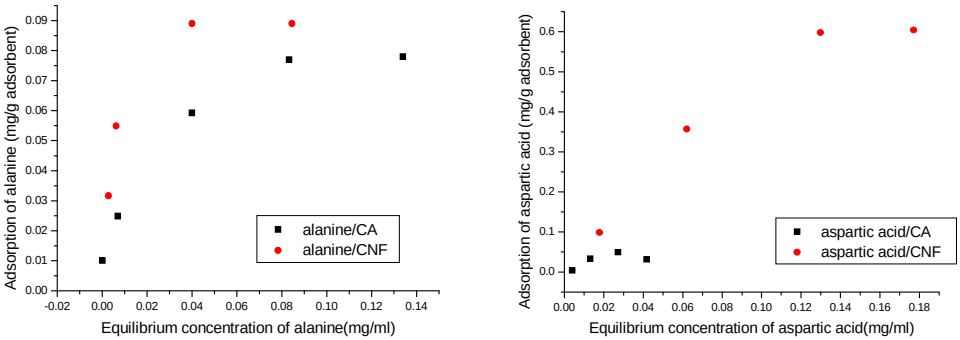

Figure 1. *The adsorption isotherms of alanine and aspartic acid on CNF and CA*

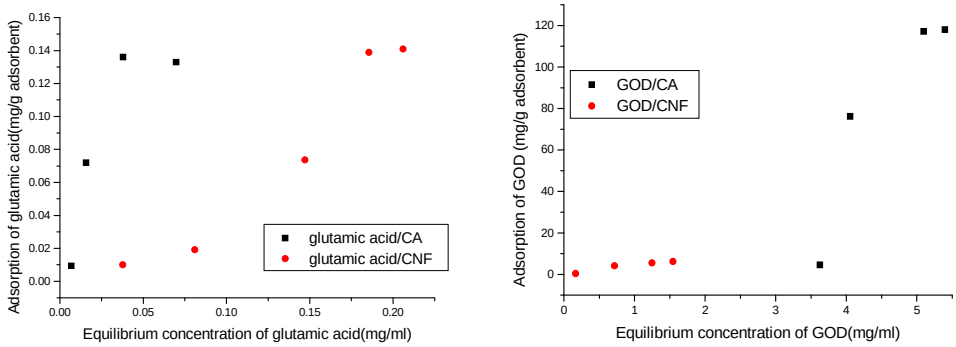

Figure 2. *The adsorption isotherms of glutamic acid and GOD on CNF and CA*

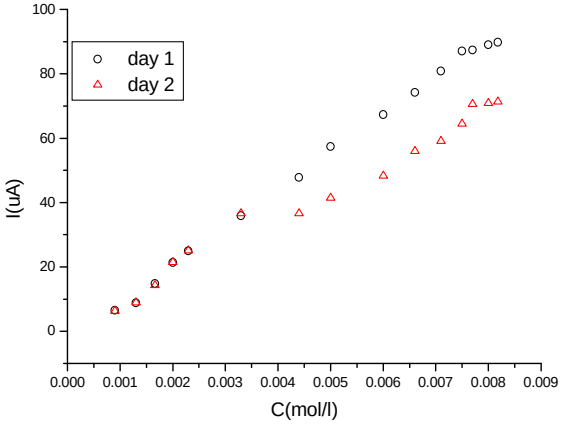

Figure 3. *The calibration curves of carbon nanofibres-glucose biosensor*

CONCLUSIONS

The surface of the samples (CNF and CA) was week acidic due to its origin, preparation and method of activation. The results obtained from acid/base titration were in general agreement with pH values.

The surface acidity/basicity of CNF is fourth/twice times greater than that of CA. The concentration of acid sites on the CNF and CA is in several times lower than that of basic sites. CNF is more hydrophobic than CA. The adsorption of amino acids on CNF increase: alanine > glutamic acid > aspartic acid, due to the molecular weight and the acid-base groups of amino acid molecule.

The adsorption of GOD on CNF and CA are similar. The interaction between enzyme and support was complex; differences in adsorption can not be explained only in the chemical properties of the surface (steric arrangements and the surface aria accessible interfere). The filamentous morphology of CNF is responsible for the greater stability of immobilized enzyme than the enzyme used in solution. The future research will verify the GOD activity for a long time. Carbon nanofibres materials show very good electrodic properties and they can be used as supports for enzymes immobilization.

REFERENCES

1. H.H.P. Bhowmik, B. Zhao, M.A. Hamon, M.E. Itkis, R.C. Haddon, Chem. Phys. Lett. 345 (2001) 25-28.
2. S.-J. Park, W.Y. Jung, Carbon Science 2 (2001), no.1, 15-21.
3. G.A. Kovalenko, E.V. Kuznetsova, Yu.I. Mogilnykh, I.S. Andreeva, D.G. Kuvshinov, N.A. Rudina, Carbon 39 (2001) 1033-1043.
4. xxx-Practical Guide, University of Pretoria, Department of Biochemistry, 2003.
5. C.G. Hu, W.L. Wang, S.X. Wang, W. Xhu, Y. Li, Diamond and Related Materials 12 (2003) 1295-1299.

STUDIA UNIVERSITATIS BABES-BOLYAI, PHYSICA, XLIX, 3, 2004

INCLUSION COMPLEX OF ATENOLOL WITH β-CYCLODEXTRIN

FELICIA DRAGAN[1], I. BRATU[2*], MIHAELA TOMA[3+], A. HERNANZ[4], M. BOJITA[5] and S. SIMON[3]

[1] *University of Oradea, Faculty of Pharmacy, 1 Armatei Romane st., Oradea, Romania*
[2] *National R&D Institute of Isotopic and Molecular Technologies, P.O. Box 700, R-400296 Cluj-Napoca 5, Romania*
[3] *"Babes-Bolyai" University, Faculty of Physics, 1 Kogalniceanu st., Cluj-Napoca, Romania*
[4] *UNED Madrid, Depto de CC y TT Físico Quimicas, Senda del Rey 9, 28040 Madrid, Spain*
[5] *"Iuliu Hatieganu" University of Medicine and Pharmacy, Cluj-Napoca*
[*] *Corresponding author, e-mail:ibratu@s3.itim-cj.ro*
[+] *Socrates/Erasmus student at UNED Madrid*

ABSTRACT. Inclusion complexes of atenolol with β-cyclodextrin (β-CD) in aqueous solution have been investigated by ^{1}H NMR an UV-vis spectroscopy. A 1:1 stoichiometry for this inclusion complex has been established. Their stability constants were determined by UV-vis spectroscopy. Molecular modeling (by using Hyperchem MM+ molecular dynamics) is in good agreement with the ^{1}H NMR data indicating the protons implied in the inclusion process and consequently a supramolecular architecture of this complex was proposed.

Introduction

Atenolol (ATE, $C_{14}H_{22}N_2O_3$, see Fig. 1) molecule is one of the most frequently drugs used in the treatment of cardiovascular diseases, being employed for their antihypertensic and antiarrhytmic properties[1].

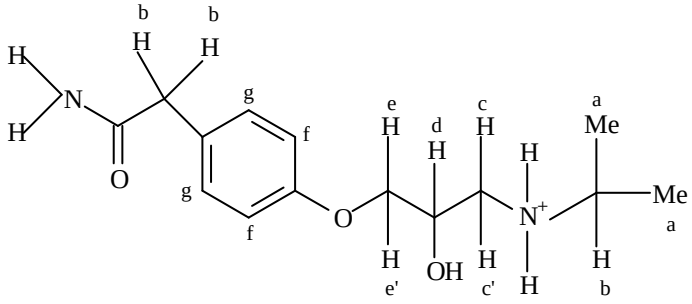

Fig. 1: *Atenolol molecule*

Cyclodextrins (CDs), see Fig. 2, are cyclic oligosaccharides formed by units of α-D-(+)-glucopyranose (six, seven, or eight) called α-, β- or γ-CD, respectively. They have the ability to encapsulate entirely, or at least partially, into their hydrophobic cavity, a wide variety of guest molecules forming inclusion complexes[2] .

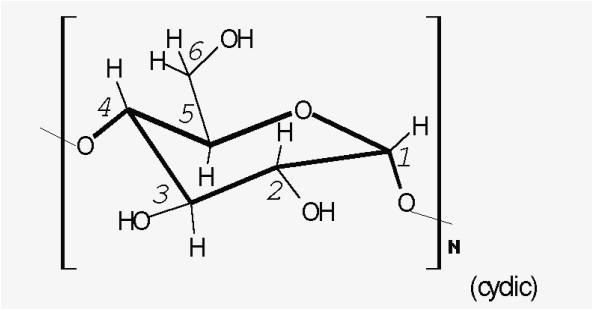

Fig. 2. *Cyclodextrin molecules*

The formation of host/guest complexes has been used in industry to increase bioavailability, taste, and stability of drugs in aqueous solution. They have also been used as enzyme models. A variety of techniques are available to observe host/guest interactions depending on the applications envisaged for the complex. However, most of these techniques are unable to discriminate between internal (inclusion) and external complexation[3] .

The mechanism of enantioselective binding of chiral ATE by β-CD derivatives (PhCD) has been studied by NMR and molecular modelling. ^{1}H NMR spectra of (R, S)-ATE enantiomers have been published[4] .

The investigation of β-CD inclusion complexes of cyclodextrins with atenolol (racemic) has been done by using NMR, XRD, differential scanning calorimetry (DSC), scanning electron microscopy (SEM) techniques[1]. The chemical shifts for the protons of ATE and of β-CD in the free and in complex states with the peak assignment for free ATE and β-CD was presented[1]. The IC is consisting on equimolar mixture of the two diastereometric complexes. UV-spectrophotometry was used also to study this IC; based on this method the association constant from the phase solubility diagrams was obtained[5] .

The molecular encapsulation of ATE in β-CD has offered promise for the development of new dosage forms and its increase the solubility and dissolution rate of ATE. The IC was prepared by co-precipitation method. The Higuchi-Connors method was used for the calculation of the stability constant K = 28,66 M^{-1} from the phase solubility studies[6]. One observes that the dissolution rate of the IC increases as compared to the ATE one.

The aim of this paper is to determine the stoichiometry of the ATE with β-CD inclusion complexes, their stability constants and the geometry of these supramolecular architectures.

Experimental

Inclusion complexes of β-CD (used as host, *H*) with ATE as guest (*G*) molecules was prepared in aqueous solutions starting from mother solutions of milimolar concentration of *G* and *H* in D_2O. β-CD (having ≤15% in water weight) was purchased from Merck (Germany) and was used without further purification. The aqueous solutions were prepared considering the molecular water present in β-CD. ATE (obtained from "*Helcor*" Baia Mare, Romania) is quite water-soluble drug.

Two starting solutions of $5 \cdot 10^{-3}$ mol dm^{-3} in D_2O (ROMAG Turnu Severin, Romania) of β-CD and ATE, respectively, were prepared. On going from these mother solutions several mixtures of constant volume and having different molar ratios of G and β-CD were prepared. The sum of the total concentration $M = ([\beta\text{-CD}]_t + [G]_t)$ (where the lower index is referred to the total concentration) was kept constant, being equal to $5 \cdot 10^{-3}$ mol dm^{-3}. The molar ratio of G, $r_G = [G]_t / ([\beta\text{-CD}]_t + [G]_t)$ was varied from 0 to 1 at 0.1 intervals.

^{1}H-NMR spectra were recorded for all these solutions with a *Bruker Avance 400* spectrometer after 15 minutes of equilibration. The spectrometer is operating at 400.13 MHz, with the following parameters: 16384 data points, pulses of 90º, 2 seconds delay between scans (32 scans) and a digital resolution of 0.588 Hz/point.

For solution studies the following procedure was applied: an aqueous solution of ATE of 2.10^{-4} mol/L concentrations was prepared. This solution was mixed with solutions of increasing β-CD concentrations. These solutions have the following concentration values: 0.01; 0.015; 0.020; 0.03; 0.04; 0.06; 0.08 mol/L. They were stored at room temperature for 12 hours. After that, they were measured by an UV-vis spectrophotometer by using standard quartz cells.

The stoichiometry of the inclusion complexes

The stoichiometry of the complex was obtained by using the well-known continuous variation method, *i.e.* the Job's method[7]. Let us assume that a complex C, having the [1 : *n*] guest:host stoichiometry, is formed:

$$G + n\beta\text{-CD} \leftrightarrows C \qquad (1)$$

The symbol δ_f will represent the chemical shift of a proton of a given species *X* (*X* = G, β-CD) when they are found to be free in solution; δ' the observed chemical shift when the observed species is found in the presence of the other; δ_C the chemical shift of a proton in the IC, the last one can not be measured experimentally but can be calculated. The following differences are also defined:

$$\Delta\delta_{obs} = \delta_f - \delta' \qquad (2)$$

$$\Delta\delta_C = \delta' - \delta_C \qquad (3)$$

If there is a rapid exchange between the free and bound states for the X species, each proton will give a unique, averaged signal. In this case, the product of $\Delta\delta_{obs}$ by the total concentration of the analyzed substance, $[X]_t$, *i.e*, $\Delta\delta_{obs}[X]_t$, will be proportional to [C].

By plotting $\Delta\delta_{obs}[X]_t$ *vs*. r_G one obtains a curve, its maximum indicating the value of r_G at which the maximum concentration of the complex is achieved. This value is related with *n* by[8,9]:

$$r_G^{max} = 1 / (1+n) \quad (4)$$

which allows the determination of the stoichiometry of the obtained inclusion complexes.

The association (stability) constant

Various methods for the determination of the association constant have been described in the literature. These are based on techniques such as[10-13]: conductometric titration, potentiometric and spectroscopic methods, solubility studies, etc.

The association constant K_C can be evaluated from the observed variation in the chemical shift difference for some drug or cyclodextrin protons. The problem is that NMR evaluation of this constant depends[14] on the proton taken into consideration. The constant being unique for the whole inclusion process, we prefer the use of UV-vis spectroscopy to determine the stability constant.

Association constant determination by UV-vis spectropohotometry

In order to determine the stability (association) constant, the differences between the absorbances corresponding to free ATE, and complexed with β-CD, respectively, were calculated. The change in absorbance between free ATE and the complexed one with β-CD was measured at 294 *nm* for ATE. The stability constant K_C for ATE-β-CD was calculated in agreement with the Scott equation[15] :

$$\frac{[MT]\cdot[CD]}{d} = \frac{1}{K_C \cdot \varepsilon} + \frac{[CD]}{\varepsilon} \quad (5)$$

where *d* is the change in absorbance between free MT (ATE) and the complexed with β-CD and ε represents the difference in the corresponding molar absorptivities.

Geometry optimisation

In order to optimize the geometry in vacuum, molecular mechanics computation have been done with the HyperChem software[16]; the details of the algorithms are given elsewhere[17]. The well-known MM+ was used with the Polak-Ribière conjugate gradient method until a RMS gradient lower than 0.015 kcal mol^{-1} $Å^{-1}$ was obtained.

Results and Discussion

Stoichiometry determined by ^{1}H NMR spectroscopy

Fig. 3 presents the ^{1}H NMR spectra of several aqueous solutions of ATE with β-CD at different molar fractions.

One can observe the protons that are influenced by the complexation process. The interaction degree between different protons of the β-CD and ATE may be estimated by plotting the chemical shifts of the β-CD and G *vs*. r_G. The application of the Job's method for the obtained complexes is presented in the Figs. 4 and 5:

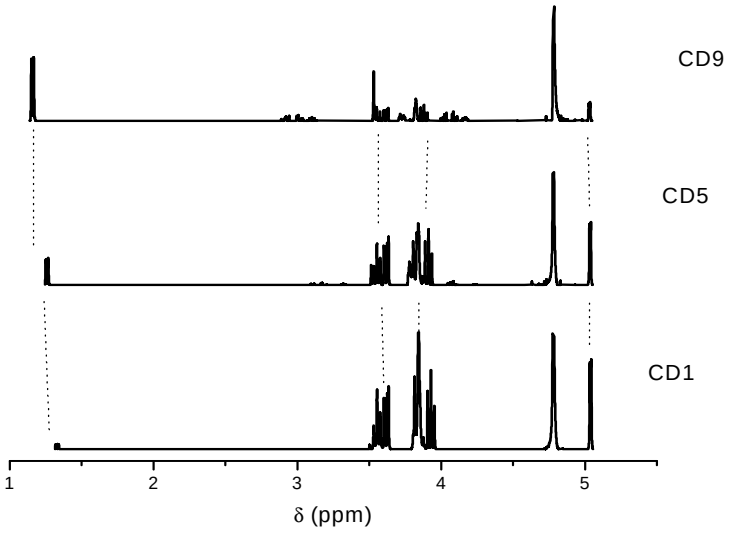

Fig. 3. *^{1}H NMR spectra for different molar ratios of β-CD and ATE. Legend: r = 0.1 for CD1; r = 0.5 for CD5 and r = 0.9 for CD9*

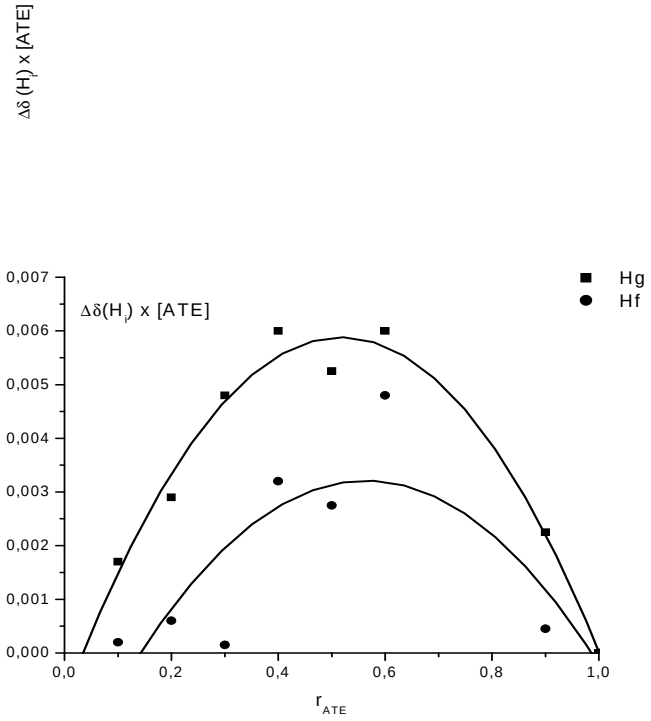

Fig. 4. *Job's plots for ATE (vs. the ATE molar fraction) (■: Hg; ●: Hf). Origin B-spline curves were fitted to the observed points[18].*

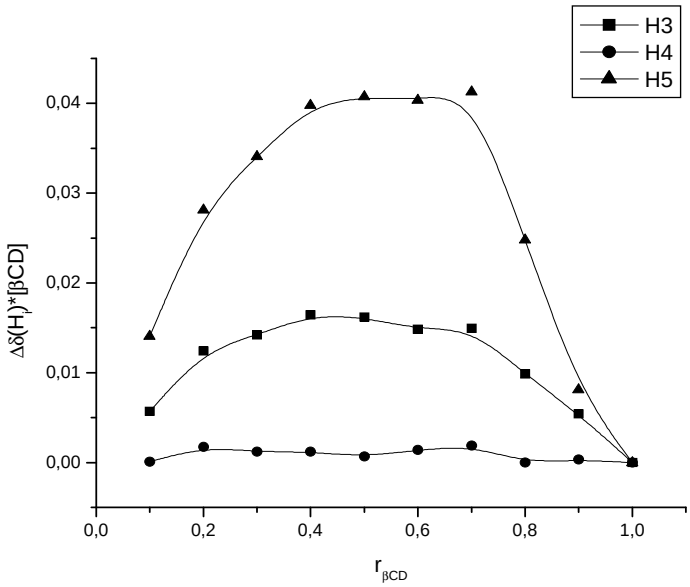

Fig. 5. *Job's plots for β-CD (vs. the molar fraction of ATE): ▲: H3; ■: H4; ●: H5.*

Origin B-spline curves were fitted to the observed points[18].

The inspection of the Figs. 4 and 5 reveals that ATE forms an inclusion complex with *β*-CD with a [1:1] stoichiometry.

The equilibrium constant for the 1:1 complex of *β*-CD+ATE is varying significantly depending on the proton taken into account, as was reported in other papers dedicated to the determination of the equilibrium constant by NMR method[14].

The ATE methylene protons suffer a small shift, suggesting that they remain outside *β*-CD cavity. The protons whose chemical shift are changed notably are Hg and Hf. Consequently, we consider that ATE molecule enters inside CD *β*-CD ring from the larger side in such a way that the Hg and Hf protons remain in the central position and the methylene groups remain outside (the hydrogen atoms are suppressed in order to simplify the drawings).

The stability constant obtained by UV-vis spectrophometric method

By plotting $\frac{[MT]\cdot[CD]}{d} = f\left(\frac{[CD]}{\varepsilon}\right)$ it is possible to determine the stability constant from the intercept of the linear plot with the Oy axis, see Fig. 6.

From the values at the intercept, by taking into account the Eq. (8) K_C value for ATE-*β*-CD as being 110 L/mol was obtained.

By analysing the chemical shifts of the cyclodextrin protons, both for ATE/*β*-CD, one see significant shifts for H3 and H5 protons situated inside CD torus. As concerning the ATE protons, significant shifts are observed for Ha, Hc, Hc', He and Hf protons *i.e.* the ether part of the ATE and the benzene ring enter inside CD torus.

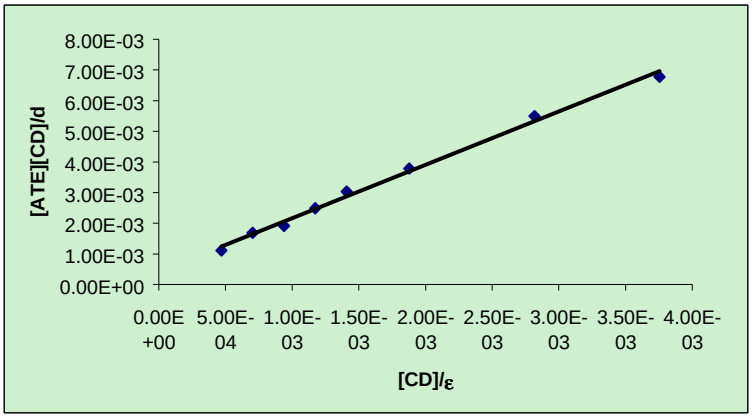

Fig. 6. *The stability constant determination for the ATE-β-CD complex.*

Molecular mechanics

In order to find a theoretical support for the previous hypotheses, molecular mechanics calculations have been done. The CDs act as complexing agents with different molecules, which enter inside CD torus, and interact with the OH groups of CD by Van der Waals, electrostatic forces and hydrogen bonding[19]. The models have been built starting by locating the ATE molecule at the larger side of the β-CD cavity. The results of the geometry optimisation in vacuum through MM+ molecular mechanics of a β-CD molecule and ATE molecule is presented in the Fig. 7.

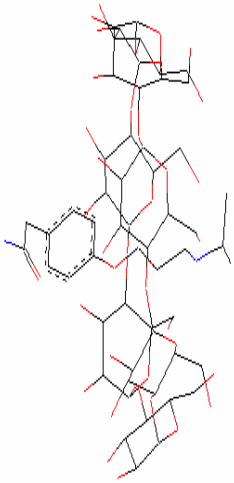

Fig. 7. *The structure of the ATE-β-CD complex obtained with the Hyperchem software.*

Conclusions

The chemical shifts observed in ^{1}H-NMR spectra of different IC mixtures demonstrate the appearance of an inclusion complex having a [1:1] stoichiometry in the case of G / β-CD, G being ATE molecules.

The stability constants, obtained from the spectrophotometric measurements is 110 M^{-1} for ATE/β-CD system. In the case of ATE/β-CD complex the stability constant obtained by us using the Scott method is somewhat higher than that[6] obtained by phase solubility test.

Molecular mechanics calculations using MM+ approximations showed that the ATE molecule enters inside β-CD cavity with the phenyl rings, its methylene groups remaining outside the cavity. The results of the molecular mechanics calculations must be taken with precaution, because there are a lot of local minima in the potential energy surface of the investigated molecules. One must take also into account the fact that the simulated system is not real, the calculations were done for the system in vacuum by neglecting the influence of the water molecules. But the obtained results are in good agreement with our hypotheses. Supplementary efforts are necessary to establish the nature[19] of the forces implied in the inclusion process. The expulsion processes of the intracavity water molecules must be taken into account[20].

To summarize, it has been shown that NMR and UV-vis spectroscopy can be used to derive satisfactory both the stoichiometry and the association constant of inclusion complexes. Based on these experimental data, molecular models of the ATE / β-CD inclusion complex in solution was proposed.

Acknowledgments

Thanks are due to Dr. L. Copolovici from the Faculty of Chemistry, "Babes-Bolyai" University for his assistance in the determination of the association constant from the optical spectra.

REFERENCES

1. R.Ficarra, P.Ficarra, M.R. Di Bella, D.Raneri, S.Tommasini, M.L.Calabrò, M.C.Gamberini, C.Rustichelli, *J. Pharm. Biomed. Anal*. 23 (2000) 33-40.
2. J. Szjejtli, *Chem. Rev*. 98 (1998) 1743-1753.
3. G.Moloney, D.J.Craik, M.N.Irkouder, T.L.Nero, *J.C.S. Perkin Trans* 2 (1998) 199-206.
4. Y.Kuroda, Y.Suzuki, J.He, T.Kawabata, A.Shibukawa, H.Wada, H.Fujima, Y.Go-oh, E.Mai, T.Nakagawa, *J. Chem. Soc. Perkin* 2 (1995) 1749-1759.
5. R.Ficarra, P.Ficarra, M R.Di Bella, B.R., S.Tommasini, M.L.Calabro, A.Villari, S.Coppolino, *J. Pharm. Biomed. Anal.* 23(2000) 231-236.
6. K.L.Park, K.H.Kim, S-H.Jung, H.M.Lim, Ch.H.Hong, J.S.Kang, *J. Pharm. Biomed. Anal.* 27(2002) 569-576.
7. P. Job, *Ann. Chem.* 9, 113-203, (1928).
8. M. Bogdan, S.I. Farcas, M. Bojita, Studia Univ. Babes-Bolyai, Ser. Phys. Special issue, 115-120, (2000).
9. I.Bratu, J.M. Gavira-Vallejo, A. Hernanz, M. Bogdan, Gh. Bora, *Biopolymers-Biospectroscopy* 73 (2004) 451-456.
10. W. Saenger, *Angew. Chem. Int. Ed. Engl.* 92, 343-361, (1980).
11. S. Li, W.C. Purdy, *Chem. Rev.* 92, 1457-1470, (1992).

12. O. Pastor, E. Junquera, A. Aicart, *Langmuir*, 14, 2950-2957, (1998).
13. Ch. D. Tran, S.H De Paoli Lacerda, *Anal. Chem.* 74, 5337-5341, (2002).
14. Mariluz. Zubiaur, C. Jaime, *J. Org. Chem.* 65(24), 8139-8145, (2000).
15. R. L. Scott, *Rec. Trav. Chim.*, 1956, 75, 787-789.
16. HyperChem™ Release 4, Hypercube, Inc. (1994), Waterloo, Ontario N2l 3X2, Canada.
17. "Computational Chemistry", Hypercube, Inc. Waterloo, Ontario N2l 3X2, Canada (1994).
18. Origin® 7.0, OriginLab Corporation, Northhampton, MA 01060, USA..
19. Lei Liu, Qing-Xiang Guo, *Journal of Inclusion Phenom. and Macrocyclic Chem.* 42, 1-14, (2002).
20. J.M. Gavira, A. Hernanz, I. Bratu, *Vibr. Spectrosc*. vol. 32, Issue 2, (2003) pp. 137-146.

STUDIA UNIVERSITATIS BABES-BOLYAI, PHYSICA, XLIX, 3, 2004

MICROWAVE CALORIMETRY STUDIES FOR PLANT EXTRACTION APPLICATION

I. BROŞ[1*], M. MOLDOVAN[2], S. COBZAC[2], E. SURDUCAN[1], V. SURDUCAN[1] and T. HODIŞAN[2]

[1]National R&D Institute of Isotopic and Molecular Technologies, P.O. Box 700, R-400296 Cluj-Napoca 5, Romania
[2]'Babes-Bolyai' University, Faculty of Chemistry and Chemical Engineering, 11 Arany Janos, 400028, Cluj-Napoca, Romania
[*]Corresponding author, e-mail:ildiko@s3.itim-cj.ro

ABSTRACT. A method of extraction based upon the selective and localized heating of residual moisture in target (usually plant) materials is microwaves. This localized heating is very rapid and results in an explosive disruption of the physical structure of the source material, leading to a direct migration of the desired components into the surrounding solvent. The solvents are chosen so as to be transparent to microwaves, meaning that only the source material is heated.

A calorimetric study of the 'microwave effect' – a modification in kinetics of transition temperatures in inorganic and organic systems under the influence of microwave radiation – is being developed. We observed that plant material, solvent polarity and treatment conditions influence the microwave power absorption.

Introduction

The extracts of natural products have been used as food and medicine since the beginning of civilization. The biological activity of the whole plant extract is usually related to the constituents that have been identified.

Today, many products are extracted from their original structure, being undoubtedly the most important step in the preparation of plant material for the analysis of bioactive compounds. In the traditional extraction process, a heated solvent slowly diffuses through the material, dissolving and carrying away target compounds. The choice of solvent is often limited by its diffusivity properties.

Extraction using microwave technology is a good alternative to conventional extraction techniques. The extraction by microwave as a new extraction technique has its own specific parameters that need to be characterized for every plant, or plant-solvent system.

Principles of the microwave extraction process

The base principles of microwave treatments are (one) the direct energy transfer of the microwave energy on the probe to be treated and (second) the selectivity of microwave absorption by the dielectric loss of the probe. These two characteristics imply a time rate of treatments between 2 to 1000 comparatively with classical processes. Other attractive characteristic of microwave treatments is the possibility of microwave power control by a local PC or microcontroller.

The microwave plant-extraction is based on the selectivity of the microwave absorption in materials. The key of this selectivity is the permittivity loss (or the loss tangent) of the materials irradiated by microwaves. The interaction microwaves-matter is characterized by the relative dielectric permittivity:

$$(1) \qquad \varepsilon = \varepsilon' - j\,\varepsilon'' \qquad j = (-1)^{1/2} \qquad tg(\delta) = \varepsilon''/\varepsilon'$$

where:

- ε' is the relative permittivity of the material and represents the amount of microwave energy cumulated in the material by dipoles orientations (or dipole structures orientations);
- ε'' is the permittivity loss and represents the microwave energy lost in different conductive processes or by the dipoles vibrations;
- $tg(\delta)$ is the loss tangent;

The expression of the microwave power absorbed in the unity volume of the material is:

$$(2) \qquad P_a = \omega\varepsilon_o\,\varepsilon'\,tg\delta\,E_i^2 \quad \text{or} \quad P_a = 2\pi f\,\varepsilon_o\,\varepsilon''\,E_i^2 \quad \text{in } (W/m^3)$$

where: $\varepsilon_o = 8.856\ 10^{-12}$ F/m; E_i - internal electric field (in the material), proportional with the incident microwave power Po; f - microwave frequency; ω - microwave pulsation ($2\pi F$).

If we assume that all the absorbed microwave power is transformed in heat, the raising rate of the material temperature is:

$$(3) \qquad (\Delta T/\delta t) = (\omega\varepsilon_o\,\varepsilon'\,tg\delta\,E_o^2)/\rho c$$

where ΔT is the temperature rise in the δt time, ρ is the density of the material, in Kg/m^3, and c is the specific heat of the material, in J/Kg^oC.

If a mixture of different materials (plant and solvent for example) were irradiated with microwave power, the microwave absorption and the local rise of temperature would be selective for the different values of the permittivity of the constituents. This is an important fact in the microwave extraction process. Usually, the natural probe, from which we intend to extract one component, is immersed in a nonpolar solvent (microwave loss-less). By microwave irradiation, the temperature rising rate of the natural probe is bigger then that of the solvent (usually by one or two magnitude orders, because of the water content) and the natural tissues (vegetal or animal) are broken up. The different temperatures between the probe and the solvent determine a local convection, which favorises the transport of the component (esther, volatile oil, organic oil, etc.), in the solvent [1,5,6].

This process allows for direct extraction of fresh material without the need to dry them prior to the extraction, as commonly being the prerequisite in most other methods. Microwave treatment conditions are important criteria and the microwave generator have to be designed in such a way that the most important process parameters can be adjusted and controlled throughout the process.

For determination of the plant extraction optimal conditions in microwaves power treatment it is necessary to determine experimental the power absorption value for a particular extraction system because the microwave power have a specific distribution inside the extraction cell as a function of probe nature, solvent, extraction cell shape and microwave incident power value.

Experimental measurements

Experimental configuration used for microwave extraction was developed on the base of three Romanian patents [7,8,9].

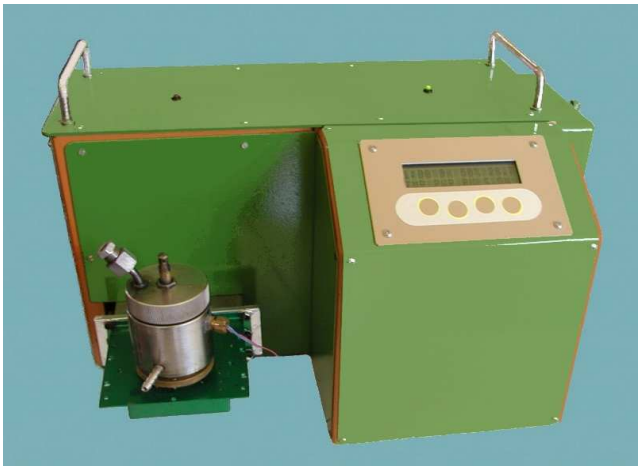

Fig. 1. *Microwave power system*

This microwave power system operates at a fixed frequency (2.45GHz) and power (500-900W). The microwave input in material is controlled in every second from 0% to 100% of time.

Extraction solvents: for extraction it was used 25 ml of: methanol, water and different methanol-water mixtures.

*Plant material: i*t was used flowers of *Tagetes patula* collected in July 2004. The powdered dried materials were Soxhlet extracted whit $CHCl_3$ to eliminate the lipophylic compounds.

In order to evaluated the energy absorbed by the sample, the following classical calorimetric relationship was used (if we assume that all the absorbed microwave power is transformed in heat, Pa = Wa) :

$$(4) \qquad Wa = (m\ c\ \Delta T)/\ t_{ef}$$

where:
- W_a = the power absorbed by the sample [W]
- m = mass of sample [Kg]
- c = mass specific heat [J/Kg ^{0}C]
- ΔT = the difference of the final and initial temperatures.
- t_{ef} = the applied microwave field effective time, defined as: $t_{ef} = t\ \boldsymbol{\delta}$
- t = working time [s]
- $\boldsymbol{\delta}$ = duty cycle [%]

For determination of optimal extraction condition measurements was performed for the same system in different operated condition, for different value of incident power, duty cycle and the time. During the measurements the extraction cell was cooled to maintain the solvent temperature at a value less as the boiling temperature.

To determinate the optimal extraction conditions of bioactive compounds from *Tagetes patula* – plant, the power absorbed W_a was represented versus the duty cycle and the treatment total time for methanol-water (50:50 v/v) system (in figure 2).

Conclusions, results and discussion

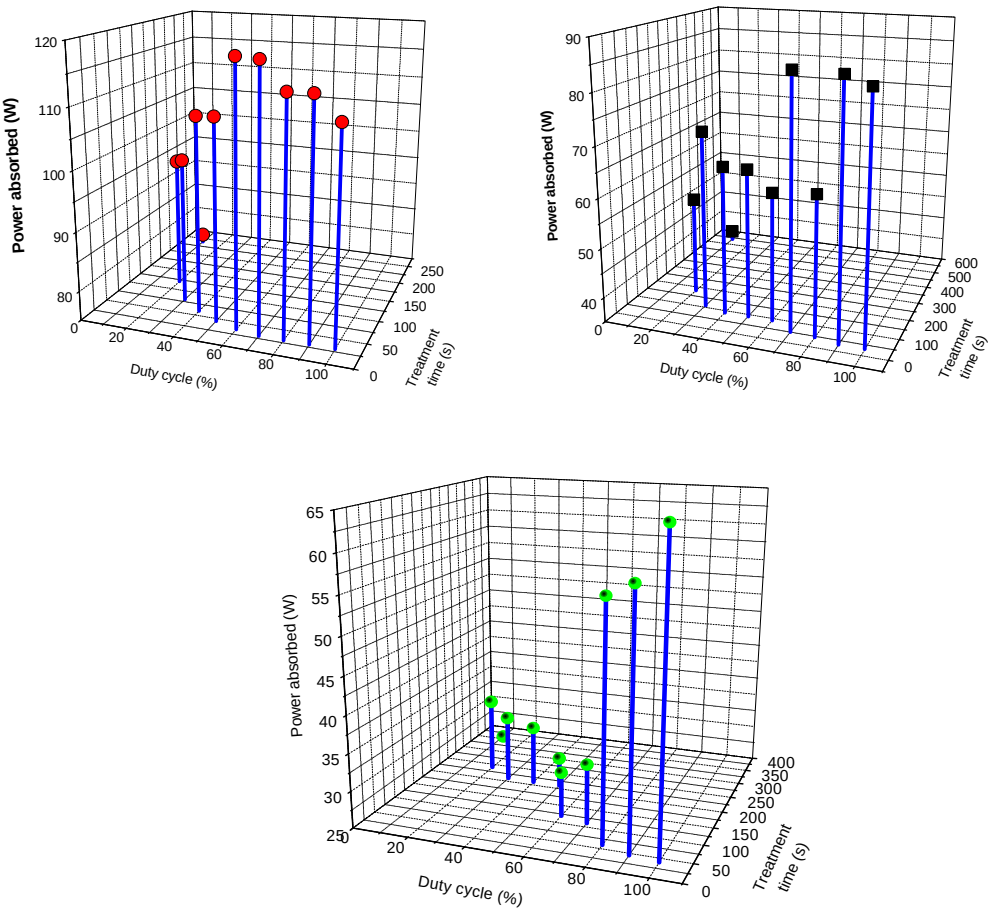

Fig. 2 *Experimental condition and the power absorbed at an incident power:* 900 W; 700 W; 600 W.

From the all experimental condition investigated, an incident power of 700W is the best choice, mainly considering the power absorbed/extraction time yield. At this incident power were done measurements for methanol, water, methanol-water mixtures and solvent-plant system at a duty cycle of 60% for the total treatment time of 90s. The power absorbed is presented in figure 3.

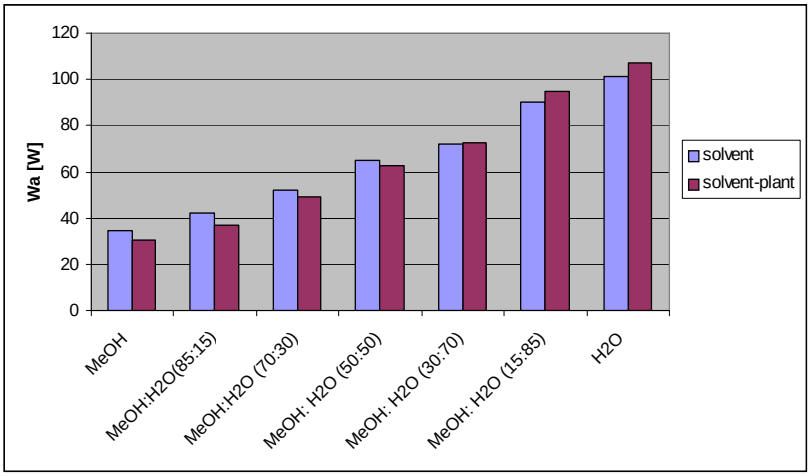

Fig.3. *The power absorbed in solvent and solvent-plat system at 700W, duty cycle 60% and 90s*

It was observed that the presence of the plant has a influence to the power absorption in the solvent-plant system, so the power absorbed by the sample is influenced by the microwave treatment conditions (incident power Po, duty cycle and treatment time), solvent polarity and in the plant presence. All these "conditions" define the microwave extraction technologies. For the best extraction, the extraction time should be not very brief (it not allow a good extraction of bioactive compounds) and not very long (the interaction prolonged of microwave with the bioactive compounds may carry at this degradation); a propre time value in rapport to the incident microwave power can be only experimental determined. In our case an incident power of 700W offer the best power absorbed / extraction time yield for this microwave power system (fig.1).

REFERENCES

1. Pare, J.R.. *Microwave-Assisted Extraction From Materials Containing Organic*
2. *Matter*, U.S.A Patent 05458897 / 1995
3. Ganzler, K.; Salgo, A.; Valko, K. *Microwave Extraction – a Novel Sample*
4. *Preparation Method for Chromatography*, J. Chromatography, 1986, 71, 299.
5. K. Li, J. M. R. Bélanger, M. P. Llompart, R. D. Turpin, R. Singhvi, and J. R. J.
6. Paré. *Evaluation of rapid solid sample extraction using the microwave-*
7. *assisted process (MAPTM)under....* Spectros. Int. J. (1997), 13, 1.
8. Popa, B., *Handbook for the Thermotechnical Engineer*; Technical Publ. House; Bucharest, 1986
9. D. Barclay, Today's Chemist at Work, 9(3), 40 (2000)

10. E.Surducan, V.Surducan, S.V.Filip, C.Neamtu, *"Temperature influence on microwave absorption for polar liquids"*Balkan Phys. Lett. 5, 235 (1997)
11. E. Surducan, V. Surducan, G. Nagy, S.V. Filip, *Installation for Treatment in Microwave Fiel*d, Romanian Patent, RO 00116514 / 2001
12. E.Surducan, V.Surducan, *The process and device for heating fluids without dielectric losses,* Romanian Patent RO116515/ 2001
13. E.Surducan, V.Surducan, *The thermographic transducer for high power microwave radiation,* Romanian Patent RO116506/ 2001.

STUDIA UNIVERSITATIS BABES-BOLYAI, PHYSICA, XLIX, 3, 2004

ATOMIC FORCE MICROSCOPY STUDIES OF LANGMUIR-BLODGETT FILMS. THE EFFECT OF SOME DRUGS ON DIPALMITOYLPHOSPHATIDYLCHOLINE

MARIA TOMOAIA-COTIŞEL[1], GHEORGHE TOMOAIA[2], VASILICA-DANIELA POP[1], AURORA MOCANU[1], ONUC COZAR[3], NECULAI APETROAEI[4] and GHEORGHE POPA[4]

[1]"Babeş-Bolyai" University of Cluj-Napoca, Faculty of Chemistry and Chemical Engineering, Physical Chemistry Department, 400028 Cluj-Napoca, Romania
[2]"Iuliu Hatieganu University of Medicine, Orthopedic Surgery, 400015 Cluj-Napoca
[3]"Babeş-Bolyai" University of Cluj-Napoca, Faculty of Physics, 400084 Cluj-Napoca,
[4]"A. I. Cuza" University, Plasma Physics Department, 700506 Iasi, Romania

ABSTRACT. We have used atomic force microscope (AFM) and Langmuir-Blodgett (LB) self-assembly technique as tools for studying the effect of two drugs, such as procaine (P) and deferoxamine (DFO), at a drug concentration of 10^{-3} and 10^{-6} mole dm^{-3} in the aqueous phase, respectively, on dipalmitoylphosphatidylcholine (DPPC) films spread as Langmuir monolayers at the air/water interface. These techniques allowed the investigation of morphology and surface properties of DPPC films in the presence of these drugs. The experimental data were compared with those of pure DPPC monolayers and indicate a highly increased stability of mixed DPPC and P and of DPPC and DFO films. Consequently, the drug effect reveals specific molecular interactions between these biologically relevant biocompounds in substantial agreement with their molecular structure and with their nano-structures evidenced by AFM on LB films. These data demonstrate that both procaine and deferoxamine can penetrate and specifically interact with membrane lipids stabilizing the biological membranes at both internal and external membrane interfaces.

1. Introduction

Langmuir-Blodgett (LB) technique and atomic force microscope (AFM) are useful research tools [1-8] to construct membrane models [4] and to explore molecular interactions among different molecules in oriented supramolecular structures [2]. On the other hand, the LB films are widely used to probe various experimental techniques, such as electron scanning microscopy [9,10], reflection-absorption IR spectroscopy [11], surface plasmon resonance [12] and fluorescent microscopy [1, 13, 14]. These LB assemblies could find potential applications in advanced spectroscopy, chemical technology, biosensor industry, microelectronic devices and targeted drug delivery systems.

It has been shown that phospholipid monolayers spread at the air/water interface [15, 16], known as Langmuir monolayers, and transferred on solid substrate [1-3, 5] by LB technique are increasingly used as models for biological membranes. The biological significance of such model systems is suggested by the fact that a phospholipid monolayer on water [15] or on a solid substrate [1, 3, 5, 8] resembles half of the lamellar bilayer membrane [3, 17, 18]. Experimentally, it was shown that electron diffraction patterns obtained from supported phospholipid monolayers appear similar to those of bilayers [19].

Among phospholipids, dipalmitoylphosphatidylcholine (DPPC) is considered a model compound which self-assembles as a Langmuir monolayer at the air/water interface [13, 14, 20-23] and forms stable LB films [3, 5]. The behavior of DPPC in Langmuir monolayers, in the absence and the presence of procaine, was earlier published by us from compression isotherms [20-22] and from epifluorescent microscopy [14]. The results indicate that procaine can both penetrate and interact with membrane lipids and proteins and it concentrates at both internal and external membrane interfaces.

In this work, we study the LB films of DPPC containing various drugs, like procaine (P) and deferoxamine (DFO), which are believed to act directly on the membrane proteins or through a perturbation of the surrounding lipid matrix. We focus on their micro- and nano-structure to further discuss their phase behavior and better understand the drug effect on lipid membrane models by using LB technique and atomic force microscopy (AFM). Both drugs are frequently used to treat various diseases and it is of interest to understand how the drug distributes throughout the lipid membrane.

2. Experimental Procedures

2.1 Reagents and Materials

Dipalmitoylphosphatidylcholine (DPPC) and the two drugs, e.g. procaine hydrochloride (P) and deferoxamine methanesulfonate (DFO), were purchased from Sigma. The n-hexane was purchased from Merck, and other chemicals were purchased from Reactivul Bucharest. All chemicals were used without further purification. Our investigations have been performed at pH 5.6, where both procaine [24] and deferoxamine [25] are positively charged and DPPC forms a stable Langmuir monolayer at the air/aqueous solutions interface. The ultrapure water with a resistivity of 18 Mohm cm used in all experiments was purified with an Elga system. The hydrophilic glass substrates with both sides optically polished having smooth surfaces were used for the LB film fabrication. Glass substrates, with a typical size of 25 x 25 mm^2 and 0.1 mm thick, were cleaned with chromic mixture according to a usual procedure adapted in our laboratory [26]. After cleaning the substrates were rinsed thoroughly with distilled water and after with ultrapure water and finally dried before they were used.

2.2 Langmuir and Langmuir-Blodgett (LB)Techniques

The Langmuir monolayers of DPPC in the absence and in the presence of drugs at the air/water interface are studied by experimental methods described by us in detail elsewhere [20-23, 27-29].

A Langmuir monolayer is generally obtained by spreading a known number of DPPC amphiphilic molecules on the air/aqueous solution interface in a Langmuir trough of a precise known area. Teflon barriers are placed across the teflon trough and serve to vary the area of the Langmuir monolayer in compression; in consequence, the mean molecular area (A, in $Å^2$) of DPPC is precisely determined, and simultaneously, the surface pressure is measured by using a surface tension sensor with Wilhelmy plate method [6, 20-23, 30].

The surface pressure (π, expressed in mN/m) is calculated as the difference between the surface tension of the pure aqueous subphase (σ_0, given in mN/m) against air phase and the surface tension (σ, in mN/m) of the air/water interface with Langmuir monolayer. Our automatic Langmuir equipment is the KSV model 5000, manufactured by KSV, Finland. For LB film deposition, the Langmuir equipment needs additional capabilities of dipping a hydrophilic glass, through the Langmuir monolayer at the air/water interface, at a controlled speed while the Langmuir monolayer is held at a constant chosen surface pressure, which is easily identified on compression isotherms (π versus A curves).

DPPC was dissolved in n-hexane at a concentration of 1 mg/ml and spread on aqueous solutions at 20 ^{o}C in a teflon trough. After waiting time for 5 to 10 minutes to allow the solvent to be fully evaporated, the monolayer was manually compressed at a speed of 10 cm^2/min. LB films were prepared as we previously reported [7, 8, 11] and DPPC monolayers were compressed at a chosen lateral surface pressure. After an equilibration period of about 10 to 15 min, the vertical transfer of the monolayer was performed by LB technique at a low transfer speed of 0.2 cm/min.

2.3 Atomic Force Microscopy (AFM) Tapping Mode

Investigation of surface morphology and domain structure of LB samples of DPPC in the presence of drugs was conducted in tapping mode on a research AFM system with a 90 x 90 (x-y) μm scanner described elsewhere [31]. The calibration of AFM scanner was checked by imaging freshly cleaved highly oriented pyrolytic graphite (HOPG) and mica sample. Non-contact conical shaped tips of silicon nitride coated with aluminum were used for AFM tapping mode. The tip was on a cantilever with a resonant frequency in the range of 200 - 300 kHz and with a spring constant of 17.5 N/m. We used low scan rates of 1 Hz and high scan rates in the range of 20-30 Hz to detect noise artifacts. The scan angle was also changed in different directions to observe real images from those corresponding to noise.

The AFM images were obtained from at least three macroscopically separated areas on each LB sample. All images were processed using the standard procedures for AFM. Dimensions of the domains were measured directly from AFM topographic images and the thickness variations were estimated from cross section profiles [7, 8]. All AFM experiments were carried out under ambient laboratory conditions (about 20 ^{o}C) as previously reported [7, 8, 31].

3. Results and Discussion

3.1 Surface Characterization of Langmuir DPPC Monolayers

The compression isotherm of pure DPPC monolayer, spread at the air/ water interface, is given in Fig.1, curve 1. At about 8 mN/m, the DPPC monolayer exhibits a two-dimensional phase transition [20], from expanded liquid (EL) to condensed liquid (CL), shown on the compression isotherm (Fig. 1, curve 1) by a sharp break in the isotherm slope. At this main transition, two phases EL and CL coexist in the DPPC monolayer.

The linear portion of high lateral surface pressures corresponds to the CL state, followed by an intermediary liquid [6] corresponding to intermediate surface pressures (between 8 and 20 mN/m) and by an EL state under 8 mN/m. In the presence of deferoxamine (10^{-6} mole dm^{-3}; curve 2, Fig. 1) or procaine (10^{-3} mole dm^{-3}; curve 3, Fig. 1) in the aqueous subphase the compression isotherms are moved to larger molecular areas of DPPC showing the drug expanding effect on DPPC monolayers.

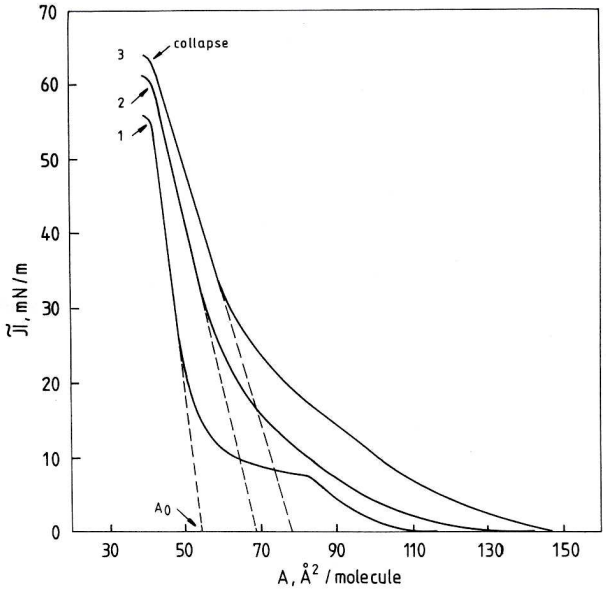

Fig. 1. *Compression isotherms at the air/ water interface for pure DPPC monolayer (curve 1) and for DPPC monolayer in the presence of DFO (10^{-6} mole/dm^3, curve 2) in the aqueous phase, or of P (10^{-3} mole/dm^3, curve 3), at 20 ^oC. Dashed lines indicate the limiting areas for DPPC molecule (A_0) in CL state. Arrows at high surface pressures indicate the incipient collapse state of monolayers.*

From compression isotherms, the surface properties of DPPC monolayers were determined and they are given in Table 1. For instance, the A_0 is the limiting molecular area for the CL state of DPPC monolayers in the absence or in the presence of drugs. These A_0 values are obtained by extrapolation at π equals zero of the linear portion of the isotherms recorded at high lateral pressures (Fig. 1). By comparing the A_0 values (Table 1) it is evidenced the drug expansion effect on the CL state of DPPC monolayers.

The incipient collapse pressure (π_c) is the highest surface pressure to which a Langmuir monolayer can be compressed at the air/water interface [30, 32] and corresponds to the sudden slope change observed on the isotherms at high surface pressures (see, arrows on Fig. 1). The corresponding mean molecular areas are the collapse areas (A_c) and they are also given in Table 1. As can be seen the A_c values are constant. This situation can be correlated with the squeezing out of penetrated drugs from mixed DPPC and drug monolayers near their incipient collapse.

Table 1.

Surface characteristics of DPPC monolayers in the absence and in the presence of P (10^{-3} mole dm^{-3}) or DFO (10^{-6} mole dm^{-3}). The mean area values (A_0, and A_c) are given in $Å^2$/molecule of DPPC. The π_c values correspond to the monolayer collapse.

Monolayer	A_0 ($Å^2$)	A_c ($Å^2$)	π_c (mN/m)	
			incipient	(advanced)
DPPC	54	42	55	-
DPPC and DFO	69	42	59	(70)
DPPC and P	78	42	63	(70)

In CL state the DPPC molecules are densely packed and A_c values (42 $Å^2$, Table 1) are in close agreement with the packing area of hydrocarbon chains in crystalline lipids, e.g. area of 38 $Å^2$ per pair of chains [33], and with data obtained for DPPC from geometric models (40 $Å^2$ [20]). Similarly, an area of 21 $Å^2$ for the hydrocarbon chain was found from AFM observations on lignoceric acid LB films [34].

It is important to emphasize that we have chosen these two very different concentrations of drugs, because for these conditions procaine and deferoxamine have an important (see, π_c in Table 1) and comparable effect (see, A_0 and A_c values) on the phase behavior of DPPC monolayers. The stability of DPPC films is highly increased and it is shown by the increased collapse pressures of DPPC monolayers at the air/water interface in the presence of drugs.

The increased stability of DPPC monolayers in presence of procaine or deferoxamine reflects stronger specific interactions between these biocompounds, due to their ability to make stable self assembled supramolecular associations primarily through hydrogen bonds and electrostatic interactions [35-38].

3.2 AFM images and analysis

3.2.1 Mixed LB Films of DPPC and P

We examine the morphology of mixed LB films of DPPC and P vertically transferred on glass at two surface pressures 8 mN/m (Fig. 2) and at advanced collapse state of 70 mN/m (Fig. 3) by AFM tapping mode, which allows simultaneous acquisition of both morphology data (topographic image) and material-properties data (phase image), such as elasticity, friction and adhesion. These data demonstrate that, generally, the topographic and phase images appear to be complementary to one another showing the structural features of LB samples.

These AFM images indicate that the mixed DPPC and P films are not homogeneous at low surface pressure (Fig. 2), which is plausible taking into account the different molecular length of the two molecules, DPPC and P, and their orientation at low pressures [20, 24, 29]. However, by increasing the surface pressures, AFM images indicate an increased cohesion among molecules reflected also in topographic profiles, along the arrows indicated in Figs. 2 and 3 (panels A), which are shown in Figs. 2 and 3 (panels C).

For example, in Fig. 2C it can be seen that the surface of some ordered domains is almost flat and the maximum height of LB film is between 1.8 and 2.1 nm, corresponding to a single molecular layer, when the DPPC molecules probably stand

with hydrocarbon chains inclined and polar groups parallel to the substrate. We suggest that this surface configuration corresponds to liquid ordered domains as determined for LB films of pure DPPC (unpublished results). This situation demonstrates that some ordering phenomena take place within the monolayers even at low surface pressures. In addition to these ordered monolayer domains the rest of the LB film is covered by islands of surface micelles and molecular nano aggregates and their heights are comprised between 9 Å and 18 Å, corresponding to a mosaic of EL domains. Probably, the procaine molecules penetrate among the DPPC domains increasing the stability of the mixed DPPC and P films.

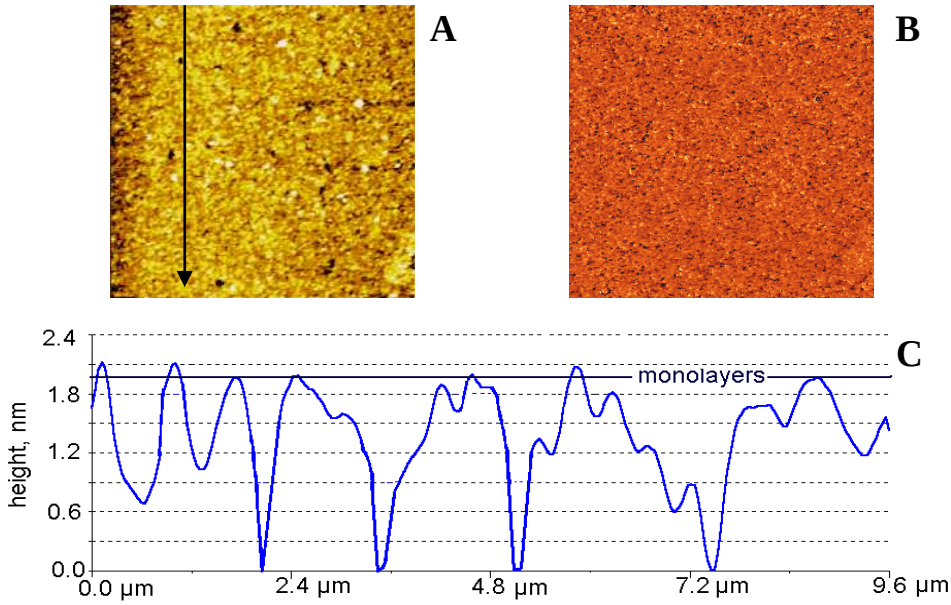

Fig. 2 *The 2D topographic (panel A) and phase (B) AFM images of mixed LB films formed by DPPC and P vertically transferred on glass at surface pressure of 8 mN/m (see Fig. 1, curve 3). Section profile (panel C) along the arrow (panel A). Scanned area of 10 x 10 µm^2.*

Further, by increasing the lateral surface pressures to 70 mN/m, an advanced collapsed state is reached, which corresponds to a two-dimensional CL in equilibrium with collapsed bulk fragments (Fig. 3). The AFM images of mixed DPPC and P film show the formation of large ordered structures, Fig. 3 (panels C). In addition to these CL highly ordered domains (Fig. 3), three layered fragments are identified (Fig. 3C), and occasionally colloidal particles are observed with their height under 20 nm (Fig. 3A).

The analysis of the DPPC film morphology in presence of procaine at advanced collapse state, given in Fig. 3 (panel A), indicates that the highest thickness of the DPPC film remains almost unchanged between 33 Å and 36 Å as shown in cross section profile Fig. 3C. This thickness corresponds to the height of DPPC molecule (36 Å [20]) in all-trans conformation of both hydrocarbon chains

(19 Å) and the extended conformation of the head phosphatidylcholine polar group (17 Å), both parts of DPPC molecule being vertically oriented on the LB surface. This value can be considered as an important parameter relevant for the thickness of a DPPC monolayer relatively well packed at collapse in large condensed domains.

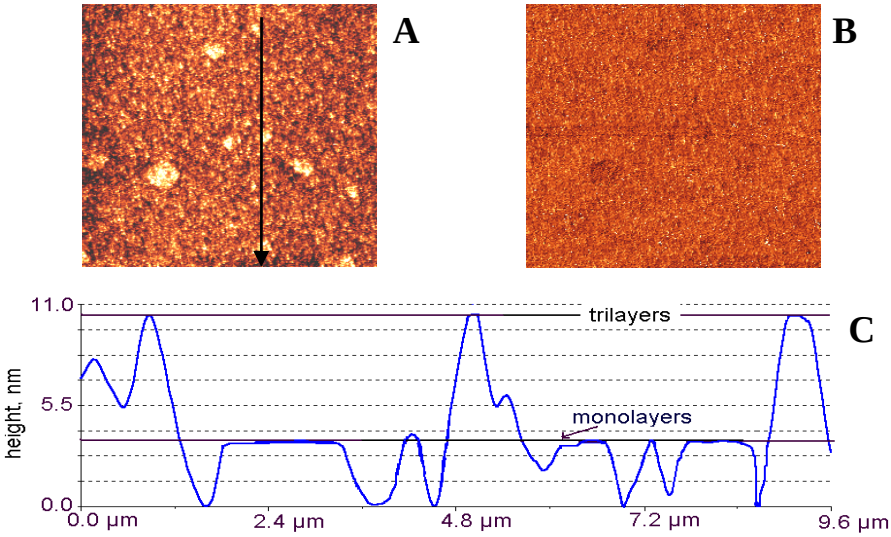

Fig. 3. *The 2D topographic (panel A) and phase image (panel B), section profile (panel C) along the arrow (panel A) for mixed LB films of DPPC and P transferred at advanced collapse state (lateral surface pressure of 70 mN/m). Scanned area of 10 x 10 µm^2.*

Therefore, it is evidenced the persistence of monolayer CL domains at very high surface lateral pressures in mixed DPPC and P films at advanced collapse state. The width of domains is up to 1.5 µm and corresponds to supramolecular aggregates, probably, made up from well oriented DPPC and P molecules primarily through hydrogen bonds and electrostatic interactions.

3.2.2. Mixed LB Films of DPPC and DFO

AFM observations were also done for the mixed LB films of DPPC and DFO at low lateral surface pressure as 8 mN/m (Fig. 4) and at advanced collapse state at 70 mN/m (Fig. 5). A good surface coverage by DPPC and DFO self-assembled patches and a relatively good adhesion of mixed LB films with the glass substrate were observed.

It is important to note that the phase transition from EL to CL, recorded at 8 mN/m for pure DPPC monolayer (Fig. 1, curve 1), vanishes completely in the presence of DFO (Fig. 1, curve 2). This drug effect suggests that the self-assembled associations between DPPC and DFO molecules are rather strong and the two-dimensional packing of the molecules is high and comparable with the case of mixed DPPC and procaine film (Fig. 1, curve 3). The thickness of condensed monolayer domains within mixed LB films of DPPC and DFO ranges between 24 Å (Fig. 4, panel C) and 38 Å (Fig. 5, panel C) for the surface lateral pressure range between 8 mN/m and 70 mN/m. Within this range of surface pressure the film roughness for the condensed bright domains is about 0.4 nm in substantial agreement with that

observed by AFM for mixed LB films of DPPC and procaine and can be attributed to the uneven alignment of DPPC molecules. However, at advanced collapse state (Fig. 5), the increase in monolayer condensed domain thickness is too large (38 Å, in panel C) to be compatible only with a molecular reorganization of DPPC molecules and perhaps it exemplifies strong specific interactions among DPPC and large DFO molecules. In addition, three layered fragments are identified but their number is small (Fig. 5A) in comparison with mixed DPPC and procaine films (Fig. 3A).

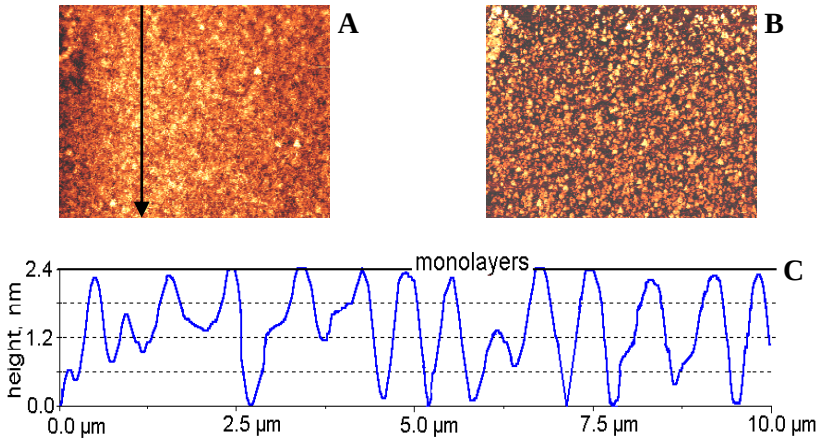

Fig.4. *The 2D topographic (panel A) and phase (B) AFM images of LB films of DPPC in the presence of DFO (see Fig. 1, curve 2) vertically transferred at surface pressure of 8 mN/m. Section profile (panel C) along the arrow (panel A). Scanned area of 10 x 10 µm^2.*

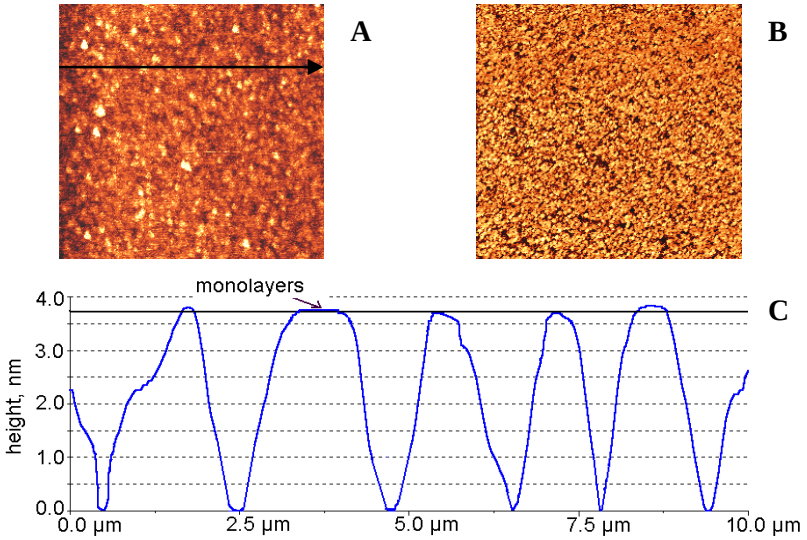

Fig. 5. *The 2D topographic (panel A) and phase (panel B) AFM images, section profiles (panel C) along the arrow (panel A) for mixed LB films of DPPC and DFO transferred at advanced collapse state (70 mN/m). Scanned area of 10 x 10 µm^2.*

The high stability of large condensed domains (with the width up to 2.5 μm), identified in mixed DPPC and DFO films (Fig. 5 C) at advanced collapse, might indicate that the flexible DFO molecules are differently oriented than DPPC molecules, and probably they are horizontally oriented beneath the DPPC monolayer. This interfacial orientation can facilitate the self – assembled molecular associations and, thus, it can stabilize the condensed monolayer domains.

4. Conclusions

We have demonstrated that atomic force microscope coupled with Langmuir and Langmuir-Blodgett techniques gives important information on the film structure of binary mixtures of DPPC and different drugs, like procaine and deferoxamine.

The AFM images on mixed LB films of DPPC and P and of DPPC and DFO obtained at a surface pressure (about 8 mN/m), corresponding to the two-dimensional phase transition from EL to CL in pure DPPC monolayers, show the coexistence of ordered and less ordered liquid domains.

The largest regular aggregates were observed at advanced collapse of 70 mN/m, which is a phase transition from two-dimensional condensed liquid to collapsed bulk phase. These self-aggregates consist primarily of highly packed DPPC molecules in interfacial condensed domains and drug molecules probably penetrate within the DPPC domains and among these domains reducing the line tension among DPPC domains.

The increased stability of mixed films of DPPC and P and of those formed by DPPC and DFO, as compared with pure DPPC films, can be described by the electrostatic interaction between the zwitterions of DPPC polar head groups and protonated amino terminal of P molecules and that of DFO molecules in addition to the interaction between the hydrophobic tail groups of DPPC and the hydrogen bond formation among these biocompounds. The collective effect of these molecular interactions might lead to the formation and to the alignment of ordered interfacial structures, which can have a physiologic role in vivo.

REFERENCES

1. A. Ulman, “An Introduction to Ultrathin Organic Films. From Langmuir-Blodgett to Self-assembly”, Academic Press, New York, **1991**.
2. D. K. Schwartz, *Surface Science Reports*, **1997**, *27*, 241.
3. X. Zhai and J. M. Kleijn, *Thin Solid Films*, **1997**, *304*, 327.
4. Y. F. Dufrene and G. U. Lee, *Biochim. Biophys. Acta,* **2000**, *1509*, 14.
5. K. S. Birdi, “Scanning Probe Microscopes. Applications in Science and Technology”, CRC Press, New York, **2003.**
6. M.I. Salajan, A. Mocanu and M. Tomoaia-Cotisel, “Advances in Thermodynamics, Hydrodynamics and Biophysics of Thin Layers”, University Press, Cluj-Napoca, **2004**.
7. M. Tomoaia-Cotisel, Gh. Tomoaia, A. Mocanu, V.D. Pop, N. Apetroaei and Gh. Popa, *Studia Univ Babes-Bolyai, Chem*., **2004**, *49*, 1.
8. M. Tomoaia-Cotisel, Gh. Tomoaia, V.D. Pop, A. Mocanu, N. Apetroaei and Gh. Popa, *Rev. Roum. Chim.,* **2004** in press.
9. H. E. Ries, Jr., *Nature*, **1979**, *281*, 287.

10. M. Tomoaia-Cotisel, A. Sen and P. J. Quinn, *J. Colloid Interface Sci.,* **1983**, *94*, 390.
11. M. Tomoaia-Cotisel, E. Chifu, S. Jitian, I. Bratu, S. Bran, P. T. Frangopol and A. Mocanu, *Studia Univ Babes-Bolyai, Chem*., **1990**, *35* (2), 17.
12. L. J. Noe, M. Tomoaia-Cotisel, M. Casstevens and P. N. Prasad, *Thin Solid Films,* **1992**, *208*, 274.
13. H. Mohwald, *Annu. Rev. Phys. Chem.,* **1990**, *41*, 441.
14. B. Asgharian, D. A. Cadenhead and M. Tomoaia-Cotisel, *Langmuir,* **1993**, *9*, 228.
15. R. Maget-Dana, *Biochim. Biophys. Acta*, **1999**, *1462*, 109.
16. G. Gabrielli, *Advances in Colloid and Interface Science,* **1991**, *34*, 31.
17. M. Tomoaia-Cotisel and P. J. Quinn, "Biophysical Properties of Carotenoids", Subcellular Biochemistry, Volume *30*: Fat-Soluble Vitamins", Chapter ***10*****,** Edited by P.J. Quinn and V. E. Kagan, Plenum Press, New York, **1998**, pp. 219-242.
18. M. Tomoaia-Cotisel and I. W. Levin, *J. Phys. Chem.*, *B*, **1997**, *101*, 8477.
19. S. W. Hui, D. F. Parsons and M. Cowden, *Proc. Natl. Acad. Sci., U.S.A.,* **1974**, *71*, 5068.
20. M. Tomoaia-Cotisel, J. Zsako and E. Chifu, *Ann. Chim. (Rome)*, **1981**, *71*, 189.
21. J. Zsako, M. Tomoaia-Cotisel, E. Chifu, A. Mocanu and P. T. Frangopol, *Gazz. Chim. Ital.,* **1994**, *124*, 5.
22. J. Zsako, E. Chifu, M. Tomoaia-Cotisel, A. Mocanu and P. T. Frangopol, *Rev. Roum. Chim.*,**1994,** *39*, 777.
23. E. Chifu, "Colloid and Interface Chemistry", Edited by, M. Tomoaia-Cotisel, I. Albu, A. Mocanu,
24. M. Salajan, Cs. Racz and E. Gavrila, University Press, Cluj-Napoca, **2000**.
25. M. Tomoaia-Cotisel, *Progr. Colloid Polym. Sci.,* **1990**, *83*, 155.
26. J. Zsako, M. Tomoaia-Cotisel, I. Albu, A. Mocanu and A. Aldea, *Rev. Roum. Chim.,* **2002**, *47*, 869.
27. E. Chifu, M. Tomoaia-Cotisel, I. Albu, A. Mocanu. M.-I. Salajan, Cs. Racz and V.D. Pop, "Experimental Methods in Chemistry and Biophysics of Colloids and Interfaces", University Press, Cluj-Napoca, **2004.**
28. M. Tomoaia-Cotisel, J. Zsako, A. Mocanu, M. Lupea and E. Chifu, *J. Colloid Interface Sci.*, **1987**, *117*, 464.
29. J. Zsako, M. Tomoaia-Cotisel, E. Chifu, A. Mocanu and P. T. Frangopol, *Biochim. Biophys. Acta*, **1990**, *1024*, 227.
30. M. Tomoaia-Cotisel and D. A. Cadenhead, *Langmuir,* **1991**, *7*, 964.
31. G. L. Gaines, Jr., "Insoluble Monolayers at Liquid-Gas Interfaces", Wiley Interscience, New York, **1966**.
32. N. Dumitrascu, G. Borcia, N. Apetroaei and Gh. Popa, *Plasma Sources Sci. Technol.*, **2002**, *11*, 1.
33. M. Tomoaia-Cotisel, J. Zsako, E. Chifu, D. A. Cadenhead and H. E. Ries, Jr., *Progress in Photosynthesis Research,* Edited by J. Biggins, Vol. *2*, Chapter ***4***, Martinus Nijhoff Publishers**,** Dordrecht, **1987**, pp 333-337.
34. D. M. Small, "The Physical Chemistry of Lipids, Handbook of Lipid Research", Plenum Press, New York, **1986.**
35. T. Kajiyama, Y. Oishi, F. Hirose, K. Shuto and T. Kuri, *Langmuir*, **1994**, *10*, 1297.
36. M. Tomoaia-Cotisel, A. Mocanu, Gh. Tomoaia, J. Zsako and T. Yupsanis, *J. Roum. Assoc. Colloid Surface Chem.,* **2001**, *4*, 5.
37. S. Schreier, S. V. P. Malheiros and E. de Paula, *Biochim. Biophys. Acta*, **2000**, *1508*, 210.
38. J. M. Boggs, *Biochim. Biophys, Acta*, **1987**, *906*, 353.
39. H. Hauser, I. Pascher, R. H. Pearson and S. Sundell, *Biochim. Biophys. Acta*, **1981**, *650*, 21.

STUDIA UNIVERSITATIS BABES-BOLYAI, PHYSICA, XLIX, 3, 2004

POSTER SESSION
Section 2: Advanced and nanostructured materials

SPECTROSCOPIC INVESTIGATIONS ON HIGH T_C YBCO THIN FILMS

M. BRANESCU*, G. SOCOL[1], D. PANTELICA[2], F. NEGOITA[2], I. BALASZ[3], C. DUCU[4], F. LIFEI

[1]National Institute for Lasers, Plasma and Radiations Physics, Bucharest, Romania
[2]National Institute for Physics and Nuclear Engineering Horia Hulubei, Bucharest, Romania
[3]University Babes Boliay, Physics Faculty, Cluj Napoca, Romania
[4]University of Pitesti, Advanced Materials Department, Pitesti, Romania

ABSTRACT. Some experimental results concerning the pulsed laser deposition parameters of post annealing epitaxially $YBa_2Cu_3O_{7-x}$ grown films are reported. We have investigated the stoichiometry, thickness morphology, crystallographic microstructure, and superconducting properties of the films using elastic recoil detection analysis, Raman spectroscopy, X-ray diffraction spectrum, and ac magnetic susceptibility measurement. High oriented *c*-axis films with high critical temperature at 87 K were obtained.

Keywords: Pulsed laser deposition, YBCO films

1. Introduction

For small-scale applications of superconducting electronics, thin films with multi-layers, smooth surface and interface, large area and epitaxial growth are required. At present high temperature superconductor (HTS) thin films for electronic applications are dominated by $YBa_2Cu_3O_{7-x}$ (YBCO) and related 123 materials. Pulsed laser deposition (PLD) is considered to be well suited for a fast process on a laboratory scale [1]. These materials are some of the most complicated materials under technological development today. Most of the physical properties are sensitive to the change in micro-structures and compositions. Therefore, controlling the microstructures is crucial to obtain high quality thin films with high reproducibility. Spectroscopic investigation allows us to analyze the morphology, structural and stoichiometric properties of the YBCO films.

The second section presents the PLD process and its main parameters.

The paper presents in the following section, some details and analyses concerning the information about the stoichiometry and the thickness morphology of the YBCO film, respectively, obtained with elastic recoil detection analysis (ERDA). We used the thickness information of the film named A to determine the typical

* *E-mail: branescu@hotmail.com; maria_branescu@yahoo.com, National Institute for R&D of Material Physics, P.O. Box MG-7, Bucharest, Romania.*

deposition rate in the PLD process of the YBCO films. The Raman spectra present information about the oxygen content and the crystal microstructure of the film named B in correlation with the X-ray diffraction spectrum of this film. The complex susceptibility of the YBCO film B as a function of temperature allows us to evaluate the critical temperature (T_C) and the superconducting properties of YBCO thin film.

The last section is dedicated to conclusions.

2. Parameters of the laser ablation process

The YBCO target was prepared as reported elsewhere [2]. The X-ray diffraction spectrum on the powder used for target manufacturing, has showed well structural data. We used the Seifert diffractometer with the Bragg-Brentano function regime (1V, 1Kcounts/sec). At 77 K the YBCO target showed a powerful magnetic flux-excluding Meissner effect.

A KrF* excimer laser with wavelength of 248 nm was used for the films deposition process. We used a laser fluence of 2.7 J/cm^2 and 2 Hz the repetition rate of the laser pulse. The laser beam was focused onto the rotating YBCO target in a vacuum chamber at 10^{-7} Torr. The target-substrate distance was at about 3.5 cm. The substrate was heated at 800°C, controlled by a thermocouple. Oxygen was added before the deposition processes at 1 Torr. We used $LaAlO_3$ single crystals as substrates, with good behavior at microwave and high temperature.They were optically polished and cleaned in an ultrasonic bath in acetone before the deposition. The deposition time varied between 4,000 and 10,000 laser pulses. With a typical deposition rate of about 0.03 nm/pulse, the films thickness in the range of 0.1 μm to 0.3 μm was obtained. After deposition, the post-ablation annealing treatment was used. The increasing temperature of the film from 25^{o}C to 750^{o}C in flowing oxygen, was followed by a slow cooling process (3 ^{o}C/min).

3. The films characterization using spectroscopic investigation

The following spectroscopic methods to characterize the YBCO thin films were used: elastic recoil detection analysis, Raman spectroscopy, and X-ray diffraction. Beside the spectroscopic investigation, we used also the ac magnetic susceptibility measurement to determine the critical temperature of the film B.

The composition of the YBCO film A deposited on $LaAlO_3$ substrate was investigated by ERDA. The measurements were carried out at the 8.5 MV tandem accelerator using an 80 MeV $^{79}Br^{11+}$ beam. The sample was mounted in a scattering chamber with a vacuum better than $6.6x10^{-5}$ mbar and tilted at 15^o with respect to the beam direction. The detector, described in detail elsewhere [3], consists in a compact total energy (ΔE – E) telescope placed at 30^o with respect to the beam. The energy loss (ΔE) is measured in transmission with a gas ionization chamber. The residual energy (E) is measured with a thick (>300μm) Si detector. The energy loss in the ionization chamber increases strongly (almost 120-fold) in going from H to Si, thus providing excellent elemental resolution. The recoil spectrometry is a fairly new technique and involves data collection of more than one parameter. For the analysis of the ERDA spectra we used our program SURFAN [4]. Note that because the recoil energy is comparable or > E_{Bragg}, the recoil stopping power depends strongly on nuclear charge.

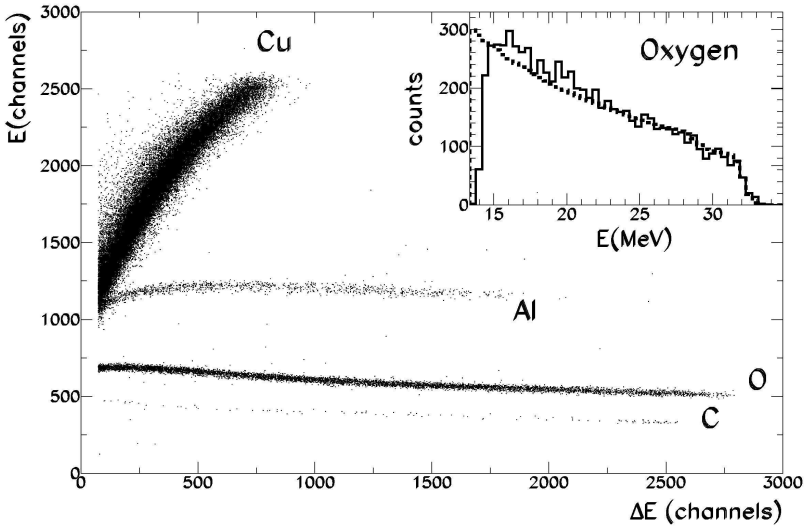

Fig.1. *ERDA on the YBCO film A and the $LaAlO_3$ substrate*

The figure 1 presents the ERDA spectrum on the YBCO film A deposited on $LaAlO_3$ substrate. On can observe mainly the oxygen, aluminum and copper, which come from the beam scattered on heavy elements (Ba, Y). A small contamination with C is observed. A film stoichiometry close to $YBa_2Cu_3O_{6.7}$ was obtained. The thickness of the film A was evaluated at about 100nm. For 3.5 cm target-substrate distance and 2.7 J/cm^2 laser fluence, a YBCO typical deposition rate of about 0.03 nm/pulse was evaluated for our available PLD equipment.

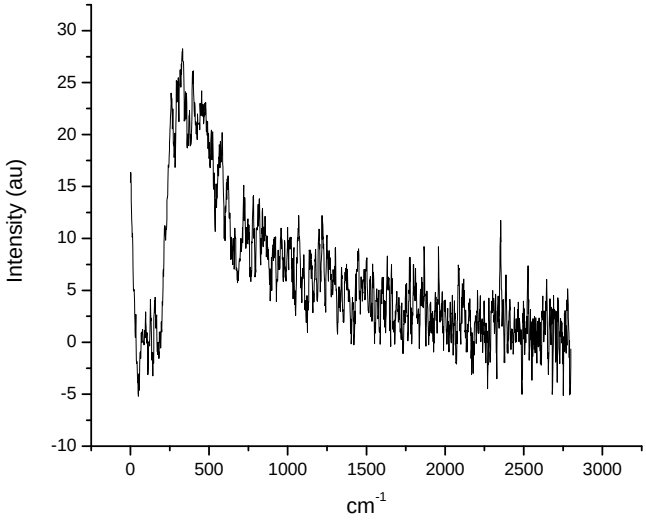

Fig. 2. *Raman spectrum of the YBCO film B*

We have investigated the film B, with thickness of about 300nm, using Raman spectroscopy, X-ray diffraction, and ac magnetic susceptibility measurement.

The local orientation of YBCO thin film B was estimated by Raman spectrum analysis. The Raman scattered light was excited by a semiconductor laser diode with λ = 785 nm and the power level 500 mW. The detector consist of 2048 Si elements CCD with 1.5 cm^{-1} frequency resolution and 50 s time resolution.

Comparison of the intensity of the apical oxygen 500 cm^{-1} mode and the anti-phase oxygen vibration in the CuO_2 planes 340 cm^{-1} mode (corresponding to non-superconducting tetragonal phase) allow as to determine the epitaxially grown orientation direction and uniformity of the film [5, 6]. Figure 2 shows a typical, not fitted, FT Raman spectrum showing the predominantly *c*-axis oriented grains of the YBCO thin film B.

The characteristic spectrum of the Raman-shifted lines for the orthorhombic YBCO phase occur at 340 cm^{-1}, 435 cm^{-1}, and 500 cm^{-1}, corresponding to the vibrations along the *c*-axis of planar oxygen in CuO_2 plane out of phase, planar oxygen in CuO_2 plane in phase, and apical oxygen, respectively. Note that the incident Raman light of our measurement equipment is not polarized. From our experience, if we have a good oxygenation of the sample (with T_C around 87 K), we observe a landing between 280 cm^{-1} and 500 cm^{-1} in the Raman spectrum.

The X-ray diffraction patterns of YBCO film was determined using CuKα radiation from a computer-controlled spectrometer Dron UM-1 with degree resolution 0.05^{o}. Figure 3 shows the X-ray diffraction pattern of the YBCO film B where the peaks of the substrate are indicated with S. It shows strong 00n orientation of the film, where n = 1-7, and also an epitaxially grown, *c*-axis textured, columnar film structure. The studies are in progress. We have to obtain a better resolution X-ray diffraction pattern in order to elucidate the lattice constants of the film B and to appropriate its superconducting phase.

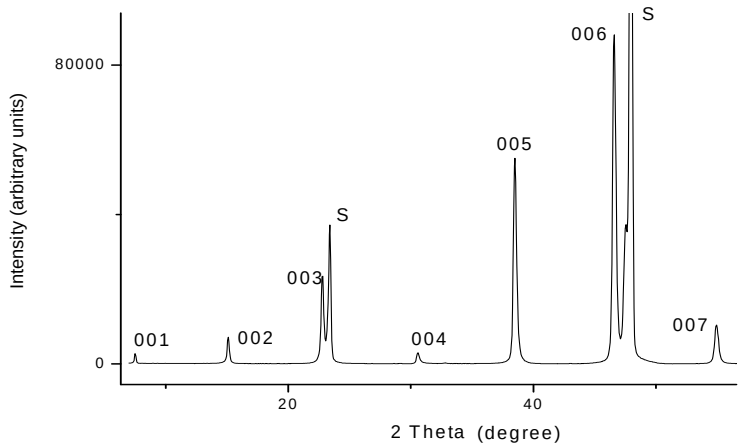

Fig. 3. *X-ray diffraction pattern of the film B*

The superconductivity of the film B was analyzed using Oxford Instruments MagLab System 2000 equipment. The complex susceptibility was measured at 1 kHz as a function of temperature, at a field amplitude H_{ac} = 0.1 Oe. Figure 4 shows the critical temperature T_C (χ) = 87 K, determined as the temperature where the

ac-susceptibility become diamagnetic for H_{ac} = 0.1 Oe. The real part of complex susceptibility (figured with negative y-axe values) shows two superconducting phases at about 70 K and 87 K. The imaginary component of the ac susceptibility, χ´´ (figured with positive y-axe values), represent a measure of the absorption of the flux inside the weak-links formed in the intra-granular and inter-granular regions [7]. χ´´ exhibit only a single broad peak at a temperature < T_C, containing both the intra-granular and inter-granular regions.

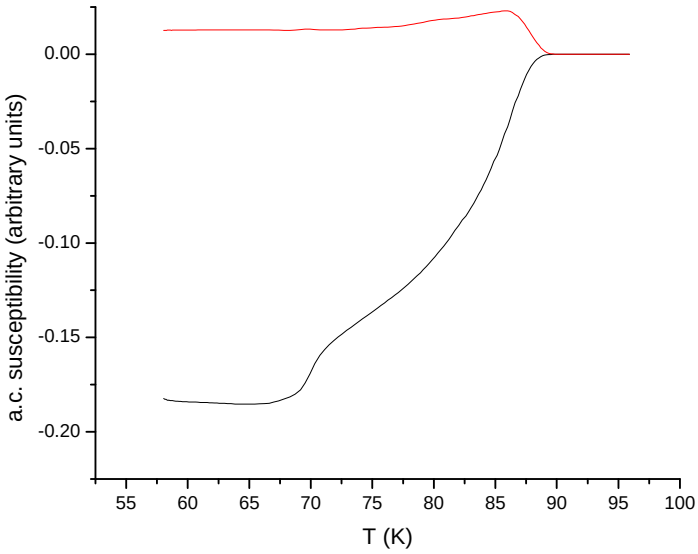

Fig. 4. *The complex susceptibility of the YBCO film as a function of temperature*

Conclusions

Using spectroscopic investigations we have determined the YBCO deposition rate of the PLD process of our available equipment and have characterized the structural features of our films. We have obtained high c-axis oriented YBCO thin films with high T_C. The nondestructive, contact-less techniques: ERDA, Raman spectroscopy and X-ray diffraction spectrum provide us useful complementary tools to investigate the YBCO films in a rapid way, at room temperature.

Acknowledgements

The authors are thankful to I. Sandu, National Institute for Lasers, Plasma and Radiations Physics, Bucharest, Romania for help in Raman spectrometry characterization of YBCO thin films.

REFERENCES

1. *Pulsed laser deposition of thin films*, D. B. Chrisey and G. K. Hubler, eds., John Wiley & Sons Inc., 1994, chs. 5, 14, 15.
2. M. Popescu, L. Miu, and E. Cruceanu, *Phil. Mag. Lett.* ***57***, 273 (1988).
3. M. Petrascu, I. Berceanu, I. Brancus, et al., *Nucl. Instrum. Methods* ***B 232***, 396 (1984).
4. F. Negoita, C. Borcan, D. Pantelica, *NIPNE-HH, Scientific Report*, pp.120, (1996).
5. G. Gibson, L. F. Cohen, R. G. Humphreys and J. L. MacManus-Driscoll, *Physica C* ***333***, 139 (2000).
6. H. Chang, Q. Y. Chen, and W. K. Chu, Physica C ***309***, 215 (1998).
7. S. Ravi, *Physica C* ***265***, 277 (1998).

STUDIA UNIVERSITATIS BABES-BOLYAI, PHYSICA, XLIX, 3, 2004

SPECTRAL CHARACTERIZATION OF ZINC SULPHIDE THIN FILMS WITH LUMINESCENT PROPERTIES

MARIA LĂDAR[1, 2], ELISABETH-JEANNE POPOVICI[1], IOAN BALDEA[2], RODICA GRECU[1] and EMIL INDREA[3]

[1]*"Raluca Ripan" Institute for Research in Chemistry, 30 Fantanele, 400294 Cluj-Napoca*

[2]*Faculty of Chemistry and Chemical Engineering, "Babes-Bolyai" University, 400028 Cluj-Napoca,*

[3] *National Institute for R &D of Isotopic and Molecular Technology, Donath 71 – 103,400295, Cluj-Napoca, Romania*

ABSTRACT. The chemical bath deposition (CBD) method has been successfully used to grow zinc sulphide thin films onto optical glass substrates, from bath containing zinc acetate, thiourea, ammonia and sodium citrate. The mono- and multilayer technique was used in order to prepare ZnS/glass/ZnS heterostructures with variable zinc sulphide film thickness. Photoluminescent copper activated ZnS films were prepared by using a special doping procedure. The samples were investigated by X-ray diffraction, UV-VIS absorption and fluorescence spectroscopy.

Keywords: Zinc sulphide, Chemical bath deposition, Luminescence

INTRODUCTION

Zinc sulphide (ZnS) is a semiconducting material with 3.7 eV direct band gap that has a wide range of applications in optoelectronics. In particularly, there is a continuous interest in the growth of high-quality zinc sulphide thin films for use in blue emitting diodes, electro-luminescent displays and solar cells. ZnS thin films could be produced by a variety of methods including chemical bath deposition, sputtering, atomic layer epitaxy, molecular beam epitaxy, chemical vapor deposition or electrodeposition [1,2]. Among all these methods, chemical bath deposition (CBD) shows many advantages such as the low cost and the low elaboration temperature as well as the easy coatings of large surfaces.

The paper presents the influence of different preparation conditions on thin film quality and, consequently, on some of the structural and optical properties of mono- and multilayer ZnS films deposited onto optical glass. The luminescence of copper activated ZnS films is also reported.

Experimental part

ZnS thin films were prepared from chemical bath containing zinc acetate, ammonia, sodium citrate and thiourea. The film growth was performed onto optical glass substrates by monolayer and multilayer deposition technique. The glass platelets (3 x 4.5 x 1 cm^2) were ultrasonically cleaned with acetone/ethanol mixture and vertically suspended into the chemical bath. The deposition temperature was 82-84℃ and the mixture pH was 9.5-10.5. The details of experimental technique

*Correspondence: *e-mail:* marialadar@yahoo.com

have been described in our previous works [3,4]. ZnS/glass/ZnS structures were annealed at 400-550℃, in a ZnS-based doping mixture containing copper salts.

Zinc sulphide thin films were characterized by thickness (micro-weighing method), crystalline structure (standard DRON-3M Diffractometer; CuK_λ radiation), UV-Vis transmittance spectra (UNICAM Spectrometer UV4) and photoluminescence measurements (Perkin Elmer 204 Fluorescence Spectrofotometer).

RESULTS AND DISCUSSION

The morpho-structural characteristics and the optical properties of zinc sulphide thin films are strongly influenced by the growing conditions and annealing regime.

ZNS THIN FILMS WERE GROWN (EQ.1) BY MONO- AND MULTILAYER TECHNIQUE, FROM CHEMICAL BATH CONTAINING ZINC ACETATE, THIOUREEA, SODIUM CITRATE AND AMMONIA. CHEMICAL BATH COMPOSITION WAS: [ZINC ACETATE] = $15X10^{-3}$ M; [SODIUM CITRATE] = $7.5X10^{-3} \div 60X10^{-3}$ M; [AMMONIA] = $300X10^{-3}$ M; [THIOUREA] = 150 X 10^{-3} M.

$$Zn(CH_3COO)_2 + (NH_2)_2CS + 2OH^- \rightarrow ZnS + H_2CN_2 + 2H_2O + 2CH_3COO^- \quad (1)$$

The influence of the concentration of the complexing agent (sodium citrate) on the ZnS films thickness has been investigated at constant zinc acetate and thiourea concentrations. The molar ratio between Zn^{2+} and $C_6H_5O_7^{3-}$ (abbreviated as Cyt^{3-}) species was varied between 1.0: 0.5 and 1.0: 4.0. The preparation conditions such as deposition technique, growing time, molar ratio between zinc acetate and sodium citrate as well as the film thickness are presented in table 1. The dependence of ZnS film thickness on sodium citrate concentration is illustrated in figure1.

Table 1.

Deposition conditions for some some ZnS/glass/ZnS heterostructures

Samples code	Molar ratio $[Zn^{2+}]$: $[Cyt^{3-}]$	DEPOSITION TECHNIQUE	Deposition time n x m*	Film thickness (nm)
F1.3	1.0: 4.00	multilayer	2 x 1h	125
F1.6		monolayer	1 x 2h	80
F2.1	1.0: 3.00	multilayer	2 x 1h	180
F2.4		monolayer	1 x 2h	130
F3.2	1.0: 2.00	multilayer	2 x 1h	145
F3.4		monolayer	1 x 2h	110
F4.3	1.0: 1.50	multilayer	2 x 1h	145
F4.4		monolayer	1 x 2h	110
F5.3	1.0: 1.00	multilayer	2 x 1h	170
F5.6		monolayer	1 x 2h	110
F6.2	1.0: 0.75	multilayer	2 x 1h	180
F6.6		monolayer	1 x 2h	120
F7.2	1.0: 0.50	multilayer	2 x 1h	200
F7.4		monolayer	1 x 2h	170

where: n = number of layers, m = single later deposition time;

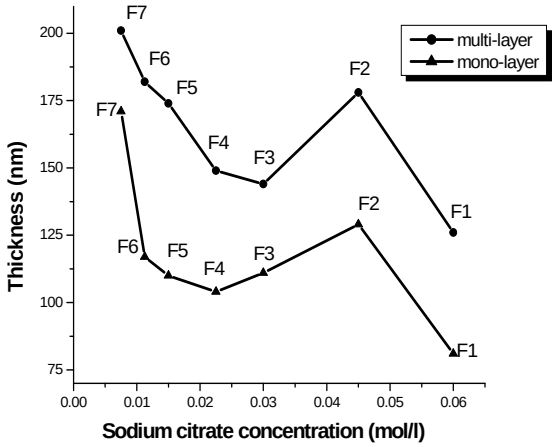

Fig. 1. *Variation of films thickness with sodium citrate concentration.*

For the same total deposition time, one can note that monolayer deposited ZnS thin films have smaller thickness than those of multilayer deposited ones.

The concentration of complexing agent influences also the film quality. Depending on Na-citrate amount, two categories of samples could be prepared namely: adherent and homogeneous films at high concentrations (0.03 ÷ 0.06 M) and powdery and less adherent films at relatively low citrate concentration.

The optical transmittance of ZnS thin films is strongly influenced by the preparation conditions of ZnS/glass/ZnS heterostructures, as illustrated by sample transmission spectra (fig.2). In both cases, the film transmittance decreases with its increasing thickness. Moreover, the optical homogeneity of the films prepared in baths with relatively low citrate concentration is poor.

The thickness values and the transmitance spectra suggest that the best films quality could be obtained in bath with the ratio $[Zn^{2+}]$: $[Cyt^{3-}]$ = 1:3. The optimal deposition bath, considering all ingredients, corresponds to the reagent ratio of: $[Zn^{2+}]$: $[Cyt^{3-}]$: $[NH_3]$: [thiourea] =1:3:20:10. These conditions were considered as standard.

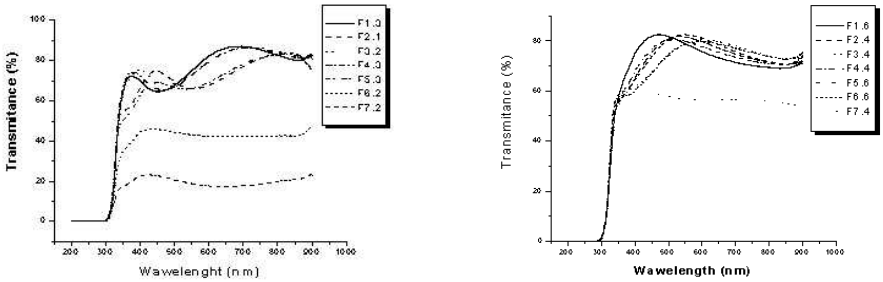

Fig. 2. *Transmission spectra of ZnS/glass/ZnS structures formed by multilayer (left) and monolayer (right) technique.*

The influence of the annealing regime on the photoluminescence (PL) characteristics of copper doped ZnS/glass/ZnS heterostructures is illustrated in figure 3. Under ultraviolet excitation (λ_{exc} =365nm), the film luminescence could be observed in the blue-green range of wavelengths. For copper doped ZnS films, the aparent maximum emission was at 495 – 515 nm resulting from the Cu-centres emision.

In fact, due to the copper ion incorporation into the ZnS host-lattice, the specific Cu-green luminescence (λ_{pk}= 515 nm) is supperimposed over the ZnS blue self-activated emission (λ_{pk}= 460 nm). Emission spectra of ZnS thin films put in evidence the intensification of copper emission, in parallel with the increasing of the annealing temperature. It is worth mentioning, for PL measurements, relatively thick (300 – 340 nm) ZnS films have to be used.

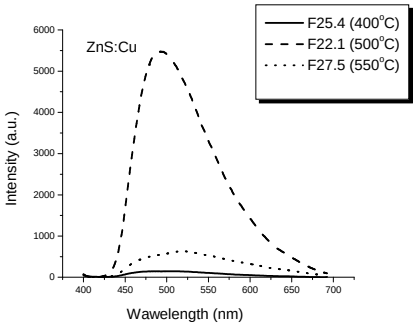

Fig. 3. *Emission spectra of ZnS: Cu films annealed at different temperatures*

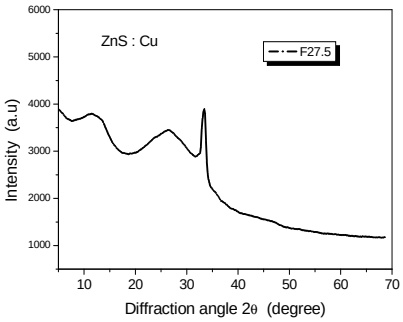

Fig. 4. *XRD pattern of the luminescent ZnS film annealed at 550℃*

The structural properties of CBD-grown ZnS thin films have been investigated by XRD technique (fig.4). The copper doped ZnS film grown in standard conditions possess a more or less crystallized hexagonal structure (wurtzite type) with crystallite dimension of about 15 nm.

CONCLUSIONS

Luminescent ZnS thin films were prepared by chemical bath deposition (CBD) route. The growth of ZnS thin films was performed from zinc acetate – sodium citrate - ammonia – thiourea system whereas the luminescence generating annealing was achieved from special doping mixtures containing copper salts. Sodium citrate concentration proved to be an important factor for the deposition of optical homogeneous nanostructured ZnS films with controllable thickness.

REFERENCES

1. I.C.Ndukwe, *Solution growth, characterization of zinc sulphide thin films,* Solar Energy. Mater. Solar Cells, 40, 1996, 123-131
2. R.S.Mane, C.D. Lokhande, *Chemical deposition method for metal calcogenide thin films*, Materials Chemistry and Physics, 65, 2000, 1-31
3. Maria Ladar, Elisabeth- Jeanne Popovici, Ligia Pascu, Rodica Grecu, Ionel-Catalin Popescu, Emil Indrea, *Specroscopic Characterization of cadmium sulphide thin layers deposited on ITO coated glass Studia Universitas Babes-Bolyai, ser. Physica*, Special issue 2, 2003 469-471
4. Rodica Grecu, Elisabeth-Jeanne Popovici, Maria Ladar, Laura Silaghi-Dumitrescu, Emil Indrea, *Investigation of optical properties of chemical bath deposited zinc sulphide thin films*, *Studia Universitas Babes-Bolyai, ser. Physica*, Special issue 2, **2003**,472-475

STUDIA UNIVERSITATIS BABES-BOLYAI, PHYSICA, XLIX, 3, 2004

ESR AND ATR-FTIR INVESTIGATIONS OF NANOSTRUCTURED POLYMERIC FILMS

MARGARETA BAKO[1], G. DAMIAN[1], O. COZAR[1], SIMINA DREVE[2]

[1]'Babes-Bolyai' University, Faculty of Physics, 1 Kogalniceanu, Cluj-Napoca, Romania
[2] National R&D Institute of Isotopic and Molecular Technologies, P.O. Box 700, Cluj-Napoca, Romania, mbako@phys.ubbcluj.ro

ABSTRACT. Understanding of a complex correlation between polymer structure and its properties is the key to the polymer-specific morphology design ready to meet new technological requirements such as "smart" polymers, electro-optical materials, artificial organs, antireflection surface coatings, permselective membranes and drug delivery devices. The paper describes the results of Electron Spin Resonance (ESR) and Attenuated Total Reflection Fourier Transform Infrared Spectroscopy (ATR-FTIR) investigations of some polymeric films made by combining in equal proportions polyvinylformaldehyde resin with protoporphyrine and Tempol as nitroxidic compound for investigating the microstructure of the prepared copolymeric films.

Keywords*:* Polyvinylformaldehyde, thin-film; ESR, ATR-FTIR

Introduction

Polymer systems of interest in applied and fundamental research become increasingly complex due to the combination of a multitude of polymers and additives to a single material and the use of nanoscale structuring as a design principle. Particularly, polymeric thin films are explored as promising basis-materials for the fabrication of microsensors, or to immobilize chemosensitive compounds.

The principles for the synthesis and preparation of polymeric nanostructured thin films generally follow specific techniques, upon the final purpose of sensing and ability to transfer the information. It is reported that the microstructure can be achieved and controlled by various fabrication techniques. At the basis of such systems are the nanostructured thin layers of polymers, co-polymers or polymeric composites, following the application purpose [1]. The need of development of such materials depends on their structural and homogeneity/heterogeneity characterization. One of technique to overcome the selectively targeting microdomains or other structural features of interest by molecular tracers, i.e. to use the electron paramagnetic resonance (ESR) spectroscopy with nitroxide spin probes as the molecular tracers. ESR spectroscopy is the experimental technique, which is able to supply extensive information on chemical structure (reflected in hyperfine structure of ESR spectrum resulting from intramolecular magnetic interactions) and concentration of paramagnetic molecules. In addition, information on rotational dynamics of paramagnetic molecules, which experience anisotropic intramolecular magnetic interactions, can be obtained. Lineshapes of ESR spectra of such molecules (typically nitroxide radicals) depend on the character of their rotational diffusion in the studied system. Nitroxides have usually been used as "reporter groups" (spin labels), which are able to report rotational dynamics inside various systems such as polymers, enzymes and others [2,3]. In

many cases they can thus closely mimic the additive of interest or they can be directed to the microdomain or structural feature of interest by specific interactions. In particular, the dynamics of spin probes on time scales between 10^{-10} s and 10^{-3} s and their relation to the dynamics of the matrix can be investigated in detail with simple experiments.

Another technique to study the nanostructured characteristics of the polymers is Fourier Transform Infrared spectroscopy (FTIR) including Attenuated Total Reflectance (ATR) method [5].

The aim of this paper is to characterise polymeric films of polyvinylformaldehyde resin with protoporphyrin and Tempol as nitroxidic radicals by Electron Spin Resonance (ESR) and Attenuated Total Reflection Fourier Transform Infrared Spectroscopy (ATR-FTIR).

Experimental

Such thin films area routinely prepared in laboratories by controlled allowance of the polymeric solution from a separation funnel, by adjusting the valve. A clean piece of thin glass is mounted on the reservoir, and the evaporation of the solvent leave a thin polymeric layer of high homogeneity wich sticks to the surface. A solution with the specific mass of 1.230 g/cm^3 of polyvinylformaldehyde, $C_{10}H_{18}O_{12}$, (Merck quality) in dichlorethane was prepared as in ref. [1]. Tempol (2,2,6,6-tetramethyl-4-hydroxy-piperidine-oxyl) was obtained from Fluka. The structural formulas of studied samples are presented in Fig.1:

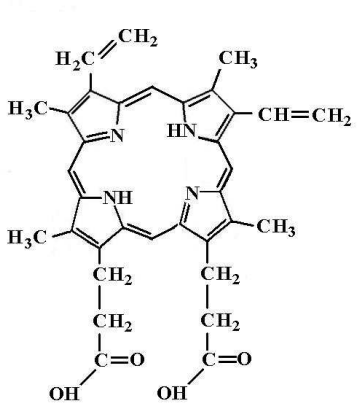

PPF = protoporphyrine

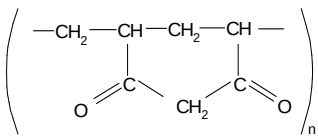

PVFM = polyvinylformaldehyde

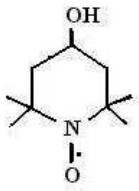

T = Tempol

Fig. 1. *Chemical structures of used compounds.*

ESR spectra were recorded with a " ADANI Portable ESR Spectrometer PS8400", operating in the X-band (9.1GHz – 9.6GHz) equipped with a computer acquisition system. The computer simulation analysis of the spectra was made by using POWFIT program that is available to the public through the internet (http://alfred.neihs.nih/LMB) for obtaining the magnetic characteristic parameters.

The FT-IR spectra of proteins were recorded in the region 4000-800 cm^{-1} by a Bruker EQUINOX 55 spectrometer, using an Attenuated Total Reflectance accessory with a scanning speed of 32 cm^{-1} min^{-1} with the spectral width 2.0 cm^{-1}. The internal reflection element was a ZnSe ATR plate (50 x 20 x 2 mm) with an aperture angle of 45°. A total of 128 scans were ac cumulated for each spectrum. Spectra were recorded at a nominal resolution of 2 cm^{-1}.

Results and discussion

Polyvinylformaldehyde was used as skeleton resin in surface and bulk nanostructured materials because of the good physico-chemical properties for multifunctional nanostructured systems.

Nitroxyl radicals, who are dispersed (spin probe) in polymer matrix or covalently bonded to polymer chains (spin label), are sensitive to the environment. Therefore, molecular motion and microstructure of polymer systems can be evaluated from the ESR spectra. The changes in the shape of the spectrum are correlated with mobility of spin label molecules. If nitroxyl radical is in liquid environment its mobility (spinning) is isotropic and rather speedy which results in averaging of the ESR spectrum anisotropy. Anisotropic interactions appear at a decreased mobility rate which leads to broadening of the lines and, correspondingly, to changes of the amplitudes of spectrum components, and then to a shift of edge components. For description of radical motion, the notion of correlation time *(*τ) is used. This time is the time of turning of free radical by an angle of 90^{o}. For correlation times within the range from $5 \cdot 10^{-11}$ to 10^{-9} s the following semiempirical formula is used [3]:

$$\tau = 6.65 \cdot 10^{-10} \cdot \Delta H_{+1} \left(\sqrt{\frac{I_{+1}}{I_{-1}}} - 1 \right) \quad (1)$$

where ΔH_{+1} is the width of the low field component of the ESR spectrum; I_{+1} and I_{-1} are the amplitudes of the high and low field lines.

At slower motions of nitroxyl radical molecule *(*$\tau > 10^{-9}$ sec) correlation time can be measured by the formula [2]:

$$\tau = a(1 - S)^{b} \quad (2)$$

where a and b are the parameters that depend on radical type and motion model. The empirical constants are tabulated in [6]. In our calculations, for small spin probe (Tempol) the intermediate jump diffusion model was considerate, with coefficients values of $a = 8.52 \cdot 10^{-10}$ and b = -1.16.

In the relation (2)

$$S = \frac{A_{zz}}{A'_{zz}} = \frac{H_{-1} - H_{+1}}{H_{-1\max} - H_{+1\max}} \quad (3)$$

where $2A'_{zz}$ and $2A_{zz}$ are the distance between the high-field and low-field components of the ESR spectrum in the given spectrum ($2A'_{zz}$) and at the maximally long correlation time ($2A_{zz}$), and H_{-1}, H_{+1}, H_{-1max}, H_{+1max} are the values of magnetic field strength corresponding to these spectrum components.

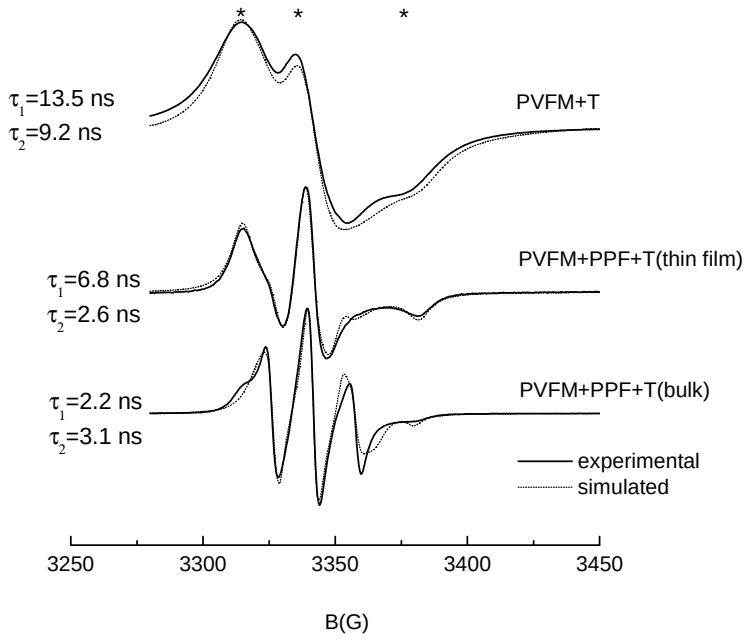

Fig. 2. *ESR experimental and simulated spectra.*

Simulation of the composite ESR spectra with a set of particular components was used to determine a fraction of slow/fast components in spectra of nitroxyl radicals (in this case T=Tempol) correlated with nonuniformity in the nanostructured polymers (Fig.2). The best fit of experimental ESR spectra, was obtained assuming two paramagnetic species and a Gaussian lineshape corresponding to two positions with different magnetic parameters [7].

Therefore, the ESR spectra of nitroxide spin label in nanostructured polimers, consist of two spectral parts; a part marked with with an asterisk, has a line shape resembling the powder spectrum of the rigid matrix and is typical for slow anisotropic rotational motion, and an another part of the spin label is typical for faster isotropic rotational fluctuations [8, 9]. The part (marked with an asterisk) have a large rotational correlation times, which must be regarded as typical for slow rotation and indicate that these spin labels are located in rigid aggregates polymer chains. The second part, with small correlation times (fast rotation) can be attributed to localization of spin label molecules inside the structured cavity polymers.

Polyvinylformaldehyde was used as skeleton resin in surface and bulk nanostructured materials because of the good physico-chemical properties for multifunctional nanostructured systems [10]. The ATR-FTIR spectra show considerable differences in the region of 1000–3600 cm^{-1}, suggesting the existence of strong interactions between the two components in the complex (polyvinylformaldehyde and protoporphyrine).

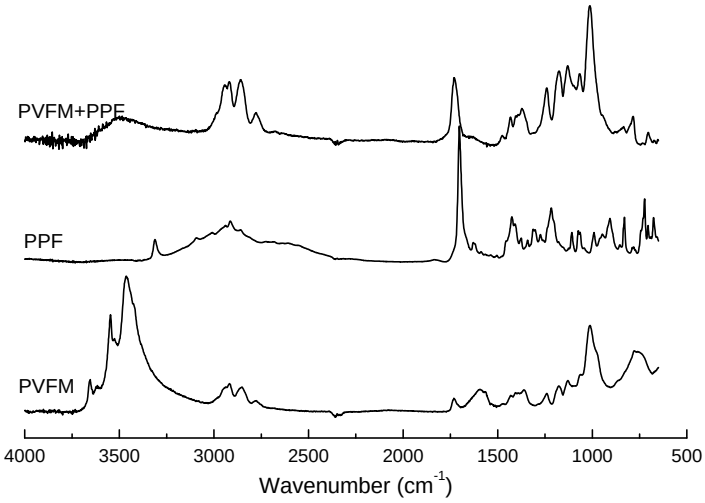

Fig. 3. *Attenuated total reflectance (ATR) spectrum of PVFM, PPF, PVFM+PPF.*

Polyvinylformaldehyde was used as skeleton resin in surface and bulk nanostructured materials because of the good physico-chemical properties for multifunctional nanostructured systems. The ATR-FTIR spectra show considerable differences in the region of 1000–3600 cm^{-1}, suggesting the existence of strong interactions between the two components in the complex (polyvinylformaldehyde and protoporphyrine). It was observed that before cross-linking there exist hydrogen bonds between PPF and the PVFM resin. In Figure 3 ATR-FTIR spectra are represented for the starting materials and the complex after the polymerization. Shifts in absorption bands indicate that the hydrogen bonds remain even after cross-linking. On the other hand, there were no considerable changes in the absorption peak intensities indicating that the number of hydrogen bonds has not been significantly [11,12]. Thus, hydrogen bonding between PVFM and PPF causes shifts in FTIR bands: a band of PVFM shifts from 1129 cm^{-1} to 993 cm^{-1}, a C-H vinyl in-plane bend band of PVFM shifts from 1432 cm^{-1} to 1425 cm^{-1}, and a hydroxyl stretching band of hydrogen bonded PVFM resin shifts from 3365 cm^{-1} to 3344 cm^{-1}. The shoulder around 3500 cm^{-1} is due to the free hydroxyl groups and it is slightly reduced in the cured blends.

Conclusions

ESR spectra with a set of particular components were used to determine the fraction heterogeneous components in spectra of nitroxyl radicals correlated with nonuniformity in the nanostructured polymers.

The ATR-FTIR spectra show some considerable differences in the region of 1000–3600 cm^{-1}. The broadening and shifting of the characteristic peaks in the ATR-FT-IR spectrum of polyvinylformaldehyde resin with protoporphyrine, as compared to the counterparts in their simple mixture, indicate the presence of certain intermolecular interactions between polyvinylformaldehyde resin with protoporphyrine in the nanostructured complex.

REFERENCES

1. Simina Dreve, E. Indrea, I. Bratu, Margareta Bako, Gh. Mihailescu, Liliana Olenic, Stela, Pruneanu, V. Znamirovschi, L. Barbu-Tudoran, *Studia Universitatis "Babes-Bolyai", Physica,* Special Issue, 1 (***2003***) 381-384.
2. L.J. Berliner (Ed.), *Spin labeling: theory and applications*, Vol. 2, Academic Press, New York (***1979***).
3. Damian,G., Miclăuş,V., *Radicali nitroxidici*, Ed. EFES, Cluj-Napoca, ***2001***.
4. Krist, Th., Mertens, P., Biersack, J.P., *Nucl. Instr. Meth.*, B2 (***1984***) 177-181.
5. P.C. Painter, M.M. Coleman, J.L. Koenig, *The Theory of Vibrational Spectroscopy and its Application to Polymeric Materia*ls, Wiley Interscience, New York, ***1982***.
6. C.P.Poole Jr., and H.A. Farach, in *Theory of Magnetic Resonance*, (John Wiley & Sons, New York, NY, ***1987***), pp 319-321.
7. G.Damian, O.Cozar, V.Miclaus, V.Znamirovschi, V.Chis, L.David, *Colloids and Surfaces A:* vol.137, 1, 1(***1998***).
8. S.Cavalu, G.Damian, M.Dânşoreanu, *Biophysical Chemistry, **2002***, 99:*2*:181-18.
9. S.Cavalu, G.Damian, *Biomacromolecules*, 4(***2003***)6, 1630-1635.
10. N. Chanunpanich, A. Ulman, A. Malagon, Y. M. Strzhemechny, S. A. Schwarz, A. Janke, T. Kratzmueller, and H. G. Braun, *Langmuir **2000***, *16,* 3557-3560.
11. Brass, I.; Brewis, D. M.; Sutherland, I.; Wiktorowicz, R. *Int. J. Adhes. Adhes.* ***1991***, 11, 150.
12. Kranz, G.; Lueschen, R.; Gesang, T.; Schlett, V.; Hennemann, O. D.; Stohrer, W. D. *Int. J. Adhes. Adhes.* ***1994***, 14, 243.

STUDIA UNIVERSITATIS BABES-BOLYAI, PHYSICA, XLIX, 3, 2004

NMR SPIN MANIUPULATIONB BY SEQUENCES OF RF PULSES IN STRONGLY INHOMOGENEOUS MAGNETIC FIELDS

M. TODICA[1] and B. BLÜMICH[2]

[1] *"Babes-Bolyai" University, Faculty of Physics, 400089 Cluj-Napoca, Romania*
[2] *Institute of Technical and Macromolecular Chemistry, University of Aachen, RWTH, Worringerveg 1, Aachen D-52056, Germany*

1. Introduction

The utilization of the sequences of radiofrequency (RF) pulses in NMR technique is one of the methods to produce selective excitation or selective saturation of the nuclear spins [1-4]. Standard selective excitation or saturation methods, in magnetic fields with linear gradients, are based on the use of a single or few high-power RF pulse with special shape, sinc, gauss, rectangle [5, 6]. The disadvantage of this method is the high-power request for excitation and the complexity of the equipment for generating pulses with special shape. Economy of the RF power can be obtained if the single high-power pulse is replaced by sequences of many short low-power RF pulses. Simplest sequences of RF pulses can be produced with simple equipment.

We tested some particularly RF pulse sequences for the spin manipulation in the strongly inhomogeneous magnetic field of the MOUSE, DANTE pulse sequence for selective excitation, and SPREAD pulse sequence for selective saturation. Experiments and simulation tested the efficiency of the excitation and the saturation.

2. Experimental

We used for our experiments an NMR-MOUSE sensor built on a bar shaped permanent magnet with the RF coil positioned on the top of the magnet [7, 8]. The experiments were performed at the resonance frequency 19.2 MHZ, corresponding to the surface induction of the magnetic field of the NMR-MOUSE. The volume averaged field gradient was approximately 20 T/m. The NMR experiments were controlled by a Brucker Minispec PC spectrometer for excitation and data acquisition. The transmitter and receiver system are characterized by a bandwidth of 0.5 MHz. We used a sample of natural rubber with the size of 2 cm x 2 cm and a thickness of 2 mm. For each experiment 100 scans were averaged for improvement the signal-to-noise ratio, with a recycling delay of 0.5s.

3. Results and discussion

a) Selective excitation

Selective NMR excitation can be obtained when the Larmor frequencies of the nuclear spins are spread over a desired spectrum of frequencies by placing the sample in a gradient magnetic field. Then the sample is irradiated with a RF pulse containing in its spectrum the desired frequencies to be excited. Only the nuclear

spins heaving the Larmor frequencies contained in the frequency spectrum of the RF pulse sequence are excited and contribute to the recorded signal.

We used for our experiments the DANTE pulse sequence because its simplicity and the possibility to generate this sequence with very simple electronics. This pulse sequence consists on **n** equidistant RF pulses of amplitude B_1 and length δ, separated by a delay time Δ (Fig. 1 a). The length and the amplitude of the component pulses are chosen so that each pulse produces a rotation of the magnetization in the rotating frame with an angle $\theta < 90°$, but the net flip angle of the entire sequence corresponds to 90° pulse, i.e. $\theta = \gamma B_1 \delta$ and $n\,\theta = 90°$ [9]. The excitation spectrum $X(\omega)$ consists of a comb of sidebands spaced by $\Delta\omega$, each spike in the comb having the form of a sinc function of width $\delta\omega \sim (n\,\Delta)^{-1}$ (Fig. 1 b).

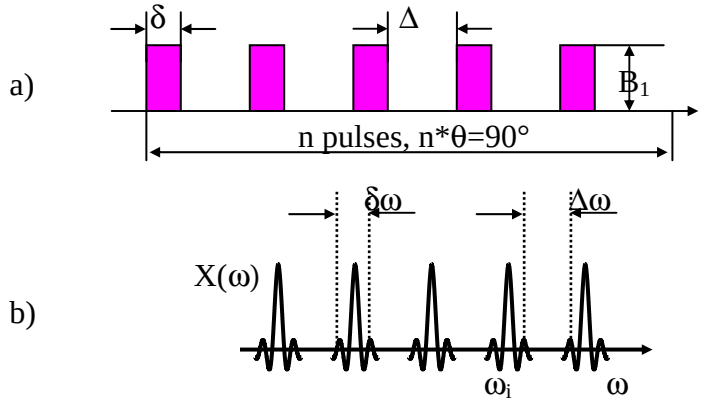

Fig. 1. a) Schematic representation of the DANTE pulse sequence. b) Excitation spectrum obtained by Fourier transformation of the DANTE pulse sequence. The spectrum consists of many excitation bands of width $\delta\omega$, centered at frequencies ω_i and separated by the frequency intervals $\Delta\omega$.

The efficiency of the selective excitation is maximum when DANTE-DANTE-echo pulse sequence is used (Fig. 2). This sequence is analogue to the standard Hahn-echo pulse sequence, but the $\pi/2$ and π pulses were replaced by DANTE pulse sequence [10]. The first DANTE pulse sequence produces selective excitation of the nuclear spins and flips the magnetization of the excited spins in the transverse plane. The second DANTE sequence contains 2 n pulses and achieves selective refocusing of the transverse magnetization at the same frequencies as the initial excitation. This second sequence also functions as a supplementary frequency filter and increases the selectivity of the entire sequence. Figure 3 shows the Fourier transform of the recorded echo $Y(\omega)$ for the sequence with the following parameters, $n = 5$, $\delta = 6\ \mu s$, and $\Delta = 6\ \mu s$. The excitation bands are neat and the appears to the correct frequencies, in agreement with the simulated spectrum. Compared with the standard Hahn-echo pulse sequence, the amplitude of the pulses of DANTE sequence is greatly reduced, that indicates an important economy of the RF power. The results obtained clearly indicate the possibility to produce selective excitation, at low RF power, in the strongly inhomogeneous magnetic fields.

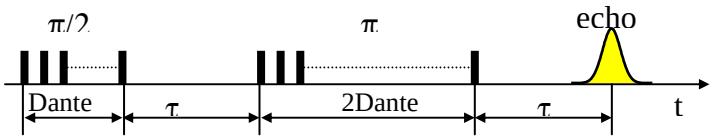

Fig. 2. *Schematic representation of the DANTE-DANTE-echo pulse sequence.*

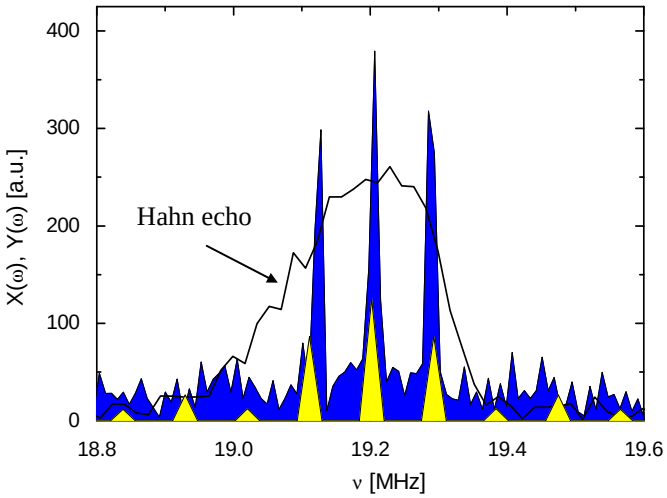

Fig. 3. *The spectrum of DANTE-DANTE-echo $|Y(\omega)|$, (black area), the calculated excitation spectrum $|X(\omega)|$, (light area), and the spectrum of Hahn echo recorded in similar conditions, (solid line). The sequence contains n = 5 pulses of length $\delta = 6\ \mu s$ and $\Delta = 6\ \mu s$.*

b) Selective saturation

Basically the saturation method builds on the same idea as selective excitation [6]. One RF pulse or pulse sequence is used to saturate the longitudinal magnetisation in a selected frequency range. Subsequently the remaining magnetisation is flipped into the transverse plane and is further manipulated by nonselective RF pulses to produce an echo. We used for selective saturation the SPREAD sequence sequence (*S*aturation *P*ulses with *Re*duced *A*mplitude *D*istribution) [11].

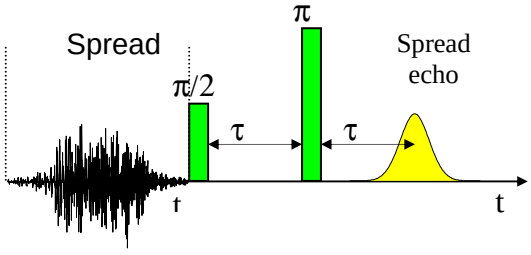

Fig. 4. *Schematic representation of the SPREAD-echo pulse sequence.*

This sequence consists of a quasi-random series of RF pulses with different amplitudes, generated on the basis of the desired spectrum by variation of the pulses phases under the constraint of minimum RF amplitude. We used this sequence to produce saturation of the nuclear spins in the strongly inhomogeneous magnetic field of the MOUSE. The effect of the saturation was tested by the following pulse sequence $(SPREAD)_{x}$- $(\pi/2)_x$ - τ - $(\pi)_{\psi}$-τ echo (Fig. 4). In this SPREAD echo pulse sequence τ is half the echo time. Following the application of the SPREAD pulse sequence the longitudinal magnetisation is saturated only in the specific frequency domains. The high power $\pi/2$ and π pulses have a large excitation spectrum and produce an echo only from the unperturbed spins. The Fourier transform of this echo $Y(\omega)$ shows signal only in the frequency windows unaffected by the saturation. The agreement between the spectrum of the recorded echo and the calculated spectrum $X(\omega)$ of the SPREAD sequence is good (Fig. 5). These results clearly demonstrate the possibility to produce selective excitation by sequences of randomly short RF pulses in strongly inhomogeneous magnetic fields.

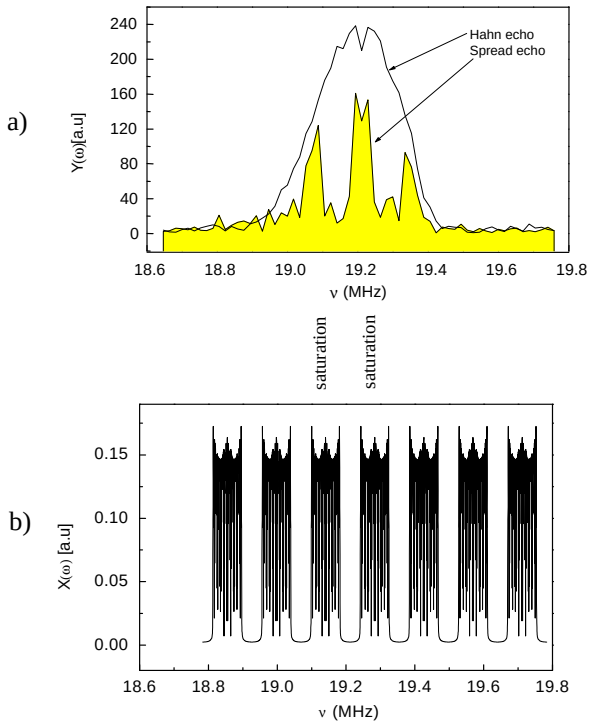

Fig. 5. *a) Comparison of the response spectra for the Hahn-echo (solid line) and the SPREAD-echo $Y(\omega)$ (shaded area) recorded under similar conditions. SPREAD sequence with the parameters $\delta = 1\ \mu s$ and $\Delta = 6\ \mu s$. b) The simulated spectrum $X(\omega)$ of the SPREAD sequence with the same parameters.*

4. Conclusions

Selective excitation in strongly inhomogeneous magnetic was obtained by sequences of short low-power RF pulses. DANTE pulse sequence is one of the simplest RF pulse sequence used for this purpose. The efficiency of the excitation is maximum when the DANTE-DANTE-echo sequence is used to obtain the spin-echo. The RF power requested for excitation is reduced when this sequence is used for excitation.

Selective saturation of parts of the sensitive volume in inhomogeneous magnetic fields can be achieved with SPREAD pulse sequence. The echo recorded after saturation shows signals only in the frequency domains unaffected by the saturation, in agreement with the calculated spectrum.

These experiments represent an important step towards the development of new simple and portable NMR equipment.

REFERENCES

1. R. Ernst, G. Bodenhausen, A. Wokaun, Principles of Nuclear Magnetic Resonance in one and two dimensions, Clarendon Press, Oxford, (1987).
2. Zhi-Pei Liang, Paul C. Lauterbur, Principles of magnetic resonance imaging, IEEE Press, New York, (2000).
3. B. Blümich, NMR imaging of materials, Clarendon Press-Oxford, (2000).
4. D. Demco, B. Blümich, Solid-State NMR Imaging Methods-Part I: Strong field gradients, Concepts in Magn. Reson. 12, 269-288, (2000).
5. P. T. Callaghan, Principles of Nuclear Magnetic Resonance microscopy, Clarendon Press, Oxford, (1991).
6. W. S. Warren, S. M. Mayr, Shaped pulses, Encyclopedia of Nuclear Magnetic Resonance, Vol. 7, 4275-4283, John Wiley and Sons, New York, (1996).
7. S. Anferova, V. Anferov, M. Adams, P. Blümer, N. Routley, K. Hailu, K. Kupferschläger, M. Mallet, G. Schroeder, S. Sharma, B. Blümich. Construction of the NMR-MOUSE with short dead time, Mag. Reson. Eng. 15, (2002), 15 – 25.
8. B. Blümich, V. Anferov, S. Anferova, M. Klein, R. Fechete, M. Adams, F. Casanova. A simple NMR-MOUSE with a bar magnet, Mag. Reson. Eng. 15, (2002), 255-261.
9. G. Bodenhausen, R. Freeman, G. A. Morris, J. Magn. Reson., A simple pulse sequence for selective excitation in Fourier Transform NMR, 23, 171-175, (1976).
10. M. Todica, R. Fechete, and B. Blümich, J. Magn. Reson., 164, 220-227, (2003).
11. H. Nilges, P. Blümer, J. Paff and B. Blümich, J. Magn. Reson., 105, 108-112, (1993).

STUDIA UNIVERSITATIS BABES-BOLYAI, PHYSICA, XLIX, 3, 2004

PROBING INTO THE LOCAL STRUCTURE OF GaAs / AlGaAs WITH NUTATION NMR / MAGNETIC RESONANCE FORCE MICROSCOPY (MRFM)

R.V.F. TURCU[*], P.KNIJN[**], G.E. JANSSEN[**], J. VAN BENTUM[**], E.R.H. VAN ECK[**], A.P.M. KENTGENS[**]

**Physics Faculty, "Babes-Bolyai" University, Cluj-Napoca, Romania*
***NSRIM Center, Radboud University, 6525ED Nijmegen, The Netherlands*

ABSTRACT. Magnetic Resonance Force Microscopy (MRFM) was originally proposed as a means of obtaining three-dimensional images of individual biological molecules, with Angstrom resolution [1,2]. MRFM also has important technological applications in material research such as imaging of (sub)surfaces in solids (down to nanometer resolution) and mapping dopant distribution in semiconductors [3]. Magnetic resonance force microscopy is a relatively new scanning probe microscopy technique that combines aspects of nuclear magnetic resonance (NMR) and atomic force microscopy (AFM) [4].

Introduction

Gallium-arsenide, a typical three-five group semiconductor, is one of the most important materials in electronic applications. However, although it is used in production of a wide range of devices, from semiconductors, lasers to high speed transistors. GaAs has a zinc-blende structure at the perfect portion. Because the crystal structure at the site of the each nucleus of GaAs is characterized by cubic symmetry, the electric field gradient (EFG) exist only in the imperfect portions where this symmetry is destroyed. The quadrupolar coupling is a parameter that offers information about lattice structure and defects as is probes the local symmetry of the nucleus under study. ^{27}Al, ^{69}Ga, ^{71}Ga, ^{75}As are quadrupolar nuclides with spin 5/2 respectively 3/2, and a normal NMR spectrum of this type of nuclide might consist of a main and four (^{27}Al) respectively two (69Ga, ^{71}Ga, ^{75}As) satellite lines. If the EFG is distributed, this often occurs in imperfect crystals, the spectral line width will be broadened. It is impossible to estimate and localized the number of imperfections by calculating the intensity loss [5], though it is often difficult to derive this latter value accurately. The fully ordered structures have been proposed as alternating AlAs and GaAs planes along, e.g., (001) (CuAu-type) or (111) (CuPt-type), respectively [see Figs. 1(b), 1(c)]. A clustering of Al (and Ga) has also been suggested.

Two-dimensional nutation NMR experiment, originally proposed by Samoson and Lippmaa [6,7] and specially MRFM nutation are efficient methods for high level of 3D structure characterizations of GaAs and $Al_xGa_{1-x}As$. In this material we present the measurements and the structural parameters (C_{qcc} – quadruploar coupling constant and η - asymmetry parameter) and 3D image obtained on GaAs – refernce sample and $Al_xGa_{1-x}As$ (with x= 0.3 and 0.5) by nutation NMR respectively MRFM.

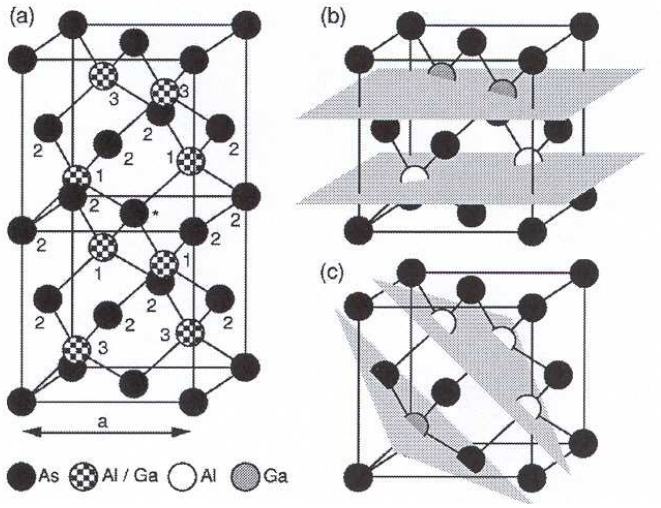

***Figure 1**. (a) Two unit cells of the fcc $Al_xGa_{1-x}As$ lattice. Filled spheres indicate anion (As) and checkered spheres cation sites (Al, Ga). The neighboring atoms the central As (asterisk) are numbered according to their coordination sphere. Coordination numbers and the distances are 4 and 2.45 Å for the first sphere (occupied by either Al or Ga), 12 and 4 Å for the second sphere (As), as well as 12 and 4.69 Å for the third sphere (Al, Ga). The lattice constant is given by a_x=5.66140+0.00809x Å (ref.10). (b) Fully CuAu ordered $Al_{0.5}Ga_{0.5}As$ with alternating AlAs and GaAs planes along the (001) direction. (c) CuPt ordered lattice where planes extend along (111)*

Experimental

The samples were grown by Metal Organic Vapor Phase Epitaxy (MOVPE) in a horizontal Aixtron 200 reactor at a grow temperature of 923 K and a rate of 1.8μm / h using trimethyl-gallium and trimethyl-aluminum as a group-III precursors and arsine as group-V precursor. Disilane was used as the dopant precursor to obtain n-type doping. Undoped GaAs wafers (2") with crystal orientation (100), 15° off towards <110> were used as substrates. A typical sample consisted of a 15nm Si-doped AlAs and a 5 μm undoped $Al_xGa_{1-x}As$ overlayer. The stoichiometry, used to identify the samples, was obtained from high resolution x-ray diffraction rocking curve measurement (HRXRD) immediately after growth. An epitaxial lift-of process [8] was applied to separate the $Al_xGa_{1-x}As$ from the substrate by selectively etching the intermediate Si-doped AlAs layer with HF solution [9]. The $Al_xGa_{1-x}As$ thin films (mg quantities, ~ 10^{18}spins) were then powderized for typical grain size of a few μm and transferred to quartz tubes for NMR measurements or glued on top of the micro size cantilever (silicon-nitrate; 320μm length) for MRFM measurements.

The nutation NMR experimentes were performed with a static high RF fields (>1MHz) probehead, in a Chemagnetics CMX-Infinity 600 MHz on an Oxford 600/89 magnet. The MRFM image was obtained using a 180 MHz MRFM spectrometer (Fig.3) on a 180/130 Oxford magnet with antivibration optical stand at the room temperature and $2*10^{-6}$ - $8*10^{-7}$ mbar pressure in the probhead.

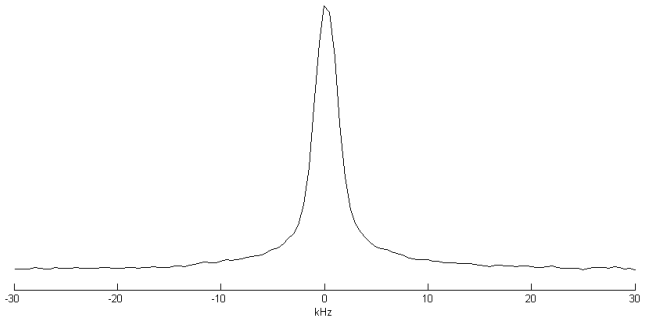

***Figure 2 (a)**. Single-pulse ^{69}Ga spectra of GaAs recorded at the room temperature and Larmor freqvency of ν_0=144.042 MHz*

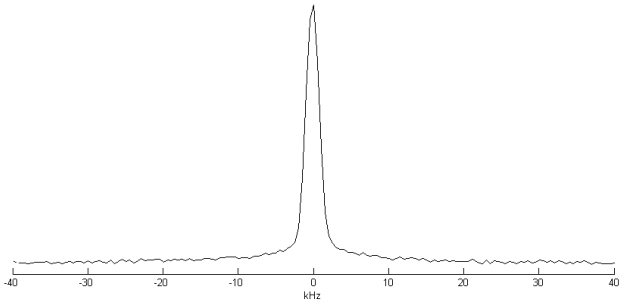

***Figure 2(b)**. Single-pulse ^{75}As spectra of GaAs recorded at the room temperature and Larmor frequency of ν_0=102.76 MHz*

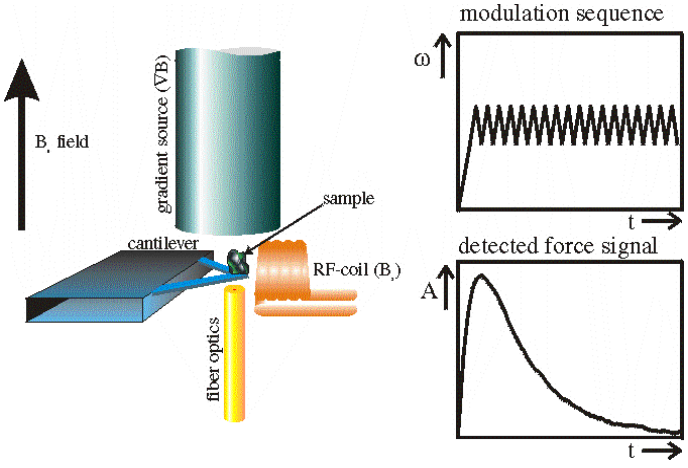

***Figure 3**. MRFM probhead setup. Sample on the cantilever, gradient source, RF-coil and optical fiber are presented.*

Results and Discussion

The first step for obtaining a complete structural characterization it was to record nutation spectra and then to extract the structure parameters. Figure 2.(a) and 2.(b) shows the ^{69}Ga (I=3/2) respectively ^{75}As (I=3/2) spectra of GaAs spectra recorded at a Larmor frequency of ν_0=144.042 MHz respectively ν_0=102.76 MHz (14.09T field). From the ^{69}Ga and ^{75}As nutation spectra of $Al_{0.5}Ga_{0.5}As$ we have calculate the quadrupolar coupling constant (C_{qcc}) and the asymmetry parameter (η) values presented in Table 1. The ^{69}Ga and ^{71}Ga spectra of $Al_{0.5}Ga_{0.5}As$ showed a single Gaussian peak with a linewidth 2.7kHz (^{69}Ga) and 2.9-3.3kHz (^{71}Ga), respectively. Furthermore it was verified by comparison with the GaAs reference that the observed resonance line intensities for this two nucleus contain the signal from all spins in the sample. This absence of the broad Ga line is consistent with the fcc lattice model of Fig.1.(a) which places both Al and Ga in a tetrahedral As cage. However here we have average signal from huge number of microcrystals and/or nanocrystals. To obtain structural information relevant for preparation of semi-conductor devices it is imperative to analyze thin layers using MRFM imaging and localized nutation spectroscopy. Figure 4 shows ^{27}Al image of an 8 μm thick $Al_{0.5}Ga_{0.5}As$ layer. The steps are 1.2μm width. From the nutation NMR we have obtained two distinct relaxation times (T_1), corresponding to ^{75}As[Ga_4] and ^{75}As[Al_4] configurations with MRFM we have confirm this situation and much more we can see in real space how the Al and Ga are distributed in sample. The white part represent ^{27}Al in our sample.

Table1.

$Al_{0.5}Ga_{0.5}As$ quadrupole coupling parameters and spin-lattice relaxation times (300 K).

Sample \Parameter	C_{qcc} (kHz)	η	T_1 (s)
^{69}Ga	520±20	>0.97	0.36±0.02
^{75}As[Ga_4]	610±20	>0.97	0.44±0.06
^{75}As[Al_4]	820±50	>0.88	0.39±0.08
^{75}As(other)	>9MHz		

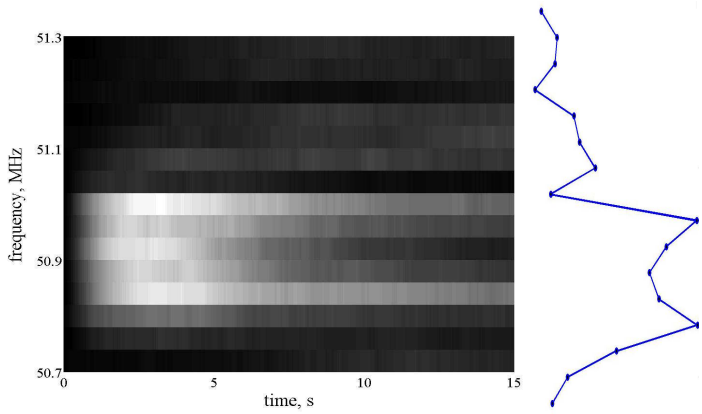

Figure 4. *^{27}Al MRFM image. 8μm sample high and ≈1.2μm step size*

Conclusion

We have presented a structural NMR / MRFM study on $Al_xGa_{1-x}As$ thin films. The locally symmetry $^{75}As[Ga_4]$ and $^{75}As[Al_4]$ sites are directly resolved in ^{75}As spectrum, while the other resonances from $As[Al_nGa_{4-n}]$ (n=1,2,3), although undetectable in the direct spectrum due to the large second-order quadrupolar broadenings, can be tracked by their solid echo.

The measured quadrupole coupling constants agree with the model of a number of random cation configuration in the second coordination as opposed to a strongly ordered structure where a dominant fraction with $C_{qcc}=0$ would be expected. We have presented the first MRFM image on $Al_xGa_{1-x}As$ thin film at the room temperature to confirm the Al and Ga distribution in our samples.

REFERENCES

1. [1] J.A. Sidles, Appl. Phys. Lett. **58**, 2854 (1991).
2. [2] J.A. Sidles, Phys. Rev. Lett. 68, 1124 (1992).
3. [3] D. Rugar and P. Grutter, Phys. Rev. Lett. 67, 699 (1991).
4. [4] D. Rugar, C.S. Yannoni, J.A. Sidels, Nature 360, 563 (1992).
5. [5] M.H. Cohen and F. Reif, Solid State Phys. 5 (1957) 321.
6. [6] A. Samoson and E. Lippmaa, Phys Rev. B, 28 (1983) 6567.
7. [7] A. Samoson and E. Lippmaa, Chem. Phys. Lett. 100 (1983) 205.
8. [8] Eli Yablonowitch, T. Gmitter, J.P. Harbison, and R. Bhat, Appl. Phys. Lett. 51, 2222 (1987).
9. [9] M.M.A.J. Voncken, J.J. Schermer, G.J. Bauhuis, P. Mulder, and P.K. Larsen, Appl. Phys. A (to be published)
10. [10] N.S. Takanahashi, in EMIS Datareviews Series: Properties of Aluminum Gallium Arsenide. Edited by S. Adachi (INSPEC, London, 1993), Vol. 7, p.3

STUDIA UNIVERSITATIS BABES-BOLYAI, PHYSICA, XLIX, 3, 2004

SPECTROSCOPIC CHARACTERISATION OF YTTRIUM OXIDE - BASED PHOSPHORS PREPARED BY SOL-GEL METHODS

LAURA MURESAN[1,2], ELISABETH-JEANNE POPOVICI[1], AMALIA HRISTEA[1,2], MARILENA VASILESCU[3] and IOAN SILAGHI DUMITRESCU[2]

1 -"Raluca Ripan "Institute for Research in Chemistry, 30 Fantanele,400294 - Cluj Napoca, Romania
2 - Faculty of Chemistry and Chemical Engineering, "Babes-Bolyai" University, 11 Arany Janos, 400028- Cluj Napoca,
3 -"I.G. Murgulescu" Institute of Physical Chemistry of Romanian Academy, 202 Spl. Independentei, Bucuresti.

ABSTRACT. Europium activated yttrium oxide based phosphors were prepared by the inorganic route of the sol-gel method, using the sequential reagent addition technique. The influence of some preparation conditions on the morpho-structural and photoluminescent properties of precursors and yttrium oxide based phosphors is presented.

Keywords: sol-gel, yttrium oxide, phosphors

INTRODUCTION

Red-emitting europium activated yttrium oxide based phosphors are components in many information display devices such as cathode ray tubes (CRT's), field emission displays (FED's), electroluminescent devices (EL) or plasma display panels (PDP's) [1]. As a result of technical importance this material has been studied with respect to the luminescent properties, morphological and structural characteristics [2,3]. The paper present the influence of some preparation conditions on the properties of some europium activated yttrium oxide (Y_2O_3: Eu) samples prepared by sol-gel method (inorganic route).

EXPERIMENTAL PART

The synthesis of Y_2O_3: Eu samples consist in the preparation of yttrium-europium precursors followed by phosphor thermal synthesis. Yttrium nitrate (Aldrich), europium nitrate, obtained from Eu_2O_3 (Aldrich) and HNO_3 (Panreac) as well as precipitation reagents i.e. ammonia (Panreac) or urea (Aldrich) or thiourea (Aldrich) were used for precursors preparation. In this purpose, the Y/Eu nitrate solution was added to the precipitating reagent solution. The precipitation was carried at 25 or 75 ^{0}C, under continuous stirring and the mixture pH was 4 ÷ 9. The precursor gels were maturated, separated by decantation, dried and milled. Phosphor synthesis was performed by firing the precursors for 2 hours at 900^{0}C, in argon flow (table 1).

Correspondence: ella-m@email.ro

Table 1.

Precursor and phosphor samples prepared in different synthesis conditions

Precursor code	Precipitation conditions				Phosphor code
	Reagent	pH	Temperature	Maturation time	
precL30	ammonia	6.0-9.1	25 ^{0}C	1 h	L30
precL32	ammonia	5.2-7.9	75 ^{0}C	1 h	L32
precL33	urea	5.2-5.4	75 ^{0}C	5 h	L33
precL34	urea	5.2-5.5	75 ^{0}C	5 h	L34
precL35	urea	5.9-5.2	75 ^{0}C	2 h	L35
precL36	urea	8.5-8.2	75 ^{0}C	5 h	L36
precL37	thiourea	8.8-8.2	75 ^{0}C	5 h	L37
precL38	ammonia	8.7-8.1	75 ^{0}C	5 h	L38

Precursors and phosphor samples were characterised by X-ray diffraction (XRD) patterns (SIEMENS D5000 powder diffractometer), morphology (JEOL-JSM-6300 Scanning Electron Microscope), thermal analysis (Perkin Elmer TGA7 Thermogravimetric Analyser) and FT-IR spectroscopy (SHIMADZU FTIR- 8300 Spectrometer). Photoluminescence (PL) was evaluated (Perkin Elmer 204 Fluorescence Spectrophotometer) and reffered to Y_2O_3: Eu (Kemira) standard.

RESULTS AND DISCUTIONS

Yttrium-precursors dopped with 5 mol% Eu were prepared by the inorganic route of the sol-gel method. Different precipitation reagents were used such as ammonia, urea or thiourea. The reagent addition was performed in *sequential addition technique* and the precipitation conditions (pH, temperature) were under controll.

The thermal analysis and FTIR spectroscopy illustrate the influence of precipitation conditions on the precursors quality (figures 1 and 2).

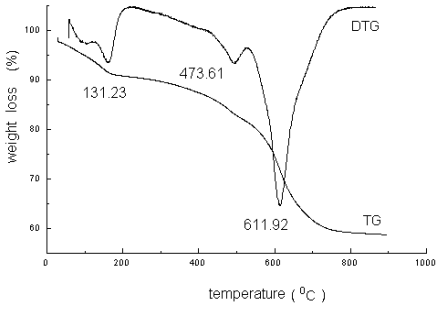

Fig. 1. DTG-TG curves of L33 sample

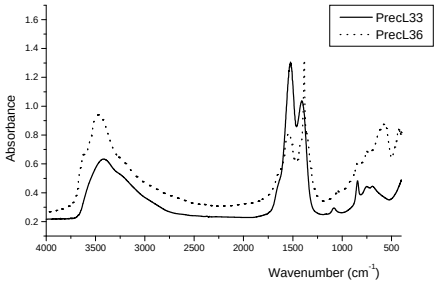

Fig. 2. FT- IR spectra of some precursors

Different FT-IR spectra were obtained for yttrium precursors prepared in various conditions. The specific IR absorptions are as follows: one strong narrow band at ~1384 cm^{-1} corresponding to NO_3^- impurity, indicating an insufficient precursor wash (PrecL36); broad bands at ~1518.64 cm^{-1}, ~1420 cm^{-1}, ~750 cm^{-1},~690 cm^{-1}, assigned to CO_3^{2-} (PrecL36, PrecL33); band at ~566 cm^{-1} corresponding to Y- O vibration; broad bands at 3450 cm^{-1} and ~3615 cm^{-1} for HO^- (precL36).

The thermal analysis (table 2) and the FT-IR data sugest that Y/Eu precursors are mainly hidroxy-carbonates that decompose according to the reactions 1-3.

Table 2.

Weight loos and the presumed formula for yttrium precursors

Code	Weight loss	Precursor formula	Preparation medium
precL30	31.30 %	$Y_2(CO_3)_3 \cdot 2.5\, Y(OH)_3 \cdot 1.6\, H_2O$	Ammonia / HO^-
precL32	34.41 %	$Y_2(CO_3)_3 \cdot 2.8\, Y(OH)_3 \cdot 2.7\, H_2O$	Ammonia / H^+
precL33	38.32 %	$Y_2(CO_3)_3 \cdot 1.8\, Y(OH)_3 \cdot 2.2\, H_2O$	Urea / H^+
precL34	39.35 %	$Y_2(CO_3)_3 \cdot 1.6 Y(OH)_3 \cdot 2.5 H_2O$	Urea / H^+
precL35	40.06 %	$Y_2(CO_3)_3 \cdot 0.7 Y(OH)_3 \cdot 0.9\, H_2O$	Urea / H^+
precL36	29.62 %	$Y_2(CO_3)_3 \cdot 5.9 Y(OH)_3 \cdot 3.3 H_2O$	Urea / HO^-
precL38	29.69 %	$Y_2(CO_3)_3 \cdot 4.0 Y(OH)_3 \cdot 3.4 H_2O$	Ammonia / HO^-

$$Y(OH)_3 \cdot yY_2(CO_3)_3 \cdot zH2O \rightarrow \quad Y(OH)_3 \cdot yY_2(CO_3)_3 + zH_2O \qquad (1)$$

$$Y(OH)_3 \cdot yY_2(CO_3)_3 \rightarrow \quad 0.5Y_2O_3 \cdot yY_2(CO_3)_3 + 1.5H_2O \qquad (2)$$

$$0.5Y_2O_3 \cdot yY_2(CO_3)_3 \rightarrow \quad (0.5+y)Y_2O_3 + 3yCO_2 \qquad (3)$$

Photoluminescence (PL) measurements show that, in spite of the relativelly low firing temperature, all Y_2O_3: Eu based phosphors exhibit red luminescence, as illustrated by the emission spectra; the characteristic emission peak is at ~ 611 nm (figure 3). Emission bands are associated to the following electronic transitions: $^5D_0 \rightarrow ^7F_0$ (~ 580 nm); $^5D_0 \rightarrow ^7F_1$ (~ 590 nm); $^5D_0 \rightarrow ^7F_2$ (~ 611 and 621 nm). Excitation spectra (figure 4) consist of many overlaped bands situated in the 280-550 nm range and reflect the involvement of both the host lattice and europium activator into the luminescence process. Luminescence peformances are influenced by the precipitating reagent. For instance, L30 (ammonia) shows only 50% of the brightness of L33 (urea).

Electronic microscopy put in evidence that the powdery phosphors are agglomerations of spherical particles whereas the fluffy precursors are formed mostly from flakes. Phosphor grains are smaller as compared with the corresponding precursor particles. Samples prepared with urea at different pH possess different particle size i.e. ~ 35 nm (L36 / HO^-) and ~200÷300 nm (L34 / H^+).

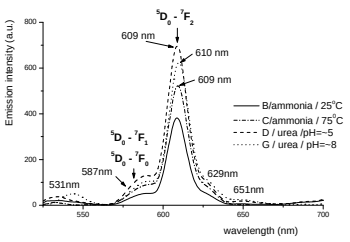

Fig. 3. Emission spectra for some Y_2O_3-Eu samples (λ_{exc}=365 nm)

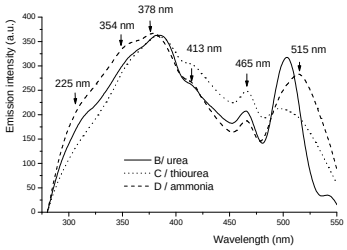

Fig. 4. Excitation spectra for some Y_2O_3-Eu samples (λ_{em}=611 nm)

XRD patterns illustrate that phosphor samples possess crystalline cubic structure. Depending on the precipitation reagent, powders with variable phase compositions and cristallinity were formed.

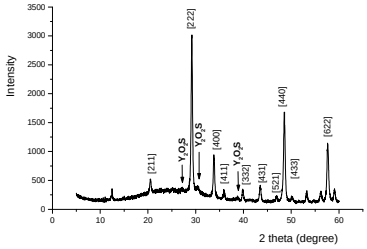

Fig. 5. XRD spectra of L37 sample

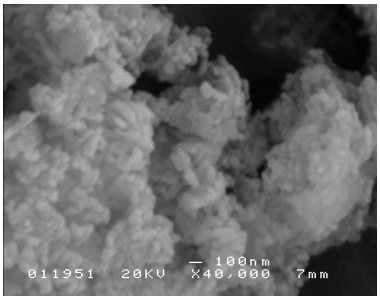

Fig. 6. SEM image of L36 sample

CONCLUSIONS

Europium activated yttrium oxide based phosphors were prepared by the inorganic route of the sol-gel method. By using the secvential reagent addition technique, yttrium hydroxicarbonate precursors were formed. The preparation conditions such as pH, temperature and the precipitation reagent type are factors that influence the morpho – structural and photoluminescence characteristics of phosphor.

Acknowledgements*: Department of Crystallography and Solid State Chemistry, Instituto de Ciencia de Materiales de Barcelona (Spain) and Romanian CNCSIS Grant 1303/2004.*

REFERENCES

1. M.H.Lee, S.G.Oh,"*Characterization of Eudoped Y_2O_3 nanoparticles preparedin nonionic reverse microemulsion in relation to their applicationfor FED",* J.Electrochem.Soc., 147(8), 2000, 3139
2. X. Jing, T. Ireland*,"Control of Y_2O_3:Eu speherical particle size, Assembly properties and performance for FED and HDTV", J. Electrochem Soc.,* 146(12), 1999, 4654;
3. D. Bolstad, A. Diaz*," Synthesis and characterization of nanocrystalline Y_2O_3:Eu phosphor", J.Chem. Ed. Chem.,* 79(9), 2002, 1101

STUDIA UNIVERSITATIS BABES-BOLYAI, PHYSICA, XLIX, 3, 2004

STUDIES ON EUROPIUM ACTIVATED YTTRIUM OXIDE PHOSPHOR PREPARED BY NON-CONVENTIONAL METHODS

AMALIA HRISTEA[1,2], ELISABETH-J.EANNE POPOVICI[1], LAURA MURESAN[1,2], RODICA GRECU[1], EMIL INDREA[3] and MARIANA VOICESCU[4]

[1]"Raluca Ripan" Institute for Research in Chemistry, 30 Fântânele, 400294 Cluj-Napoca, Romania
[2]Faculty of Chemistry and Chemical Engineering "Babes- Bolyai" University, 11 Arany Janos, 400028, Cluj Napoca,Romania
[3]National Institute for R &D of Isotopic and Molecular Technologies, Donath 30; 400295 Cluj-Napoca, Romania
[4]"I.G. Murgulescu" Institute of Physical Chemistry of the Romanian Academy, 202 Spl. Independentei, Bucureşti, Romania

ABSTRACT. The aim of this study is the synthesis of finely divided Y_2O_3:Eu powders for different opto-electronic devices. In this purpose, rare-earth oxide-based precursors were prepared by *homogeneous precipitation* route with urea, by using the reagent simultaneous addition technique. There are presented our preliminary results illustrating the influence of some preparative parameters on the quality of precursors and the corresponding luminescent materials.

Keywords: yttrium oxide, phosphors, luminescence

INTRODUCTION

Europium doped yttrium oxide (Y_2O_3:Eu) is a classical phosphor that is used as red emitting material for display manufacture. Usually, the synthesis of Y_2O_3:Eu phosphor proceeds by solid state reaction route.[1] Non-conventional methods were evaluated in order to prepare phosphors for the manufacture of high-resolution displays such as plasma displays panels, field emission displays or cathode ray tubes. Sol-gel methods spray pyrolysis, or combustion routes are currently used in order to prepare highly dispersed powders with good luminescence performances i.e. superior brightness and high cromatic purity. Depending on the phosphor synthesis route, nano- or micro-structured luminescent powders can be obtained.[2,3] The aim of this study is the synthesis of finely divided Y_2O_3:Eu powders for different opto-electronic devices. In this purpose, rare-earth oxide-based precursors were prepared by homogeneous precipitation route with urea, by *using the reagent simultaneous addition technique*. There are presented our preliminary results illustrating the influence of some preparative parameters on the quality of precursors and the corresponding luminescent materials.

EXPERIMENTAL PART

Europium activated yttrium oxide phosphor samples were prepared by homogeneous precipitation route, with the reagent simultaneous addition technique. In this purpose, yttrium/europium precursors were prepared and fired to give Y_2O_3: Eu samples. $Y(NO_3)_3$ and $Eu(NO_3)_3$ solutions with known concentration were prepared by dissolving Y_2O_3 and Eu_2O_3 in nitric acid. Equal volumes of rare earth nitrate and

Correspondence: amaliahristea@yahoo.com

urea solutions were simultaneously added into the diluted urea bottom solution. During the precipitation stage, the pH and the temperature were kept constant. The as-obtained precursors were maturated, centrifuged, washed with de-ionized water and dried. Yttrium/europium precursors were fired at 1150^0C, 1h, in air, closed system to form crystalline particles.

Precursors and/or phosphor samples were characterised by thermal analysis (Paulik–Erdely OD-102 Derivatograff), X-ray diffraction (DRON 3M Diffractometer; Cu Kα radiation) and FT-IR spectroscopy (JASCO 610 Spectrometer; KBr pellets technique). The photoluminescence (PL) properties of Y_2O_3: Eu samples were evaluated on the basis of emission and excitation spectra (204 Perkin Elmer Spectrofluorimeter).

RESULTS AND DISCUSSION

The synthesis of europium doped yttrium oxide was performed by homogeneous precipitation (HP) route. In this purpose, Y-precursors comtaining 2% mol Eu-precursors were prepared by the simultaneous addition technique of reagents and fired at high temperature. The precursor precipitation conditions are presented in table 1.

Table 1.

Precursor and phosphor samples prepared by HP technique

Precursor code	Precipitation conditions					Phosphor code
	Reagent ratio	*Reagents concentration*		$\overline{pH}$	*Temp.*	
		Y-Eu nitrate	*Urea*			
SG 1	1:1	0.1M	0.1M	7.5	80 ºC	S1
SG 2	1:1	0.1M	0.1M	8.2	80 ºC	S2
SG 3	1:2	0.1M	0.2M	8.0	80 ºC	S3
SG 4	1:4	0.1M	0.4M	8.0	80 ºC	S4

All precursors prepared by HP route are similar in composition as illustrated by FT-IR absorption spectroscopy. Figure 1 presents a typical precursor FT-IR spectrum in comparison with the corresponding phosphor. The most prominent IR absorption bands are: $\nu_{H\text{-}O}$~3500 cm^{-1}; ν_{NO2} ~1384 cm^{-1}; $\nu_{Y\text{-}OH}$ ~640 cm^{-1} in precursors and $\nu_{Y\text{-}O}$ ~574 cm^{-1} in the corresponding phosphors. FTIR spectroscopy suggests that during the homogeneous precipitation with urea, the reagent simultaneous addition technique leads to yttrium-europium basic nitrates precursors.

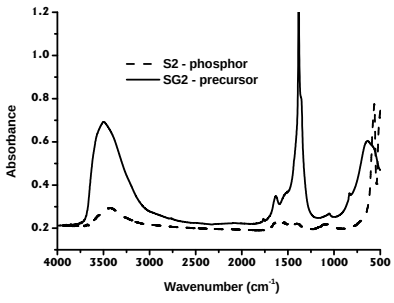

Figure 1. *FT-IR spectra of SG2-S2 samples*

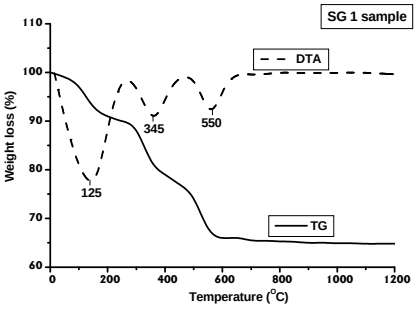

Figure 2. *TG-DTA curves of SG1 samples*

The thermal behavior of precursors is also similar, as suggested by TG-DTG-DTA data. The representative TG and DTA curves depicted in figure 2 illustrate that yttrium-europium precursor undergo a three-step weight loss. The presumed precursor formula is presented in table 2.

Table 2.

TG-DTA data and formula of precursor samples

Precursor code	Δw (%)		DTA peaks	Formula
SG 1	10	35	125^{0}C: endo	$Y(NO_3)_3 \cdot 8.5Y(OH)_3 \cdot 9.0H_2O$
	15		345^{0}C: endo	
	10		550^{0}C: endo	
SG 2	11	38	140^{0}C: endo	$Y(NO_3)_3 \cdot 6.0Y(OH)_3 \cdot 7.6H_2O$
	14		340^{0}C: endo	
	13		560^{0}C: endo	
SG 3	12	35	145^{0}C: endo	$Y(NO_3)_3 \cdot 7.3Y(OH)_3 \cdot 9.8H_2O$
	12		350^{0}C: endo	
	11		555^{0}C: endo	
SG 4	12	36	145^{0}C: endo	$Y(NO_3)_3 \cdot 6.5Y(OH)_3 \cdot 9.0H_2O$
	12		340^{0}C: endo	
	12		545^{0}C: endo	

On basis of FT-IR spectra and thermal analysis data, the following decomposition mechanism is proposed for europium-yttrium (RE) precursors:

$$xRE(OH)_3 \cdot yRE(NO_3)_3 \cdot zH_2O \rightarrow xRE(OH)_3 \cdot yRE(NO_3)_3 + zH_2O$$
$$xRE(OH)_3 \cdot yRE(NO_3)_3 \rightarrow x/2RE_2O_3 \cdot yRE(NO_3)_3 + 3x/2H_2O$$
$$x/2RE_2O_3 \cdot yRE(NO_3)_3 \rightarrow (x+y)/2RE_2O_3 + 3yNO_2 + 3y/4O_2$$

The firing of yttrium-europium basic nitrates precursors generates Y_2O_3: Eu powders that, under UV excitation, emit strong red luminescence. PL properties are in agreement with the literature data. Emission spectra (figure 3) consist in some characteristic narrow emission bands that could be assigned to certain electronic transitions: $^5D_0 \rightarrow {}^7F_1$ (~ 590 nm); $^5D_0 \rightarrow {}^7F_2$ (~ 610 nm) ; $^5D_0 \rightarrow {}^7F_3$ (~ 650 nm). Excitation spectra put in evidence the strong sensitivity of phosphors at ultraviolet radiation of about 254 nm (figure 4).

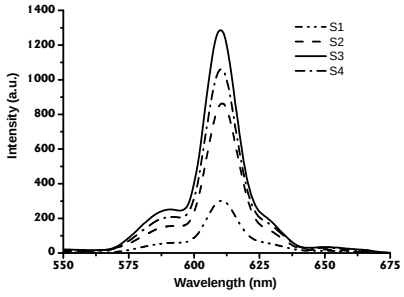

Figure 3. *Emission spectra of Y_2O_3: Eu samples (λ_{exc}= 254 nm)*

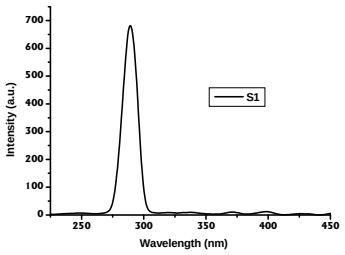

Figure 4. *Typical excitation spectrum of Y_2O_3: Eu sample (λ_{em}= 611 nm)*

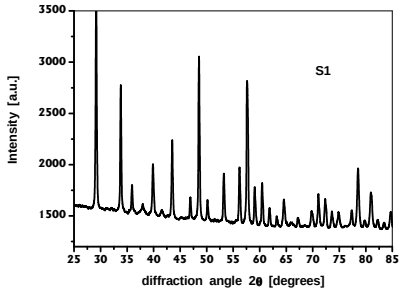

Figure 5. *XRD spectra for S1 sample*

X-ray diffraction patterns illustrate that all Y_2O_3: Eu phosphor samples possess cubic crystalline structure whereas the corresponding precursors are amorphous. The thermal synthesis conditions (1h; 1150℃) are in the favor of the crystalline organisation of the host lattice – activator system (figure 5).

CONCLUSIONS

The precipitation technique, reagent ratio and concentration and medium pH are extremely important for the synthesis of Y_2O_3: Eu phosphor through the ureea homogeneous precipitation route. The reagent simultaneous addition techniques lead to yttrium-europium basic nitrates precursors that, in our thermal synthesis conditions, assure an efficient incorporation of europium ions into the cubic crystalline lattice of yttrium oxide phosphor.

Acknowledgements:

The financial support for this research was provided by the Ministry of Education, Research and Youth of Romania (CNCSIS Grant 1303).

REFERENCES

1. F. Zhang, H. Paris, C. Summer *"Synthesis and characterization of $Y_2O_3:Eu^{3+}$ powder phosphor by a hydrolysis technique"*, J. Mater. Res. 1998, 13, 2950-2955.
2. G. Blasse, B. C. Grabmaier, *"Luminescence materials"*, 1994, Berlin-Heidelberg.
3. D. B. Bolstad, A. L. Diaz, *"Synthesis and characterization of nanocrystalline $Y_2O_3:Eu^{3+}$ phosphor"*, J. of Chemical Education, 2002, 79, 1101-1104.

STUDIA UNIVERSITATIS BABES-BOLYAI, PHYSICA, XLIX, 3, 2004

EPR INVESTIGATIONS ON SOME CALCIUM-PHOSPHATE GLASSES WITH VANADIUM IONS

[*]N. VEDEANU, O. COZAR, I. ARDELEAN

Department of Physics, Babes-Bolyai University,
1 Kogalniceanu Str., 400084 Cluj-Napoca, Romania,
nvedeanu@phys.ubbcluj.ro

ABSTRACT. EPR and IR investigations were performed on $xV_2O_5(100-x)[P_2O_5 \cdot CaF_2]$ glass system with 0.5≤x≤40mol%. The changes observed in the EPR spectra of these glasses are explained supposing a superposition of two EPR signals, one with a well-resolved hyperfine sructure typical for isolated V^{4+} ions and the other one consisting in a broad line without hyperfine sructure characteristic for clustered ions. These ions are coupled by dipole-dipole interaction until x= 5mol% and by superexchange interaction at high content of oxide vanadium.

INTRODUCTION

Vanadyl ion(VO^{2+}) incorporated in the glass systems as a spectroscopic probe have been investigated by several researchers in order to characterise the glass structure[1-11]. The results involve many particular aspects as the geometry of the structural units of the glass network, the character of the chemical bonds in glasses or the local symmetry(coordination polihedra) of transitional metal ions.

Hosono et al.[5,6] and Bogomolova et al.[4] found two sets of hyperfine structure(hfs) for vanadyl ions in some phosphate glasses containing Mg^{2+}, Zn^{2+}, Be^{2+} and Cd^{2+} as modifier cations whereas only a single kind of hfs for other phosphate glasses with Na^{+}, Li^{+}, Ca^{2+}, Pb^{2+}, Sr^{2+} and Ba^{2+} was found.

Shames et al. [9] have reported a superposition of hfs signals from three magnetically nonequivalent VO^{2+} centers in O-phenantroline sol-gel differing in their parameters and concentrations.

Phosphate glasses usually possess low melting temperature, high thermal expansion coefficient, low glass transition temperature and are very important from the point of view of technological applications [12,13]. The developement of inorganic phosphate glasses has attracted both academic and industrial interest in recent years[14,15]. V_2O_5 is one of the transition metal oxides which is of more interest in the contemporary and emerging technology or application in the fields like micro-electronics, solid state ionics, opto-electronics, etc. [16].

The vanadyl ion VO^{2+} is known to form an octahedral oxygen complex and the V=O direction is the predominant axial direction.

The present work is an EPR study on $xV_2O_5(100-x)[P_2O_5 \cdot CaF_2]$ glasses with 0.5≤x≤40mol%, following the influence of V_2O_5 content on the local order, the interactions between vanadium ions and a possible influence of the fluorine on the EPR spectrum of VO^{2+}.

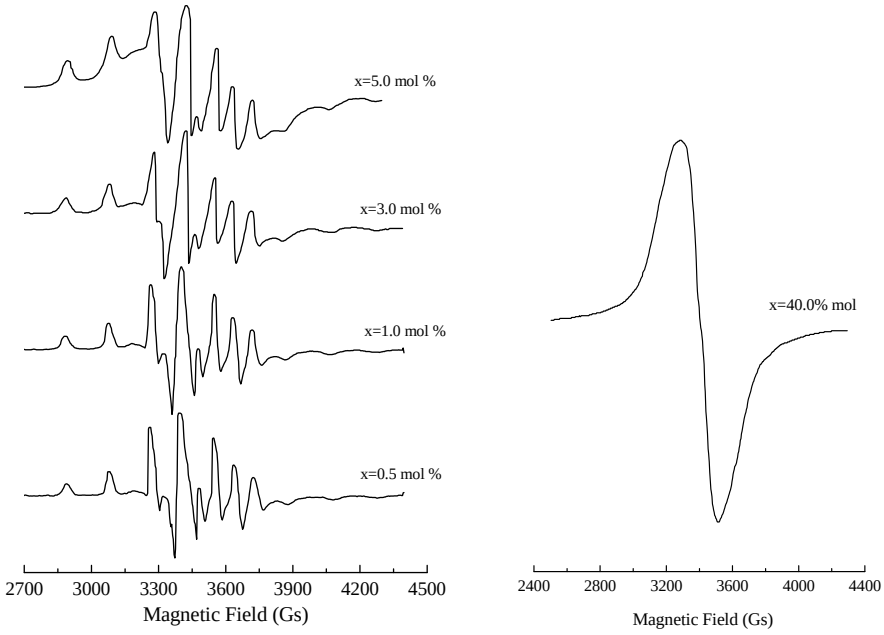

Fig. 1. *EPR spectra of the $xV_2O_5(100-x)[P_2O_5{\cdot}CaF_2]$ glasses*

EXPERIMENTAL

In order to obtain the $xV_2O_5(100-x)[P_2O_5{\cdot}CaF_2]$ glass system ($0.5 \leq x \leq 40$mol%) was first prepared the matrix $[P_2O_5{\cdot}CaF_2]$ by mixing $(NH_4)_2HPO_4$ with CaF_2 and melting these admixtures at 1000ºC for 12 minutes in a sintered corundum crucible using a technique previously reported[19]. The matrix was crushed and the resulting powder was mixed with appropriate amounts of V_2O_5 before final melting at 1250ºC for 30 minutes. The melted glasses were under cooling at room temperature by quickly pouring onto stainless steel plates.

The EPR measurements were performed at 9.4 GHz(X-band) at room temperature using a JEOL-JES 3B spretometer.

RESULTS AND DISCUSSION

The EPR spectra obtained for the studied glasses with a small content of V_2O_5($x<10$mol%) show a well-resolved hfs typical for isolated vanadium ions in a C_{4v} symmetry, present as vanadyl ions (Fig. 1).

The appropriate spin Hamiltonian for these spectra is:

$$H_S = \beta_0 g\ B_z S_z + \beta_0 g_\perp (B_x S_x + B_y S_y) + A_{\parallel} S_z I_z + A_\perp (S_x I_x + S_y I_y) \qquad (1)$$

where: β_o = Bohr magneton; g and $g_\perp$ = components of g tensor; B_x, B_y, B_z = components of the magnetic field; S_x, S_y, S_z = components of the electron spin operator; I_x, I_y, I_z = components of the nucleus spin operator; $A_\parallel$ and $A_\perp$ = principal components of the hyperfine coupling tensor.

The values of the magnetic field for the hfs peaks from the parallel and perpendicular absorbtions are given by the eqs. (2) and (3)[10]:

$$B\ (m) = B\ (0) - A_{||}\ m - [(63/4) - m^2]\ A_{\perp}^2/2B_{||}(0) \quad (2)$$

$$B_{\perp}(m) = B_{\perp}(0) - A_{\perp}\ m - [(63/4) - m^2](A^2 + A_{\perp}^2)/4B_{\perp}(0) \quad (3)$$

where: m = magnetic nuclear quantum number for vanadium nucleus having the following values: ±7/2, ±5/2,±3/2 and ±1/2;

$$B\ (0) = hv/g\ \beta_o \quad (4)$$

$$B_{\perp}(0) = hv/g_{\perp}\beta_o \quad (5)$$

where v is the microwave frequency.

Spin- Hamiltonian parameters of VO^{2+} ions determined from the observed positions of hfs lines and eqs.(2-5) are given in table 1.

Tab.1.

EPR parameters of VO^{2+} ions in $xV_2O_5(1-x)[P_2O_5 \cdot CaF_2]$ glasses

x(mol%)	$g_{||}$	$g_{\perp}$	$A_{||}$ $[10^{-4}\ cm^{-1}]$	$A_{\perp}$ $[10^{-4}\ cm^{-1}]$
0.5	*1.945*	*1.986*	*152.6*	*58.9*
1	*1.932*	*1.981*	*157.9*	*59.2*
3	*1.948*	*1.989*	*152.4*	*60.3*
5	*1.950*	*1.987*	*154.5*	*60.4*

The values of of these parameters confirm that the vanadium ions exist in the studied glasses as VO^{2+} ions in octahedral coordination with a tetragonal compression, particularly C_{4v} symmetry. The V^{4+} site in the VO^{2+} ion forms coplanar bonds with each of the four oxygen ligand(xOy plane). The vanadyl oxygen is attached axially above the V^{4+} site along the z-axis (V=O bond) while the sixth oxygen forming the O-VO_4-O unit lies axially bellow the V^{4+} site. The predominant axial distortion of the VO^{2+} octahedral oxygen complex along V=O direction may be the reason for nearly equal g and A values for all the glass samples[10].

The shape of the spectra are modified with the increasing of vanadium ions content. This modification consists in the partial dissapearance of the vanadyl hfs and the appearance of a broad line due to the clustered ions coupled by dipole-dipole interaction. At high content of vanadium ions (x > 8 %) the superexchange interaction prevails between clustered ions.

The EPR spectra may be regarded as the superposition of two EPR signals; one with a well resolved hfs typical for isolated VO^{2+} ions and another one consisting in a broad line typical for associated (clustered) vanadium ions.

The composition dependence of the linewidths of the broad line ΔB characteristic for clustered ions is given in Fig. 2. It increases with V_2O_5 content until x ≈ 5 mol% suggesting that the dipole – dipole interaction prevail among V^{4+} ions and decreases for the V_2O_5 content over x > 5 mol% showing that in this range the superexchange interaction prevails between resonance centers [11].

In order to give attention to the effect of fluorine on the VO^{2+} complex, it is possible that one fluorine atom to coordinate at V^{4+} ion in the transposition with respect to the "yl" oxygen. This fact leads to the weakness of the V=O bond and consequently

to the decrease in the tetragonal character of the vanadium coordination polyhedra. The most probable is that the fluorine atom substitutes the sixth oxygen. In consequence the possible superhyperfine coupling with the fluorine nucleus leads to the broadening of the vanadium hfs lines[18].

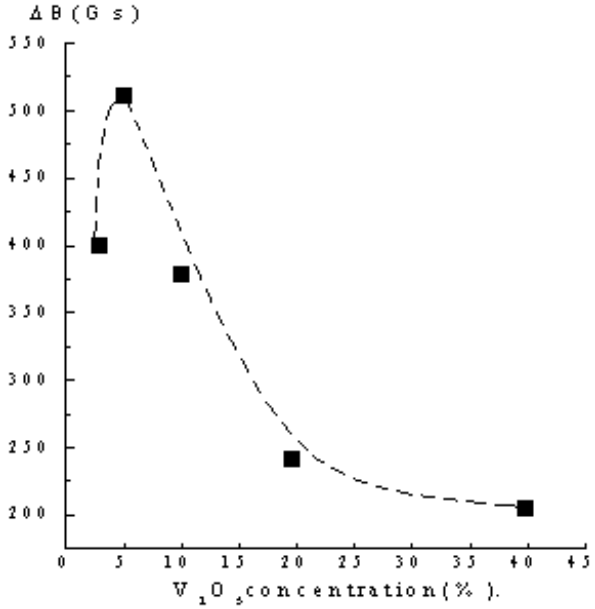

Fig. 2. *Dependence of the linewidth with V_2O_5 concentration*

CONCLUSIONS

EPR investigations on $xV_2O_5(100-x)[P_2O_5 \cdot CaF_2]$ glass system inform about the structural effect of V_2O_5 on the calcium-phosphate glass matrix. The EPR spectra may be considered as the superposition of two EPR signals; one with a well resolved hfs typical for isolated VO^{2+} ions and another one consisting in a broad line typical for associated vanadium ions. For x >5 mol% the superexchange interactions prevails between the paramagnetic centers.

A careful analysis on EPR spectra gives information also about the randomness of the glassy network which contains fluorine ions. They can substitute the sixth oxygen atom from the transposition with respect to the "yl"oxygen (V=O).

REFERENCES

1. G. Hochstrasser, *Phys. Chem. Glasses* 7, 178 (1966).
2. H. Toyuki, S. Akagi, *Phys. Chem. Glasses* 13, 15 (1972).
3. A. Paul, F. Assabghy, *J. Mater. Sci* 10, 613 (1975).
4. L. D. Bogomolova., V. N. Jackin., V.N. Lazukin, T. K. Pavlushkina., V. A. Shmuckler, *J. NonCryst. Solids* 28, 375 (1978).

5. H. Hosono, H. Kawazoe, T. Kanazawa, *J. NonCryst. Solids* 33, 125 (1978).
6. H. Hosono, H. Kawazoe, T. Kanazawa, *J. NonCryst. Solids* 37, 427 (1980).
7. V. P. Seth, S. Gupta, A. Jindal, S. K. Gupta, *J.NonCryst.Solids* 162, 263 (1993).
8. D. Prakash, V.P. Seth, I. Chand, P. Chand, *J.NonCryst.Solids* 204, 46 (1996).
9. A. Shames, O. Lev, B. Iosefzon-Kuyavskaya, *J.NonCryst.Solids* 163, 105 (1993).
10. V. R. Kumar, R. P. S. Chakradhar, A. Murali, N. O. Gopal, J. L. Rao, *Int. J. Modern Physics B*, 17, 3033 (2003).
11. O. Cozar, I. Ardelean, V. Simon, L.David, V. Mih, N. Vedeanu, *Appl. Magn. Reson*., 16, 529 (1999).
12. L. D. Bogomolova, T. K. Pavlushkina, A. V. Roshchina*, J.NonCryst.Solids*,58,99 (1983).
13. Y. He, D. E. Day, *Glass Technol*. 33, 214 (1992).
14. M. J. Weber, *J.NonCryst.Solids*, 123, 208 (1990).
15. Y. B. Peng, , D. E. Day*, Glass Technol*., 32, 166 (1991).
16. A. Talledo, C. G. Granqvist, *J. Appl. Physics* 77, 4655 (1995).
17. I. Ardelean, O. Cozar, G. Ilonca*, J.NonCryst.Solids* 68, 33 (1984).
18. G. Scholz, R. Stosser, S. Sebastian, T. Grande, S. Aasland, M. Nofz, *Ber. Bunsenges. Phys. Chem.* 100, 1617 (1996).

STUDIA UNIVERSITATIS BABES-BOLYAI, PHYSICA, XLIX, 3, 2004

RAMAN SPECTROSCOPY ON SOME PHOSPHATE GLASSES WITH MOLYBDENUM IONS

D.A. MAGDAS, O. COZAR, I. ARDELEAN, D. MANIU, L. DAVID

Faculty of Physics, Babes-Bolyai University,
400084 Cluj-Napoca, Romania,
amagdas@phys.ubbcluj.ro

ABSTRACT. The structure of $xMoO_3 \cdot (100-x)[2P_2O_5 \cdot PbO]$ glass system with $0 \le x \le 5$ mol% was investigated by Raman spectroscopy.

The characteristic bands of these glasses due to the stretching and bending vibrations were identified and analysed by the increasing of MoO_3 content. This fact allowed us to identify the specific structural units which appear in these glasses and thus to point out the network modifier role of the molybdenum oxide.

Introduction

The most common glasses are formed by mixing "glass forming oxides" (typically, SiO_2, B_2O_3, P_2O_5) with "modifier" metal oxides. The oxygen from this metal oxide becomes part of the covalent glass network by creating new structural units. Changing the concentration units can control many glass properties. The structural characterization of glasses with competitive network formation is a challenging task, because we have to determine whether the coordination of a glass former changes when mixed with another one, and how the modifiers oxygens are distributed among the units of the different species [1].

Phosphate glasses are of technological interest due to their several unique properties, such as high thermal expansion coefficient, low viscosity resulting in low melting and softening temperatures, UV transmission and other optical properties, and electrical conduction. The technological importance of these glasses requires a detailed understanding of the molecular and structural chemistry in order for glasses to be designed for particular applications [2].

Phosphorus is four-coordinated in the phosphate glasses and the modifier decreases the number of bridging oxygens in a (PO_4) unit, while increasing its negative charge. In order of increasing negative charge the phosphate units are: the neutral "branching unit", with three bridging oxygens and one double bond P=O bond; the "middle unit" $-O-PO_2^-$ -O-, often called the metaphosphate unit; the "end unit" $-O-PO_3^{2-}$ and the "monomer PO_4^{3-} or orthophosphate unit [1].

The structure of phosphate glasses has been investigated by different spectroscopies, such as infrared and Raman scattering. The phosphate network is based on corner sharing PO_4 units that form chains, ring or isolated PO_4 groups [3].

The role of PbO is known [4] to be unique, because it plays a dual structural role both as network modifier [5] and as a network former [6,7]. Similarly, it is well-known [6,8] that P_2O_5 exhibits a pronounced tendency to form a glass in

two- or three-dimensional networks. In these networks, the coordination number of network-forming phosphorus P atom is typically low. The bonding in these oxides is predominantly covalent the bonds being strong and directional [9].

In this work the glass system $xMoO_3 \cdot (100-x)[2P_2O_5 \cdot PbO]$ are characterized by Raman spectroscopy, in order to understand the role of molybdenum oxide on the local structure.

Experimental Details

The starting materials used in the present investigation were $(NH_4)_2HPO_4$, PbO and MoO_3 of reagent grade purity. The samples were prepared by weighing suitable proportions of the components, powder mixing and mixture melting in sintered corundum crucibles at 1250^0C for five minutes. The mixtures were put into the furnace directly at this temperature. The melts were poured onto stainless steel plates.

The Raman spectra have been recorded on a GDM 1000 double monochromator instrument equipped with a Coherent Innova 90 argon-ion laser. The 514 nm emission line was used with an incident power of about150 mW. A 90^0 geometry and a spectral slit width of 3-4 cm^{-1} were used for collecting the scattered light. The spectra were recorded without polarizer in the gathering optics. The measurements were carried out at room temperature.

Results and Discussion

The Raman spectrum for x=0 mol% shows the characteristic bands of $2P_2O_5 \cdot PbO$ matrix (Fig.1). So, the band from 696 cm^{-1} is attributed to the P-O-P stretching vibration. The P-O stretching vibration arises at 1068 cm^{-1}, whereas the O-P-O stretching vibration appears at 1174 cm^{-1}. The O-P-O asymmetric stretching vibration is present at 1220 cm^{-1} [1,10]. It is know that PbO oxide acts as modifier or network former in glass matrix. The presence in the Raman spectra of the two bands at 300 cm^{-1} and 380 cm^{-1} may be attributed to the presence of PbO in these glasses. The 380 cm^{-1} band increases in intensity and is shifted to high wavenumber (414 cm^{-1}) with the MoO_3 content. This fact could be explained by the appearance of the Pb-O-Mo bands in these glasses, as in the case of $Pb\text{-}O\text{-}Ga_2O_3\text{-}SiO_2$ system [11]. The other bands from 300 cm^{-1} remain almost constant with the increase of MoO_3 content. On the other hand the presence of the PbO influences the structure of the P_2O_5 [1,10] which are manifest in the shifts and shape changes of the specific vibrational bands.

The position and shape of these bands have been found to be sensitive to the phosphate chain length and the network modifier species.

The shapes of the most bands of the Raman spectra are strongly influenced by the MoO_3 content. These changes occur even at low concentrations of the MoO_3 ($x \leq 1$ mol%).

For x=0.5mol% the P-O-P stretching vibration and the O-P-O stretching vibration increase in intensity and are shifted to lower wavenumbers at 693 cm^{-1} and 1153 cm^{-1} respectively. The P-O stretching vibration is also shifted to lower wavenumbers (1053 cm^{-1}), whereas the O-P-O asymmetric stretching vibration is shifted at higher (1244 cm^{-1}) wavenumbers.

The shape of the x=1 mol% spectrum is related to the x=0.5 mol% spectrum. Nevertheless, a further shift to lower wavenumbers of the P-O-P and O-P-O stretching vibrations is observed.

In the Raman spectrum for x=3 mol% the MoO_3 content acts as a strong modifier of the glass network. The changes in the spectral shape become more evident related to the previous spectra. The O-P-O stretching vibration appears shifted to lower wave numbers at 1145 cm^{-1}. The P-O-P stretching vibration decreases strongly in intensity, appearing as a weak band at 701 cm^{-1}.

In the case of x=5mol% spectrum the O-P-O stretching vibration decreases in intensity and shifts to higher wavenumbers at 1150 cm^{-1} whereas the P-O-P stretching vibration almost disappears.

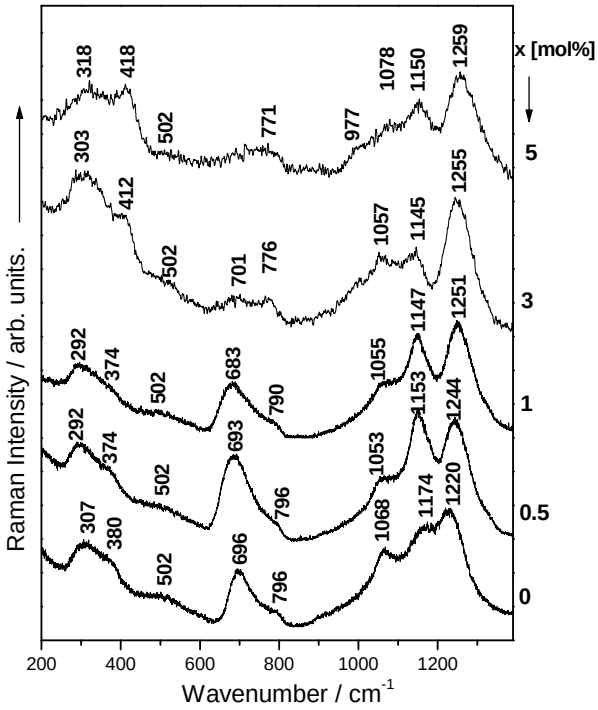

Fig.1. *The Raman spectra of $xMoO_3 \cdot (100-x)[2P_2O_5 \cdot PbO]$*

There are two frequency regions in the Raman spectra that contain information about the structure of the phosphate glasses. The frequency bands region 600-850 cm^{-1} is characteristic for the in-chain P-O-P stretching vibrations. The bands from the 950-1400 cm^{-1} region are due to the out-of-chain $-PO^{2-}$ stretching vibrations [2]. In the frequency region of P-O-P vibration, a main band near 700 cm^{-1} and a shoulder at ~ 800 cm^{-1} appear too (Fig. 1.).

The asymmetric band at ~ 700 cm^{-1} is assigned to the symmetric stretch of in-chain P-O-P vibration in the long-chain phosphate species. It has been previously observed in similar phosphate glasses that this band increases in frequency as the chain length decreases [2]. The shift in the frequency of the band is attributed to a change in the in-chain P-O-P bond angle depending on the effect of the network

modifier on phosphate glass structure [2]. The larger wavenumber of the band is a result of the smaller P-O-P bond angle, which results from shorter phosphate chain length or smaller metal cation size [2]. The phosphate chain length is shorter in the phases with high MoO_3 content due to the depolymerization of phosphate structure.

The shoulder near 800 cm^{-1} may be due to very short phosphate chain units or ring structures that are know to be increasingly important in the composition region between the ultraphosphate and metaphosphate compositions.

The change in the wavenumber and width of the bands depending on the kind and concentration of network modifiers in phosphate glasses has also been investigated and reported by others authors [12,13]. Rouse et al. [14] have pointed out that the decrease of the O-P-O stretching frequency is essentially due to an increase of the O-P-O angle and to larger metal-oxigen force constant [1].

Conclusions

The shape of the Raman spectra is influenced by the presence of molybdenum oxide in the studied glasses.

At low concentration of MoO_3 ($x \leq 1$ mol%) the P-O-P and O-P-O stretching vibrations increase in intensity and are shifted to lower wavenumbers, at 693 cm^{-1} and 1153 cm^{-1} respectively. On the other hand the O-P-O asymmetric stretching vibration is shifted at higher wavenumber (1251 cm^{-1}). The 701 cm^{-1} and 1150 cm^{-1} bands corresponding to the P-O-P and O-P-O stretching vibrations decrease strongly in intensity for x=3-5 mol% MoO_3 content.

These changes are correlated with the phosphate chain length, which decreases with the increase of MoO_3 content due to the depolymerization of the phosphate structure. Thus, the number of short phosphate chain units or ring structures increase also with the MoO_3 content.

REFERENCES

1. M. Scagliotti, M. Villa and G. Chiodelli, J. Non-Cryst. Solids, 93, 350 (1987).
2. J. Koo, B. Bae and H. K. Na, J. Non-Cryst. Solids, 212, 173 (1997).
3. I. Ardelean, C. Andronache, C. Campean and P. Pascuta, Mod. Phys. Letters B, 18, 45 (2004).
4. U. Selvaraj and K. J. Rao, J. Non-Cryst. Solids, 104,300 (1988).
5. A. J. Bourdillon, F. Khumalo and J. Bordas, Philos. Mag. B37, 731, (1978).
6. S. R. Elliott, "Physics of Amorphous Materials", 2nd Edn, Longman, New York, 1990).
7. K. J. Rao, B. G. and S. R. Elliott, J. Mater. Sci., 20,1678, (1985).
8. P.Balta and E. Balta, "Introduction to the Physical Chemistry of the Vitreous State", Abacus, Kent, 1976.
9. C. Dayanand, G. Bhikshamaiah, V. Jaya Tyagaraju, M. Salagram, and A. S. R. Krishna Murthy, J. Mater. Sci, 31,1945 (1996).
10. T. Iliescu, I. Ardelean, V. Simon and D. Lazar, Studia Univ. Babes-Bolyai, Physica, 39, 25, (1994).
11. J.A. Ruller, J.M.Jewell, J. Non-Cryst. Solids, 175, 91, (1994).
12. G. J. Exarhos, Nucl.Instrum. Meth. B1 498 (1984).
13. A. Bertoluzza, M. A. Battaglia, R. Simoni and D. A. Long, J. Raman Spectrosc., 14,178, (1983).
14. G. B. Rouse Jr., P. J. Miller and W. M. Risen, J. Non-Cryst. Solids, 28, 193 (1978).

STUDIA UNIVERSITATIS BABES-BOLYAI, PHYSICA, XLIX, 3, 2004

EPR INVESTIGATION OF GADOLINIUM DOPED BISMUTH GERMANATE GLASSES AND VITROCERAMICS

D. UDVAR*, S. SIMON

Faculty of Physics, Babes-Bolyai University, M. Kogalniceanu no 1, 400084 Cluj-Napoca, Romania

ABSTRACT. The local structure of the glasses belonging to the $0.5Gd_2O_3 \cdot 99.5[xBi_2O_3(1-x)GeO_2]$ system, with $0.12 < x < 0.875$ were studied by electron paramagnetic resonance (EPR). Differential thermal analysis (DTA) was used in order to investigate the thermal behavior of the vitreous samples and to establish the heat treatment temperature for crystallization of the samples. Vitroceramic samples were obtained by heat treatment of the glass samples at 600℃ for 24 hours. The crystalline phases induced in the glass matrix by heat treatment were identified by X-Ray diffraction. EPR data show that Gd^{3+} ions are homogeneously distributed in the host glass. After partial crystallization the environments of Gd^{3+} ions are more uniform proving a local structure relaxation and are function of the structure of the identified crystalline phases.

Keywords: Electron paramagnetic resonance; local structure, glasses, vitroceramics.

1. Introduction

Bismuth germanates are intensively investigated for applications in optical devices [1]. The sillenite crystals, $Bi_{12}GeO_{20}$ are interesting for applications such as optical memories, holography or optical phase conjugating devices [2]. The eulytite crystals, $Bi_4Ge_3O_{12}$ are used as scintillators or, when doped with rare-earth elements, as laser materials [3,4]. The study of glassy systems, having similar properties to those of crystals, is of high interest because of the lower cost and easier production of glasses with respect to crystals. Vitreous germanates have been proposed as materials for optical waveguides, due to their transmission characteristics in the infrared region. In addition, the high Raman scattering cross-section makes these glasses good candidates for devices such as fiber-optic amplifiers [5].

In recent years, many studies on sillenite and eulytite crystals and mixed crystals have been performed in order to understand their structural properties.

In order to extend the available information concerning glasses containing gadolinium ions, in this work we performed a systematic investigation of the $0.5Gd_2O_3 \cdot 99.5[xBi_2O_3\ (1-x)GeO_2]$ system, with $0.12 < x < 0.875$, using electron paramagnetic resonance (EPR) and differential thermal analyses (DTA).

2. Experimental

Bismuth germanate glasses were prepared with different ratio betwen bismuth and germanium oxides. The glass samples were obtained by melting, of corresponding mixture from pure oxides. The component powders were mixed and then melted in an

* *Corresponding author: udvar@phys.ubbcluj.ro.*

electric furnace in an air atmosphere at temperature 1250℃. The time of 10 minutes at the melting temperature was chosen to permit good mixing of the components while preventing the evaporation of the highly volatile bismuth oxide. The glass was obtained by quenching onto a stainless steel plate at room temperature.

The samples were heat treated at the 600℃ for 24 ho urs in order to obtain crystalline phases in the glass matrix. The proper heat treatment temperature was established by DTA. The DTA traces of the glass samples were recorded using MOM thermal analysis system in the temperature range 30–800℃. The heating rate was 10℃ $/min^{-1}$.

The vitreous state of the samples was confirmed by X- ray diffraction with a Bruker X-ray diffractometer. The crystalline phases obtained after heat treatment were identified by the same method.

The structural order arround Gd^{3+} ions were investigated by electron paramagnetic resonance, before and after heat treatment. The EPR measurement was made using a ADANI EPR spectrometer system in the range 700-4700 Gauss of the magnetic field, in the X-band, at room temperature.

3. Results and discussion

Figure 1 shows the DTA traces of the samples with x=0.67. The exothermic effect corresponding to the crystallization temperature is around 600℃. No weight loss of the samples was observed from the TG curve.

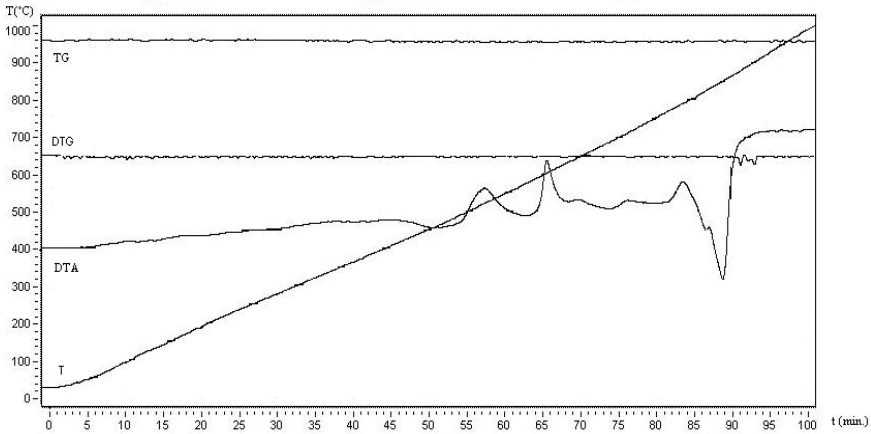

Fig. 1. *Differential thermal analysis curves for x = 0.67 sample.*

The increasing of bismuth oxide content determined changes in the local structure of the matrix reflected in the evolution of the EPR spectra. The EPR spectra for the glass samples with the concentration of Bi_2O_3 up to 40% are illustrated in figure 2. These spectra show the resonance lines at g ~2; 2.85; 4.8 and 5.9 being typical for disordered matrices [7 - 11]. The two EPR lines at g ~ 4.8; and 5.9 have almost the same intensity, and are associated to the Gd^{3+} ions with a coordination number lower ($N_c < 6$), and respectively higher ($N_c \geq 6$) than six, located in sites with intense crystal fields [9, 10].

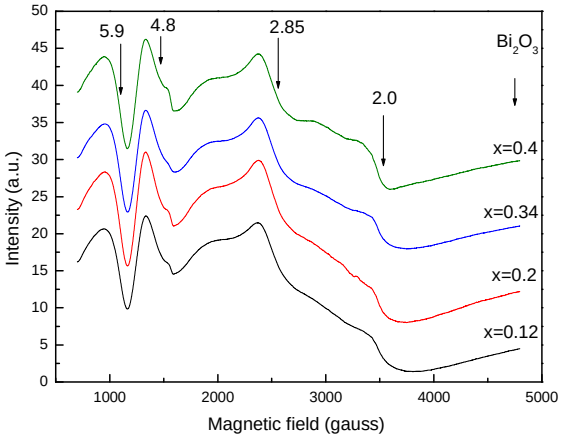

Fig. 2. *EPR spectra of $0.5Gd_2O_3 \cdot 99.5[xBi_2O_3(1-x)GeO_2]$ glasses with low bismuth content.*

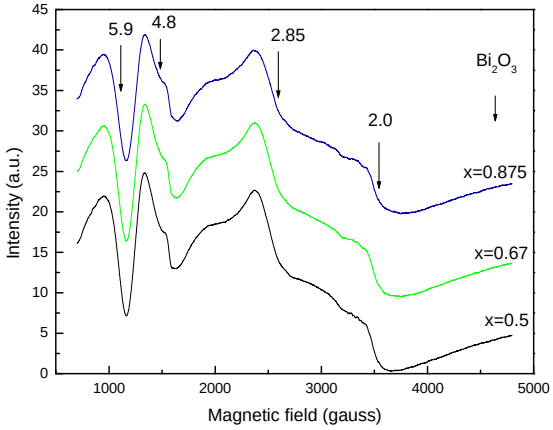

Fig. 3. *EPR spectra of $0.5Gd_2O_3 \cdot 99.5[xBi_2O_3(1-x)GeO_2]$ glasses with high bismuth content.*

Figure 3 shows the EPR spectra for samples with higher bismuth content. For these samples the same type of spectra as for the samples with lower bismuth oxide content was observed, showing that the gadolinium environments are not very much dependent on bismuth content. As resulted from X- ray diffraction patterns, for the sample with x = 0.12 the structure is only partial crystallized and for the sample with x=0.2 the 1:2 (Bi:Ge) phase was identified. For sample with x=0.3 the structure containing the 1:1 (Bi:Ge) phase and in the sample with x = 0.4 the 4:3 (Bi:Ge) phase was observed. Beside the last mentioned phase, 2:1 (Bi:Ge) phase is present in the samples with x=0.5 and 0.67. In the sample with high bismuth content almost only the 12:1 (Bi:Ge) phase were identified; the 2:1 (Bi:Ge) phase being present as impurity phase.

The EPR spectra of investigated samples after heat treatment are show in Fig. 4 and Fig. 5. In the EPR spectra of these samples several changes appear (Fig. 4).

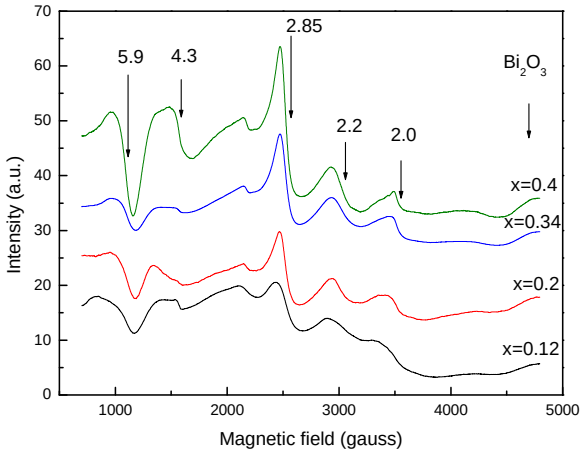

Fig. 4. *EPR spectra of partially crystallized* $0.5Gd_2O_3 \cdot 99.5[xBi_2O_3(1-x)GeO_2]$ *samples with low bismuth* content.

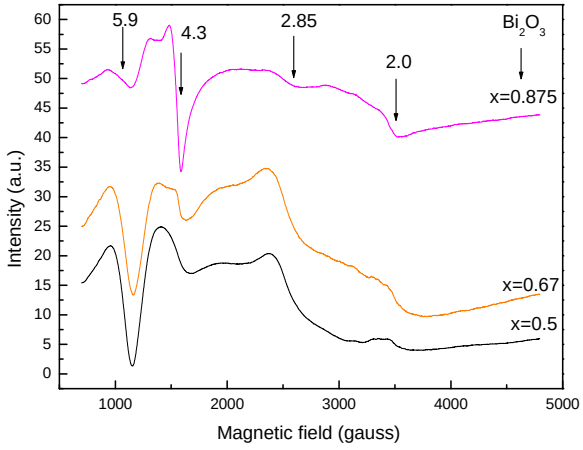

Fig. 5. *EPR spectra of partially crystallized* $0.5Gd_2O_3 \cdot 99.5[xBi_2O_3(1-x)GeO_2]$ *samples with high bismuth content.*

For the samples with high germanium content a new line at g ~ 2.2 arise. The intensity of the resonance line at g ~ 4.8 for samples with 0.12; 0.2; 0.34 is attenuate in comparison with that corresponding glass samples, while for the sample with x = 0.4, this line is not visible being replaced by a new line at g ~ 4.3, superimposed on that coming from iron impurities. The main increase is observed for line with g ~ 2.85 its intensity increasing with bismuth oxide concentrations.

In figure 5 are presented the EPR spectra of the crystalline samples with higher bismuth oxide content. It is surprising that even from X-ray structural point of view the samples with x = 0.5 and 0.67 consist of a mixture of crystalline 1:1 (Bi:Ge) and 2:1 (Bi:Ge) phases, the EPR spectra are like for the vitreous samples, with less intense line at g ~ 2.0 and 4.8, suggesting that the surrounding of Gd^{3+} are very much distorted in these mixture of crystalline phases. For the samples with highest bismuth content (x=0.875) the EPR spectra confirm that this crystalline samples is a mixture of 12:1 phase as a major phase and 2:1 phase as impurity. The line belonging to the 12:1 phase is the preponderant one and is characteristic for cubic sites as expected in this cubic crystalline phase[6]. The others lines typically for U type spectrum [7] are assigned to Gd^{3+} ions disposed in a distorted 2:1 phase or at interfaces. The sample with x=0.875 reveals a strong absorption at g ~ 4.3 associated to a 12:1 structural phase.

4. Conclusions

Glasses based on the heavy metal oxide have the capacity to accept rare earth ions in the network modifier sites. The spectra for the gadolinium doped bismuth germanate glasses are typically “U“ spectrum with the resonance lines at g ~2; 2.85; 4.8 and 5.9, specific for non-crystalline systems.

The results suggest that the Gd^{3+} ions are homogeneously distributed in the host glass and play both the network former and network modifier role in the studied glasses. After heat treatment the intensity of the resonance line at g ~4.8 is decreasing by increasing the concentration of the Bi_2O_3 content evolution accompanied by the developing of the new line with g ~4.3 associated with Gd^{3+} ions in a cubic environment. For different concentration of the bismuth oxide in the samples composition the following crystalline phases: 1:2, 1:1, 4:3, 2:1 and 12:1 phases were observed. As results, the EPR spectra for crystalline samples are superposition of spectra belonging to these different phases.

REFERENCES

1. P. Gunther and H. P. Huignard, eds, Photorefractive Materials and Their Applications, Topics in Applied Physics, Vols. 61 and 62 (Springer, Berlin, 1988).
2. S. L. Hou and D.S. Oliver, Appl. Phys. Lett. 18 (1971) 325.
3. M. J. Weber and R. R. Monochamp, J. Appl. Phys.44 (1973) 5495.
4. P. P. Lottici, I. Manzini, G. Antonioli, G. Gnappi and A. Montenero, J. Non-Cryst.Solids 159 (1993) 173.
5. D.Hall, N. Newhause, N. Borrell, W. Dumbaugh and D. Weidman, Appl. Phys. Lett., 54 (1989) 1293.
6. M.F. Carrasco, S.K. Mendiratta, L. Marques, A.S.B. Sombra – Journal of Mat. Sci. Lett., 21, 12 (2002) 963.

7. D. L. Griscom, Glass Science and Tehnology, eds. D.R. Uhlman and N.J. Kreidl, vol. 4B, Academic Press, 1990.
8. L. E. Iton, J. Turkevich, J. Phys. Chem., 81, 5 (1977) 435.
9. D.L. Griscom, J. Non-Cryst. Solids 40 (1980) 211.
10. I.E. Iton, C.M. Brodbeck, S.L. Suib, G.D. Stucky, J. Chem. Phys. 79 (1983) 1185.
11. S. Simon, R. Pop, V. Simon, M. Coldea, Journal of Non-Cryst. Solids 331 (2003), 1-10.

STUDIA UNIVERSITATIS BABES-BOLYAI, PHYSICA, XLIX, 3, 2004

MAS-NMR AND EPR INVESTIGATIONS OF Y_2O_3-FE_2O_3-AL_2O_3-SIO_2 GLASSES

S. SIMON[1*], D. ENIU[2], R.V.F. TURCU[1], V. SIMON[1]

[1]Babes - Bolyai University, Faculty of Physics, 3400 Cluj-Napoca, Romania
[2]University of Medicine and Pharmacy, Faculty of Pharmacy, 3400 Cluj-Napoca, Romania

ABSTRACT. ^{27}Al MAS-NMR (Magic Angle Spinning Nuclear Magnetic Resonance) and Fe^{3+} EPR (Electron Paramagnetic Resonance) investigations on Y_2O_3-Fe_2O_3-Al_2O_3-SiO_2 system evidence the changes produced by iron doping in samples structure with respect to the coordination of aluminum atoms and to the vicinity of the iron ions. Mainly tetra- and six-fold coordinated aluminum atoms and two types of iron environments were identified in the investigated samples. The change in the relative intensity and position of the peaks corresponding to different aluminum species can be assigned to the influence of the iron ions on the glass structure. In samples with low Fe_2O_3 content ($x \leq 1$ mol %) the iron ions are mainly disposed in isolated sites of low symmetry and strong crystalline fields, but as Fe_2O_3 content increases to 3 mol % the surrounding of iron ions becomes more symmetric and Fe^{3+} ions experience dipolar and exchange interactions.

Introduction

Despite its proven efficacy in the treatment of cancer, external beam radiotherapy is limited to suboptimal doses because of healthy tissue exposure within the radiation field. Radioimmunotherapy (RIT), targeting radiation to tumor by using beta emitting specific and efficient delivery of cytotoxic radiation to systemic metastases while sparing radioisotopes conjugated to a monoclonal antibodies, has been proposed to achieve exposure to normal tissues [1]. Even though positive results in preclinical models were obtained, RIT has failed to achieve reproducible clinical efficacy in carcinomas [2].

A particularly valuable alternative mode of therapy is the use of intra-arterially injected radioactive particles of a size sufficient to lodge in endarterioles. The basis for such therapy is that tumours are usually rich in vasculature and that liver metastases are almost exclusively dependent on arterial blood supply. This is very different for the normal liver, which receives most of its flow from the portal vein [3]. This selectivity can also be increased by the use of vasoactive drugs, which cause vasoconstriction of the normal liver arterioles, but to which tumour vessels, lacking smooth muscle, are insensitive [4].

Advanced and special glasses play important roles in biomedical uses. Some of the glass compositions have distinctive properties that make them preferred materials for certain applications. For instance, radiotherapy glasses are produced in the form of small microspheres and are used to irradiate diseased organs inside the body [5]. The advantage of using these microspheres as in-situ radiation delivery

[*] *Corresponding author: simons@phys.ubbcluj.ro*

vehicles is that much larger doses of radiation can be safely delivered to the target site, eliminating exposure of other healthy parts of the body. If this internal radiotherapy is accompanied by the local hyperthermia, easily realised by magnetic crystals heating under electromagnetic field exposure, the treatment efficiency is enhanced.

The present study is focused on $17Y_2O_3 \cdot 19Al_2O_3 \cdot xFe_2O_3 \cdot (64\text{-}x)SiO_2$ glass system. The application of this system in the cancer therapy is due to beta emitting Y-90 isotope activable by neutron irradiation and to iron containing crystals developed in the glass matrix. The behaviour of these glasses in interaction with human body fluid and implicitly their biocompatibility is very much dependent on the glass structure, particularly on the local symmetry around the component cations. For characterising this local symmetry in the investigated system we used ^{27}Al MAS NMR and Fe^{3+} EPR measurements.

Experimental

Glass samples of $17Y_2O_3 \cdot 19Al_2O_3 \cdot xFe_2O_3 \cdot (64\text{-}x)SiO_2$ system ($0 \le x \le 3$ mol %) were prepared by melting the component oxides of p.a. purity at 1500^oC for 30 minutes and fast quenching to room temperature by pouring and pressing between stainless plates.

^{27}Al MAS NMR spectra were recorded at room temperature from powder samples on MAS NMR AVANCE 400 Bruker spectrometer, at 104.2MHz, in magnetic field of 9.4 T and spinning frequency 15 kHz, using $Al(NO_3)_3$ water solution as reference.

Fe^{3+} EPR spectra were recorded at room temperature from powder samples on ADANI spectrometer, in X band.

Results and discussion

The prepared $17Y_2O_3 \cdot 19Al_2O_3 \cdot xFe_2O_3 \cdot (64\text{-}x)SiO_2$ samples are vitreous, as evidenced by X-ray diffraction analysis.

Figure 1 shows the recorded ^{27}Al MAS NMR spectra of investigated glasses function of iron oxide content. The spectra are quite large, being extended from 70 ppm to –40 ppm. Usually the ^{27}Al MAS NMR spectra in amorphous and crystalline aluminates [6-13] consist of three lines centred at 0-10 ppm, 20-40 ppm and 60-70 ppm corresponding to three types of aluminium: hexa- penta- and tetra-coordinated with ogygens, respectively. In the case of our samples the spectra are less resolved, so the mentioned lines are overlapped suggesting a high local disorder degree. Despite this fact it is evident that the main contribution to the spectra is coming from aluminium tetra-coordinated and only in a small amount from aluminium penta- and hexa-coordinated. Having in view that the chemical shift anisotropy for tetra-coordinated aluminium is quite large in silicate glasses [6], one can estimate that around 80 % from the total visible aluminium atoms are tetra-coordinated.

By increasing the Fe_2O_3 content, in the low concentration range, no major influence on the aluminium environment is evidenced, but the total intensity of the NMR spectra increases as result of the favourable paramagnetic effect on the relaxation time of ^{27}Al nuclei. For the sample with $x = 3$ Fe_2O_3 mol % the total intensity is decreasing, showing that a part of the aluminium atoms became NMR invisible as result of the local magnetic field experienced by them due to the presence of a higher amount of iron ions in their surrounding. At the same time one remarks that the features characteristic for penta- and hexa-coordinated aluminium disapeare.

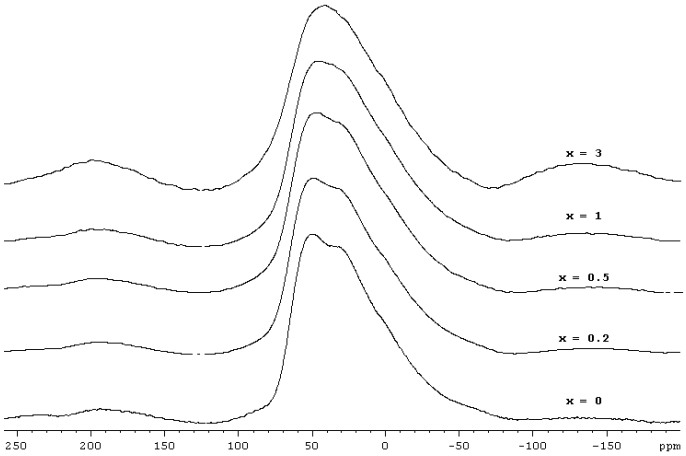

Fig. 1. *^{27}Al MAS NMR spectra for $17Y_2O_3 \cdot 19Al_2O_3 \cdot xFe_2O_3 \cdot (64-x)SiO_2$ glass samples.*

The Fe^{3+} EPR spectra from the investigated glasses are presented in Figure 2. For $x \leq 1$ they are typical for isolated iron ions contained in disordered matrices [14 - 22]. The resonance signal with $g \approx 9.8$ was assigned to Fe^{+3} ions disposed in environments of rhombic symmetry [14 - 18]. The major absorption line occurs at $g \approx 4.3$ and arises from isotropic transitions inside the central Kramers doublet [14 – 16]. When Fe^{+3} ions are experiencing strong crystalline field they usually occupy octahedral or tetrahedral distorted sites [14 - 22]. The absorption line around $g \approx 2.0$ is considered to arise from isolated species occupying sites of octahedral symmetry and/or from spin-spin exchange coupled pairs of paramagnetic ions [14]. For the sample with 3 % Fe_2O_3 the EPR spectra mainly consists of a relatively narrow line (220 Gs) with $g \approx 2.0$, typical for

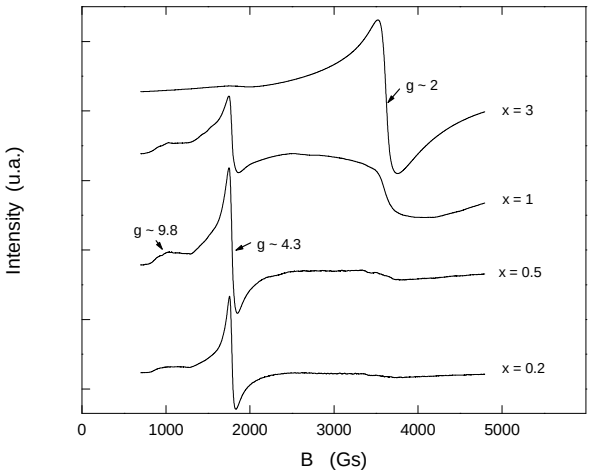

Fig. 2. *Fe^{3+} EPR spectra of $17Y_2O_3 \cdot 19Al_2O_3 \cdot xFe_2O_3 \cdot (64-x)SiO_2$ glass samples.*

samples containing small magnetic crystals [23], wherein iron ions are subjected to exchange interactions. The presence of these crystals can explain also the decrease of the MAS NMR spectrum intensity of this sample (Fig. 1). The fact that these crystals are not observed by X-ray diffractions indicate their small size and, on the other hand, their low amount. This means that even for low Fe_2O_3 concentration magnetic nanocrystalline phases can be developed in these glass matrices, indicating that they could be indeed used for medical applications both for radiotherapy and for hyperthermia.

Conclusions

Mainly tetra- and only small amount of penta- and hexacoordinated aluminum atoms were identified in the investigated samples by MAS NMR. The change in the relative intensity and position of the peaks is assigned to the effect of paramagnetic iron ions. EPR results indicate for the samples with low iron content ($x \leq 1$ mol %) the presence of isolated Fe^{3+} ions in sites of different symmetries and crystal field intensity. As Fe_2O_3 content increases to 3 mol % the surrounding of iron ions becomes more symmetric and Fe^{3+} ions experience dipolar and exchange interactions.

REFERENCES

1. V. K Langmuir, Nucl. Med. Biol. 19**,** 213 (1992).
2. A.M. Mello, E.K.J. Pauwels, F.J. Cleton, J. Cancer Res. Clin. Oncol. 120**,** 121 (1994).
3. C.A. Hoefnagel, Eur. J. Nucl. Med., 18, 408 (1991).
4. J. Folkman, in Cancer Medicine, eds. J.F. Holland, E. Frei, R.C. Bast Jr., D.W. Kufe, D.L. Morton, R.R. Weischelbaum, Lea & Febiger, Philadelphia, 1993, p.153–170.
5. G.J. Ehrhardt, D.E. Day, Nucl. Med. Biol., 14, 233 (1987).
6. M.E. Smith, Appl. Magn. Reson., 4, 1 (1993).
7. R.K. Sato, P.F. McMillan, P. Dennison, R. Dupree, J. Phys. Chem., 95, 4483 (1991).
8. D. Iuga, S. Simon, A.P.M. Kentgens, E. de Boer, J. Phys. Chem. B, **3**, 103, 7591 (1999).
9. P.E.Stallworth, P.J.Bray, in Glass Science and Technology, Eds. D.R.Uhlmann and N.J.Kreidl, Acad. Press Inc., Boston, 1990, p. 77-100.
10. B.C.Bunker, R.J.Kirkpatrick, R.K.Brow, G.L.Turner, C.Nelson, J. Am. Ceram. Soc. **6**, 14, 30 (1991).
11. R.K.Brow, D.R.Tallant, G.L.Turner, J. Am. Ceram. Soc. **79**, 9, 1410 (1996).
12. S.Simon, G.J.M.P.van Moorsel, A.P.M.Kentgens, E. de Boer, Solid St. NMR, 5, 163 (1995).
13. L.Züchner, J.C.C.Chan, W.Müller Warmuth, H.Eckert, J. Phys. Chem. B, 102, 4495 (1998).
14. D. L. Griscom, J.Non-Cryst. Solids, 40, 211 (1980).
15. H.H. Wickman, M.P. Klein, D.A. Shrley, J. Chem. Phys., 42, 2133 (1965).
16. D. Loveridge, S. Parke, Phys. Chem. Glasses 9, 73 (1968).
17. D.W. Moon, M.J.M Aitken, R.K. Maccrone, G.S. Cieloszky, Phys. Chem. Glasses,16, 91 (1975).
18. M. Nofz, R. Stosser, F.G. Wishmann, Phys. Chem. Glasses, 31, 57 (1992).
19. S.Simon, I. Ardelean, M.Peteanu, M. Pop, R.Stefan, Mod. Phys. Lett. B, 14, 1, 1 (2000).
20. A.S. Rao, R.R. Reddy, T.V.R. Rao, J.L. Rao, Solid State Commun., 96, 701 (1995).
21. I. Ardelean, M. Peteanu, S. Filip, V. Simon, G. Gyorffy, Solid State Commun. 102,4, 341 (1997).
22. S. Simon, A. van der Pol, E. J. Reijerse, A.M.P. Kentgens, G.J.M.P. van Morsel, E. de Boer, J. Chem. Soc. Faraday Trans., 91, 10, 1519 (1995).
23. S. Simon, D. Eniu, A. Pasca, D. Dadarlat, V. Simon, Mod. Phys. Lett. B, 15, 21, 921 (2001).

STUDIA UNIVERSITATIS BABES-BOLYAI, PHYSICA, XLIX, 3, 2004

DTA AND PHOTOPYROELECTRIC INVESTIGATION OF FE_2O_3-BI_2O_3-GA_2O_3 GLASS SYSTEM

V. SIMON[1*], C. NEAMTU[2], S. SIMON[1]

[1]*Babes - Bolyai University, Faculty of Physics, 3400 Cluj-Napoca, Romania*
[2]*National Institute for Research and Development of Isotopic and Molecular Technologies, 3400 Cluj-Napoca, Romania*

ABSTRACT. Differential thermal analysis (DTA) under several conditions regarding the heating rate was carried out on glasses of $xFe_2O_3(80-x)Bi2O3{\cdot}20Ga2O3$ system, where $x \leq 20$ mol %. The crystallization has been studied by using DTA curves. The gallium bismuthate matrix shows a more pronounced tendency towards crystallization than the other compositions.

The thermal diffusivity for the investigated samples range from $2.6{\cdot}10^{-7}$ m^2/s for the gallium bismuthate host glass to $1.5{\cdot}10^{-7}$ m^2/s for the sample containing 5 mol % Fe_2O_3. Further addition of iron oxide up to x =20 mol % determines a slight increase of the thermal diffusivity, but it does not exceed the value obtained for the gallium bismuthate matrix.

Introduction

Heavy metal oxide glasses are investigated as potential hosts for fiber-optic amplifiers because of their low phonon energy, thermal stability and good emission properties [1]. Heavy-metal oxides have large optical non-linearities which make them promising for optoelectronic applications [2].

The present paper aims to investigate the activation energy of crystalisation and the glass sytability of Fe_2O_3-Bi_2O_3-Ga_2O_3 samples as well as their thermal diffusivity.

Experimental

$xFe_2O_3{\cdot}(80-x)Bi_2O_3{\cdot}20Ga_2O_3$ glass samples with x = 0, 5, 10 and 20 mol % were obtained from Fe_2O_3, Bi_2O_3 and Ga_2O_3 melted at 1200^oC for 30 minutes in air. The melts were quickly poured and pressed between stainless steel plates at room temperature. The colour of the samples changes from metallic yellow for x = 0 to reddish brown by addition of Fe_2O_3 up to x = 20.

The glass transition temperatures (T_g) and crystallisation temperatures (T_{cr}) of the samples have been determined in the temperature range $20\text{-}1000^0C$ by using a MOM equipment. In order to determine the activation energy of the crystallisation (E_a) the DTA traces were recorded at three heating rates *a* = 5, 10 and 20^0C/min.

For thermal diffusivity measurements the samples were mechanically polished as plates with plan parallel faces. The measurements were performed in the standard photopyroelectric (PPE) configuration with thermally thick sensor and sample and optically opaque sample [3]. The room temperature value of the thermal diffusivity was obtained by performing a frequency scan of the phase of the PPE signal in a

* *Corresponding author; E-mail: viosimon@phys.ubbcluj.ro*

frequency range for which both sample and sensor are thermally thick. A layer of a PPE detection cell is considered thermally thick when its geometrical thickness is larger than the thermal diffusion length in the material.

Results and discussion

Thermogravimetric (TG) and differential thermogravimetric (DTG) curves show that there are no weight losses for these samples up to 1000°C (Fig. 1). One also observes (Table 1) that the glass transition temperature (T_g) for all samples is around 420°C, denoting that T_g in this gallium-bismuthate glass matrix is poorly affected by substitution of Bi_2O_3 with Fe_2O_3 up to 20 mol %.

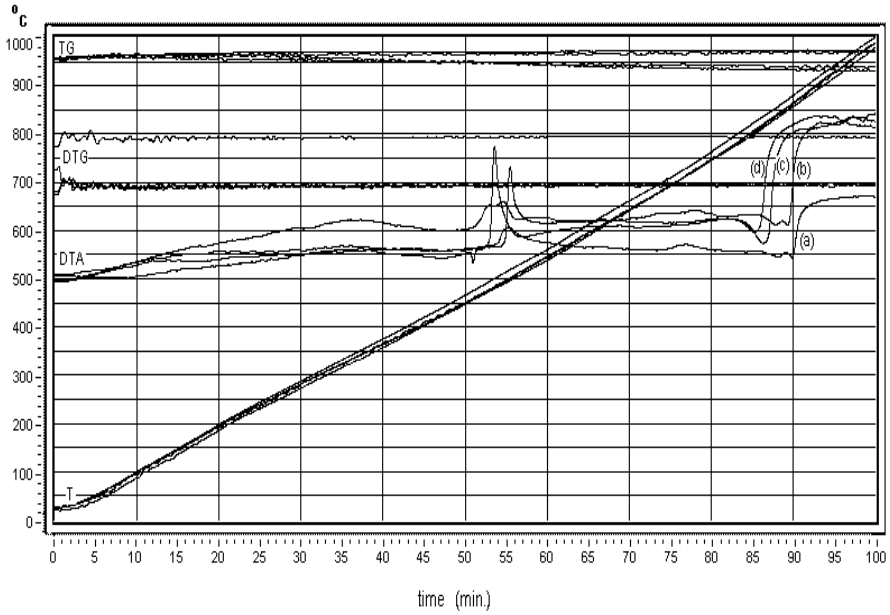

Fig. 1. *Thermal analysis curves recorded from $xFe_2O_3(80-x)Bi_2O_3{\cdot}20Ga_2O_3$ glass samples with x = 0 (a), x = 5 (b), x = 10 (c) and x = 20 (d), with a heating rate of 10°C/min.*

An exothermic peak around 500°C (Table 1) corresponding to a crystallisation process (T_{cr}) is evidenced in the DTA curves. For all samples, without or with iron oxide content, the exothermic peak is followed by an endothermic event assigned to the melting of the glass (T_m). The melting temperature linearly decreases by Fe_2O_3 addition to gallium-bismuthate matrix from 850°C for x = 0 to 810°C for x = 20 mol % as can be observed from Figure 2.

For different heating rates, *a* (a = 5, 10, 20 degree/min), the glass transition activation energy was discussed according to Kissinger's formula [4], as given by equation:

$$\ln (T_g^2/a) = E_a/RT_g + \text{const.}$$

where T_g is the glass transition, E_a is the glass transition activation energy and R is the gas constant.

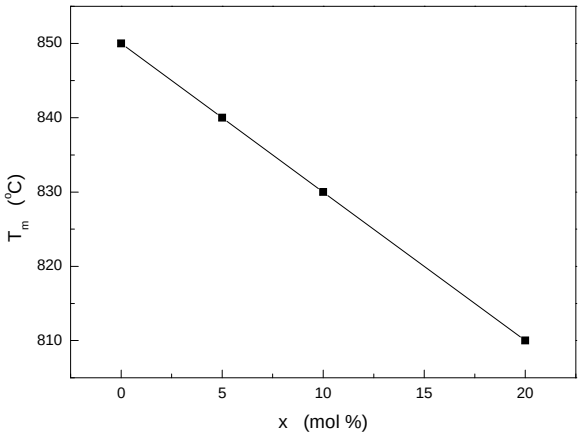

Fig.2. *Composition dependence of melting temperature for $xFe_2O_3(80-x)Bi_2O_3{\cdot}20Ga_2O_3$ glass samples.*

Figure 3 shows the plots of $\ln(T_g^2/a)$ versus the reciprocal crystallisation temperature, T_g^{-1}, for different heating rates. The glass transition activation energy, E_a, was calculated from a linear fitting of Kissinger's equation.

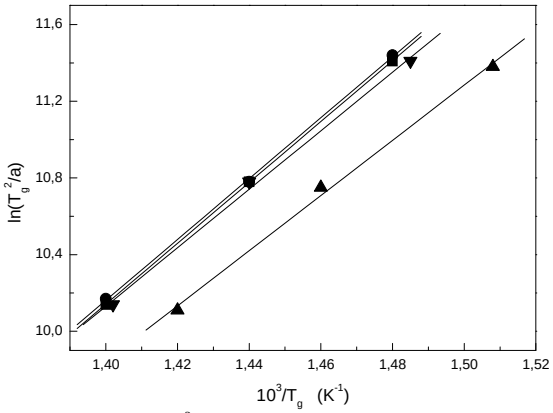

Fig.3. *Plot of $\ln(T_g^2/a)$ versus $10^3/T_g$ of the samples with x = 0 (■), 5 (●), 10 (▲) and 20 (▼) mol % Fe_2O_3.*

The glass stability can be expressed [5, 6] by the difference of crystallisation and glass transition temperatures, $S = \Delta T = T_{cr}-T_g$. Larger values of ΔT lead to higher thermal stability of the glasses. The glass stability can be also expressed also by parameters like the Hruby parameter, $K_{gl}=(T_{cr}-T_g)/(T_m - T_{cr})$ [7], or the ratios $(T_{cr}-T_g)/T_g$, T_g/T_m, $(T_{cr}-T_g)/T_m$ [8].

In Table 1 are summarised glass transition and crystallisation temperatures as well as the calculated values of glass transition activation energy and stability parameters. Inspecting these data one remarks that the glass with 10 mol % Fe_2O_3·has the highest thermal stability (Fig. 4) as indicated by almost all glass stability parameters (Table 1). The gallium bismuthate matrix (x = 0) shows a tendency towards crystallization more than the other compositions. The glass stability for classical silicate systems, expressed for example as T_g/T_m, is $0.5 \leq T_g/T_m \leq 0.74$ [9].

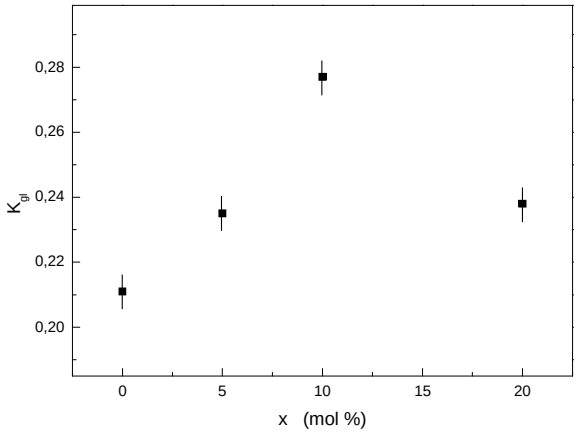

Fig. 4. *Composition dependence of* Hruby parameter *for* $xFe_2O_3(80\text{-}x)Bi_2O_3{\cdot}20Ga_2O_3$ *glass samples.*

Table 1.

Glass transition temperature (T_g), crystallisation temperature (T_{cr}), glass stability S, K_{gl}, S/T_g, T_g/T_m and S/T_m and glass transition activation energy (E_a) for $xFe_2O_3(80\text{-}x)Bi_2O_3{\cdot}20Ga_2O_3$ glass samples.

x (mol%)	T_g (K)	T_{cr} (K)	T_m (K)	S (K)	S/T_g	T_g/T_m	S/T_m	K_{gl}	E_a kJ/mol
0	693	768	1123	75	0.108	0.617	0.067	0.211	132
5	693	773	1113	80	0.115	0.623	0.072	0.235	121
10	688	778	1103	90	0.131	0.624	0.082	0.277	120
20	693	768	1083	75	0.108	0.640	0.069	0.238	127

The glass transition activation energy (E_a) of $80Bi_2O_3{\cdot}20Ga_2O_3{\cdot}$glass matrix is diminished by Fe_2O_3 addition from 132 to 120 kJ/mol. According the values reported by Kubuki et al. for the activation energy of $50CaO{\cdot}10BaO{\cdot}(40\text{-}x)Ga_2O_3{\cdot}xFe_2O_3$ glasses, a decrease from 7.66 to 5.44 eV is obtained when x increases from 5 to 25 [10].

One observes that E_a differently changes with $Fe_2O_3{\cdot}$ content. Without doubt, by progressive addition of Fe_2O_3 up to 10 mol % E_a decreases and then weakly increases, as can be observed for x = 20 %. These results prove that Fe_2O_3 causes weakening of the bond strength but this is not accompanied by a lowering of the thermal stability. The narrow values range for the changes obtained both for glass transition activation energy and for glass stability indicates a good thermal stability of $xFe_2O_3(80\text{-}x)Bi2O3{\cdot}20Ga2O3$ glass samples for the studied compositions.

The thermal diffusivity measurements were performed in the standard photopyroelectric (PPE) configuration with thermally thick sensor and sample and optically opaque sample. The room temperature values of the thermal diffusivity α, were calculated for all samples using the the thickness of the sample and the slope of the linear part from the curve representing the dependence of photopyroelectric signal phase versus frequency square root.

The thermal diffusivities for the investigated samples is of same magnitude order like for other oxide glasses [11, 12] and range from $2.6 \cdot 10^{-7}$ m^2/s for the gallium bismuthate host glass to $1.5 \cdot 10^{-7}$ m^2/s for the sample containing 5 mol % Fe_2O_3. The further addition of iron oxide up to x =20 mol % determines a slight increase of the thermal diffusivity (Fig. 5), but it does not exceed the value obtained for the gallium bismuthate matrix.

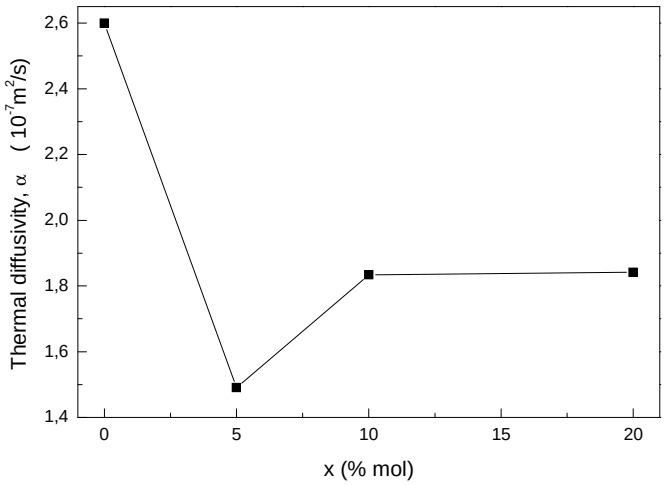

Fig. 5. *Composition dependence of thermal diffusivity for $xFe_2O_3(80\text{-}x)Bi_2O_3 \cdot 20Ga_2O_3$ glass samples*

Conclusions

The melting temperature of $xFe_2O_3 \cdot (80\text{-}x)Bi_2O_3 \cdot 20Ga_2O_3$ glass samples diminishes commensurate with the iron content. Glass transition and crystallisation temperatures are slightly affected as x increases from 0 to 20 mol %, however the data point out higher values for glass stability of iron containing glasses. The values calculated for the activation energy are ranging from 132 to 120 kJ/mol by progressive addition of iron in the investigated composition range.

The thermal diffusivity data are ranging from $2.6 \cdot 10^{-7}$ m^2/s, for the gallium bismuthate host glass, to $1.5 \cdot 10^{-7}$ m^2/s, for the sample containing 5 mol % Fe_2O_3. Further addition of iron oxide up to x =20 mol % determines a slight increase of the thermal diffusivity, but it does not exceed the value obtained for the sample without iron oxide.

Both DTA and thermal diffusivity results indicate a good thermal stability of the investigated iron-gallium-bismuthate glass system.

REFERENCES

1. J. H. Song, J. Heo, S. H. Park, J. of Appl. Physics 93, 12, 9441 (2003).
2. V. C. Solano Reynoso, L.C. Barbosa, O.L. Alves, N. Aranha, C.L. Cesar, Journal of Materials Chemistry, **4,** 4, 529 (1994).
3. A. Mandelis, M.M. Zver, J. Appl. Phys., 57, 4421 (1985).
4. H. Kissinger, J. Res. Nat. Bur. Stand, 57, 217 (1956).
5. E.B. Araujo, J.A. Eiras, E.F. de Almeida, J.A.C. de Paiva, A.S.B. Sombra, Phys. Chem. Glasses, 40, 5, 273 (1999).
6. R. El-Mallawany, Proc. Int. Congr. Glass, Volume 2. Extended Abstracts, Edinburg, Scotland, 1-6 July, 2001.
7. A. A. Jr. Cabral, C. Fredericci, E. D. Zanotto, Non-Cryst. Solids, 219, 182 (1997).
8. P. Subbalakshmi, N. Veeraiah, J. Non-Cryst. Solids, 298, 89 (2002).
9. I. Avramov, E.D. Zanotto, M.O. Prado, J. Non-Cryst. Solids, 320, 9 (2003).
10. S. Kubuki, K. Fukuda, A. Ikeda, T. Nishida, The Fifth Conference on Solid State Chemistry, 7-12 July, 2002, Bratislava, Slovakia.
11. D. Almond, A. Patel, Phototherml Science and Techniques, Chapman & Hall, London, 1996.
12. S.Simon, C. Neamtu, D. Eniu, D. Dadarlat, V. Simon, Mod. Phys. Lett. B, 16, 17, 631 (2002).

STUDIA UNIVERSITATIS BABES-BOLYAI, PHYSICA, XLIX, 3, 2004

XRD, EPR, MAGNETIC AND MÖSSBAUER STUDIES ON GALLIUM BISMUTHATE GLASSES CONTAINING IRON

V. SIMON*[1], J.M. LE BRETON[2], S. SIMON[1]

[1] Babes - Bolyai University, Faculty of Physics, 3400 Cluj-Napoca, Romania
[2] Groupe de Physique des Matériaux, UMR CNRS 6634 – Université de Rouen, 76801 Saint Etienne du Rouvray Cedex, France

ABSTRACT. Fe_2O_3-Bi_2O_3-Ga_2O_3 glass samples containing up to 80 mol % Bi_2O_3 and 20 mol % Ga_2O_3 were obtained by annealing of melts from 1200°C to room temperature. The effect of iron addition to the gallium bismuthate matrix was followed both from structural point of view and with regard to the magnetic properties of samples in correlation with iron valence states. As Fe_2O_3 content reaches 20 mol % on the account of Bi_2O_3, crystalline phases of $(Bi_{1-\varepsilon}Fe_\varepsilon)_4O_6$, $Bi_2(Fe,Ga)_4O_9$ and Fe_3GaO_6 type are developed, which are presumably in a nanocrystalline state.

Introduction

Current interests in functional glasses include gallium systems, which have useful optical properties. Due to their high optical nonliniarity, high magneto-optic effect and extended IR transparency the heavy metal glasses containing gallium are of technological importance for potential application in optical switching, optical isolators (Faraday rotators) used to avoid self-focusing in high power laser systems, IR windows and sensors [1-3]. Gallium bismuthate glasses appear to be promising host materials for waveguide devices in the microwaves telecommunication windows, broad band amplifier and high power laser applications [4-7].

The present paper aims to investigate the structure of Fe_2O_3-Bi_2O_3-Ga_2O_3 samples and their properties as shown by electron paramagnetic resonance (EPR), Mössbauer spectroscopy and magnetic measurements.

Experimental

The starting material used to prepare $xFe_2O_3 \cdot (80-x)Bi_2O_3 \cdot 20Ga_2O_3$ glass samples (x = 0, 5, 10 and 20 mol %) were analytically pure reagents Fe_2O_3, Bi_2O_3 and Ga_2O_3. They were obtained by melting oxide mixtures of desired compositions in sintercorundum crucibles at 1200°C for 30 minutes in an electric furnace in air. The melts were quickly undercooled at room temperature by pouring onto stainless steel support and pressing in form of thin plates. The gallium bismuthate matrix is metallic yellow. By addition of iron to this matrix the glasses become reddish brown.

The X-ray diffraction (XRD) analysis of as prepared samples was carried with a Bruker spectrometer on powder samples. EPR spectra were recorded at room temperature in X band (9.4 GHz) using ADANI spectrometer. Mössbauer spectral analysis was performed also at room temperature. The magnetic susceptibility measurements were carried out on a Faraday type magnetic balance in the temperature range 80 - 300 K.

* *Corresponding author; E-mail: viosimon@phys.ubbcluj.ro*

Results and discussion

The cations entering in the structure of investigated samples are bismuth, gallium and iron. Ionic radius, coordination type and ionic field strength of Fe^{3+} and Ga^{3+} are relatively close and both are considerably different from that of Bi^{3+} ions [8, 9]. These data support the role of glass former for Bi_2O_3 and of glass modifier for Ga_2O_3 and Fe_2O_3 in a heavy metal glass system. Heavy metal oxide glasses might be defined as those glasses containing over 50 cation percent of bismuth and/or lead which participate in the glass structure as network formers [10].

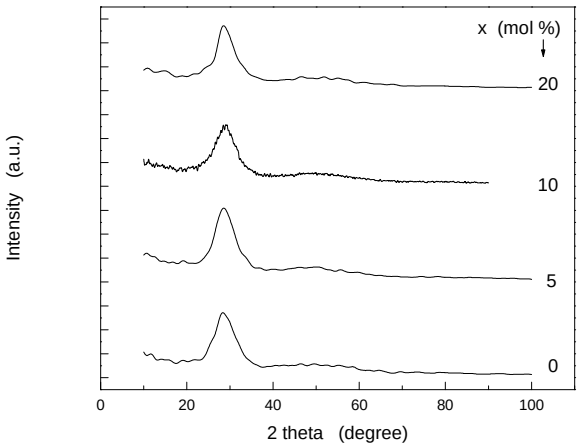

Fig. 1. *X-ray diffraction patterns for $xFe_2O_3(80-x)Bi_2O_3{\cdot}20Ga_2O_3$ as prepared glass samples.*

The structure of the as prepared samples was analysed by X-ray diffraction. The XRD patterns are shown in Figure 1. They consist of a relatively broad line typical of vitreous systems. The patterns do not evidence any narrow lines corresponding to crystalline phases. The same samples were investigated after an year and new XRD patterns were recorded (Fig. 2). The samples containing up to 10 mol % Fe_2O_3 show similar

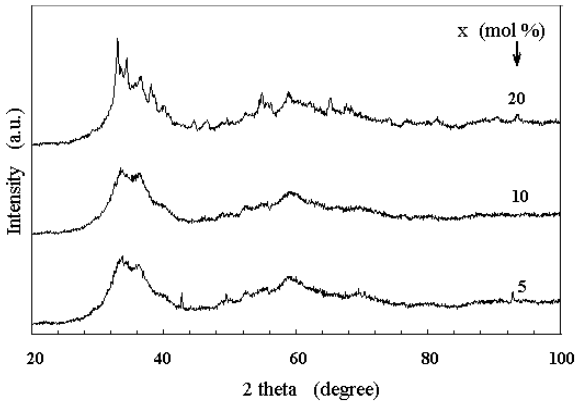

Fig. 2. *X-ray diffraction patterns for $xFe_2O_3(80-x)Bi_2O_3{\cdot}20Ga_2O_3$ relaxed samples.*

DRX patterns, consisting of very broad lines, typical for the vitreous state, and broad lines corresponding to poorly crystalline regions. For the sample with x = 20, over the broad line are superposed sharp peaks which correspond to $(Bi_{1-\varepsilon}Fe_{\varepsilon})_4O_6$, $Bi_2(Fe,Ga)_4O_9$ and Fe_3GaO_6 phases, presumably in a nanocrystalline state.

The electron paramagnetic resonance investigation searched for additional information on the vicinity of Fe^{3+} iron resonant centres. The EPR spectrum of the sample with x = 5 mainly consists of the line with g ≈ 4.3 associated to isolated Fe^{3+} ions [11, 12], while for the sample containing 10 mol % Fe_2O_3 there is almost only a large line with g ≈ 2.1 (Fig. 3). This line could be assigned to Fe^{3+} resonance centres arranged in nanodomains of crystalline phases with high iron content. As Fe_2O_3 content increases to 20 mol % in the EPR spectrum occurs beside the g ≈ 2.1 line a superimposed one with g ≈ 2.0, characteristic for the systems relaxed from structural point of view or with high iron content [13], associated to dimers of Fe^{3+}- Fe^{3+} or Fe^{3+} - Fe^{2+} ions. Although the derivative spectrum of the sample with x = 5 does not easily point out the existence of the last two types of lines, the integrative spectrum (Fig. 4) shows that even for this low Fe_2O_3 content there are iron ions involved in clusters.

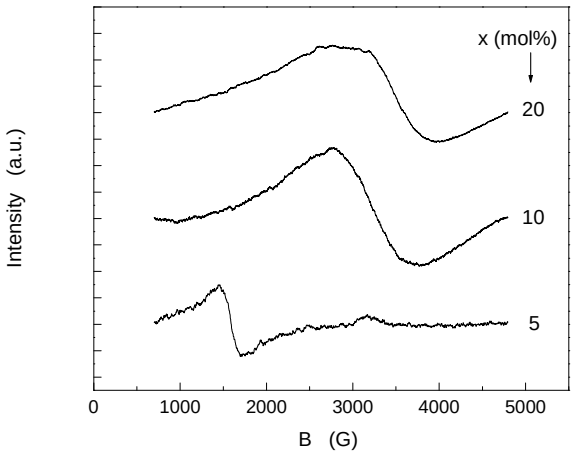

Fig.3. *EPR spectra of $xFe_2O_3(80-x)Bi_2O_3{\cdot}20Ga_2O_3$ samples.*

The existence of both Fe^{3+} and Fe^{2+} iron ions in the investigated composition range is confirmed by the magnetic data. The effective magnetic moments range from 5.58 to $4.99{\cdot}\mu_B$ as x increases from 5 to 20 and are much below $5.9{\cdot}\mu_B$, the value corresponding to Fe^{3+} ions in free state. The temperature dependence of the reciprocal magnetic susceptibility is presented in Figure 4. For all samples the reciprocal magnetic susceptibility obeys the Curie-Weiss law with a negative paramagnetic Curie temperature, θ_p, for the samples containing up to 10 mol % Fe_2O_3 and positive for x = 20. For the first samples the magnetic susceptibility data indicate that the iron ions experience negative superexchange interactions and they are predominantly antiferromagnetically coupled. For x = 20 the temperature dependence of the reciprocal magnetic susceptibility indicate that the iron ions are dominantly ferrimagnetically coupled [14, 15].

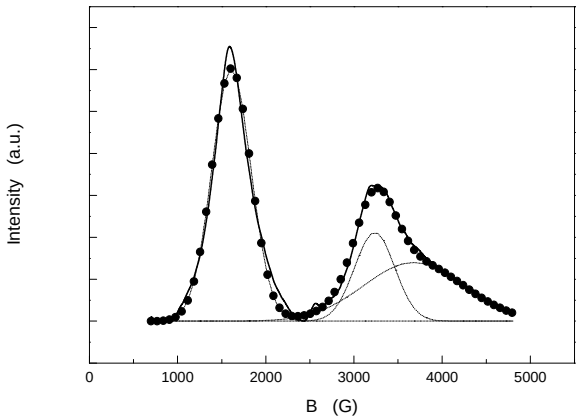

Fig. 4. *Integrated EPR spectrum of 5Fe2O3·75Bi2O3·20Ga$_2$O$_3$ sample (experimental – solid line, and fitted •• with three lorentzian lines --)*

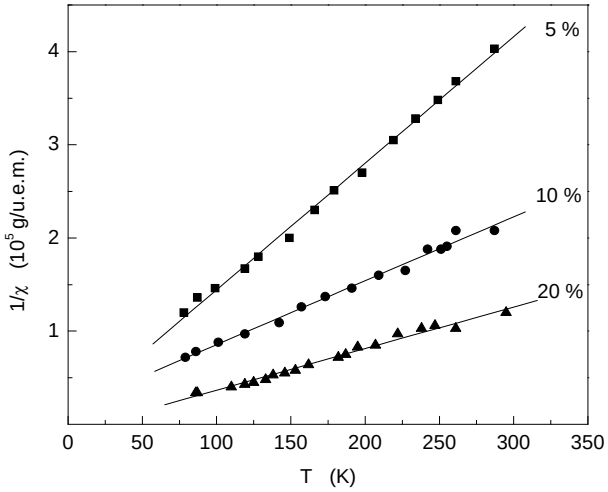

Fig. 5. *Temperature dependence of reciprocal susceptibility for xFe$_2$O$_3$(80-x)Bi$_2$O$_3$20Ga$_2$O$_3$ samples.*

The Mössbauer spectra of the samples with x = 5 and 10 were fitted with a singlet and a doublet (Fig. 6). The singlet could correspond to iron atoms in non-magnetic environments, Fe atoms dispersed in a non magnetic phase [16-18]. The doublet corresponds to iron atoms in paramagnetic environments. As the Fe_2O_3 content increases, the fraction of the singlet decreases and may indicate that the fraction of the paramagnetic phase increases, in relation with the increase of the Fe_2O_3 content. The Mössbauer spectrum of the sample with x = 20 reveals only a paramagnetic doublet. An enlarged spectrum allows to obtain more accurate data. The spectrum shown in Fig. 7 is slightly asymmetric, and is fitted with two paramagnetic doublets, with isomer shifts that are characteristic of Fe^{3+} ions.

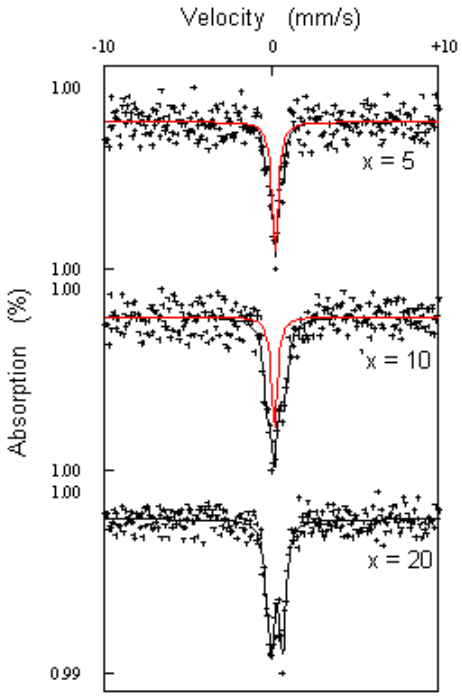

Fig. 6. *Room temperature Mössbauer spectra for $xFe_2O_3(80-x)Bi_2O_320Ga_2O_3$ samples (v = ±10 mm/s).*

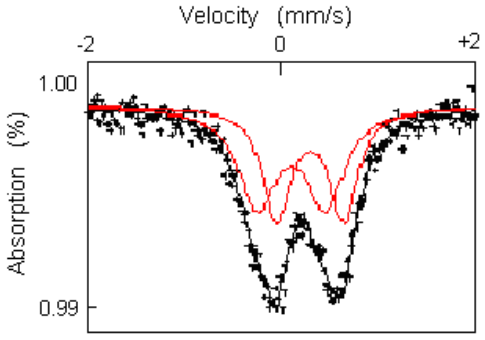

Fig. 7. *Enlarged room temperature Mössbauer spectrum for $20Fe_2O_3{\cdot}60Bi_2O_3{\cdot}20Ga_2O_3$ samples.*

Conclusions

In the heavy metal glass system $xFe_2O_3{\cdot}(80-x)Bi_2O_3{\cdot}20Ga_2O_3$ ($x \leq 20$) the iron ions occur both in Fe^{3+} and Fe^{2+} valence states, as evidenced by magnetic, EPR and Mössbauer results. The XRD data indicate that up to x = 20 all as prepared samples are in vitreous state but $20Fe_2O_3{\cdot}60Bi_2O_3{\cdot}20Ga_2O_3$ sample shows a lower glass stability and over a time relaxed sample contains relatively well developed

crystalline phases. The magnetic susceptibility data indicate for $x \leq 10$ mol % Fe_2O_3 that the iron ions experience negative superexchange interactions and they are predominantly antiferromagnetically coupled. For $x = 20$ the temperature dependence of the reciprocal magnetic susceptibility indicate that the iron ions are dominantly ferrimagnetically coupled. On the other hand, the EPR data show that part of the iron ions are associated in clusters and this is already observed for low Fe_2O_3 content.

REFERENCES

1. A.C. Hannon, J M Parker, B Vessal, J Non-Crystalline Solids, 232-234, 51 (1998).
2. A C Hannon, J M Parker, B Vessal, J Non-Cryst Solids, 196, 187 (1996).
3. M. J. Weber, Journal of Applied Physics, 63, 8, 3118 (1988).
4. S. Q. Man, E.Y.B. Pun, P.S. Chung, J. Opt. Soc. Am. B, 17, 1, 23 (2000).
5. S. Q. Man, S.F. Wong, E.Y.B. Pun, J. Opt. Soc. Am. B, 19, 8, 1839 (2002).
6. T.Murata, M. Torisaka, H.Takebe, K. Morinaga, J. Am. Ceram. Soc., 81, 8, 2135 (1998).
7. S. Q. Man, E.Y.B. Pun, P.S. Chung, Appl. Phys. Lett., 77, 4, 483 (2000).
8. J.E. Huheey, E.A. Keiter, and R.L. Keiter in Inorganic Chemistry: Principles of Structure and Reactivity, 4th edition, HarperCollins, New York, USA, 1993.
9. J.A. Kerr in CRC Handbook of Chemistry and Physics, D.R. Lide, (ed.) CRC Press, Boca Raton, Florida, USA, 81-st edition, 2000.
10. W.H. Dumbaugh, J.C. Lapp, J. Am. Ceram. Soc., 75,9,2315 (1992).
11. R.H. Sands, Phys. Rev. 99, 1222 (1955).
12. R. Stößer, M. Notz, Glastechn. Ber. Glass Sci. Technol., 67, 156 (1994).
13. D.L. Griscom, Glass Science and Technology, eds. D.R. Uhlman and N.J. Kreidl, Vol. 4B, Academic Press, 1990, p.151.
14. N. F. Borelli, D. L. Morse, J. W. H. Schreurs, Journal of Applied Physics, **54**, 6, 3344 (1983).
15. N. Rezlescu, l. Rezlescu, M.L. Craus, E. Rezlescu, Cryst. Res. Technol. **34,** 7, 829 (1999).
16. H. Binczycka, J. A. Sawicki, J. Phys. D: Appl. Phys. 16, 197 (1983).
17. E. Burzo, I. Ursu, D. Ungur, I. Ardelean, and V. M. Nazarov**,** J. Appl. Phys., **58**, 9, 3628 (1985).
18. R. Berger, J. Kliava, J.-C. Bissey, V. Baïetto, J. Appl. Phys., 87, 10, 7389 (2000).

STUDIA UNIVERSITATIS BABES-BOLYAI, PHYSICA, XLIX, 3, 2004

EPR AND MAGNETIC STUDIES OF $CuO-B_2O_3-TeO_2$ GLASS SYSTEM

I. ARDELEAN* and R. CICEO LUCACEL*

** Faculty of Physics, Babes-Bolyai University, 400084 Cluj-Napoca, Romania*

ABSTRACT. The $xCuO\cdot(100-x)[2B_2O_3\cdot TeO_2]$ glass system with $0 < x \leq 30$ mol % have been studied by means of EPR and magnetic susceptibility measurements. In present work is investigate the influence of gradual increases in CuO on both local glass structure and magnetic interactions that involved Cu^{2+} ions in binary glasses containing two network formers, B_2O_3 and TeO_2. EPR absorption spectra show Cu^{2+} ions in axially distorted octahedral environments. Both EPR and magnetic measurement data pointed out the simultaneous presence in the glasses with $x > 5$ mol % of Cu^{2+} and Cu^{+} ionic species. The Curie behavior of magnetic susceptibility indicates the presence in these glasses of isolated or/and coupled by dipole-dipole interactions of Cu^{2+}.

1. Introduction

EPR investigation of transitional metal (TM) ions in glasses are interesting and have received a considerable attention because the EPR parameters are very sensitive to the symmetry and strength of the ligand field in the neighbourhood of paramagnetic impurities [1-3]. Copper (II) Cu^{2+} is the most amenable ion for EPR studies. The main advantage of using Cu^{2+} as the spin probe is that its EPR spectra can be easy recorded at room temperature, the spectrum is simple and the spread of the spectrum are large enough to detect detailed changes in the coordination sphere [4]. Information about the valence states and interactions involving the TM ions in vitreous systems were also obtained by means of magnetic measurements. Different types of magnetic interactions (dipolar, superexchange) between copper ions placed in borate [5-6] glasses were revealed by the temperature dependence of the magnetic susceptibility. Mixed valence states of copper ions were also evidenced [5-7].

This paper presents our results obtained by means of EPR and magnetic susceptibility measurements performed on $2B_2O_3\cdot TeO_2$ glass matrix doped over a wide range concentration with copper ions.

2. Experimental details

Glasses of the xCuO·(100-x)[$2B_2O_3\cdot TeO_2$] system were prepared using pure reagent grade compounds, *i.e.* H_3BO_3, TeO_2 and CuO in appropriate ratios. Melting was performed in sintered corundum crucibles, in an electric furnace. To avoid material losses due to the evaporation, the oxide mixtures were introduced directly at 1250^oC in the pre-heated furnace. After 30 minutes the molten materials were quenched to room temperature by pouring on a stainless- steel plate.

The structure of the samples was tested by means of X-ray diffraction. No crystalline phase was detected from the diffraction patterns up to 30 mol % CuO.

EPR measurements of the samples were performed using a Portable Adani PS8400 spectrometer, in the X frequency band, at room temperature. To avoid the alteration of the glass structure due to the ambient condition, especially humidity, samples were poured immediately after preparation and enclosed in tubular holders of the same caliber. Equal quantities of samples were studied.

The magnetic susceptibility measurements were performed using Oxford Instruments, MagLab2000 balance in the 10-250 K temperature range.

3. Results and discussion

3.1. EPR data

According to figure 1 the obtained absorption spectra are asymmetric, characteristic for Cu^{2+} ($3d^9$) ions in axially distorted octahedral symmetric sites. Within Fig.1 EPR absorption spectra of Cu^{2+} ions in xCuO·(100-x)[$2B_2O_3$·TeO_2] glasses with $0.1 \leq x \leq 30$ mol % the entire concentration range the spectrum keeps its overall aspect, suggesting a great structural stability of the vitreous matrix to accept Cu^{2+} ions in units having more or less the same symmetry and configuration.

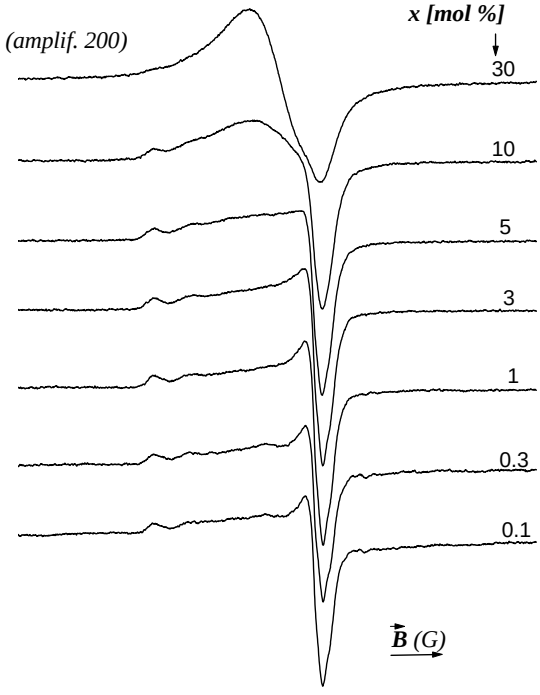

Fig.1. EPR absorption spectra of Cu^{2+} ions in xCuO·(100-x)[$2B_2O_3$·TeO_2] glasses with $0.1 \leq x \leq 30$ mol %

Within the low concentration range ($0.5 \leq x \leq 5$ mol %), the spectra shows the hyperfine structure (hfs) due to the interaction of the unpaired electron spin with the nuclear one, $I = 3/2$, characteristic to Cu^{2+} ions for both ^{63}Cu (the natural abundance 69 %) and ^{65}Cu (natural abundance 31 %). The hfs is resolved in both parallel and perpendicular bands of the spectra, four hyperfine components being observed in each part of the EPR spectra. The evolution of the perpendicular hfs bands when increasing the CuO content is illustrated in figure 2 for some representative spectra of the glass system. The best resolution was obtained at a low degree of impurification. As the Fig. 2 Evolution of hfs in perpendicular band when increasing concentration in xCuO·(100-x)[$2B_2O_3$·TeO_2] glasses with $0.1 \leq x \leq 30$ mol % concentration of paramagnetic Cu^{2+} ions raising the resolution diminishes due to the individual lines broadening, the hfs smears out, so for samples with high paramagnetic ions content the line reduces to the broad envelope of all contributions to the EPR absorption. The relatively broad range in which the spectrum shows a resolved hfs denotes an appreciable degree of short range ordering in vitreous matrix built by approximately identical structural units, involving Cu^{2+} ions.

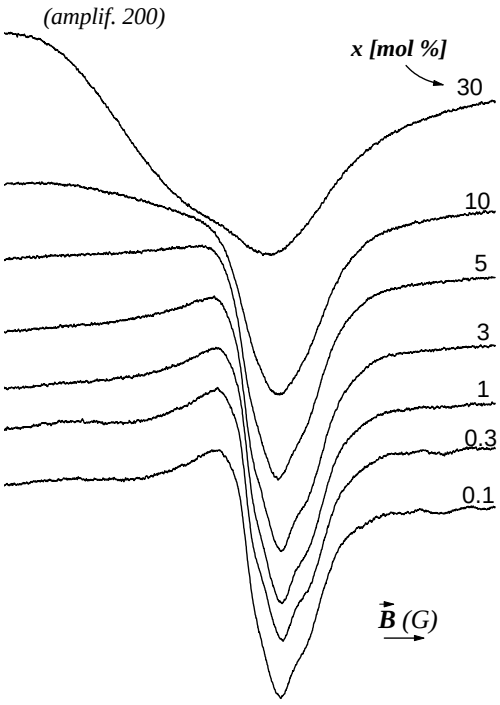

Fig. 2. Evolution of hfs in perpendicular band when increasing concentration in xCuO·(100-x)[$2B_2O_3$·TeO_2] glasses with $0.1 \leq x \leq 30$ mol %

The accuracy in estimating the EPR parameters of the spectra obtained for the investigated systems ($g_{\|}$ and $g_{\perp}$ factors, hyperfine constants) was compromised by the progressive broadening of the hfs components. The estimated values of $g_{\|}$ and $g_{\perp}$ satisfy the relationship $g_{\|} > g_{\perp} > g_e = 2.0023$ characteristic to Cu^{2+} ions coordinated with six ligand atoms in a distorted octahedron, elongated along one axis. The value of the g factors and hyperfine constants reveal the predominantly ionic character of bonding between Cu^{2+} and the ligand atoms [8, 9] but there are also covalence effects that have to be taken into account. Because CuO could be network-modifier in our sample [10], there is competition between Cu^{2+} and the network-forming cations B^{3+}, to attract the oxygen pairs available in their vicinity. The covalence of Cu^{2+}-O bonds increases when the strength of the B-O bonds decreases.

The line width of parallel and perpendicular hyperfine lines increases in order of m (the magnetic quantum number denoting each hf transition). This broadening may be attributed to the micro environmental fluctuations around Cu^{2+} ion that is intrinsic to the glass state [10, 11]. For samples containing $x < 5$ mol % CuO the shape and structure of the resonance line is typical for isolated Cu^{2+} ions in sites of axial symmetry. The distance between Cu^{2+} ions is higher than 5Å, the minimum values for that the hfs is not cover by the dipolar interactions [12]. As the CuO content rises, the line resolution becomes poor due to the individual lines broadening as the effect of dipolar interaction between Cu^{2+} ions and to ligand field fluctuations from the neighborhood.

The absorption signal intensity, I, estimated as the line integrate, is proportional to the number of spins involved in the resonance phenomenon. The intensity of the absorption line has the concentration dependence given in figure 3. The evolution of

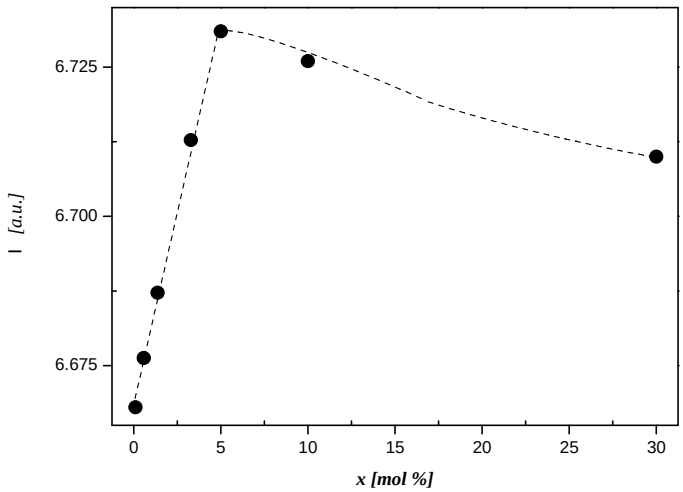

Fig. 3. Concentration dependences of the EPR line-intensity corresponding to xCuO·(100-x)[$2B_2O_3$·TeO_2] glasses

I = *f*(*x*) follows the progressive accumulation of Cu^{2+} ions during the doping process. According to figure 3, I does not follow linearly the doping level of the sample suggesting, for *x* > 5 mol % CuO, other valence state of copper ions, namely Cu^{+} ions, Fig. 3 Concentration dependences of the EPR line-intensity corresponding to$x$CuO·(100-x)[$2B_2O_3$·TeO_2] glasses which do not contribute to the EPR absorption. These new ions balance the paramagnetic Cu^{2+} species so that the addition of CuO implies no more proportional changes of the EPR line intensity with the *x* values. The Cu^{+} ionic species simultaneously present with the Cu^{2+} ones occur when preparing samples, being favored in the oxygen rich melt.

3.2. Magnetic susceptibility data

The temperature dependence of the reciprocal magnetic susceptibility of some investigated glasses is presented in figure 4.

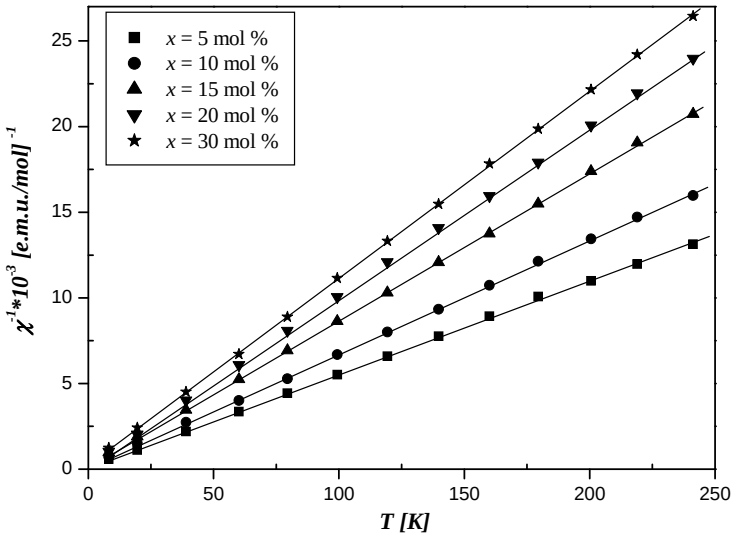

Fig. 4. Temperature dependence of the reciprocal magnetic susceptibility for xCuO·(100-x)[$2B_2O_3$·TeO_2] glasses with $5 \le x \le 30$ mol %

The magnetic susceptibility data correlate well with the EPR result and also complete them. For the investigated glasses, the Curie law is observed for $\chi^{-1} = f(T)$, suggesting that copper ions are predominantly isolated or/and participates to the dipolar interactions in the glass matrix. The values of molar Curie constant, C_M and the Fig. 4 Temperature dependence of the reciprocal magnetic susceptibility for

xCuO·(100-x)[$2B_2O_3$·TeO_2] glasses with $5 \le x \le 30$ mol %

effective magnetic moments, $\mu_{eff,}$ were calculated and are given in Table 1. The μ_{eff} values were estimated as $\mu_{eff} = 2.827 \cdot [C_M/x]^{1/2}$. This estimation of the μ_{eff} implies the assumption that all the copper ions introduced in the batch have 2+ valence states and contribute to the magnetic moment of the glasses.

For all the investigated glasses experimental values obtained for molar Curie constant and consequently for effective magnetic moments are lower than those which correspond to the CuO content, considering that all copper ions are in Cu^{2+} valence state ($\mu_{Cu^{2+}}=1.73\mu_B$) [13]. Therefore we consider that in these glasses are present both Cu^{2+} and Cu^{+} ions. The concomitant presence of monovalent and divalent copper ions was also reported in various glasses [6-11, 14]. From the μ_{eff} relation we estimate in first approximation the molar fraction of the Cu^{2+} ions (*y*), which contribute to the magnetic moment (Table 1).

Table 1.

*Molar Curie constant, C_M, effective magnetic moment, μ_{eff}, and molar fraction of Cu^{2+} (**y**) ions in $xCuO\cdot(100-x)[2B_2O_3\cdot TeO_2]$ glasses*

x [mol % CuO]	$C_M\cdot10^2$ [emu/ mol]	μ_{eff} [μ_B]	***y*** [mol % $Cu^{2+}O$]
5	1.8725	1.73	5
10	1.49476	1.09	4
15	1.15844	0.79	3.1
20	1.00896	0.64	2.7
35	0.8686	0.49	2.4

It observes that the molar fraction of the Cu^{2+} is equal with the CuO molar fraction only in case of samples with 5 mol %. After 10 mol %, the molar fraction of the Cu^{2+} ions decreases with the addition of the CuO in the vitreous samples. It can be remark, that the obtained data from magnetic susceptibility measurements are in agreement with those obtained from EPR as regards evolution of I parameter.

4. Conclusions

The glasses corresponding to $xCuO\cdot(100-x)[2B_2O_3\cdot TeO_2]$ system with $0 \le x \le 30$ mol % were studied.

For all samples EPR absorption spectra due to Cu^{2+} ions were obtained. Up to 5 mol % CuO, isolated Cu^{2+} ions in axially distorted octahedral site were detected. The hyperfine structure, resolved in both parallel and perpendicular bands of the spectra, shows structural stable matrices in accepting Cu^{2+} ions within a relatively broad concentration range.

Both, EPR and magnetic measurements revealed that the Cu^{2+} are isolated and/or involved in dipolar type interactions. For samples with $x > 5$ mol % mixed valence of copper ions, i.e. Cu^{2+} and Cu^{+}, were evidenced by mean of both EPR and magnetic measurements.

REFERENCES

1. H. Imagawa, Phys. Stat. Solidi 30 (1968) 469.
2. O. Cozar and I. Ardelean, J. Non-Cryst. Solids 92 (1987) 278.
3. N.C. Biswas, R. Dayal and P. Chand, Phys. Chem. Glasses 37 (1) (1996) 31.

4. I. Siegel and J.A. Lorence, J. Chem. Phys. 45 (1966) 2315.
5. I.Ardelean, R. Ciceo Lucacel and S. Filip, J. Magn. Magn. Mat. 272-276P1 (2004) 337.
6. I.Ardelean, G.Salvan, M.Peteanu, V.Simon, C.Himcinschi and F.Ciorcas, Mod. Phys. Lett. B 13(22/23) (1999) 801.
7. I. Ardelean, M. Peteanu, R. Ciceo-Lucacel and I. Bratu, J. Mat. Sci.: Mat. Electronics 11 (2000) 11.
8. M.Peteanu, I.Ardelean, S. Filip and F.Ciorcas, J. Mat. Sci.: Mat. Electronics 7 (1996) 165.
9. M.Peteanu, I.Ardelean, E. Burzo and F.Ciorcas, Solid State Commun. 98 (1996) 351.
10. I.Ardelean, M.Peteanu and R. Ciceo-Lucacel, Mat. Sci. Forum 373-376 (2001) 261.
11. G. Ramadevuvu, M. Shareefuddin, N.S. Bai, M.L. Rao and M.N. Chary, J. Non-Cryst. Solids 278 (2000) 205.
12. R. Stefan and S. Simon, Studia Univ. Babes-Bolyai, Physica XLVII (2003) 143.
13. L. M. Mulay, Magnetic Susceptibility (Interscience, New York, 1973) p.1773.
14. E. Metwalli, J. Non-Cryst. Solids 317 (2003) 221.

STUDIA UNIVERSITATIS BABES-BOLYAI, PHYSICA, XLIX, 3, 2004

SPECTROSCOPIC AND MAGNETIC STUDY OF $xEu_2O_3(1-x)(3Bi_2O_3{\cdot}PbO)$ GLASSES

E. CULEA[1], LIDIA POP[1], I. BRATU[2], S. SIMON[3], I. VIDA SIMITI[1] AND D. UDVAR[3]

[1]Technical University of Cluj-Napoca, Cluj-Napoca
[2]National Institute for Development and Research of Izotopic and Molecular Technology, Cluj-Napoca
[3]Babes-Bolyai University, Cluj-Napoca

1. Introduction

Rare-earth elements incorporated in vitreous matrices have been widely studied due to their important applications in the field of telecommunications and laser technology [1-8]. In the last years, glasses containing europium ions became very studied because these materials gained important positions in telecommunications.

In order to obtain information concerning magnetic and structural properties of europium ions incorporated in bismuthate glass matrices we studied the $xEu_2O_3(1-x)(3Bi_2O_3{\cdot}PbO)$ glass system by means of IR spectroscopy, magnetic susceptibility and electron paramagnetic resonance (EPR).

2. Experimental

Samples of the xEu_2O_3 $(1-x)[3Bi_2O_3{\cdot}PbO]$ vitreous system (noted xEBP) with x = 0.01, 0.05, 0.10, 0.15, 0.20 and 0.25 were obtained using reagent grade Bi_2O_3, PbO and Eu_2O_3. The preparation technique was previously described [7].

IR spectra were recorded in the 400÷2000 cm^{-1} range with an EQUINOX 55 spectrophotometer using the KBr pellet technique.

EPR spectra were obtained from powdered samples at room temperature using a standard Bruker EPR 300E equipment.

Magnetic susceptibility measurements were performed on a Faraday type balance in a magnetic field of 1T over the 80 to 300 K temperature range.

3. Results and discussion

Fig.1 shows the IR absorption spectra recorded for the xEBP glasses. These spectra present the features characteristic of the base glass matrix, $3Bi_2O_3{\cdot}PbO$. Some of the most important spectral features, namely those located at 478 and 847-869 cm^{-1}, are associated to the structural units involving the Bi^{3+} cation [5].

The IR absorption band from 847-869 cm^{-1} represents the convolution of the absorption bands reported for different bismuthate glasses at 847 and 860 cm^{-1}, assigned to the total symmetric stretching vibrations of the $[BiO_3]$ and $[BiO_6]$ polyhedra, respectively [5]. Based on the IR spectra obtained for the xEBP glasses, we assumed that the structure of these glasses is built up by both $[BiO_3]$ and $[BiO_6]$ structural units.

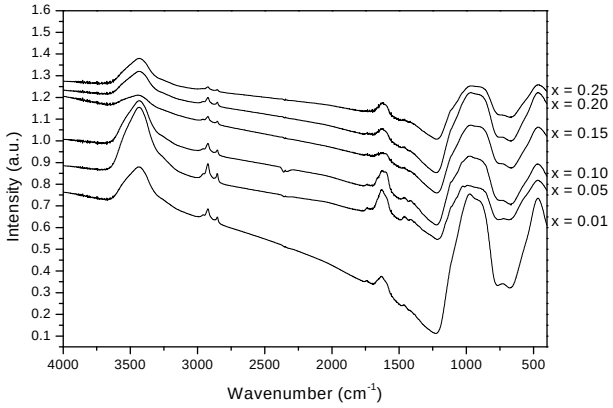

Fig.1. IR spectra of the xEBP glasses.

The increase of the Eu_2O_3 concentration, x, of the xEBP samples determines the slow shift of the absorption band located at 869 cm^{-1} for x=0.01 to 847 cm^{-1} for x=0.25. This suggests the increase of the amount of [BiO_3] structural units with increasing x. This should be due to the increase of the number of nonbridging oxygens provided by the Eu^{3+} ions, having as effect the conversion of [BiO_6] into [BiO_3] structural units.

The IR absorption band at 478 cm^{-1} is also related to the [BiO_6] polyhedra [8]. The increase of the Eu_2O_3 concentration of the xEBP glasses determines a slow shift of this band to higher wavenumbers due to the increase of the degree of distortion of the [BiO_6] polyhedra [8].

Fig.2 shows the temperature dependence of the inverse molar magnetic susceptibility for the xEBP glasses.

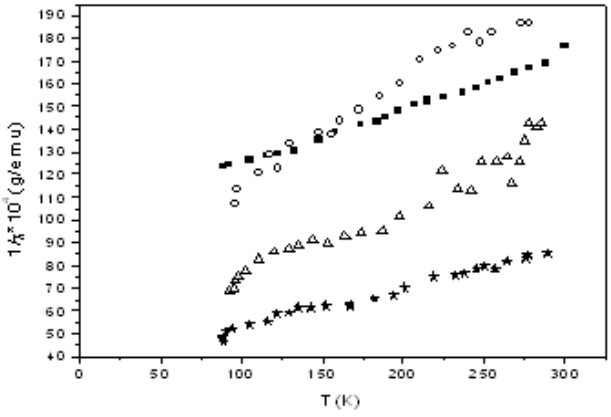

Fig.2. Temperature dependence of the inverse molar magnetic susceptibility for some of the xEBP glasses (o = 0.10, ■ = 0.15, Δ = 0.20 and ⋆ = 0.25).

The magnetic behaviour of the xEBP glasses is due to the presence of the europium ions since the host glass matrix was found diamagnetic. The magnetic susceptibility data collapse to straight lines indicating a modified Curie-Weiss type behaviour ($\chi = \chi_o + C/(T-\theta_p)$, where χ_o is the temperature independent contribution, C is the Curie constant and θ_p is the paramagnetic Curie temperature). The negative values of θ_p obtained for the xEBP glasses ($9\ K \leq /\theta_p/ \leq 140\ K$) suggest that the magnetic interactions between the europium ions are predominantly antiferromagnetic. The effective magnetic moments of the europium ion, μ, were calculated using the experimentally determined C values. The obtained μ values were between 3.34 and $5.95\mu_B$, where μ_B is the Bohr magneton. Note that the effective magnetic moment of the free Eu^{2+} and Eu^{3+} ions is $7.12\mu_B$ and respectively $3.40\mu_B$ [6]. The μ values obtained for the xEBP glasses indicate that the europium ions are present in the host glass matrix both in their 2+ and 3+ valence states. The compositional evolution of C shows first a rapid increase for $x \leq 0.10$ and a slower one for higher x values). This behaviour suggests a decrease of the ratio of Eu^{2+} ions/Eu ions with increasing x.

The EPR spectra recorded for the xEBP glasses are due to the Eu^{2+} ions [6]. The increase of the europium content of the EPR glasses exerts only a weak influence on the EPR spectra consisting in a certain decrease of their intensity. This shows that increasing x produces the shift of the redox equilibrium between the Eu^{2+} and Eu^{2+} valence states toward the second one. Thus the EPR data are in good agreement with those provided by the magnetic susceptibility measurements.

REFERENCES

1. M. Dejneka, B. Samson, Mater.Res.Soc.Bull 24 (1999) 39.
2. M.J. Weber, J.Non-Cryst.Solids 42 (1980) 189.
3. S.V. Lakshman, Y.C. Ratnakaran, Phys.Chem.Glas-ses 29 (1988) 26.
4. E. Burzo, I. Ardelean, D. Mitulescu, J.Mater .Sci.Lett.11(1992) 1492 -1497.
5. E. Culea, L. Pop, V. Simon, M. Neumann, I. Bratu, J.Non.Cryst. Solids 337 (2004) 62.
6. D. Matulescu, M.I. Chipara, E. Burzo, I. Ardelean, Phys. Stat. Solidi (a) 161 (1997) 451.
7. E. Culea, L. Pop, S. Simon, Materials Science and Engineering B 112 (2004) 59-63.
8. K. Gerth, C. Russel, J.Non-Cryst.Solids 221 (1997) 10.

STUDIA UNIVERSITATIS BABES-BOLYAI, PHYSICA, XLIX, 3, 2004

THE STRUCTURE OF MO-B_2O_3-SrO GLASS SYSTEM BY RAMAN SPECTROSCOPY (MO=CuO, V_2O_5)

D. MANIU[1], T. ILIESCU[1], I. ARDELEAN[1], W. KIEFER[2]

[1]Babes-Bolyai University, Faculty of Physics, Kogălniceanu 1, 400084, Cluj-Napoca, Romania.
[2]Institut für Physicalische Chemie, Universität Würzburg, Am Hubland, D-97074 Würzburg, Germany.

ABSTRACT. The influence of CuO and V_2O_5 content on the structure of $3B_2O_3$·SrO glass was investigated by Raman spectroscopy.

For the sample without transition metal oxide, the Raman spectrum indicates a structure with majority pentaborate groups. At high wavenumbers there is a broad and intense band probably due to fluorescence induced by strontium oxide. The addition of copper or vanadium oxides in $3B_2O_3$·SrO glass causes changes in the feature of the Raman spectra. The boroxol units, appears when copper oxide content rises. Further increase of CuO content determines the decrease of pentaborate groups, the disappearance of orthoborate and diborate groups and the formation of pyroborate groups. When the V_2O_5 content increases the number of pentaborate groups decreases and orthoborate groups are formed. The number of non-bridging oxygen increases with vanadium oxide concentration and the glass structure becomes more randomized. At high content of vanadium oxide pyroborate groups are present. Therefore, the copper and vanadium ions act as network modifier in the studied glasses.

1. Introduction

Most glasses are formed by mixing glass-forming oxides (SiO_2, B_2O_3, P_2O_3, ..) with modifier metal oxide [1]. The oxygen from the metal oxide becomes part of the covalent glass network by creating new structural units [2]. Raman spectroscopy becomes a very useful tool for resolving the structure of local arrangements in glasses. Raman spectra and identification of glass forming structural units in borate glasses were also analyzed by other authors [3, 16]. The introduction of the third element in the glasses leads to the changes in the glass structure, metal oxide acting as modifier [5,6]. The structural units from $xCuO·(1-x)$ [$3B_2O_3$·SrO] and $xV_2O_5·(1-x)$ [$3B_2O_3$·SrO] glasses with different molar concentration of copper ($0 \le x \le 0.35$) and vanadium ($0 \le x \le 0.1$) oxides were investigated by means of Raman spectroscopy.

2. Experimental

The glasses were obtained by mixing H_3BO_3, $SrCO_3$ and CuO or V_2O_5 in suitable proportion and by melting the admixture in sintered corundum crucibles at T = 1150 º C for 0.5 h. The samples were obtained by pouring the melts in stainless steel forms. Vitrification was achieved by rapid cooling of the melts at room temperature and atmospheric pressure. In order to obtain Raman spectra the 514.4 nm line of an Ar-ion laser (Spectra Physics model 2016) was used. The plasma lines were avoided by means of a filter prism (Anaspek) and the laser beam was focused on the sample with an Olympus microscope objective (Olympus ULWD 80,

NA 0.75). The back-scattered light was collected by the same objective and then was focused on the entrance slit of the detection system. A Dilor XY Raman triple monochromator with a Peltier cooled, intensified array with 1024 diodes is employed as the light detection system. The back-scattering configuration allows the observation of the sample surface before light exposure. The measurements were carried out at room temperature. The spectral data are processed using Dilor hardware and specially developed software. The spectra were recorded with a resolution of 2 cm^{-1} and spectral data were analyzed with XMGR software.

3. Results and discussion

Raman spectra of $xCuO \cdot (1-x)[3B_2O_3 \cdot SrO]$ glasses with various content of copper oxide ($0 \le x \le 0.35$) are given in Fig. 1. The following bands are present in these spectra: 470 cm^{-1}, 670 cm^{-1}, 770 cm^{-1}, 800 cm^{-1}, 930 cm^{-1}, 960 cm^{-1}, 1050 cm^{-1}, 1350 cm^{-1} and 1450 cm^{-1}. In Fig. 2 few borate groups and their main vibration are present. The Raman spectra of $xV_2O_5 \cdot (1-x)[3B_2O_3 \cdot SrO]$ glasses with various content of vanadium oxide ($0 \le x \le 0.1$) are shown in Fig. 3. In these spectra the following bands are present: 475 cm^{-1}, 670 cm^{-1}, 770 cm^{-1}, 800 cm^{-1}, 935 cm^{-1}, 970 cm^{-1} and 1300 cm^{-1}.

In the spectra with low content of CuO and V_2O_5 a broad and intense band situated at high wavenumbers occurs.

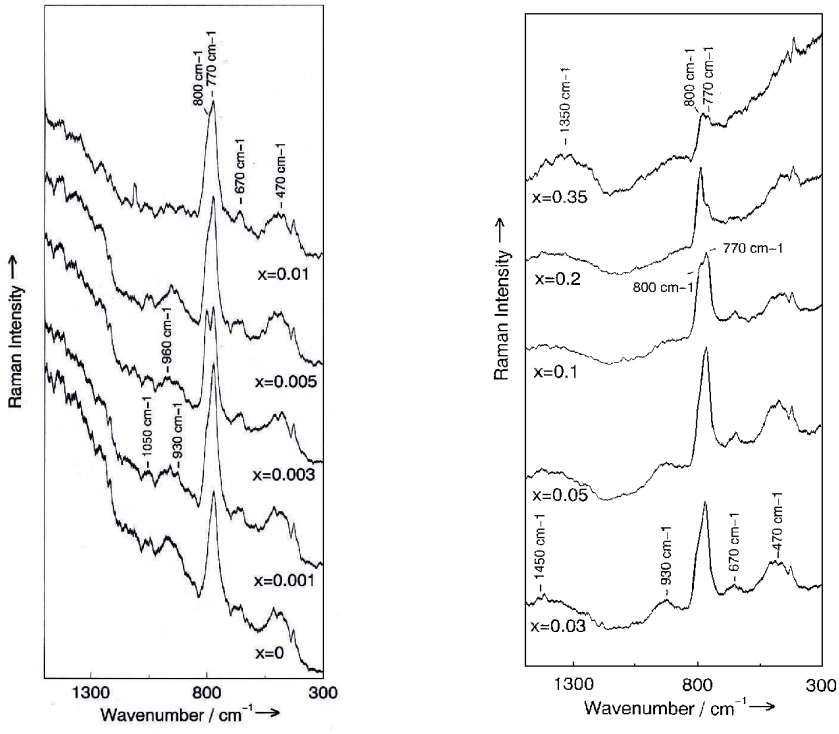

a) b)

Fig. 1. Raman spectra of $xCuO \cdot (1-x)[3B_2O_3 \cdot SrO]$ glasses
a) $0 \le x \le 0.01$, b) $0.03 \le x \le 0.35$.

The dominant band in the Raman spectra of vitreous B_2O_3 is situated at ~806 cm^{-1}. This band was assigned to the boroxol ring oxygen breathing involving a very little boron motion (boron atom coordinate is 3) [7]. (Meera et al. [4] give a list of borate groups found in borate compounds).

The addition of a modifier oxide determines the appearance of a strong band at ~770 cm^{-1} and the shift of the 806 cm^{-1} band to a lower wavenumbers (~800 cm^{-1}) [4]. Bril [10] assigned the ~770 cm^{-1} Raman band to the symmetric breathing vibration of six membered rings with one BO_4 tetrahedron (i.e. triborate, tetraborate, or pentaborate). The lower wavenumbers band (~775 cm^{-1}) was assigned to the symmetric breathing vibration of six membered rings with two BO_4 tetrahedra (i.e. diborate, ditriborate or dipentaborate) [8]. Because in presented Raman spectra the 770 cm^{-1} band appears and the 775 cm^{-1} band does not appear, we conclude that our glasses contain six membered rings with one BO_4 tetrahedron.

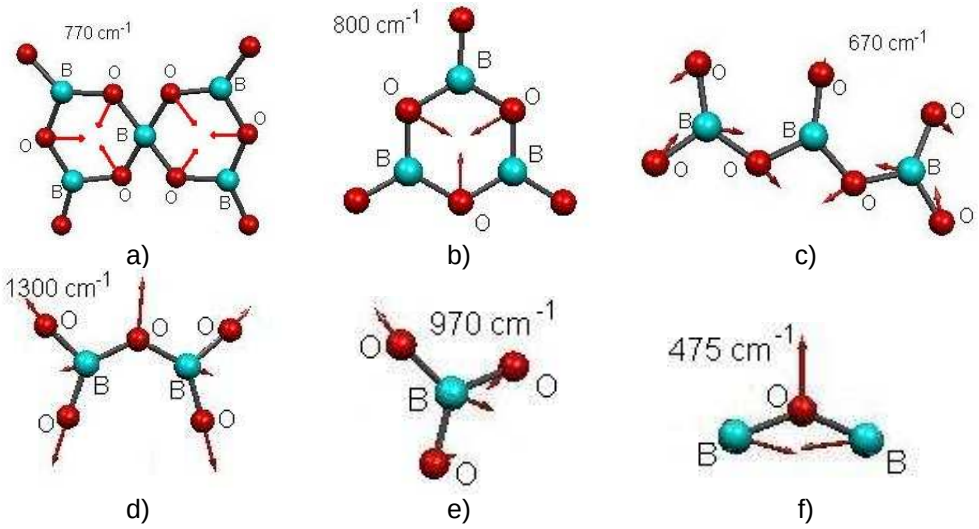

Fig. 2. The main borate groups: a) pentaborate group; b) boroxol ring; c) metaborate group, d) pyroborate group; e) orthoborate group; f) B-O-B angle bending.

Since is not possible to distinguish which units are present by taking into account only this band, additional information has to be added. Crystalline α and β K_2O-$5B_2O_3$, which contain only pentaborate units, give Raman bands at 765 and 885 cm^{-1} and at 785 and 925 cm^{-1}, respectively [9]. Crystalline Na_2O-$4B_2O_3$ (consisting of tetraborate groups) and crystalline Cs_2O-$3B_2O_3$ (consisting of triborate groups) have only a very weak response in the 900 cm^{-1} region [9]. Thus, the 770 cm^{-1} band together with ~930 cm^{-1} band can be taken to be indicative of the presence of pentaborate groups in the studied glasses.

The addition of copper oxide

For the Raman spectra with $0 \leq x \leq 0.1$ CuO the 770 cm^{-1} and 800 cm^{-1} bands rise above the other Raman bands, the intensity of the 770 cm^{-1} band being higher than that of 800 cm^{-1} band. Thus, we conclude that pentaborate groups and boroxol rings dominate the structure of studied glasses. The number of pentaborate

groups are higher than the number of boroxol rings because the difference in intensity of the characteristic bands (the cross section of these two borate groups are very similar). For x > 0.2 CuO the intensity of the 770 cm^{-1} band decreases. This fact involves the decreasing of the number of pentaborate units when copper oxide content increases. This behavior can be explained through the transformation of pentaborate units in another borate units when many copper atoms are connected in the glass network.

At low CuO content the 930 cm^{-1} band appears like a shoulder of 960 cm^{-1} band. This band decreases in intensity when the concentration of CuO rises and for x =0.03 it turns into a shoulder of 930 cm^{-1} band. Crystalline lithium and magnesium orthoborates exhibit a strong peak in the 950 cm^{-1} region [10,11]. Therefore, the 960 cm^{-1} band can be attributed to orthoborate groups. The behavior of 960 cm^{-1} band, indicates the presence of orthoborate groups in the structure of studied glasses only at low content of CuO ($x \leq 0.03$).

For $0 \leq x \leq 0.01$ CuO we can observed a small band centered at 1050 cm^{-1}. In borate glasses, the 1050 cm^{-1} band has been attributed to the presence of diborate groups [12]. This band does not appear in Raman spectra of glasses with high content of CuO. Therefore, we can presume that the glasses with high content of CuO do not contain diborate groups.

For all studied spectra, the 670 cm^{-1} and 470 cm^{-1} bands also appear. The 660-670 cm^{-1} band is assigned to metaborate units [4]. The 470 cm^{-1} band is assigned to a ring angle bending (B-O-B) from borate units [13]. The intensity of 470 cm^{-1} band slowly increases when copper oxide content increases.

For low CuO content our spectra present a broad and intense band, probably due to the fluorescence induced by strontium. The intensity of this band decreases when CuO content grows. For high CuO content, this band disappears and the characteristic borate bands at high wavenumbers are present. We presume that the presence of CuO in B_2O_3-SrO glasses determines the inhibition of the answer of strontium to incident laser beam.

For $x \geq 0.03$ a large Raman band is present at 1450 cm^{-1}. This band indicates the presence of the chain-type metaborate groups [14]. Because the 670 cm^{-1} band (characteristic to metaborate groups) is present in all spectra and the 1450 cm^{-1} band appears at high CuO content, we consider that in our glasses metaborate groups are only chain-type. We presume that the 1450 cm^{-1} band was cover by the fluorescence band at low CuO content.

For x = 0,35 CuO the 1450 cm^{-1} band is not so clearly evidenced, but we observed a band at 1350 cm^{-1}, assigned to the formation of pyroborate groups [15]. Therefore, we conclude that at high CuO content the pyroborate groups are formed.

The addition of vanadium oxide

For the Raman spectra with $0 \leq x \leq 0.01$ V_2O_5 the 770 cm^{-1} and 800 cm^{-1} bands rise above the other Raman bands, the intensity of the 770 cm^{-1} band being higher than that of 800 cm^{-1} band. Accordingly, pentaborate groups (770 cm^{-1}) and boroxol rings (800 cm^{-1}) dominate the structure of studied glasses in the mentioned range of concentration [8,9], and the number of pentaborate groups is higher than the number of boroxol rings. This affirmation is sustained by the difference in intensity of the characteristic bands (the cross section of this two borate groups are very similar).

The introduction of the third element in $3B_2O_3 \cdot SrO$ glass leads to the changes in the glass structure, clearly evidenced by Raman spectra from Fig 3. High content of vanadium oxide, determines the growing of the 935 cm^{-1} band intensity and the appearance of 970 cm^{-1} band. This behaviour indicates the presence of orthoborate groups [10,11]. The increase in intensity of the 970 cm^{-1} band compared with that of 770 and 800 cm^{-1} band indicates that the number of non-bridging oxygen (involved in orthoborate groups) increases with vanadium oxide concentration and the glass structure becomes more randomized.

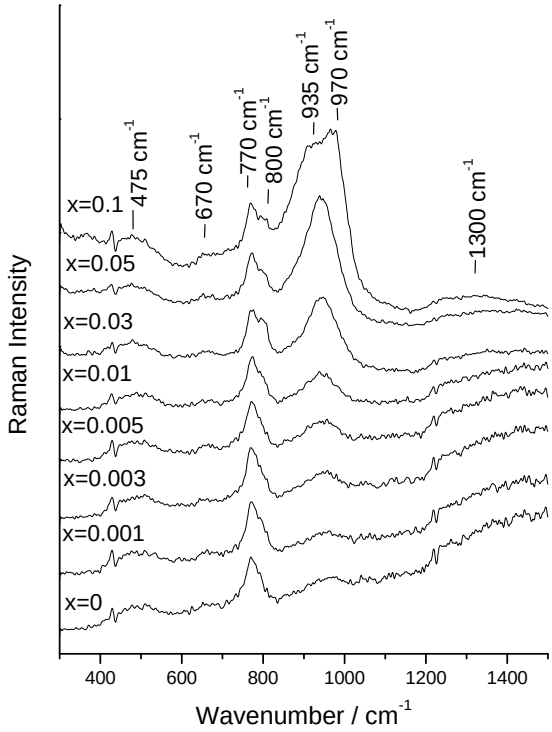

Fig. 3. Raman spectra of $xV_2O_5 \cdot (1-x)[3B_2O_3 \cdot SrO]$ glasses with $0 \leq x \leq 0.1$.

The very large band at ~1300 cm^{-1} indicates the presence of pyroborate groups [15] for high content of vanadium oxide.

For all concentrations, the ~670 cm^{-1} band indicates the presence of metaborate groups [4], while the 475 cm^{-1} band indicates the ring angle bendings (B-O-B) from borate groups [13].

The broad and intense band situated at high wavenumbers which occurs in spectra with low V_2O_5 content is due to strontium fluorescence, as we said in previous section. The addition of vanadium oxide have similar effect with the addition of copper oxide on the fluorescence band. The fluorescence band due to strontium ions decreases and at high content of metal oxide it disappears.

4. Conclusions

Raman spectra reveal bands specific to borate groups such as boroxol rings, pentaborate groups, orthoborate groups, pyroborate groups, diborate groups and metaborate groups. The main bands in the observed spectra are characteristic to boroxol rings and pentaborate groups.

The introduction of the third element in $3B_2O_3 \cdot SrO$ glass leads to the changes in the glass structure. When CuO content increases the number of pentaborate groups decreases, orthoborate and diborate groups disappear and pyroborate groups are formed. When the V_2O_5 content increases the number of pentaborate groups decreases and orthoborate groups are formed. The addition of copper or vanadium oxides in $3B_2O_3 \cdot SrO$ glass causes changes in the feature of the Raman spectra; thereby diversify of the glass structure. The strontium fluorescence band decreases when CuO or V_2O_5 content grows and vanishes at high content of modifier oxide.

Therefore, we conclude that the copper and vanadium ions act as network modifier in the studied glasses. The number of non-bridging oxygen increases with copper and vanadium oxides concentration and the glass structure becomes more randomized.

REFERENCES

1. M. Scagliotti, M. Villa, G. Geiodelli, J. Non-Cryst. Solids 93 (1987) 350.
2. E. I. Kamitsos, A. P. Patsis, G. D. Chryssikos, J. Non-Cryst. Solids 152 (1993) 246.
3. E. I. Kamitsos, G. D. Chryssikos, J. Molec. Struct. 247 (1991) 1.
4. B. N. Meera, A. K. Sood, N. Chandrabhas, J. Ramakrishna, J. Non-Cryst. Solids 126 (1990) 224.
5. D. Maniu, I. Ardelean, T. Iliescu, J. Mat. Sci. Lett. 16 (1997) 19.
6. E. I. Kamitsos, M. A. Karakasides, G. D. Chryssikos, J. Phys. Chem. 91 (1987) 1073.
7. B. P. Dwivedi, M. H. Rahman, Y. Kumar And B. N. Knanna J. Phys. Chem. Solids 54 (1993) 621.
8. T. W. Bril, Philips Res. Rep. Suppl. 2 (1976) 117.
9. W. L. Konijnendijk, Philips Res. Rep. Suppl. 1 (1975) 224.
10. E. I. Kamitsos, M. A. Karakassides, Phys. Chem. Glasses 30 (1989) 19.
11. E. I. Kamitsos, M. A. Karakassides, G. D. Chryssikos, J. Phys. Chem. 91 (1987) 1073.
12. J. Krong-Moe, Phys. Chem. Glasses, 61 (1965) 46.
13. W. L. Konijnendijk, J. M. Stevels, Mater. Sci. Res. 12 (1977) 259.
14. T. Iliescu, S. Simon, D. Maniu, I. Ardelean, J. Molec. Struct. 294 (1992) 201.
15. B.N. Meera, J.Ramakrishna, J. Non-Cryst. Solids 159 (1993) 1.
16. L. Baia, R. Stefan, J. Popp, S. Simon, W. Kiefer, J. Non-Cryst. Solids 324 (2003) 109.

STUDIA UNIVERSITATIS BABES-BOLYAI, PHYSICA, XLIX, 3, 2004

GROWTH OF PERIODIC ARRAYS OF CARBON NANOTUBES AND THEIR CHARACTERIZATION BY SCANNING ELECTRON MICROSCOPY AND RAMAN SPECTROSCOPY

ZS. SZEKRÉNYES, AL. DARABONT and S. AŞTILEAN

Faculty of Physics, Babeş-Bolyai University, Cluj-Napoca, Romania

ABSTRACT. Nickel nanoparticles were fabricated *via* nanosphere lithography and successfully employed in chemical vapor deposition chamber to catalyze the growth of large arrays of carbon nanotubes on solid substrate. Spatial organization and structure of as prepared carbon nanotubes were analyzed by scanning electron microscopy and Raman spectroscopy.

Introduction

Carbon-based materials, such as graphite, diamond, diamond-like carbon, amorphous carbon, fullerenes, carbon nanotubes, and carbon nanofibes, are attractive materials due to their diverse forms and remarkable properties, and have tremendous applications in many mechanical, physical, chemical, electrochemical, and microelectronic fields [1]. Carbon nanotubes (CNTs) are of particular interest for field-emission flat-panel displays due to their low operation voltage and high-emission current [2]. However, the growth of well-aligned, periodic CNTs is a critical issue for such potential applications. The first large arrays of aligned CNTs of controlled diameter and length were made in 1998 using plasma enhanced chemical vapor deposition (CVD) [3]. In that case spacing and location of CNTs were predefined on the substrate by using a pattern of nickel (Ni) nanoparticles fabricated via electron beam lithography. Although electron beam, x ray, and scanning tunneling microscope lithography are techniques able to yield submicron dots with perfect edge definition, they are limited by the low processing speed and high cost. Other approaches, like magnetron sputtering or electrochemical deposition on porous and masked/prepatterned substrates, were attested as alternatives to yield catalytic Ni/Fe/Co dots with some inconveniences related to a poor control over dot position and size.

Recently, a new technique called nanosphere lithography (NSL) has been emerged to generate regular arrays of noble-metal dots with well-controlled size, shape and interparticle spacing [4-6]. A monolayer of close packed nanospheres is used as metal deposition mask in order get periodic arrays of triangular nanoparticles on a solid substrate. The NSLS appear to be much simpler, faster and less costly compared to above methods. To our best knowledge there are only few reports in literature focused on the synthesis of CNTs by using regular arrays of catalytic nanoparticles made *via* NSL. Z.F. Ren and co-workers was the first group to apply NSL to carbon nanotube growth [7].

Here, we report our first work aiming to get periodic arrays of CNTs by using NSL. Firstly, we employ self-assembled polystyrene nanospheres as lithographic masks to fabricate periodic arrays of nickel nanoparticles. Secondly, a thin nickel film is deposited by electron beam evaporation through nanoholes exhibited by the polystyrene mask, and, subsequent removal of the nanospheres leaves an array of triangular nickel nanoparticles on substrate. Then, we successfully employed these nickel nanoparticles in chemical vapor deposition chamber to catalyze the growth of large arrays of carbon nanotubes on a solid substrate. Spatial organization and structure of carbon nanotubes were analyzed by scanning electron microscopy and Raman spectroscopy.

Experimental

In the first step of our experiment we had to define both the position and size of catalytic nickel nanoparticles on silica substrate. To accomplish that we employ NLS because is fast, cheap and efficient to yield periodic arrays of dots of 20–100 nm lateral size [8-9]. Specifically, we used a single layer of self-assembled polystyrene nanospheres as lithographic masks to deposit a thin nickel film on silica substrate. In order to get lithographic masks, water suspension of polystyrene nanospheres of 390 nm diameter was dropped onto cleaned and functionalized silica substrate and placed in an oven at 45 ^{0}C to evaporate water and initialize ordering of polystyrene nanoparticles [9]. Fig. 1 shows a SEM picture with self-assembled polystyrene nanospheres.

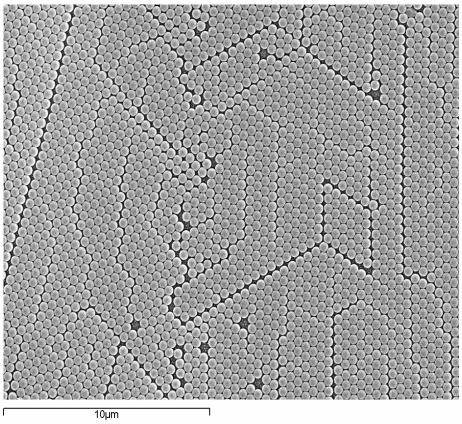

Fig. 1. SEM picture of self-assembled polystyrene nanospheres (scale bar represents 10 µm)

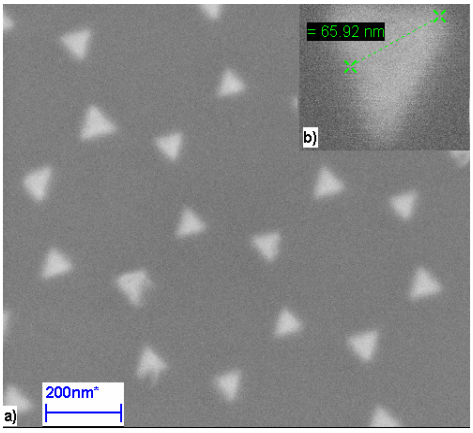

Fig. 2. SEM image of regular nickel dots left left on silica substrate after removing polystyrene spheres

In a second step we used an electron beam evaporation system (tungsten filament working at 5 KV voltage and pressure of 10^{-6} Torr) to deposit a nickel film of 30 nm thickness through predefined holes made in the polystyrene mask. Finally, polystyrene nanospheres were removed by dissolution in toluene and we got regular arrays of nickel dots on substrate, as can be seen in Fig. 2. The metric of nickel nanoparticle is directly defined from the mask geometries in Fig. 1. In a

third step it follows the chemical vapor deposition process and carbon nanotubes synthesis. This process was conducted in an oven heated at 875 ^{0}C under a continue flow rate of 1 ml/minute for benzene and 500 l/h for argon as inert gas. The topography and structure of synthesized CNTs were analyzed *via* scanning electron microscopy (SEM) and Raman spectroscopy. SEM images were collected using a JEOL electronic microscope and FT-Raman spectra were recorded in back scattering configuration with a Bruker Equinox 55 spectrometer equipped with an integrated FRA 106 Raman module. The experimental resolution was of 2 cm^{-1} and radiation of 1064 nm from a Nd-YAG laser was employed for excitation.

Results and discussions

A) SEM characterization of the carbon nanotubes

A piece of 25x25 mm silica substrate patterned with regular arrays of nickel dots (as seen in Fig. 2) was broken in 4 smaller pieces, each of them being subsequently kept in oven for different exposition times. Figures 3 and 4 show two representative SEM images of substrates kept in CVD chamber for 2 minutes (Fig. 3) and 15 minutes (Fig. 4), respectively. Both pictures prove clearly the formation of carbon nanotubes. From many similar pictures we infer diameteres between 10-50 nm, values which agree with lateral size of Ni particles given in Fig. 2. The length of CNTs varies from tens to hundreds of microns. Fig. 3 shows quasi-periodic arrays of globular forms and nanotubes, those positions correspond well with nickel dots distribution on the substrate. From the second picture (Fig. 4), the formation of periodic structure of CNTs appears to be less convincing. In our opinion the exposition time (15 minutes) was set too long, and, as a result of formation of other carbonic forms in-between nickel dots, the regular structure situated underneath is hidden. It is likely that beside well-defined arrays of CNTs, our synthesis produces many other carbon forms, most likely globular, nanofibers and nanoflakes.

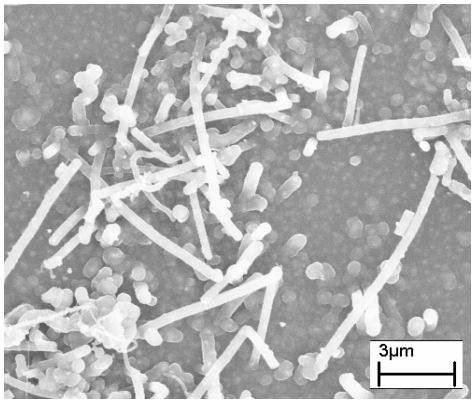

Fig. 3. Carbon nanotubes growth by chemical vapor deposition on nickel dots arrays. The exposition time in CVD chamber was 2 minutes.

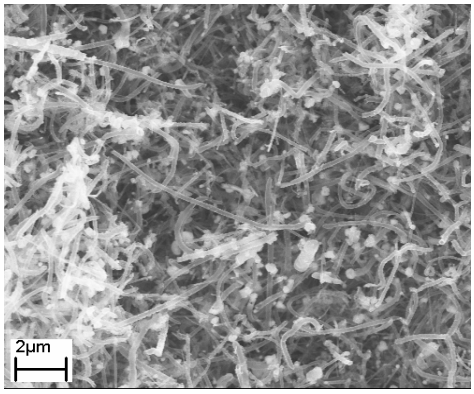

Fig. 4. Carbon nanotubes growth by chemical vapor deposition on nickel dots arrays. The exposition time in CVD chamber was 15 minutes.

Our present research is focused on finding solutions to remove such carbonic forms or to reduce their formation.

B) FT-Raman characterization

Raman spectroscopy is a standard nondestructive tool for the structural characterization of different carbon materials [10]. The Raman spectrum of as synthesized carbon nanotubes is presented in Fig. 5. In the first order Raman spectra of carbon nanotubes, the dominant features are the radial breathing modes (RBM) located in the 80– 400 cm^{-1} range and the tangential modes located in the 1530– 1610 cm^{-1} range [10,11]. Both these features occur indeed in Fig. 5.

The dominant feature in the spectrum is the first-order tangential band (T-band) occurring at 1591 cm^{-1}. The line broadening is attributed to laser-induced electronic resonances and to the coupling between phonons and conduction electrons in metallic nanotubes. Therefore from this line shape, we infer that the dominant contribution to the spectrum comes from metallic nanotubes. It is known that RBM for an isolated nanotube depends on the nanotube diameter d in accordance with $d=A/\omega$, where A is a constant (A=234 cm^{-1}) and ω is the RBM frequency, independent of the chirality of the nanotube. The large structured features we show in Fig. 5 in the 123-481 cm^{-1} range can be assigned to RBM frequencies in nanotubes of smaller diameters than nickel nanoparticles size.

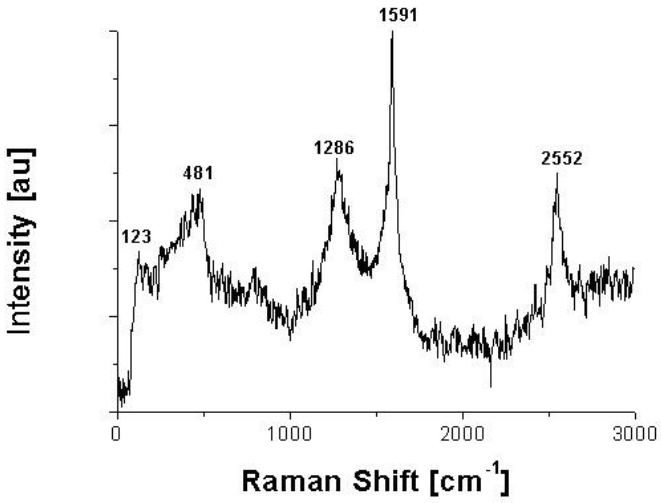

Fig. 5. We observe a strong first-order band at 1591 cm^{-1} (corresponding tangential mode region), a weaker band at 1286 cm^{-1} and a reasonably sharp second order Raman bands at 2552 cm^{-1}.

Surprisingly, in other spectra (results not shown) no radial breathing mode was present, which can be due to the relatively large diameters of CNTs (> 5 nm) or breaking of resonance conditions. An unusual intense band is observed at 1286 cm^{-1}, which exhibits an asymmetric profile in its low frequency side. The mode is usually assigned in literature to a disorder structure with nanometric size, such as carbon nanoparticules, amorphous carbon or defects in CNTs but also to an intense D band

verifying the presence of single-wall CNTs in our sample. As a matter of fact that a well-defined second order Raman band is observed at 2552 cm^{-1}, CNTs structural defects are likely to contribute to 1286 cm^{-1} band, though further investigation is needed. In any case the CNTs density is too high to be able to measure Raman spectra from identical and/or isolated single (-wall) nanotubes.

Conclusion

In conclusion, our contribution demonstrates clearly that nanosphere lithography is an operative and inexpensive technique able to grow arrays of CNTs with controlled location and spacing. We employed a single layer of self-assembled polystyrene nanospheres as a mask for subsequent nickel dots deposition on silica plate. CNTs were successfully grown on nickel dots exposited to chemical vapor deposition. Spatial organization and structure of as prepared carbon nanotubes were successfully analyzed by scanning electron microscopy and Raman spectroscopy.

Acknowledgements

We thank T. Petrişor, T. Petrişor jr. and M. Gabor for their help with the nickel film deposition and SEM images.

REFERENCES

1. R. Saito, G. Dresselhaus, and M. S. Dresselhaus, *Physical Properties of Carbon Nanotubes,* Imperial College, London, (1998).
2. R. H. Baughman, A. A. Zakhidov, and W. A. de Heer, Science 297, 787 (2002).
3. Z. F Ren,.; Z. P. Huang, J. W Xu, J. H. Wang, P. Bush, M. P. Siegal, and P. N. Provencio, Science 282, 1105 (1998).
4. T.R. Jensen, M. Duval Malinsky, C.L. Haynes, and R.P. Van Duyne, J. Phys. Chem. B 104, 10549 (2000).
5. C.L. Haynes and R.P. Van Duyne, J. Phys. Chem. B 105, 5599 (2001).
6. W.A. Murray, S. Astilean, and W.L. Barnes, Phys. Rev. B 69 165407 (2004).
7. Z.P. Huang, D.L. Carnahan, J. Rybczynski, M. Giersig, M. Sennett, D.Z. Wang, J.G. Wen, K. Kempa, and Z.F. Ren, Appl. Phys. Lett. 82, 460, (2003)
8. M. Baia, L. Baia, and S. Astilean, Chem. Phys. Lett, in press, (2005).
9. C.A. Farcau, Felicia Toderas, S. Astilean, in “Proceedings of Advanced Spectroscopies on Biomolecular and Nanostructured Systems”, Cluj-Napoca, 19-22 Sept. 2004, paper published in Studia, Seria Physica, UBB Cluj-Napoca (2004).
10. M. S. Dresselhaus, G. Dresselhaus, Ph. Avouris (Eds.): Carbon Nanotubes, Topics Appl. Phys. 80, 213 (2001).
11. P. Corio, S.D. M. Brown, and A. Marucci, M.A. Pimenta, K. Kneipp, G. Dresselhaus, and M. S. Dresselhaus, Phys. Rev B 61, 13202 (2000).

STUDIA UNIVERSITATIS BABES-BOLYAI, PHYSICA, XLIX, 3, 2004

RAMAN CHARACTERIZATION OF CARBON NANOSTRUCTURES OBTAINED BY CCVD METHOD

M. BAIA[1], C. POPA[1], T. ILIESCU[1], D. LUPU[2], A. R. BIRIŞ[2], A. WEIDENKAFF[3], C. DIECKER[3] AND W. KIEFER[4]

[1]Molecular Spectroscopy Dept., Faculty of Physics, Babeş-Bolyai University, 400084 Cluj-Napoca, Romania
[2]National Institute for Research and Development of Isotopic and Molecular Technologies, P. O. Box 700, Cluj-Napoca, Romania
[3]Institute of Solid State Chemistry, Universität Augsburg, D-86159 Augsburg, Germany
[4]Institute of Physical Chemistry, Universität Würzburg, D-97074 Würzburg, Germany

ABSTRACT. The conventional catalytic chemical vapor deposition (CCVD) method with electric outer furnace heating as well as induction heating (IH) was employed for the synthesis of carbon nanostructures. The as obtained samples were characterized by Raman spectroscopy, using several excitation energies, and it was found that they are single wall carbon nanotubes of different diameters. The samples obtained with the CCVD-IH method are more abundant but they are less pure as compared to those obtained with the conventional CCVD method with outer furnace. From the analysis of the Stokes and anti-Stokes spectra it was found that the samples contain a mixture of metallic and semiconducting tubes, with a higher rate for the semiconducting ones.

Introduction

Because of their tremendous potential for future technological applications, carbon nanotubes are presently one of the most exciting molecular systems. Their exceptional electronic and mechanical properties make them the best candidates for future nano-scale electronic devices and composite materials having a strong resistivity for minimum weight [1].

The procedures most commonly used for single-wall nanotube (SWNT) production include arc discharge, laser ablation and catalytic decomposition of carbon-containing compounds over a metal catalyst (CCVD), which attracted much attention because it appears to be promising technique for scalling-up the production process at a relatively low cost. By using the induction heating (IH) during the laser synthesis process of SWNT it was demonstrated the great ability of this particular heating mode to control the reaction temperature even at high temperatures, whithout significant heat transfer to the quartz tube containing the reaction region [2]. This fact stimulated us to explore the possibilities of coupling the induction heating with the CCVD method in the synthesis of carbon nanotubes.

One of the most powerful techniques employed for the characterization of SWNTs is Raman spectroscopy. Raman spectra of SWNTs exhibit several important bands: a radial breathing mode in the low wavenumber range, whose position can be used to calculate the nanotube diameter, a so-called D-band at around 1350 cm^{-1}, and a tangential mode G band appearing in the 1400-1700 cm^{-1} region [3]. Because

the Raman intensity is strongly affected by resonance phenomena, the radial breathing mode peaks obtained at a laser energy do not reflect the entire diameter distribution of the sample but rather the subset of nanotubes that are in resonance with the laser photons. Therefore, it is necessary to probe the SWNTs with several excitation energies. The anti-Stokes spectra of SWNTs are unique relative to other crystalline systems, especially in exhibiting large asymmetries with regard to their corresponding Stokes spectra [4]. According to simple Raman theory and demonstrated by many experiments, one expects the anti-Stokes spectrum to display the same Raman shifts as the Stokes-spectrum. The asymmetry of the anti-Stokes spectra of SWNTs is due to the unique resonant enhancement phenomena arising from their one-dimensional (1D) electronic density of states.

The aim of the present work was to distinguish between the samples prepared by CCVD method with electric outer furnace heating and those obtained with the CCVD-IH technique regarding the SWNTs production, their diameter distribution, purity and electronic features by using Raman spectroscopy.

Experimental

All carbon nanostructures have been prepared with the CCVD method. Samples denoted **1** and **3** have been obtained through the conventional CCVD technique with electric outer furnace heating, while for the samples **2** and **4** the CCVD-IH method has been employed.

The samples have been obtained by using the Fe:Mo:Al_2O_3 (1:0.2:16 weight ratios) catalyst prepared according to the literature [5]. The synthesis of the samples **1** and **2** was conducted at 800^{o}C with 12 ml/min methane flow and 80 ml/min purified argon for 30 min, while in the case of samples **3** and **4** the synthesis was conducted at 850^{o}C for 60 min.

The Raman spectra were recorded with a Dilor LabRam spectrometer equipped with an Olympus LMPlan Fl 50 microscope objective. The 633 nm (1.96 eV) and 514 nm (2.41 eV) laser lines were employed for excitation with a power incident on the sample of 50 and 3 mW, respectively. The resolution was of about 2 cm^{-1}.

Results and discussion

TEM pictures of carbon nanostructures synthesized with the CCVD method with outer furnace (**1**) and IH (**2**) are displayed in Fig. 1.

The TEM images illustrate standard SWNTs organized in bundles mixed with isolated SWNTs. A close analysis of the TEM pictures shows that the carbon nanostructures are more abundant in the case of the CCVD-IH method and their quality is increased as compared to those obtained with the CCVD technique. These characteristics should be further revealed by Raman measurements.

Raman spectra of all samples recorded by using the 633 nm (1.96 eV) and 514 nm (2.41 eV) laser lines are presented in Fig. 2. By looking at the spectra one can remark the fingerprint bands of the carbon nanostructures.

Moreover, one can also observe the higher intensity of the Raman bands of the samples **2** and **4** that suggests the existence of more abundant SWNTs obtained by CCVD-IH method relative to those obtained with the conventional CCVD technique.

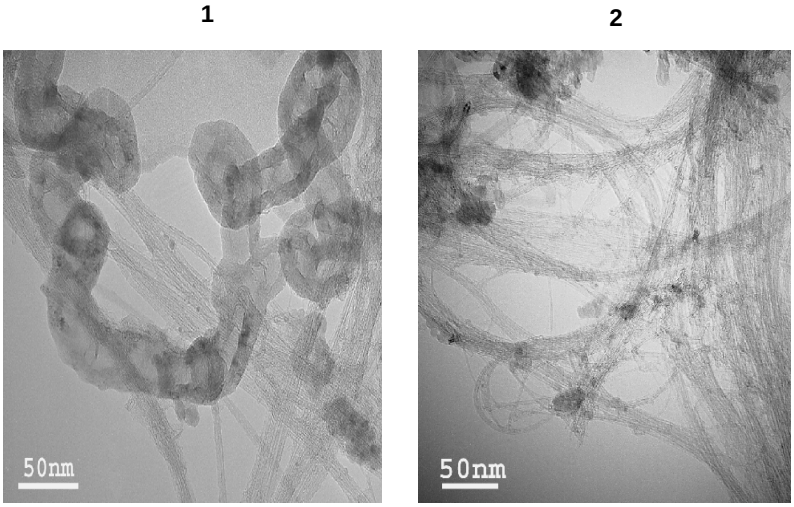

Fig. 1. TEM images of nanostructures obtained with the CCVD method with outer furnace (sample **1**) and CCVD-IH technique (sample **2**).

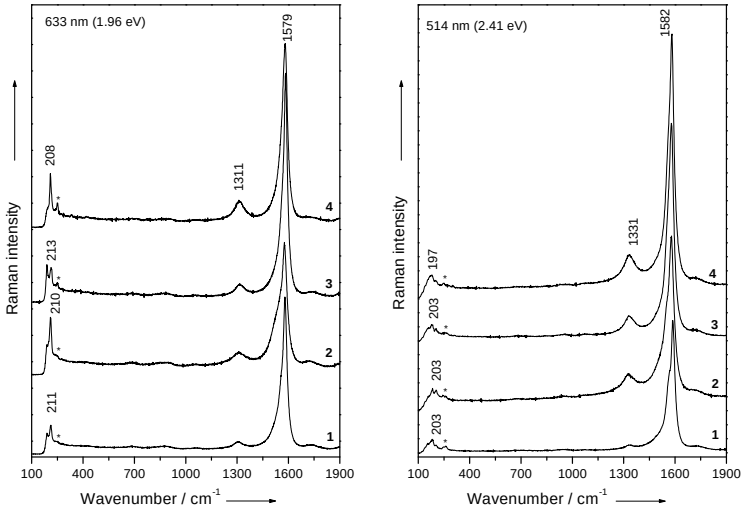

Fig. 2. Raman spectra of carbon nanostructures recorded with the 633 and 514 nm laser lines.

For an isolated SWNT, theoretical calculations have shown [6] that radial mode frequency $\omega_R^{'}$ exhibits a particularly simple dependence on the tube diameter $d^{'}$ as $\omega_R^{'} \approx 224cm^{-1} \cdot nm/d^{'}$. For a SWNT bundle, it has been shown that an additional constant term (14 cm^{-1}) is needed to include the effect of tube-tube interactions within a bundle. In this case [6], $\omega_R \approx 14 + 224cm^{-1} \cdot nm/d$.

In Table 1 we display the SWNT diameters calculated from the expression above and based on the observed radial breathing mode frequencies. By analyzing the data from Table 1 one can see that no significant differencies concerning the diameter distribution appear between the samples obtained with the different heating techniques.

It should be noted that the spectral features present in the radial breathing mode region around 250 cm^{-1} indicated with asterisk are associated with the catalyst/alumina [5].

Table 1.

Raman radial breathing mode and corresponding tube diameter.

Sample	Radial mode peaks (cm^{-1})		Tube diameter (nm)	
	λ = 633 nm	λ = 514 nm	λ = 633 nm	λ = 514 nm
1	188, 211	154, 180, 203	1.28, 1.13	1.6, 1.34, 1.18
2	188, 210	156, 182, 203	1.28, 1.14	1.57, 1.33, 1.18
3	188, 213	160, 179, 203	1.28, 1.12	1.53, 1.35, 1.18
4	188, 208	153, 179, 197	1.28, 1.15	1.61, 1.35, 1.29

The 1000-2000 cm^{-1} spectral region of the Stokes and anti-Stokes spectra of the samples **1** and **2** for two different laser excitation energies are shown in Fig. 3. As one can see the behavior of the Stokes and anti-Stokes spectra for the tangential band does not change significantly as a function of excitation energy and relative to one another. At both laser energies the Stokes and anti-Stokes spectra are almost similar and are typical of resonant Raman spectra of semiconducting nanotubes [4, 7] (strongest feature at about 1580 cm^{-1}). Small contributions from metallic nanotubes (the shoulder around 1550 cm^{-1}) can be also observed in the Stokes and anti-Stokes spectra of both samples for both excitation energies.

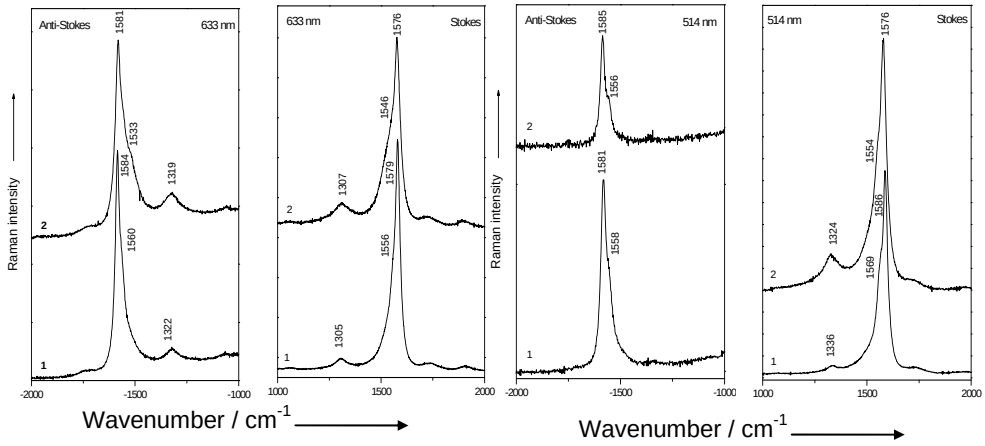

Fig. 3. Stokes and anti-Stokes spectra for samples **1** and **2** at 633 and 514 nm.

The Stokes and anti-Stokes spectra of the samples **3** and **4** for the 633 and 514 nm laser lines are shown in Fig. 4. As can be observed for both excitation energies the Stokes scattering appears mainly from resonant semiconducting nanotubes (strongest Raman line near 1580 cm^{-1}), whereas the anti-Stokes scattering benefits also from small resonance enhancement of metallic nanotubes, and therefore features near 1580 and 1560 cm^{-1} associated with metallic nanostructures appear at the anti-Stokes side.

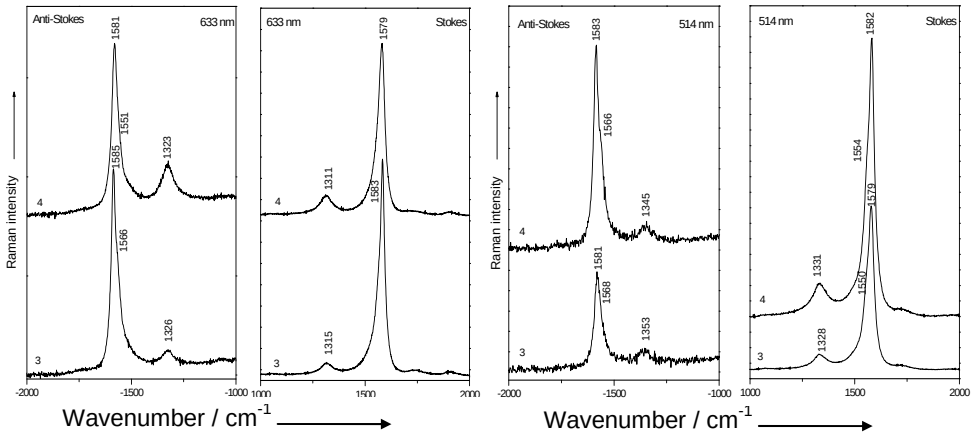

Fig. 4. Stokes and anti-Stokes spectra for samples **3** and **4** at 633 and 514 nm.

The Raman spectra can be used to qualitatively describe the purity of SWNTs. An increase in the ratio of the area of the tangential G peak to that of the D peak (G:D ratio) is correlated to increasing graphite crystallite size and a decrease in the amount of unorganized carbon in graphitic materials [8]. By comparing the calculated G:D area ratios for all samples for both laser energies it was found that the SWNTs obtained through the CCVD method are more pure that those obtained with the induction heating technique.

Conclusion

Carbon nanostructures have been obtained through the conventional CCVD method with electric outer furnace heating as well as induction heating (IH) and characterized by using TEM and Raman spectroscopy. It was shown that the samples produced by CCVD-IH method are more abundant but they are less pure as compared to the samples obtained by CCVD technique. The diameters of the SWNTs produced through both methods have been calculated and no significant differences have been evidenced. From the analysis of the Stokes and anti-Stokes spectra it was found that the samples contain a mixture of metallic and semiconducting tubes, with a higher rate for the semiconducting ones.

REFERENCES

1. J. L. Sauvajol, E. Anglaret, S. Rols, L. Alvarez, *Carbon*, **40**, (2002), 1697.
2. T. Gennett, A. C. Dillon, J. L. Alleman, K. M. Jones, M. J. Heben, *Mat. Res. Soc. Symp. Proc., (*2001), 633.
3. M. S. Dresselhaus, P. C. Eklund, *Adv. Phys.,* **49**, (2000), 705.
4. S. D. M. Brown, P. Corio, A. Marucci, M. S. Dresselhaus, *Phys. Rev. B*, **61**, (2000), 5137.
5. A. R. Harutyunyan, B. K. Pradhan, U. J. Kim, G. Chen, P. K. Eklund, *Nano Letters,* **2**, (2002), 525.
6. A. M. Rao, J. Chen, E. Richter, U. Schlecht, P. C. Eklund, R. C. Haddon, U. D. Venkateswaran, Y. K. Kwon, D. Tomanek, *Phys. Rev. Lett.,* **86**, (2001), 3895.
7. K. Kneipp, H. Kneipp, P. Corio, S. D. M. Brown, K. Shafer, J. Motz, L. T. Perelmen, E. B. Hanlon, A. Marucci, G. Dresselhaus, M. S. Dresselhaus, *Phys. Rev. Lett.,* **84**, (2000), 3470.
8. K. L. Strong, D. P. Anderson, K. Lafdi, J. N. Kuhn, *Carbon*, **41**, (2003), 1477.

STUDIA UNIVERSITATIS BABES-BOLYAI, PHYSICA, XLIX, 3, 2004

FABRICATION AND CHARACTERISATION OF SILVER-POLYSTYRENE TWO-DIMENSIONAL COMPOSITE NANOSTRUCTURES

C. A. FARCAU, FELICIA TODERAS, S. ASTILEAN

Babes-Bolyai University, Faculty of Physics,
400084 Cluj-Napoca, Romania

ABSTRACT. We report the fabrication of silver-polystyrene composite nanostructures via nanosphere lithography procedure. Both scanning electron microscopy (SEM) and optical measurements were employed to characterize the as fabricated samples. We are interested in their potential for operating as active substrates for surface-enhanced Raman scattering (SERS), fluorescence control and optical biosensing.

Introduction

In the last decade there has been an increased interest in the development of nanostructured materials and study of their size-dependent properties. These nanostructures show novel optical, electrical, magnetic, thermal properties all being determined by the nanoscale features they present. The reduced dimensions, degree of ordering, interparticle interactions, chemical or biological function are the main parameters which control these properties. One of the main directions in nanosciences is the investigation and exploitation of these properties with the aim to develop performant (nano)devices. That is why it is very important to design and develop methods to prepare in a controlled manner nanostructures of well-defined size, shape, composition, chemical or biological functions.

Regular two-dimensional (2D) arrays of metallic nanoparticles or thin metallic films with nanoscale features are examples of nanostructures that can exhibit interesting physics resulting from the behavior of the free electrons confined in these systems. It is known that contrarily to a planar dielectric-metal interface, in a nanostructured metallic film, surface plasmonic (SP) modes can be excited by simply illuminating the film with a laser beam [1]. The relevant principle that governs the coupling between a laser photon and a surface plasmon is given by the momentum matching conditions. In the planar case the photon wavevector is always smaller than the SP momentum. The periodicity on the scale of visible wavelengths enables photons to scatter increasing their momentum, thus the SP momentum can be matched. Therefore the fabrication of metallic nanostructured films or 2D arrays of nanoparticles with a high degree of ordering is one of the challenges of nanotechnology.

There are two possible approaches to build these metallic nanostructures: the so called top-down and bottom-up techniques. The first category includes photolithography, holographic interferometry, electron beam lithography, X-ray lithography. Recent development of scanning tunneling microscopy, atomic force microscopy and scanning probe lithographic techniques shows also great promise [2]. The alternative for these hard, expensive, high sample cost techniques comes from nanosphere lithography (NSL), which is a powerful fabrication technique to inexpensively produce nanoparticle arrays with well controlled shape, size and interparticle spacing.

In this paper we report the fabrication of a silver-PS composite nanostructure obtained via nanosphere lithography. We obtained highly ordered 2D arrays of 400 nm diameter PS nanospheres by using the simplest experimental setup. What we obtained is a silver nanostructured film on top of the nanosphere array. Both scanning electron microscopy (SEM) and optical measurements were employed in order to characterize the samples.

Experimental

We used 24x24mm glass microslides as substrates. First the substrates have to be carefully cleaned and functionalized. This process comprises several steps: first the glass slides are sonicated in isopropylic alcohol for 30min for degreasing. Afterwards the slides are treated in piranha solution (three parts 95% H_2SO_4 and one part 30% H_2O_2) for 24h followed by rinsing ultrapure water. This is followed by functionalization of the glass surface by sonication in a mixture of ultrapure $H_2O/NH_4OH/H_2O_2$ in a 5:1:1 volumic ratio. This last step is very important because it yields a hydrophilic surface, due to the –OH groups attached to it, without which the drop-coating would be impossible. The so derivatized substrates are stored in deionized, ultrapure water until nanosphere deposition. A suspension of polystyrene nanospheres was dropped onto the cleaned and functionalized substrate (Fig.1A).

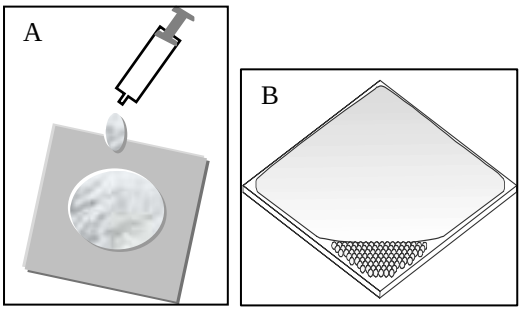

Fig.1. Preparation of periodic arrays of PS spheres: (A) drop-coating, and (B) self-assembling of the spheres

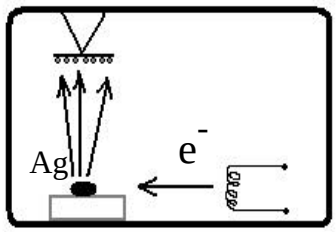

Fig.2. Schematic representation of the vacuum chamber of the vapor deposition system

The volume of solution that is directly deposited on the substrate in order to cover its entire surface can be determined from simple geometric considerations, and is $V = \mathrm{A}\frac{L^2 D}{c}$; L^2 is the substrate area, D is the diameter of the spheres, c is the volume concentration of the PS solution and A is a numeric constant. The coated substrate is placed on a glass plate and put in an oven at a slight angle to initialize ordering along a particular edge (Fig.1B). The temperature is maintained constant at 65^0C. Evaporation of the water takes about one hour. We prepared several samples, and used the best three of them for their characterization. A sample was kept as it is, and on the other two samples we deposited, by means of vacuum evaporation, silver films of different thickness, 30nm and 60nm respectively. A schematic representation of the electron beam evaporation system is shown in

figure 2. It must be mentioned that silver is deposited on top of the nanospheres and directly on the glass substrate also, through the interstices between the spheres. Therefore what we obtained is a composite nanostructured material consisting of an array of silver triangular nanoparticles deposited directly on the substrate, an array of PS spheres, and finally a silver film on top of them.

We measured transmission spectra of each of the three probes by the use of a spectrophotometer (JASCO-530). Spectra were taken for three different incident angles: normal incidence, 20^0 and 40^0 incident angles. SEM imaging (JSM-5510) was also employed to check the topology of the samples.

Results and disscution

In the literature it is generally accepted that the mechanism and the governing forces of the 2D particle assembly in evaporating wetting films involve a two-stage process: (1) formation of a nucleus, under the action of attractive capillary immersion forces, and (2) crystal growth, through convective particle flux caused by the water evaporation from the already ordered array [3]. This implies that the 2D crystal nuclei are formed under the capillary attraction arising when the tops of the spheres protrude from the water layer. The origin of the lateral capillary forces is the overlap of perturbations in the shape of the liquid surface surrounding the PS nanospheres. The dynamics of ordering is strongly dependent on the evaporation rate [9], which we control only by choosing the suitable volume of the glass covering our coated substrate and the right temperature.

The first proof that the regular array was formed is given by the naked eye. The as prepared probes show in reflection beautifully iridescent colours of green, blue, violet depending on angle of observation. This phenomenon is explained in terms of diffraction on a two-dimensional grating. The various colours we can see at the same angle of observation are due to different domain orientations and to the fact that on the substrate there are several grating constants. Contrarily, if observed in transmission the probes appear to be brownish-red coloured.

Optical transmittance of the samples was measured for three different incident angles. As the reference we put a glass slide of the same type with the ones used as substrates. The upper spectrum in figure 3 corresponds to the first sample, the one with no silver deposited; the second and third ones from up to down are spectra of the samples with 30nm and 60nm silver film thickness respectively. Resonant phenomenon between the incident light and the eigenmodes of the regular array of nanospheres [4] are responsible for the clear dip around 480nm, observed in the uppermost spectrum. Its existence demonstrates the ordering of the spheres, bulk polystyrene film not being an absorber at these wavelengths. Diameter of the nanospheres and refractive index of polystyrene are parameters that determine the position of this dip, while polycrystallinity and defects play on its width.

Looking at the other two upper spectra in panels B) and C) a redshift of this dip is observed when increasing incident angle. As the angle of incidence increases the photon wavevector projection in the plane of the array also increases, meaning the increase of the incoming wavelength to match the eigenmodes of the PS lattice.

After silver deposition this dip shifts to lower wavelengths; this shift could be attributed to changes in the overall refraction index of the array, which affects the photonic bands of the crystal. The features observed at lower wavelengths of the spectrum could be associated with the apparition of higher orders of diffraction and excitation of surface plasmons modes. It is also clearly seen from the spectra that as the silver film gets thicker these features are more pronounced, the transmission being very much decreased. A strong dependence on the incident angle is observed below 575 nm. At larger wavelengths something more interesting happens: a new transmission gap appears as silver is deposited on the samples and the position of this dip depends only slightly on incident angle. In order to clarify this let us remember that during evaporation silver was deposited directly on the substrate also. This has led to the formation of a lattice of triangular nanoparticles. In a study of Van Duyne's group [5] for Ag triangular nanoparticles of 120nm perpendicular bisector and 46nm height an absorption peak at 638nm was observed. From ideal geometric calculations our particles should have a perpendicular bisector of about 95nm, but they are definitely larger (small divergence of the beam of depositing Ag atoms). In another study [6] for a similar array of triangular nanoparticles obtained with 390nm PS spheres a dip in the transmission at 615 nm was reported. According to these results and the fact that the position of the dip doesn't depend too much on angle of incidence, we believe that this dip can be attributed to localized surface plasmon resonant absorption of silver triangular nanoparticles.

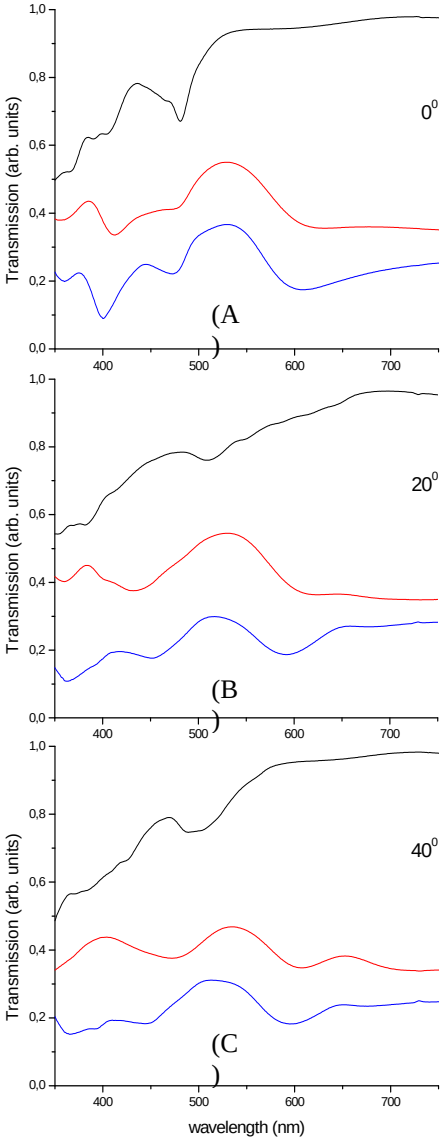

Fig.3. Transmission spectra of arrays of PS spheres: (A) normal incidence, (B) 20^0, (C) 40^0 incident angle; upper lines-no Ag, mid lines-30nm Ag, lower lines-60nm Ag deposited.

Employing transmission electron microscopy (TEM) reveals that the PS nanospheres form a regular hexagonal close packed array, as can be seen in figure 4A. A few domains where the spheres form a rectangular lattice can also be

observed. The polycrystallinity and formation of rectangular array domains is due to the fact that the growth of the hexagonal lattice starts in more than one point at a time. If a number of spheres are confined between two or more such hexagonal domains they are forced to form a rectangular array.

In higher magnification images (not displayed here) it can be seen that the silver film follows the morphology of the PS spheres, which appear to be covered in a fluffy material.

There are some zones on the probe where a multilayer structure occurred in the process of self-assembling (fig.4B). This is a clear indication that this self-assembling method could be further improved for the fabrication of 3D photonic crystals.

The interesting defects in figure 4C should be objects of further investigations. Line defects could find applications as waveguides and the places where a sphere is missing could support localized optical modes. For example placing a molecule in one of these “hot-sites” should modify its fluorescence lifetime.

In some of the defect regions of the probe some of the spheres felt out from the substrate after the silver deposition. It can be seen in figure 4C that in this region a metallic film with nanoholes is obtained. These nano-apertures where shown to be ideal for isolating individual nanometer-sized objects in luminescence studies [7].

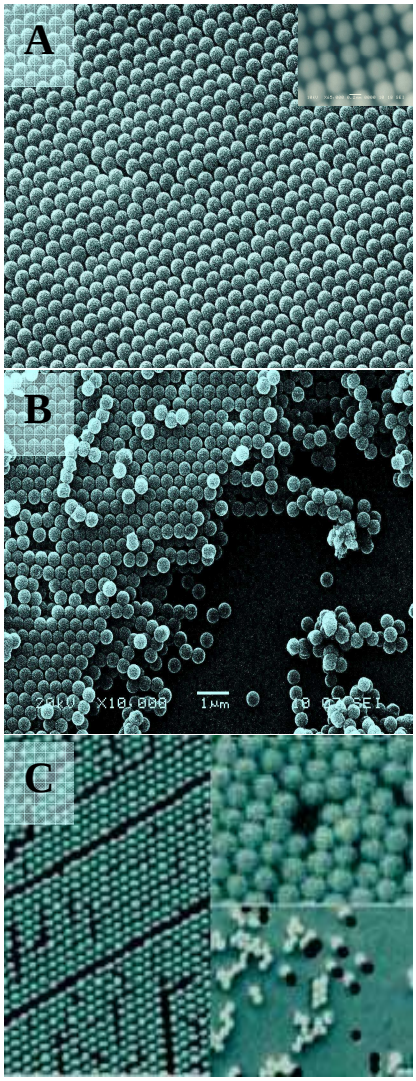

Fig.4. TEM images of self-assembled PS spheres: (A) monolayer; inset shows a rectangular array domain, (B) multilayer, and (C) some defects

Conclusions

Regular arrays of 400 nm diameter PS nanospheres on solid substrate were prepared by a self-assembling method. A thin nanostructured silver film on top of the nanosphere array was obtained by evaporative deposition and characterized by optical transmission spectra and scanning electron microscopy. As the optical response of these nanostructures is dominated by the excitation of surface plasmons, we are investigating their potential for operating as active surfaces in surface-enhanced Raman scattering (SERS), fluorescence control and optical biosensing.

REFERENCES

[1] W. Knoll, *Annu. Rev. Phys. Chem*., 49, (1998), 569-638.
[2] C. L. Haynes, R. P. Van Duyne, J. Phys. Chem. B, 105, (2000) 5599-5610.
[3] Peter A. Kralchevsky and Nikolai D. Denkov, *Current Opinion in Colloid & Interface Sci*. 6, (2001) 383-401.
[4] T. Fujimura, T. Tamura, T. Itoh, C. Haginoya, Y. Komori and T. Koda, Appl. Phys. Lett., Vol. 78, No. 11, (2001).
[5] T. R. Jensen, M. Duval Malinsky, C. L. Haynes, and R. P. Van Duyne, *J. Phys. Chem. B, 104,* 2000**,** 10549-10556.
[6] W. A. Murray, S. Astilean, and W. L. Barnes, Phys. Rev. B, 69, 2004, 165407-165414.
[7] U. Hakanson, J. Persson, F. Persson, H. Svensson, L. Montelius, M. K-J. Johansson, *Nanotechnology*, 14, (2003), 675-679.

STUDIA UNIVERSITATIS BABES-BOLYAI, PHYSICA, XLIX, 3, 2004

NANOSCALE HEAT TRANSFER FOR ENERGY CONVERSION APPLICATIONS

D. RISTOIU*[1]*, O. COZAR[2], C. COSMA[1], T. RISTOIU[3], D. CENAN[3]

[1]University Babes-Bolyai, Faculty of Environmental Science, M. Kogalniceanu 4, 400084, Cluj-Napoca, Romania,
[2]University Babes-Bolyai, Faculty of Physics, M. Kogalniceanu 1, 400084, Cluj-Napoca, Romania,
[3]Technical University, Cluj-Napoca, Constantin Daicoviciu 15, 400020 Cluj- Napoca, Romania

ABSTRACT. Experimental and theoretical studies in recent years have shown that heat transfer in nanostructures differs significantly from in macrostructures. Solid-state energy conversion technologies such as thermoelectric and thermoionic refrigeration and power generation require materials with low thermal conductivity but high electrical conductivity and Seebeck coefficient, which are difficult to realize in bulk semiconductors. This paper summarizes some of the past experimental and modeling work and our current understanding of the heat conduction mechanisms in nanostructures. Applications of the nanoscale heat conduction phenomena in energy conversion and conversion between nanoscale and macroscale.

Introduction

Modern technology has enabled the fabrication of materials and devices with characteristic dimensions of a few nanometers. Examples are superlattices, nanowires, and quantum dots. At these length scales, the familiar continuum Fourier law for heat conduction is expected to fail due to both classical and quantum size effects [1-4]. Heat conduction in dielectric materials and most semiconductors is dominated by phonons. Size effects appear if the structure characteristic length is comparable to or smaller than the phonon characteristic lengths. Two kinds of size effects can exist: the classical size effect, when phonons can be treated as particles, and the wave effect, when the phonon wave phase information becomes important. Distinction between these two regimes depends on several characteristic lengths, which we discuss below.

Characteristic lengths and heat transfer regimes

From quantum mechanics, the energy carriers have both wave and particle characteristics. At macroscale, wave phenomena such as interference and tunneling usually do not appear and we often treat the energy carriers as particles. At nanoscale, however, wave effects become important and even dominant in some cases. A key question is when one should start to consider the wave characteristics. There are a few important characteristic length and time scales that determine the answer to this question, including the mean free path, the phase coherence length, the wavelength, and the thermal (de Broglie) wavelength, which we will explain.

* dristoiu@chem.ubbcluj.ro

The mean free path is the average distance that energy carriers travel between successive collisions, such as the phonon-phonon collision in a dielectric material and the electron-phonon collision in a conductor or semiconductor. The corresponding average time between successive collisions is the relaxation time. Direct calculation of the mean free path is generally difficult, particularly for electron and phonon transports in solid. The kinetic theories and experimental thermal conductivity, *k*, data are often used to estimate the mean free path. The important characteristic lengths of phonon heat conduction are the mean free path, the wavelength, and the phase coherence length [5]:

$$k = \frac{1}{3} C v^2 \tau = \frac{1}{3} C v \Lambda \qquad (gases) \tag{1}$$

$$k = \frac{\pi^2 n k_B^2 T}{m v_F} \Lambda \qquad (electrons\ in\ metals) \tag{2}$$

$$k = \frac{1}{3} \int_0^{\omega_{\max}} C_\omega v_\omega^2 \tau_\omega d\omega = \frac{\Lambda}{3} \int_0^{\omega_{\max}} C_\omega v_\omega d\omega \qquad (phonons) \tag{3}$$

where *C* is the volumetric specific heat (i.e., the specific heat per unit volume), τ is the relaxation time, *v* is the velocity of carriers, Λ is the mean free path, *m* is the electron mass, *n* is the electron number density, and v_F is the electron velocity at the Fermi surface. The integration in Eq. (3) is over all the phonon frequency and correspondingly, C_ω, v_ω, and τ_ω are the volumetric specific heat, the velocity, and the relaxation time at each frequency, respec-tively. This distinction is necessary because phonons are highly dispersive. If Eq. (1) is used to estimate the phonon mean free path, using the measured specific heat and the speed of sound, the mean free path can be an order of magnitude lower than that based on Eq. (3) [1-6].

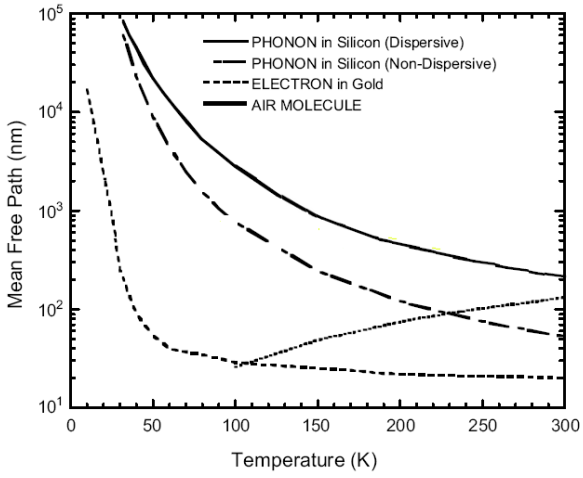

Figure 1. Mean free path for representative energy carriers.

In Figure 1, we show the mean free path in representative media. Also shown in this figure is an example of the phonon mean free path in silicon estimated based on Eq. (1), using the reported data on specific heat and the speed of sound, which is an order of magnitude shorter than that estimated from considering the phonon dispersion.

Heat conduction in nanostructures

Thermal boundary resistance

For heat conduction perpendicular to an interface, phonon reflection implies that energy transfer by heat carriers will be reduced compared to the case when there is no interface, or, equivalently, a resistance for heat flow exists at the interface. This phenomenon, called Kapitza resistance or thermal boundary resistance, has been known since the pioneering work of Kapitza for liquid helium-solid interfaces [8]. Extensive experimental and theoretical studies have been carried out in the past. At extremely low temperature when the phonon thermal wavelength is long, the interface reflection is close to specular, models based on acoustic reflection and refraction for thermal boundary resistance agrees well with experimental data. At room temperature, however, the phonon wavelength is short and diffuse scattering can be dominant. There is no proven easy way to model the phonon reflectivity and transmissivity for such diffuse scattering processes. For two solids in perfect contact, the thermal boundary resistance is on the order of 10^{-8}-10^{-9} m^2K/W. Such a thermal boundary resistance corresponds to the thermal resistance of a solid layer of thickness 1 nm - 1 μm with a bulk thermal conductivity of 1-100 W/m K. When dealing with films of comparable thickness or smaller, the interface thermal resistance contributes significantly to the total thermal resistance.

Heat conduction in thin films, nanowires, and nanotubes

A thin film has two interfaces. If the mean free path is longer than the film thickness, phonons will be scattered more frequently at the interfaces and may experience multiple scattering events. For heat conduction perpendicular to the film plane (cross-plane), the phonon reflection and the corresponding thermal boundary resistance phenomena add additional resistance to the heat flow, which is manifested as a smaller effective thermal conductivity. Along the film-plane direction (in-plane), the thermal conductivity will be reduced if the interface scattering is diffuse, because diffuse scattering means some phonons that originally travel along the film plane direction are redirected backward. However, if the interface is specular, the classical size effect model leads to an in-plane thermal conductivity of a free-standing film identical to that of the bulk material. This is because the thin film acts simply as a waveguide for the heat flow. When the film thickness is thinner than the thermal wavelength, wave effects may be important. However, lattice dynamics calculations show that wave effects on the energy density and group velocity lead only to a small reduction in thermal conductivity for specular interfaces [9], although there are also suggestions that the scattering mechanisms will be significantly changed, which leads to a lower thermal conductivity. Quite extensive experimental studies have been carried out on the thermal conductivity of thin films [1, 2, 10].

Thermal conductivity of nanowires is also attracting great interest. Naturally, the interest is in transport along the wire axis direction. If the surface of the wire is specular and there is no scattering inside the wire, energy transport is ballistic and phonon energy states are quantized. A universal phonon thermal conductance was predicted [12], and experimentally demonstrated at very low temperature under 0.8 K [13]. At slightly higher temperature (>3K), the diffuse interface scattering effects begin to appear.

Experimental data on single nanowires at near room temperature are just becoming available on some nanowires and indicate a significantly lower thermal conductivity, again suggesting the importance of diffuse interface scattering [13]. In contrast to nanowires, a free-standing single wall carbon nanotube has all the atoms on the surface and the phonons can only propagate along the axial direction [14]. This latter attribute also means that unlike a solid nanowire in which the phonon modes inside the wire can hit the boundary (assuming boundary scattering is strongly phase breaking), phonons on the carbon nanotubes sheet have no boundaries to interact with. In addition, the strong modification of the phonon dispersion can also change the scattering mechanisms. It is thus suggested that carbon nanotubes can have a thermal conductivity even higher than that of diamond. Measurements and simulation data so far vary widely. Measurements on an isolated multiwall carbon nanotubes lead to high thermal conductivity values [15], but tangled and aligned carbon nanotubes have values orders of magnitude smaller [16]. At this stage, reasons for such a large discrepancy are unclear. It is quite possible that although a free-standing nanotubes has high thermal conductivities, a nanotube embedded in a host sees increased interface scattering which reduces its thermal conductivity values.

Nanoscale heat transfer phenomena

With the discussion on various characteristic lengths and heat transfer regimes, we will now move on to discuss several size effects associated with three different modes of heat transfer. Because all energy carriers have both wave and particle characteristics, we will discuss first some general phenomena associated with transport in the coherent and incoherent regimes. For optical waves, a particularly interesting phenomenon is the total internal reflection when the refractive index of the incident medium is larger than that of the second medium and when the angle of incident is larger than the critical angle; that is [19], where n_1 and n_2 are the refractive indices of the two media. In this case, there is an evanescent field in the second medium that does not carry a net energy into the second medium. The evanescent field decays exponentially, $e^{-x/\Delta}$, in the second medium, with a characteristic decay length

$$\Delta = \frac{\lambda_o}{2\pi n_2 \sqrt{(n_1 \sin\theta_1 / n_2)^2 - 1}} \tag{10}$$

Although the example is given for an electromagnetic wave, the total reflection and the evanescent wave phenomena also exist for electrons and phonons. In addition to the evanescent wave, there can also exist surface waves that decay exponentially at both sides of the interface and propagate along the interface, such as surface plasmons which are mixtures of electron and photon waves and surface phonon-polaritons which are mixed states of photons and phonons, and surface acoustic waves [20]. Some of the impacts of surface waves on heat transfer processes have only recently begun to be explored [21, 22].

When there are two interfaces or the interfaces have closed topology themselves, such as the two interfaces of a thin film or the surface of a sphere/wire, the waves can experience multiple reflections inside the structure. If the phase of each reflection is preserved, the superposition of the waves creates interference/

diffraction effects. The new wave functions inside the structure can also be interpreted as new energy states from quantum mechanical point of view, which can also be obtained from solving the Schrödinger equation. If the interfaces are periodic (i.e., the structures are periodic), there can be regions (for specific wavelength and periodicity combination) in which the waves are completely cancelled and no wave exists, either in specific directions or in all the directions. An example is for electromagnetic waves traveling inside a periodic thin film structure, as shown in Figure 4. In the stop band region, the reflectivity is 100% and no waves at this frequency exist inside the film.

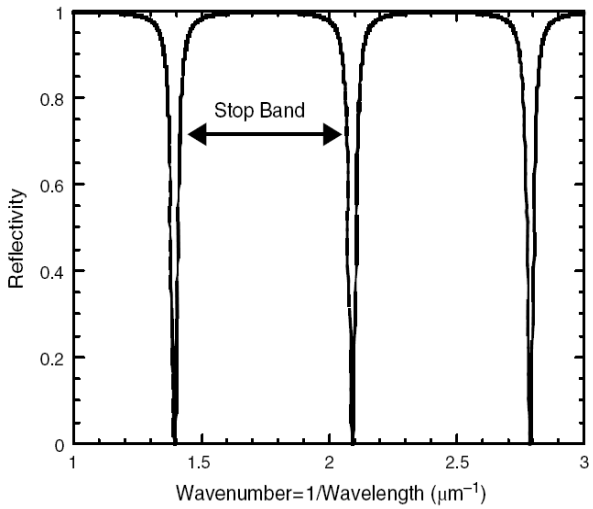

Figure 4. Calculated reflectivity of a Bragg reflector as a function of the incident photon wavelength. The refractive indices of each layer are 3 and 3.5 and the corresponding thicknesses are 417 and 352 Å for each layer, respectively.

The corresponding quantum phenomenon is the formation of electronic bandgaps that distinguish metals from semiconductors and insulators, due to the reflection of electrons in the periodic atomic potentials. Wave effects offer rich possibilities because the end results depend sensitively on the phase of the waves. By changing the structures slightly, one can significantly change the phase of the waves and thus potentially engineer the transport processes. However, the phases are not always preserved. Phase breaking scattering events inside the solid and at the interfaces can destroy the phases and thus the wave effects. In the incoherent transport regime, the interfaces can still impact the transport because of interface scattering. These interface scattering processes generally reduce the energy flux, which can be either a problem, as for the thermal management of electronic and photonic devices [3, 4], or a blessing for other applications that demand good thermal insulation, as for thermoelectric energy conversion [6, 11]. With these general pictures, we now move on to discuss some specific heat transfer phenomena observed in nanostructures.

Application to thermal-electric energy conversion

The nanoscale heat transfer phenomena discussed above have important implications for microelectronics, optoelectronics, data storage technologies, and energy conversion technologies [5]. An example is thermoelectric cooling and power generation based on the Peltier effect and the Seebeck effect, respectively [17]. The efficiency of a thermoelectric device is determined by the thermoelectric figure-of-merit of the material $\mathbf{ZT = \sigma S^2 T/k}$, where S is the Seebeck coefficient, σ is

electrical conductivity, k is the thermal conductivity and T is the absolute temperature. Currently, the best commercially available thermoelectric materials based on Bi_2Te_3 and its alloys have a ZT of around 1.

Thermoelectric devices based on this material cannot compete in performance with other well-established technologies for energy conversion. Several approaches have been explored to increase the thermoelectric figure-of-merit. Among those, low-dimensional thermoelectric materials structures such as quantum wells, superlattices and nanowires have been extensively investigated [18]. Quantum size effects on electrons in nanostructures can be utilized to improve the electron energy conversion capability [23], while the reduced thermal conductivity of nanostructures due to increased scattering of heat carriers from interfaces can be exploited in reducing the denominator of *ZT*. In the past two years, different low dimensional thermoelectric materials that show improved cooling capacity as compared to bulk materials have been reported [23, 24]. This suggests that phonon engineering is a primary tool in developing better thermoelectric materials. The wave effects on radiation heat transfer can be utilized for thermophotovoltaic energy conversion in different ways. Photonic crystals can have the spectral emissivity tuned to match the bandgap of semiconductor photovoltaic cells [25]. Tunneling effects are being explored to increase the energy density delivered from the heat source to the photovoltaic cells [13, 26]. Surface waves, such as surface plasmons and surface phonons, can be utilized for nearly monochromatic thermal radiation, which increases the efficiency of thermophotovoltaic energy conversion [7, 24, 27] as well as the energy density if small gaps are employed to take advantage of the high energy density of surface waves. The analysis and modeling of nanoscale heat transfer phenomena are challenging and complicated by several factors. One is that the mechanisms of nanoscale heat transfer are not well understood. Figure 3 shows different possible regimes of heat transfer. The determination of which regime a specific problem at hand falls into is nontrivial. Another major problem is that heat transfer rarely occurs only at nanoscale because eventually heat is dissipated into the macroscopic environment. Many heat transfer problems are multidimensional and multiscale spanning from nanoscale to macroscale.

SUMMARY

This paper discusses some nanoscale heat conduction phenomena. Nanoscale heat transfer phenomena can have significant implications for a variety of contemporary technologies, some undesirable as the classical size effects on the thermal management of microelectronics and optoelectronic devices, while others can be utilized to improve the data storage density or energy conversion efficiency, as in thermoelectric cooling and power generation and in thermophotovoltaic energy conversion.

Nanoscale heat transfer is also related to nanomaterial synthesis and nanofabrication and some emerging biotechnologies. Size effects occur when the heat carrier characteristic lengths, particularly the mean free path, become comparable or longer than the characteristic lengths of the structures or the transport processes (such as the diffusion length). A well-documented example is the reduced thermal conductivity in nanostructures such as thin films and superlattices, which has important implications for microelectronics, photonics, and thermoelectric energy

conversion. The nanoscale heat transfer processes also have implications for fast laser materials interactions and photothermal diagnosis techniques that remain to be explored further.

REFERENCES

1. Goodson, K.E. and Ju, Y., Ann. Rev. Mater. Sci. **29** (1999), 261.
2. Chen, G., Semicond.. & Semimetals. **71** (2001), 203.
3. Cahill, D.G., Ford, W.K., Goodson, K.E., Mahan, G.D., Majumdar, A., Maris, H.J., and Merlin,R. J. Appl. Phys. **93** (2003) 793.
4. Chen, G., Nanoscale Energy Transport and Conversion, (Oxford University Press, in press).
5. Chen, G., Borca-Tasciuc, D., Yang, R., "Nanoscale Heat Transfer," Encyclopedia of Nanoscience and Nanotechnology, H.S. Nalwa, Ed., (IAP Press, in press).
6. Chen, G., Phys. Rev. B., **57** (1998), 14958.
7. Grefett. J., R. Carminati, K. Joulain, J. Mulet, S. Malnguy, and Y. Chen, *Nature* 416, 61 (2002).
8. Little, W.A., Can. J. Phys., **37** (1959), 334.
9. Siegel, R. and J.R.Howell, "Thermal Radiation Heat Transfer." Hemisphere, Washington, 1992.
10. Yang, B. and Chen, G., Thermal Conductivity-2003, T.M. Tritt, Ed. (Kluwar Press, in press).
11. Yao, T., Appl. Phys. Lett. **51** (1987), 1798.
12. Angelescu, D.E., Cross, M.C., and Roukes, M.L., Superlattices Microstruct. **23** (1998), 673.
13. Li, D., Wu, Y., Kim, P., Shi, L., Yang, P., and Majumar, A., Appl. Phys. Lett., **83** (2003), 2934.
14. Dresselhaus, M.S., Dresselhaus, G., Eklund, P.C., Science of Fullerenes and Carbon Nanotubes, (Academic Press, San Diego, 1996).
15. Kim, P., Shi, L., Majumdar, A., and McEuen, P.L., Phys. Rev. Lett., **87** (2001), 215502
16. Hone, J., Whitney, M., Piskoti, C., and Zettl, A., Phys. Rev. B, **59** (1999) R2514.
17. Hyldgaard, P. and G. D. Mahan, "Thermal Conductivity." Technomic, Lancaster, UK, 1996.
18. Chen, G., *Trans. ASME, J. Heat Transf.* 119, 220 (1997).
19. Born, M. and E. Wolf, "Principles of Optics," 6th ed. Pergamon Press, Oxford, 1980.
20. Raether, H. "Surface Plasmons." Springer-Verlag, Berlin, 1998.
21. Grefett, J., R. Carminati, K. Joulain, J. Mulet, S. Malnguy, and Y. Chen, *Nature* 416, 61 (2002).
22. Hillenbrand, R., T. Taubner, and F. Keilmann, *Nature* 418, 159 (2002)
23. Venkatasubramanian, R., E. Siivola, T. Colpitts, and B. O'Quinn, *Nature* 413, 597 (2001).
24. Harman, T. C., P. J. Taylor, M. P. Walsh, and B. E. LaForge, *Science* 297, 2229 (2002).
25. Fleming, J. G., S. Y. Lin, I. El-Kady, R. Biswas, and K. M. Ho, *Nature* 417, 52 (2002).
26. Whale, M. D. and E. G. Cravalho, *IEEE Trans. Energy Convers.* 17, 130 (2002).
27. Chen, G., Dresselhaus, M.S., Fleurial, J.-P., and Caillat, T., Int. Materials Rev., 48 (2003), 45.

STUDIA UNIVERSITATIS BABES-BOLYAI, PHYSICA, XLIX, 3, 2004

NANOPARTICLES BASED ON THE GADOLINIUM COMPOUNDS AND THEIR POSSIBLE APPLICATION IN MEDICINE

ILIOARA COROIU[1], AL. DARABONT[2], M. BOGDAN[3], E. CULEA[1]

[1]*Physics Department, Technical University, Cluj-Napoca, Romania, coroiu@phys.utcluj.ro*
[2]*Faculty of Physics, Babes-Bolyai University, Cluj-Napoca, Romania*
[3]*National Institute for R& D of Isotopic and Molecular Technology, PO Box 700, R-3400, Cluj-Napoca, Romania*

ABSTRACT. $5Fe_2O_3 \cdot 3Gd_2O_3$ micropowder and $5Fe_2O_3 \cdot 3Gd_2O_3$–dextran nanoparticles were prepared and studied by magnetic susceptibility and nuclear magnetic resonance measurements. The magnetic behavior of $5Fe_2O_3 \cdot 3Gd_2O_3$–dextran nanoparticles in the presence of the blood was also examined. Interesting applications in varied biological fields can be estimated.

1. Introduction

In the last years the study of the nanoparticles has received increasing attention. Altered electrical, magnetical, electrooptical and chemical properties accompany reducing of particle size to nanometer range. These special properties are caused by the changes of band structure with quantum – size effect [1]. Besides their employment for obtaining new devices, techniques based on using magnetisable solid-phase supports have found application in numerous biological fields. Thus, it can mention the susceptibility contrast agents for Magnetic Resonance Imaging, drug targeting, molecular biology, hyperthermia-causing agents for cancer therapy, etc [2-3].

The purpose of this paper is to study the magnetic properties of $5Fe_2O_3 \cdot 3Gd_2O_3$ compound obtained as micropowder and as nanoparticles, by magnetic susceptibility and nuclear magnetic resonance measurements. The behavior of nanoparticles in the presence of the blood was also investigated.

2. Experimental

Synthesis of $5Fe_2O_3 \cdot 3Gd_2O_3$ microparticles was described in reference [4]. The size of the micropowder was about 0.02-0.1μm. The particles size was determined by width of the peaks from X-ray diffraction spectrum that were performed on a DRON3 diffractometer using CuK_α radiation.

The $5Fe_2O_3$ $3Gd_2O_3$ nanoparticles coated in dextran were prepared by microemulsion method [4]. The molecular weight of dextran was 40000. We appreciated that the median diameter of the dextran-stabilized particles was distributed between 800Å and 1200Å, whereas the ($5Fe_2O_3 \cdot 3Gd_2O_3$) core mean diameters were about 35-45Å.

Magnetic susceptibility measurements were performed on a Faraday type balance in the temperature range 80-300K.

Measurements of the longitudinal and transverse relaxation rates T_1^{-1} and T_2^{-1} respectively, have been carried out as a function of molar concentrations of particles. All measurements have been made at room temperature (about 25℃) at a proton Larmor frequency ν_0 = 90MHz. The pulsed NMR spectrometer utilized was a commercial Bruker SXP4/100 spectrometer. Transverse relaxation rates were measured using the Carr-Purcell method, while longitudinal relaxation rates measurements using the inversion recovery pulse sequence, 180°-τ-90°. All data exhibited single – exponential behavior.

R_1 and R_2 relaxivities, in $mM^{-1}s^{-1}$ were obtained from the least-squares determination of the slopes of plots $1/T_{1,2}$ versus molar concentration of the compound, using at least five independent measurements at several concentration between 0 and 2mM.

3. Results and discussion

Figure 1 shows the dependence of the inverse magnetic susceptibility as a function of temperature for the $5Fe_2O_3{\cdot}3Gd_2O_3$–dextran nanoparticles and also for the $5Fe_2O_3{\cdot}3Gd_2O_3$ micropowder. The data collapse to straight lines indicating that the magnetic susceptibility follows a Curie-Weiss type behavior.

$$\chi^{-1} = (T - \theta_p)/C \qquad (1)$$

where C is the Curie constant and θ_p is the paramagnetic Curie temperature. The solid lines in Figure 1 represent the computer fit of experimental data according to Eq. (1). These plots permitted to derive the two important magnetic parameters namely θ_p and C_m (the molar Curie constant). The values obtained for these constant are θ_p= -40K, C_m=103.68emu·K/mole for $5Fe_2O_3{\cdot}3Gd_2O_3$–dextran nanoparticles and θ_p= -52K, C_m=66.74emu·K/mole for $5Fe_2O_3{\cdot}3Gd_2O_3$ micropowder. The paramagnetic Curie temperature θ_p is a rough indicator of magnetic interaction between the iron and gadolinium ions (Fe^{+3}, Fe^{+2} and Gd^{+3}). The negative values obtained for θ_p suggest that the interaction between the magnetic ions is antiferromagnetic and its intensity is higher for the micropowder sample.

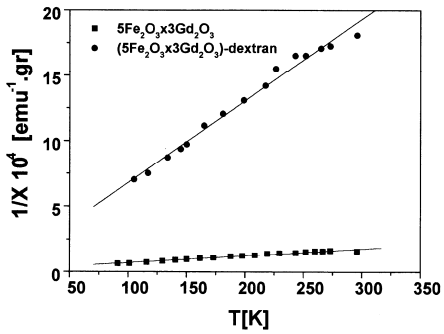

Fig. 1. Temperature dependence of the inverse magnetic susceptibility

The measured R_1 and R_2 relaxivities of nanoparticles and microparticles studied in blood, aqueous and respectively in carboximethylcellulose solutions are shown in Table 1. For purpose of comparison the R_1 and R_2 relaxivities of magnetite and SPIOs (the commercial magnetite coated in dextran) are shown too.

Table 1.

R_1 and R_2 relaxivities for the studied particles

Compound	$R_1(mM^{-1}s^{-1})$	$R_2(mM^{-1}s^{-1})$	R_2/R_1
$5Fe_2O_3 \cdot 3Gd_2O_3$ microparticles	2.54	207.83	81.82
$5Fe_2O_3 \cdot 3Gd_2O_3$-dextran nanoparticles	61.78	201.4	3.26
$5Fe_2O_3 \cdot 3Gd_2O_3$ – dextran and blood	11.86	188.73	15.91
Magnetite [5]	3.02	55.29	18.31
SPIOs [6]	30	100	3.33

The proton relaxation rates (Figures 2 and 3) are linearly dependent on concentration of compounds. This certifies the absence of solute – solute interaction [7].

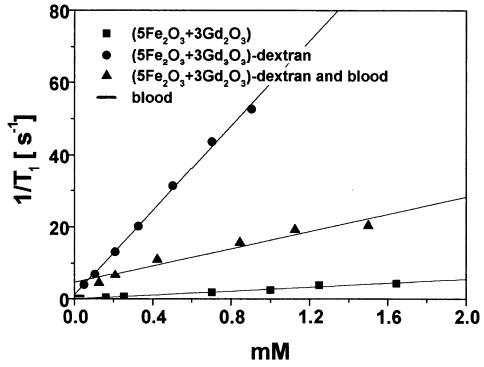

Fig.2. Proton longitudinal relaxation rates as a function of particles concentration

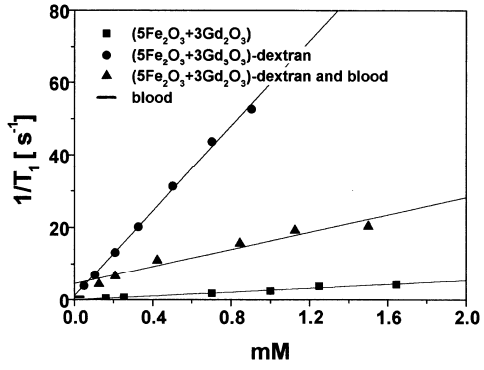

Fig. 3. Proton transverse relaxation rates as a function of particles concentration

The relaxation rate increase produced by magnetic particles is a contribution of several complex mechanisms. The size and the composition of these particles represent the essential parameters. The particles possess very large magnetic moments

in the presence of a static magnetic field. Dipolar interactions between the magnetic cores and surrounding solvent protons results in increasing both longitudinal and transverse relaxation rates, especially for nanoparticles (below 100Å).

Smaller particles are adequately described by the microscopic outersphere theory [8] which predicts that the transverse relaxivity R_2 of water will increase with the radius of the particle, whereas the longitudinal relaxivity R_1, will first increase then reach a maximum for $\omega_H\tau_R \approx 1$ and finally decrease. ω_H is the proton Larmor frequency and τ_R is the time required for a water molecule to diffuse over a distance equal with radius of the particle. Due to the small dimension of the magnetic core, iron oxide – gadolinium oxide –dextran nanoparticles and also SPIOs have higher values for R_1 and consequently lower values for the ratios R_2/R_1.

The susceptibility difference between the particles and the surrounding medium generates strong magnetic field gradients, particularly around the periphery of each inclusion. Diffusion of protons leads to an irreversible dephasing of the transverse magnetization that cannot be completely rephased by application of a 180° radio-frequency pulse. Thus in a Carr-Purcell (90 - τ -180) sequence, where τ is the spacing between the 90° and 180° pulse, the estimated transverse relaxation rate is considerably increased. The magnetized particles with large size domains (up to 100 Å) affect T_2 more that T_1. For this case the mechanism of action can be related more to diffusion-induced magnetic field gradients than to dipole-dipole interactions.

Decreasing in R_1 relaxivity observed for iron oxide-gadolinium oxide-dextran nanoparticles in the presence of the blood should be moreover explained by PRE effect [9]. The PRE effect is operative when metal ion or intact compound is covalent or non-covalent attached to a macromolecule (for example to protein amino acid residues). This decreasing of R_1 relaxivity in the presence of the blood implies probably a covalent binding to proteins, consequently a higher mass and size, high degree of internal flexibility and a low number of bounded water molecules.

4. Conclusions

$5Fe_2O_3{\cdot}3Gd_2O_3$ micropowder and $5Fe_2O_3{\cdot}3Gd_2O_3$–dextran nanoparticles were prepared and their magnetic susceptibilities and R_1 and R_2 relaxivities were measured. Magnetic susceptibility data suggest the presence of antiferromagnetic interactions between the magnetic ions (Fe^{+3}, Fe^{+2} and Gd^{+3}) of the samples, these interactions being stronger for the micropowder sample. The increase or decrease of R_1 and R_2 relaxivities depends on the number of factors as compound mass, size and composition, and is the combined result of more than one type of relaxation processes. The relaxation measurements in the presence of the blood recommend the $5Fe_2O_3{\cdot}3Gd_2O_3$–dextran nanoparticles as contrast agents in NMR tomography. These nanoparticles could be applicable to improved visualization of the reticuloendothelial system, possibly through the use of carrier-delivery systems of other tissues. An efficient accumulation in liver and spleen could allow successful diagnosing maligned tumors or metastases in these organs. The MR lymphography and MR angiography are also feasible. The $(5Fe_2O_3+3Gd_2O_3)$-dextran compound should be taken into account too for magnetic fluid hyperthermia (MFH) method [11], a

promising approach for cancer treatment. In view of the fact that gadolinium compounds have higher pyromagnetic coefficients than other compounds [10], this fact seems reliable. Because the “thermal bystander effect” offers broad perspectives in drug targeting, gene and immune therapy [2], the ($5Fe_2O_3$+$3Gd_2O_3$)-dextran compound could be used in these areas.

REFERENCES

1. Y. Wang, N. Herron, J.Phys.Chem., 95, 525 (1991).
2. M. Safarikova and I. Safarik, Magn. Electr. Sep., 10, 223 (2001).
3. C.N. Ramchand, P. Priyadarshini, P. Kopcansky and R.V. Mehta, Indian J. Pure Appl. Phys., 39, 683 (2001).
4. I. Coroiu, Al. Darabont, M.Bogdan, D.E. Demco, Rom.J.Biophys.,7, 103 (1997).
5. P.F. Renshaw, C.S. Owen, A.C. Mc.Laughlin, T.C. Frey, J.S. Leigh Jr., Mag.Reson.Med., 3, 217 (1986).
6. D.E. Canet, D.Revel, R.Forrat, G. Baldy-Porcher, L. Sebbag, J.P. Vallee, D. Didier, M.Amiel, Magn.Res.Imaging, 11, 1139 (1993).
7. K. Marcus, in: Ion Solvation, chap.5, Wiley Chichester, U.K., 1985.
8. R.N. Muller, P. Gillis, F. Moiny, A. Roch, Magn.Reson.Med., 22, 178 (1991).
9. R.B. Lauffer, T.J. Brady, R.D. Brown, S.H. Koenig, Magn. Reson.Med., 3, 541 (1986).
10. K. Mandal, Y.Yan, O. Gutfleisch, JEMS’04, Dresden, Sept. 9-11.
11. A.A. Kuznetsov, European Cells and Materials, 3, 2 (2002).

STUDIA UNIVERSITATIS BABES-BOLYAI, PHYSICA, XLIX, 3, 2004

XPS STUDIES ON POWDERED $CeNi_5$ OXIDIZED IN AIR

M. COLDEA[*], M. NEUMANN[**], C. NOVAC[*], L. G. PASCUT[*]

[*] *Babes-Bolyai University, Faculty of Physics, 3400 Cluj-Napoca, Romania.*
[**] *Universität Osnabrück, Fachbereich Physik, 49069 Osnabrück, Germany.*

ABSTRACT. The synthesis and X – photoelectron spectroscopy (XPS), X – ray diffraction (XRD) and transmission electron microscopy (TEM) of Ni isolated single domain particles, obtained from powdered $CeNi_5$ oxidized in air at different temperatures up to 800°C, are reported.

Introduction

Nanosized particles of ferromagnetic metals (Fe, Co, Ni) have been widely studied as they present an interest both for fundamental physics and potential applications such as catalysis and magnetic recording. Several methods have been used to produce these particles : evaporation, e.g. [1–4], sputtering, e.g. [5], and various chemical methods, e. g. [6–8]. Evaporation techniques allow to produce isolated particles whereas the others are used to produce particles dispersed in an insulating matrix.

Magnetic nanoparticles covered with a layer of antiferromagnetic oxides exibit large coercive forces due to the exchange anisotropy at the ferromagnetic – antiferromagnetic interface [9]. This anisotropy could lead to improved permanent magnets if antiferromagnetic coating materials with a Néel temperature above room temperature can be produced (e. g., T_N = 525 K for NiO).

Rare earth oxides are potentially useful materials for various optical and electronic applications. One such material is cerium dioxide (CeO_2) due to his high refractive index (~2), high transparency in the visible and near – infrared region and large dielectric constant (~ 26) [10].

The compound $CeNi_5$ crystallizes in the hexagonal $CaCu_5$ structure type (Pearson symbol hP6) with the Ni – Ni distances very close to that in Ni metal. This compound is an exchange – enhanced Pauli paramagnet and Ce ions are in the intermediate valence state [11]. The magnetic susceptibility of $CeNi_5$ arises mainly from the Ni 3d electrons which are very close to the onset of ferromagnetism [12]. Taking into account the great oxygen affinity of Ce and the strong magnetic interactions between Ni atoms in this compound, we tried to obtain isolated single domain particles of Ni by transforming mechanically the bulk $CeNi_5$ in a very fine powder followed by a thermal treatment in air at different temperatures up to 800 ºC.

X – ray photoelectron spectroscopy has been proved to be of central importance both in the surface analysis and in the study of the electronic structure of various groups of materials [13].

Experimental

The starting material $CeNi_5$ was prepared by argon arc melting. The purity of the elements was 99.9% for both Ce and Ni. X – ray powder diffraction measurements showed that the compound is single phase with the expected structure type and lattice parameters a = 0.487 nm and c = 0.402 nm. The Ni – Ni distances in $CeNi_5$ and Ni metal are 0.244 nm and 0.249 nm, respectively.

The XPS spectra were recorded using a PHI 5600ci ESCA spectrometer with a monochromatized Al K_α radiation ($h\nu$ = 1486.6 eV) at room temperature. The spectrometer has an argon etching system and the pressure in the ultrahigh-vacuum chamber was about 5×10^{-9} mbar during the measurements. The particle features were observed with a TESLA BS – 500 transmission electron microscop.

Results and discussion

The powder of $CeNi_5$ becomes magnetic upon exposure to air for 40 min. at 400 °C. Taking into account that Ce is much more sensitive to oxygen than Ni, this results suggest that Ni atoms diffuse into particles to form magnetic clusters, due to the strong magnetic interactions between the nearest - neighbors Ni atoms, and Ce ions migrate to the surface of the particles during heat treatment to form the oxide layers of CeO_2 and Ce_2O_3. The Ce oxide layers and in a very small quantity NiO formed on the surface of Ni particles are not continuous and consist of very small crystallites. The surface of Ni particles is completely oxidized after a new heating for 1 h at 590 °C.

The response of the surface of $CeNi_5$ fine particles upon oxidation has been studied by following the modification of the XPS valence bands and Ni 2p and Ce 3d core levels with the treatment temperature and time. Futhermore, the as – prepared sample were sputter using an argon ion beam and a surface profile depth was performed. In Figs. 1 and 2 are shown the valence bands and Ni 2p and Ce 3d cores levels, respectively, of the as-prepared samples at the treament temperatures 340°C and 590 °C before etching and after a 10 min. and 17 min argon etching. The spectra point out the occurrence of the NiO, CeO_2 and Ce_2O_3 oxides on the particles surface. The quantity ratio of cerium oxides CeO_2 / Ce_2O_3 and the thickness of the NiO layer

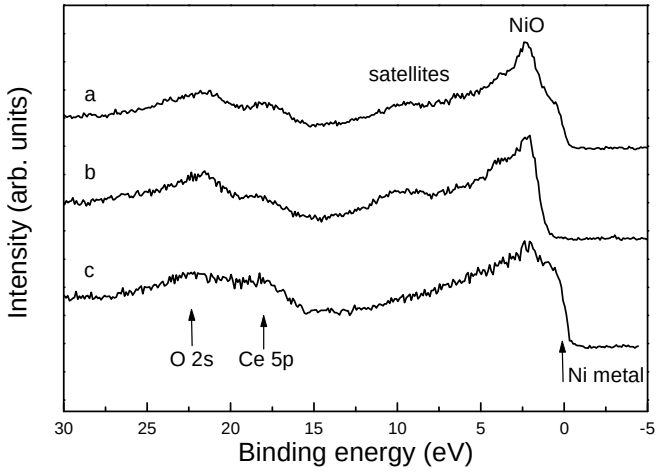

Fig. 1. XPS valence bands of powdered $CeNi_5$ oxidized in air at a) t = 590 °C for τ = 1h and exposure time to ion etching τ' = 10 min., b) t = 590 °C for τ = 1h without sputtering and c) t = 340 °C for τ = 40 min.and τ' = 17 min.

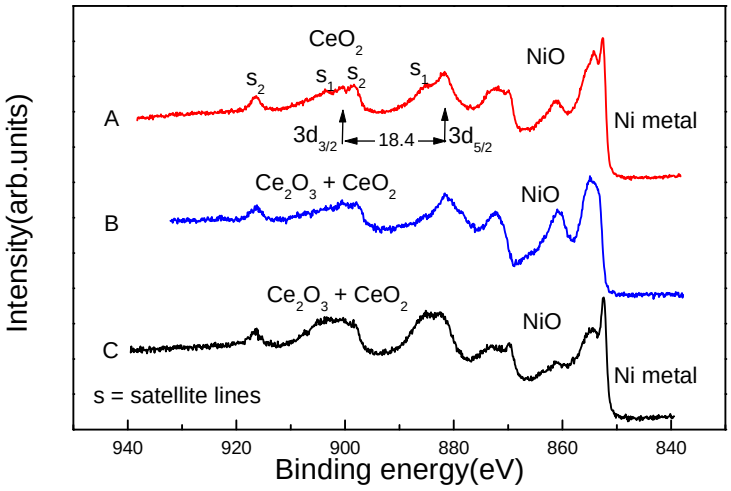

Fig. 2. XPS Ni 2p and Ce 3d core levels of powdered $CeNi_5$ oxidized in air at a) t = 590 °C for τ = 1h and exposure time to ion etching τ' = 10 min., b) t = 590 °C for τ = 1h without sputtering and c) t = 340 °C for τ = 40 min.and τ' = 17 min.

increase with the annealing temperature. The Ni metallic component was detected both in the valence bands and core levels spectra only after sputtering. At 800 °C only CeO_2 was detected. In Fig. 3 is shown the XPS Ni 2p and Ce 3d spectra for as – prepared sample after a time sputtering of 10min. One can observe the specific spectra of pure NiO[14] and CeO_2[10] with their satellite structures and the spin-orbit splitting for Ni metallic component [15].

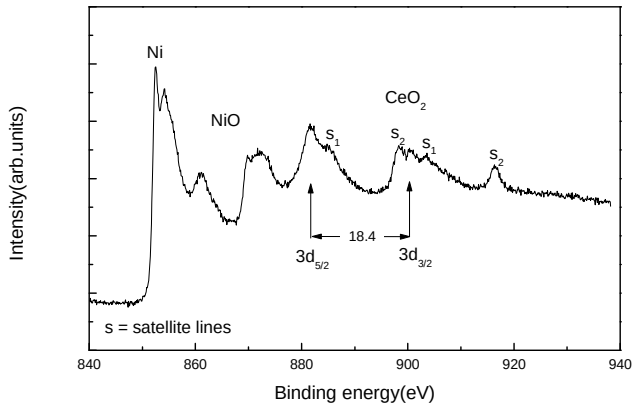

Fig. 3. XPS Ni 2p and Ce 3d core levels of powdered $CeNi_5$ oxidized in air at t = 800 °C for τ = 1h and exposure time to ion etching τ' = 10 min.

Fig. 4 shows the X-ray diffraction pattern of powdered $CeNi_5$ oxidized at 800°C for τ = 1h. All peaks can be indexed according the characteristic lines of crystalline Ni metal, NiO and CeO_2 oxides. Using Scherrer's equation[8], $d = 0.9\ \lambda / \beta \cos\theta$, wherein λ is the X – rays wavelength, β, the angular width at half-maximum intensity and θ, the diffraction angle, it is possible to estimate the diameter d of the particles. The average crystalline size of the Ni core and of the oxides layers NiO and CeO_2 formed on the surfae of Ni particles were evaluated to be 19 nm, 10 nm and 15 nm, respectively.

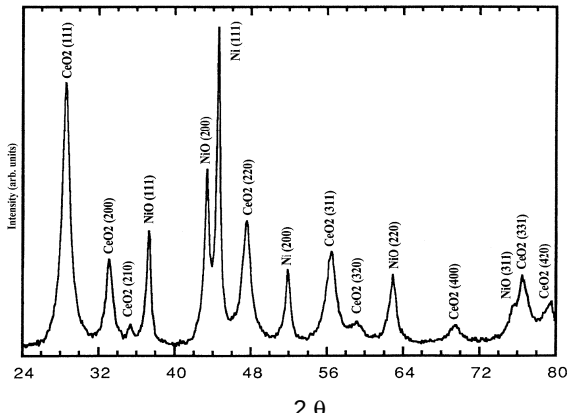

Fig. 4. XRD pattern of powdered $CeNi_5$ oxidized at 800 °C for τ = 1h

The transmission electron microscopy picture (Fig.5) shows the presence of darker particle centers surrounded by a light colored coating in most of the particles. This could be attributed to a core-shell type of structure, where the core consists of metallic Ni and the lighter shell due to NiO and Ce_2O_3 oxides. The mean Ni partcle diameters are in agreement with the results from XRD.

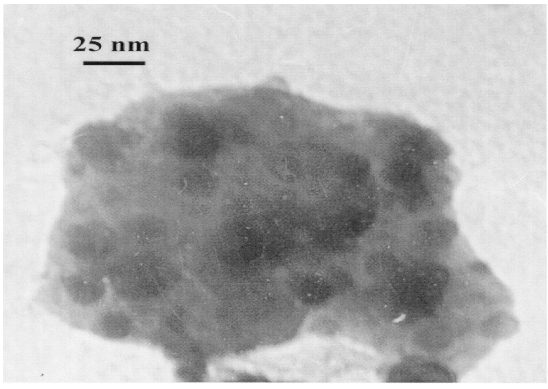

Fig. 5. TEM micrograph demonstrating the nucleation of Ni metal in powdered $CeNi_5$ oxidized at t = 800^{o}C for τ = 1h

REFERENCES

1. S. Gangopadyay, G.C. Hadjipanagis, C. M. Sorebsen, K. J. Klabunde, MRS Symp. Proc., 206 (1991) 55.
2. W. Gong, H. Li, Z. Zhao, J. Chen, J. Appl. Phys.,69 (1991) 5119.
3. T Hayashi, T. Ohno, S. Yatsuya, R. Uyeda, Japanese J. Appl. Phys., 16 (1977) 705.
4. M. B. Stern, Y. Cheng, J. Appl. Phys.,75 (1994) 6894.
5. 5 A. Gavrin, C.L. Chien, J. Appl. Phys., 73 (1993) 6949.
6. J. M. Broto, J. C. Ousset, H. Rakoto, S. Askenazy, Ch. Dufor, M. Brien, P. Mauret, Solid State Commun., 85 (1993) 263.
7. J. P. Wang, D. H. Han, H. L. Luo, N. F. Gao, Y. Y. Liu, J. Magn. Mater., 135 (1994) L251.
8. C. Estournes, T. Lutz, J. L. Guille, J. Non-Cryst. Solids,197 (1996) 192.
9. A. H. Morrish, The Physical Principles of Magnetism, John Wiley and Sons, 1965.
10. K. B. Sundaram, P. F. Wahid, O. Melendez, J. Vac. Sci. Technol., A15 (1997) 52.
11. M. Coldea, D. Andreica, M. Bitu, V. Crisan, J. Magn. Mater., 157/158 (1996) 627.
12. D. Gignoux, F. Givord, R. Lemaire, H. Launois, F. Sayetat, J. Physique, 43 (1982) 173.
13. St. Hüfner, Photoelectron Spectroscopy, Springer-Verlag, New York, Berlin, Heidelberg,1996.
14. G. K. Wertheim, S. Hüfner, Phys. Rev. Lett., 28 (1972) 1028.
15. J. F. Moulder, W. F. Stickle, P. E. Sobol, K. D. Bomben, Handbook of X-Ray Photoelectron Spectroscopy, Perkin-Elmer Corporation, Physical Electronics Division, Eden Praire, Minnesota, 1992.

STUDIA UNIVERSITATIS BABES-BOLYAI, PHYSICA, XLIX, 3, 2004

NEUTRON SCATTERING INVESTIGATION OF STRUCTURE AND MIXING BEHAVIOR OF POLYOL AQUEOUS SOLUTIONS

N. K. SZÉKELY[a], L. ALMÁSY[a], CS. MUZSNAY[b], L. ROSTA[a]

[a]Research Institute for Solid State Physics and Optics, POB 49, Budapest, H–1525, Hungary, e-mail: szekely@szfki.hu
[b]Babes-Bolyai University, Faculty of Chemistry and Chemical Engineering, str. Arany Janos 11, Cluj-Napoca, Romania

ABSTRACT. We report results of small angle neutron scattering studies on aqueous solutions of 1,2-hexanediol and 1,2,3-octanetriol above their CMC, at different temperatures. The radii of the micelles, the correlation lengths of the attractive interactions between them were determined, and the aggregation numbers were calculated. The experimental results indicate that 1,2,3-octanetriol forms more compact micelles than 1,2-hexanediol.

Introduction

The study of structure and properties of hydroxylic compound solutions is of much interest because of molecular self organization due to intermolecular hydrogen bonding. Diols are amphiphilic molecules with two distinct parts, very much unlike concerning their solubility. Such a molecular shape makes possible the arrangement of these organic compounds in various structures in their solutions: concentration fluctuations, compact micelle-like aggregates, or lamellar structures.

Many structural and thermodynamic investigations indicate the aggregation of these molecules. Kato in 1962 determined the CMC of a series of glycols using various methods, such as refractive index, surface tension, and solubilization measurements [1]. Micellar behavior of 1,2,3-octanetriol (abbreviated as OT) was demonstrated by Durand with light scattering, refractive index and specific heat measurements [2].

Small angle neutron scattering (SANS) is a direct method for measuring the aggregation of the similar species in a multi-component solution, if the sizes of the aggregates are of the order of 1-100nm. D'Arrigo et al. [3,4] carried out SANS measurements of some diol and triol solutions, and analyzed the data in terms of micelles coexisting with concentration fluctuations. In a recent SANS study we showed that the 1,7-heptanediol aqueous solutions could be well characterized by assuming statistical concentration fluctuations [5].

In the present work the structure of 1,2-hexanediol (HD) and OT heavy water solutions were studied by SANS. Their aggregation dependence on concentration and temperature was observed.

Experimental

The measurements have been carried out at the Yellow Submarine SANS spectrometer of the Budapest Neutron Centre. The alcohols were purchased from Fluka, and used without further purification. Heavy water was used as solvent, in this way the scattering length density difference (the contrast) between the two components is increased, thus giving higher scattering intensity. The studied

concentrations were above CMC. Because of low solubility of OT these samples were measured only at 70°C. The HD solutions were measured at: 15°C, 25°C and 60°C, the temperature was kept constant with accuracy of ±0.5°C. The measurements were made in the momentum transfer (q) range 0.02-0.4 Å^{-1}, where $q = \frac{4\pi}{\lambda}\sin\frac{\Theta}{2}$, λ being the neutron wavelength, Θ being the scattering angle. The measured scattering curves were brought to absolute units.

Result and discussion

The scattering intensities I(q) are displayed in Fig.1 for HD and Fig.2 for OT. The enhanced scattering is due to the aggregated alcohol molecules in the solution. The scattering curves were analyzed with the model used by D'Arrigo et al. [3] which assumes spherical micelle like aggregates with spatial correlation between them, surrounded by a homogeneous mixture of D_2O and free alcohol molecules:

$$I(q) = 9A\left(\frac{\sin(qR) - qR\cos(qR)}{(qR)^3}\right)^2\left(1 + \frac{B}{1+q^2\xi^2}\right) + Bg \qquad (1)$$

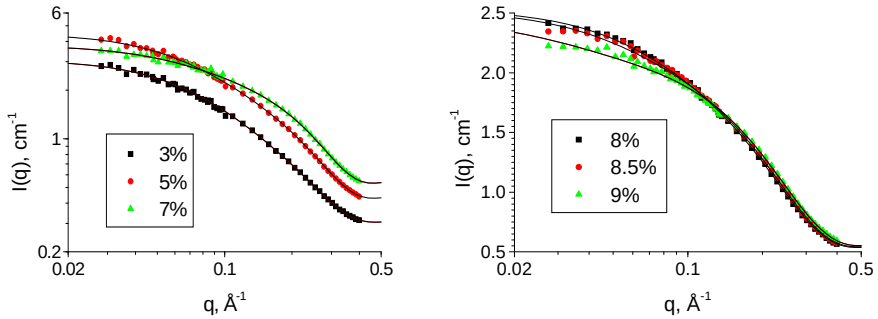

Fig.1. SANS scattering curves of 1,2-hexanediol solutions

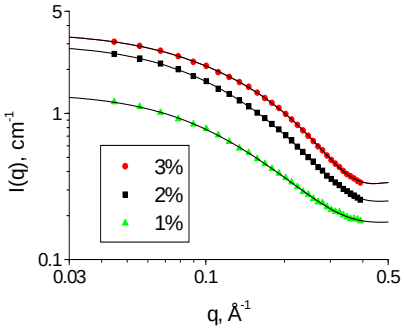

Fig.2. SANS scattering curves of 1,2,3-octanetriol solutions

The fitting parameters are: scaling parameter *A* (cm^{-1}), radius of the sphere *R* (Å), dimensionless amplitude of the concentration fluctuations *B*, correlation length of the fluctuations ξ (Å), and the background *Bg* (cm^{-1}). The first part of the equation is the form factor of a sphere; the second one is the Ornstein-Zernike structure factor describing the spatial correlation between the micelles.

The results of the least squares fitting of equation 1 are collected in Table1 and Table2. In the case of HD in the concentration range 3-5 mol%, and in the case of OT (in the studied concentration range), the alcohol aggregation increases with increasing concentration and temperature. For HD solutions, with increasing the alcohol content above 7 mol%, an intensity decrease was observed. Starting with this concentration the temperature dependence is reversed, and it can be observed from the increase of the variance of residuals (χ^2), that the used model is describing with less accuracy the measured data.

Table 1.

Fitting results for 1,2-hexanediol solutions.

conc. (mol%)	A (cm^{-1})	R (Å)	B	ξ (Å)	Bg (cm^{-1})
3	0.458	9.4	4.901	11.5	0.303
5	1.013	9.6	2.718	11.6	0.425
7	1.678	9.8	0.841	12.5	0.530
8	1.428	9.4	0.387	12.7	0.536
8.5	1.496	9.4	0.306	15.6	0.542
9	1.530	9.2	0.240	27.6	0.553

The radii of the hexanediol micelles are bigger than the length of one molecule (L_{HD}≈7.1Å), while for octanetriol they are approximately the same (L_{OT}≈9.7Å). It can be said that OT forms more compact micelles than HD in their solutions. Assuming dry OT micelles their aggregation numbers vary from 18 to 21.

The fitting results of the 1% OT solution generally agree with those found by D'Arrigo at the same concentration [3], but in our case the radius of the micelle is smaller, this may be due to the fact that our measurements were carried out at a much higher temperature. It can be mentioned that the radii collected in Table 2 are much smaller than the hydrodynamic radius found by Durand for OT in aqueous solution (19.4Å) [2].

Table 2.

Fitting results of eq.1 to the SANS data of 1,2,3-octanetriol.

conc. (mol%)	A (cm^{-1})	R (Å)	B	ξ (Å)	Bg (cm^{-1})	N_{agr}
1	0.173	9.6	5.947	9.4	0.180	18
2	0.602	9.8	3.554	9.6	0.251	19
3	1.290	10.2	1.507	10.7	0.331	21

Conclusion

Our observations indicate the presence of dry 1,2,3-octanetriol micelles and more loose 1,2-hexanediol micellar aggregates, and a significant attractive interaction between them.

REFERENCES

1. Y. Kato, *Chem. Pharm. Bull. 10* (1962) 771.
2. R.R. Durand, S.M. Hajji, R. Coudert, A. Cao, E. Taillandier, *J Phys. Chem.,* 92 (1988) 1222.
3. G. D'Arrigo, R. Giordano, J. Texeira, *Langmuir* 16 (2000) 1553.
4. G. D'Arrigo, R. Giordano, J. Texeira, *The Eur. Phys. J. E*, 10 (2003) 135.
5. L. Almásy, N.K. Székely, A. Len, Cs. Muzsnay, K.N. Király, *J. Mol. Liq.*, in press.

STUDIA UNIVERSITATIS BABES-BOLYAI, PHYSICA, XLIX, 3, 2004

LIGHT SCATTERED ON DISORDERED SYSTEMS – COMPUTER SIMULATION AND EXPERIMENTAL RESULTS

DAN CHICEA

Physics Department, University Lucian Blaga, Str. Dr. Ion Ratiu nr. 7-9, Sibiu, 550012, Romania, dan.chicea@ulbsibiu.ro

ABSTRACT. A computer program was developed to simulate coherent light scattering on disordered systems. The typical target is a suspension having RBC as scattering centers. The pattern variation with the scattering centers concentration was analyzed and found to be in good agreement with experimental results on both inorganic and organic scattering centers. The outcome of the study is a fast method of assessing the scattering centers concentration in a suspension.

Keywords: light scattering, biological fluid, disordered systems

1. Introduction

Laser light scattering on random surfaces was extensively studied and the literature abounds on reports. The diffraction pattern contains a large number of small bright spots, called laser speckles, described in papers like [1 - 4]. A typical image is presented in [3]. A similar pattern should result when laser light is scattered on disordered systems like a biological fluid as blood, where the scattering centers are randomly distributed. A computer code was developed and used to simulate coherent light scattering on suspensions. Scattering center concentrations over a wide range were considered as input data. The configuration and the way the program works are described in the next section (section 2). The light intensity on a screen was calculated for different number of scattering centers and configurations. The light intensity variation on the square area and the results of the statistical calculations are presented in section three, experimental results in section 4.

2. The computer code

A coherent light beam is assumed to be incident on a sample containing scattering centers, randomly distributed. The model of the sample is erythrocytes (Red Blood Cells, hereafter RBC) randomly distributed in diluted blood, having a complex movement, which is the overlapping of sedimentation in gravitational field and the Brownian motion. The dimensions of the scattering centers are those of RBC, that is a 7.5 μm diameter disk [5]. The scattering center concentration range was selected in such a way to make multiple scattering improbable. The RBC volume is about $90\mu m^3$ [5] and that yields a maximum of $8*10^4/mm^3$ corresponding to a hematocrit of $5*10^{-3}$. The number of scattering centers was selected in the range 50 -10000.

The cuvette-screen distance was considered to be 2 m. The screen area where the scattered light intensity was calculated was a square of 2x2 cm^2, having an angular deviation of 4 degrees. Over the 2 cm that is the screen area dimension, the angular variation of the scattered beam is less than 0.6 degrees; therefore, the phase factor variation was neglected [6].

3. Computer simulation results

The calculated light intensity on the screen was plotted for each of the calculated images. A speckled image was found, in good agreement with the experimental work reported in [4] and [7] and with the computer simulation reported in [8].

Examining the intensity variation plots for the whole set of 26 different scattering center configurations and numbers we found that that the pattern is the same, with randomly distributed maxima and minima. The number of maxima was carefully counted for each configuration. The average number of maxima is 47 and the variation from one configuration to another is within 0.5 standard deviations, therefore we can conclude that the number of maxima does not depend of the number of scattering centers in a sample.

Examining the plots of the average light intensity on the screen and of the average standard deviation per point with the number of the scattering centers we found that both variations are linear, which is confirmed by the values of the R^2 parameter very close to unity (0.9929 for the average intensity fit and 0.9896 for the average standard deviation per point, $R^2 = 1$ meaning the perfect fit).

4. Experimental results

In order to verify the computer simulation results an experiment using a collimated laser beam incident on a 1 mm thick cuvette having both inorganic (barium sulphate) and organic suspensions (human diluted blood, natural juices) was conducted. The image produced by the laser beam on a screen and the average light intensity values are in very good agreement with the computer simulation results. These results suggest a fast procedure to determine the scattering centers concentration in a sample by first getting a digital image of the scattered light, normalizing the image, performing statistical calculations and comparing the results with the calibration data. A direct application might be a fast way of assessing RBC Count and of the scattering centers concentration in biological fluids.

5. Conclusion

The results of the computer simulation performed so far reveal that the number of maxima on the screen does not depend of the number of scattering centers in the sample. Moreover, the average of the light intensity on a certain location on the screen and the average standard deviation have a linear increase with the concentration of the scattering centers. The good agreement of the computer simulation with the experimental results suggests a simple and fast procedure of assessing the scattering centers concentration in a sample (like the RBC count in human blood) as described in the previous section. Work is in progress on this subject.

6. Acknowledgements

I am deeply indebted to Dr. Ioan Turcu and Cristian Pop of INDCTIM Cluj-Napoca for fruitful discussions and direct support.

REFERENCES

1. J.W. Goodman, Statistical Optics, John Wiley & Sons, New York, 1985, p.1.
2. J.C. Dainty, Laser Speckle and Related Phenomena. Topics in Applied Physics, Springer, Berlin, 1975, p.1.
3. S. S. Ulyanov, Statistical Models for Speckles with a small number number of scatterers, Asian Journal of Physics, 2002, http://optics.sgu.ru/~ulianov/ajp3.pdf.
4. S. S. Ulyanov, Speckled Speckle Statistics With a Small Number of Scatterers: Implications for Blood Flow Measurement, Journal of Biomedical Optics 3(3), 237-245, 1998.
5. D. Wysoczanski, J. Mroczka, F. Onofri, Optical Parameters and Scattering Properties of Red Blood Cells, Optica Applicata 32(4), 691-700, 2002.
6. I. Turcu, Effective phase function for light scattered by disperse systems – the small angle approximation, J. Opt. A: Pure Appl. Opt. 6, 1-7, 2004.
7. I. Turcu, C. V. L. Pop, S. Neamtu, Intensity Fluctuating Pattern of Light Scattered on Microparticles, The 3-rd PIM Conference, 240-245, September 2003.
8. C. V. L. Pop, I. Turcu, C. Vamos, Simulation of Fluctuating Interference Pattern for Light Scattered on Erythrocytes in Suspension, The 3-rd PIM Conference, 511-514, September 2003.

STUDIA UNIVERSITATIS BABES-BOLYAI, PHYSICA, XLIX, 3, 2004

FT-IR AND RAMAN STUDIES ON NEW 2-CARBOXYALKYL-THIO-5-MERCAPTO-1,3,4-THIADIAZOLE DERIVATIVES

M.M. VENTER,[*1] S. CINTA-PINZARU,[2] I. HAIDUC[1] AND V. BERCEAN[3]

[1] *"Babes-Bolyai" University, Dept. of Chemistry, Cluj-Napoca, Romania*
[2] *"Babes-Bolyai" University, Dept. of Physics, Cluj-Napoca, Romania*
[3] *Technical University, Dept. of Chemistry, Timisoara, Romania*

ABSTRACT. Preliminary vibrational studies on new 2-carboxyalkyl-thio-5-mercapto-1,3,4-thiadiazole derivatives, $C_2N_2S_3HR$, R = $-(CH_2)_nCOOH$, n = 1 (**1**), 2 (**2**), 3 (**3**) are discussed, using FT-IR and Raman spectroscopy. The spectroscopic data are consistent with the molecular structures of **1** – **3** and suggest that all compounds exist mainly as thione tautomers (HN-C=S) in solid state.

Introduction

Recent developments in the structural chemistry of heterocyclic ligands containing SCN fragments has produced interesting supramolecular architectures, revealing nanometric cavities and channels.[1] Many of these compounds have proved excellent zeolitic properties.[1-4] The design of such patterns requests the election of molecules with a flat, rigid geometry and containing an extended number of electronegative heteroatoms (E) and E-H groups, able to generate intermolecular interactions. Moreover, the presence of exo- and endocyclic sulfur atoms may give rise to S···S interactions which are of great importance in the supramolecular construction of nonconventional superconductors (commonly known as "organic metals").[5,6] In this respect, we become interested in mercapto-aza heterocyclic derivatives, partly from the aspect of applications in analytical chemistry, biology and industry and also because of their specific molecular structure which can generate supramolecular assemblies *via* E-H···E' (E, E' = N and/or S) and short S···S interactions.[7-11]

The aim of this work is to provide the first preliminary IR and Raman characterization of three new compounds: 2-carboxyalkyl-thio-5-mercapto-1,3,4-thiadiazole derivatives, $C_2N_2S_3HR$, R = $-(CH_2)_nCOOH$, n = 1 (**1**), 2 (**2**), 3 (**3**) (Scheme I) and to elucidate their tautomeric form (thione, HN-C=S / thiol, N=C-SH) in solid state.

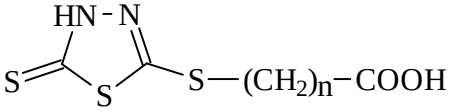

n = 1 (**1**), 2 (**2**), 3 (**3**)

Scheme I

Experimental

The starting materials were purchased from commercial sources (Aldrich) as analytical pure reagents and were used with no further purification. Compound **2** was prepared by literature method.[12] Compounds **1** and **3** were prepared by the reaction of Bismuthiol I with the appropriate $Cl(CH_2)_nCOOC_2H_5$ (n = 1, 3) derivative in chloroform at room temperature, followed by the acid hydrolysis of the resulting ester at 100°C. The reactions worked with a global yield of 40 – 80%. Purification was performed by recrystallization from methanol. The products are air stable and soluble in alcohols.

FT-IR and FT-Raman spectra on solid samples were recorded using a Bruker FT-IR Equinox 55 spectrometer with an integrated FRA 106 S Raman module. The excitation of the Raman spectra was performed using the 1064 nm line from a Nd:YAG laser with an output power of 250 mW. An InGaAs detector operating at room temperature was used. The spectral resolution was 2 cm^{-1}.

Results and Discussion

The FT-IR (3500 - 500 cm^{-1}) and Raman (3500 - 200 cm^{-1}) spectra of **1** – **3** are presented in Fig. 1 and 2, respectively. The spectral data and vibrational assignments of **1** – **3** are presented in Table 1. The following discussion is based on the comparison of the spectral data recorded for **1** – **3** with the literature data published for dimercapto-thiadiazole (Bismuthiol I, DMTD), methyl-mercapto-thidiazole (MMTD) and amino-mercapto-thiadiazole (AMTD).[8,9,13]

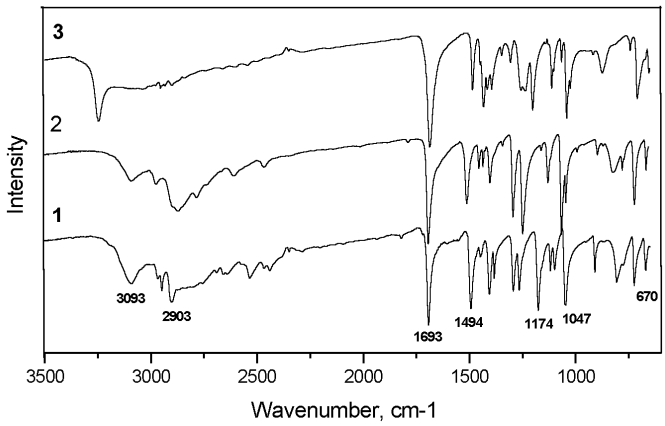

Fig. 1. FT-IR spectra of 1 - 3.

The 3500 – 1800 cm^{-1} spectral range – Both IR and Raman spectra of compounds **1** - **3** reveal bands at 3250 - 3088 cm^{-1}, characteristic for the ν(NH) stretching mode. These assignments are in good agreement with those reported for MMTD (3051 - 3049 cm^{-1}) and AMTD (3139 cm^{-1}), both found as thione tautomers in solid state.[13] On the opposite, the Raman spectra show no spectral behavior of **1** - **3** in the approx. 2500 - 2400 cm^{-1} range where the fundamental ν(SH) stretching mode would be expected, while the IR spectra are irrelevant due to plethora of OH bands. In

addition, the characteristic (OH) band (*ca*. 3400 cm^{-1}) is absent in all spectra which might suggest a tautomer equilibrium between the –COOH group and the neighboring endocyclic N atom.

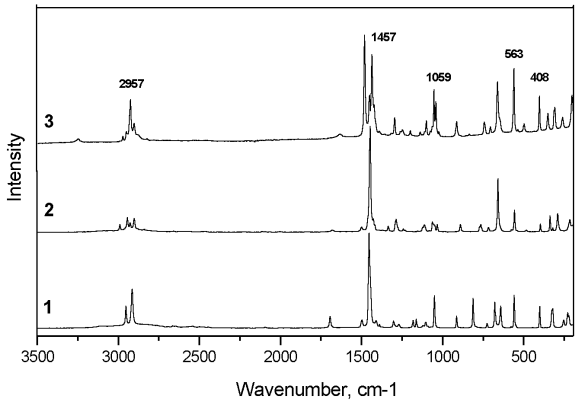

Fig. 2. FT-Raman spectra of 1 - 3

Table 1.

Selected FT-IR and FT-Raman data (cm^{-1}) for the compounds 1 – 3 and the proposed assignments.

1		2		3		Vibrational Assignment
IR	**Raman**	**IR**	**Raman**	**IR**	**Raman**	
3093m		3088w	2995w	3249s	3250w	ν(NH)
2950m	2953m	2967w	2948mw	3030-2896br	2957m	$\nu_{as}(CH_2)$
2903ms	2915s	2898m	2907mw		2907w	$\nu_s(CH_2)$
1693vs	1694m	1687vs	1687vw	1687vs	1638vw	ν(C=O)
1494vs	1498mw	1506s	1505w	1484m	1489vs	ν(C=N)
1453w	1453vs	1449m	1452vs	1449m	1457ms	ν(C=N)
1407s 1293s	1410mw 1302mw	1397ms 1288s	1290mw	1412m 1307w	1303mw	δ(ring) + ν(C-N) + $\delta(CH_2\alpha)$ + ν(C-O)
1266s	1270w	1243vs	1243vw	1257m	1254w	δ(ring) + $wag(CH_2)$
1047vs	1051s	1059vs 1040s	1056mw	1065w 1042s	1059s 1048m	ν(C=S) + ν(N-N)
724ms	726w	717s	720w	707s	710w	ν_{as}(CSC)endo
670m	678s	662m	663s		669s	ν_s(CSC)endo
	559s		561m		504w	ν(C-S')exo
	402ms		401mw		408m	δ(NCS)op
	321ms		341m		353mw	δ(NCS,CCS)

Abreviation: vs – very strong, s – strong, ms – medium strong, m – medium, mw – medium weak, w – weak, vw – very weak, br – broad, ν - stretching, δ - bending, wag – wagging, endo – endocyclic, exo – exocyclic.

The 1800 – 1000 cm^{-1}spectral range – is the most relevant spectral region as it concerns the identity of the heterocyclic skeleton and the carboxyalkyl substituent. The most important bands fall in the approx. 1700 - 1450 cm^{-1} spectral range and are assigned to the ν(C=O) and ν(C=N) modes. The later stretching mode is assigned in all spectra to two bands (1506 - 1489 and 1457 - 1449 cm^{-1}), comparable with the two fundamentals found for DMTD (C_{2v} symmetry): ν_{as}(C=N) (1510 -1506 cm^{-1}) and ν_s(C=N) (1452 -1450 cm^{-1}), respectively.[13] As the molecules of **1** - **3** have a lower symmetry (C_s), we suppose that the two ν(C=N) modes correspond to two differently delocalized CN units. The assignment of ν(C=S) mode in the approx. 1070 - 1040 cm^{-1} range is in good agreement with the spectral data reported for DMTD[8,9] and support the proposed thione tautomer form of **1** - **3**.

The 1000 – 200 cm^{-1}spectral range – The most relevant bands of this region are assigned to fundamentals of endocyclic CSC and exocyclic C-S goups, in the 724 - 504 cm^{-1} spectral range.

Aknowledgements

M.M.V. thanks The National Council of Academic Research (CNCSIS) for financial support during the course of this work.

REFERENCES

1. I. Haiduc, F. T. Edelman, *Supramolecular Organometalic Chemistry,* Wily-VCH, Weinheim*,* 1999.
2. V. R. Pedireddi, S. Chatterjee, A. Ranganathan, C.N.R. Rao, *J. Am. Chem. Soc.,* 1997, **119**, 10867.
3. A. Ranganathan, V. R. Pedireddi, S. Chatterjee, C.N.R. Rao, *J. Mater. Chem*., 1999**, 9**, 2407.
4. A. Ranganathan, V. R. Pedireddi, C.N.R. Rao, *J. Am. Chem. Soc.,*1999, **121**, 1752.
5. J.M. Williams, J.R. Ferraro, R.J. Thorn, K.D. Carlson, U. Geiser, H.H. Wang, A.M. Kini, M.-H. Whangbo, *Organic Superconductors (Including Fullerenes). Synthesis, Structure, Properties and Theory,* Prentice Hall, New Jersey, 1992.
6. D.W. Bruce, D. O'Hare, *Inorganic Materials*, J. Wiley&Sons, New York, 1999.
7. L. Huang, F. Tang, B. Shen, T. Yu, Q. Meng, *J. Phys. Chem*., 2001, 1**05**, 7984.
8. M.M. Osman, *Bouletin de la societe chimiq de France*, 1980, **11-12,** 452.
9. S.A.A. Zaidi, *Acta Chimica Academie Sc. Hun, Tomus*, 1977, **95(4)**, 383.
10. V. Berceanu, C. Crainic, I. Haiduc, M.F. Mahon, K. C. Molloy, M.M. Venter, P.J. Wilson, *J. Chem. Soc., Dalton Trans*, 2002, 1036.
11. M.F. Mahon, K.C. Molloy, M.M. Venter, I. Haiduc, *Inorg. Chim. Acta.*, 2003, **348**, 75.
12. B. Stanovnik, M. Tiser, *Croat. Chem. Acta*, 1965, **37**, 17.
13. H.G.M. Edwards, A.E. Johnson, E.E. Lawson, *J. Molec. Struct*, 1994, **351**, 51.

STUDIA UNIVERSITATIS BABES-BOLYAI, PHYSICA, XLIX, 3, 2004

STRUCTURE AND VIBRATIONAL SPECTRA OF TETRAMETHYL 3,7-DIHYDROXYBICYCLO[3.3.1]NONA-2,6-DIENE-2,4,6,8-TETRACARBOXYLATE AND BICYCLO[3.3.1]NONANE-3,7-DIONE

N. TOSA[1], **A. BENDE**[2], **S. CÎNTĂ PÎNZARU**[3], **I. GROSU**[1], **E. SURDUCAN**[2]

[1]*Organic Chemistry Department, Babes-Bolyai University, 11 Arany Janos, RO 400028 Cluj-Napoca, Romania*
[2]*National Institute for R&D of Isotopic and Molecular Technologies, 71-103 Donath, RO 400293 Cluj-Napoca, Romania*
[3]*Molecular Spectroscopy Department, Babes-Bolyai University, Mihail Kogalniceanu 1, RO 400084 Cluj-Napoca, Romania*

ABSTRACT. The conversion of *tetramethyl 3,7-dihydroxybicyclo[3.3.1]nona-2,6-diene-2,4,6,8-tetracarboxylate* into *bicyclo[3.3.1]nonane-3,7-dione* was achieved by using a conventional method and under microwave irradiation. The IR and Raman spectra were obtained and vibrational assignments could be made. The Density Functional Theory (DFT) was applied to calculate the structure and spectra and good agreement with experimental data was obtained.

Introduction

Supramolecular chemistry offers the potential to construct synthetic macromolecules with control at molecular level, a goal which has only truly been realised in natural bio-macromolecular systems. The performances of synthetised materials are critically dependent on the spatial arrangement of the constituents at molecular level. An additional development direction is to apply the synthetised material for nanofilms[1] obtaining. The investigated compounds are potential macrocycles precursors, the major application of the method developed here being the films growing in situ, under similar reaction conditions on a surface or interface[2].

The aim of our work was to elucidate the structure of the ***tetramethyl 3,7 - dihydroxybicyclo[3.3.1]nona-2,6–diene - 2,4,6,8-tetracarboxylate*** ***(1)*** and ***bicyclo[3.3.1]nonane-3,7-dione*** ***(2)*** using vibrational spetroscopy, in conjunction with DFT calculation. The straightforward conversion of the tetramethyl 3,7 – dihydroxybicyclo [3.3.1]nona - 2,6 - diene - 2,4,6,8 – tetracarboxylate into bicyclo[3.3.1] nonane-3,7-dione by the one step conventional and microwave irradiation conversion was proposed in our earlier work[3]. Our spectroscopic study reveals that such kind of molecules participate into a keto-enol tautomeric equilibrium[4]. The compound **1** mainly exist as a dienol whereas the compound **2** exists as a diketone at ambient temperature[5]. Theoretical calculations were used in order to gain a deeper understanding of the vibrational experimental spectra and structure of these complex molecules.

In particular, we used DFT as it is known that this method is a performant computational alternative to the conventional quantum chemical methods, since it is less computationally demanding and take account of the effects of the electron correlation.

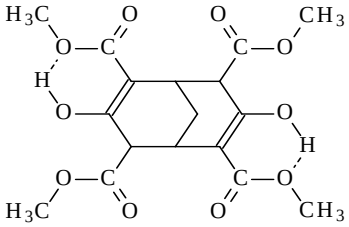

1

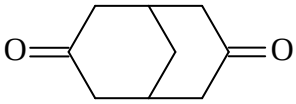

2

Fig. 1. Theoretical structures for compound **1** and compound **2**.

Results and Discussion

The theoretical study has been done at DFT method with the B3LYP exchange-correlations functional, using 6-31G** Pople's basis sets implemented in GAMESS[6] quantum chemical program package. The geometry structures were optimized at B3LYP with analytical gradient method, while the harmonic vibrational frequency values of theoretical IR and Raman spectra were obtained considering 6-31G** basis set.

Tetramethyl 3,7-dihydroxybicyclo[3.3.1]nona-2,6-diene-2,4,6,8-tetracarboxylate. The large number of harmonic vibrational frequency makes very difficult the identification and assignment of the normal modes of different molecular fragment with the different frequency values. Since a lot of vibrational frequencies have small intensity only that values can be picked out from the spectra which have a significant intensity and which could have implication in our investigation. In the spectral segment of 800 – 820 cm^{-1} several theoretical frequency lines were found, corresponding only to the ρ(C-O-H) fragment vibrations, where three different IR active and a single Raman frequency can be observed with a significant magnitude of intensity. In the 980 – 1060 cm^{-1} spectral region of the IR spectra, for the different theoretical spectra can be found a number of five-six IR active and two Raman active modes with significant intensity. Their vibrations are more difficult to locate because of the complexity of vibrational motion. Even so, for most of case in the collective motion of atoms can be observed a characteristic vibration of the -C-C-C- bridge situated in the molecular skeleton. The segment situated at the 1140 – 1290 cm^{-1} interval of absorption spectra is the largest compact band region and the most densely loaded with frequency lines. Similarly to the previous region the vibrations of this spectral region are also complex being involved simultaneously the motion of the tetracarboxyl groups, the -C-O-H groups, and the molecular skeleton. Some frequency values could be found also in the bicyclo[3.3.1]nonane-3,7-dione IR spectra, such as ν_{86}. The few frequency lines are present in the 1320 – 1400 cm^{-1} spectral region, that are characteristic to the bridge of molecular skeleton and to the -C-O-H fragment. The region 1620-1780 cm^{-1} is characteristic for double bond vibrations of >C=O situated into the methoxycarbonyl groups and the -C=C- into the molecular skeleton, having the highest intensity in the whole spectrum. The frequency intensities of these normal mode vibrations are some of the most intense lines in the whole IR and Raman spectra, supporting the

explanation of the local character of fragment's vibrations. The experimental spectra reveal also very strong IR bands at 1661, 1734 and 1743 cm^{-1}, and 1627 (very strong), 1729 and 1740 cm^{-1} as weak-medium bands in the FT-Raman spectrum (Fig. 2).

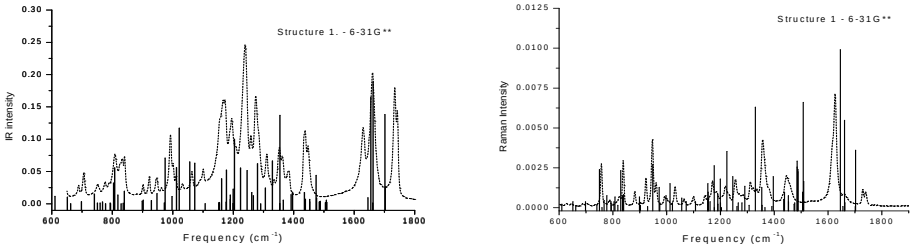

Fig. 2. The experimental and theoretical FT-IR and FT-Raman spectra of **1**.

Bicyclo[3.3.1]nonane-3,7-dione (2). Due to the molecular symmetry a considerable number of frequency lines are missing both from the IR and Raman spectra, while the other lines have very small intensity. However, both absorption spectra are more simple than in the case of structure (**1**). The frequency line at 708 cm^{-1} is characteristic for the carbon rings motion and due to the molecular symmetry the Raman shape is more intense than the analogous IR line intensity. An excellent confirmation was experimentally observed in the FT-Raman spectrum (Fig. 3), where this is the most intense band.

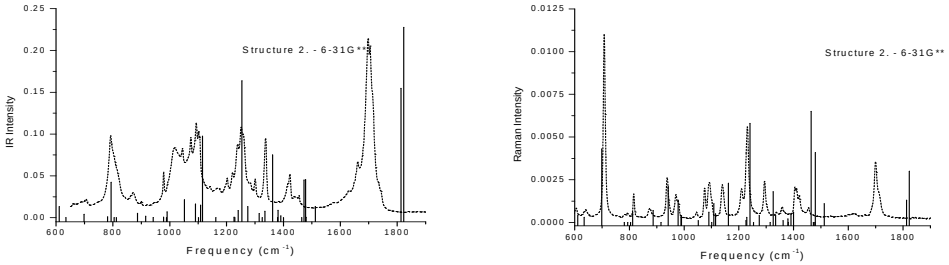

Fig. 3. The experimental and theoretical FT-IR and FT-Raman spectra of **2**.

In 1000-1400 cm^{-1} spectral region can be found the bulk of the lines in both vibrational spectra. The vibrational motion of these normal modes are very complex and could not be localized to the single bond distance or bond angle. Besides of the C-C-C bridge and C-C-C ring vibrations, different C-H vibrations (bending, rocking, and twisting) could be observed. The 1600-1750 cm^{-1} spectral region is characteristic to the >C=O stretching vibrations, which are both IR and Raman active. The experimental spectra reveal very intense bands at 1698 and 1705 cm^{-1} (FT-IR) and a strong band at 1700 cm^{-1} with a shoulder at 1710 cm^{-1} (FT-Raman) (Fig. 3).

Conclusions

The investigations of the molecular structure of compounds **1** and **2**, in solid state, using FT-IR and FT-Raman spectroscopy in conjunction with the DFT calculations, revealed both tautomers of **1** (major enolic form) and exclusively ketonic form for the compound **2**. The intramolecular O…H bonds from the molecule of **1** are established between the H atom of the ρ(C-O-H) fragment and O atom of C-O-CH_3 fragment of the methoxycarbonyl group, both connected in the C=C moiety.

REFERENCES

1. I. Sapurina, A. Riede, J. Stejskal, *Synth. Met.,* **2001**, 123, 503.
2. R. Yerushalmi, A. Scherz, M.E. van der Boom, *J.Am.Chem. Soc.,* **2004**, 129, 9, 2700.
3. N. Tosa, A. Bende, S. Cîntă Pînzaru, I. Grosu, E. Surducan, *Chem. Phys.* (submitted).
4. U. Weiss, J.M. Edwards, *Tetrahedron Letters*, **1968**, 47, 4885.
5. (a) J.M. Radcliffe, A. Gutiérrez, J.F. Blount, K. Mislow, *J.Am.Chem.Soc.*, **1984**, 106, 682; (b) P. Champ, *Tetrahedron Letters*, **1974**, 46, 4067; (c) S.H. Bertz, G. Rihs, R.B. Woodward, *Tetrahedron*, **1982**, 38, 63.
6. Program GAMESS; M.W. Schmidt, K.K. Baldridge, J.A. Boatz, S.T. Elbert, M.S. Gordon, J.J. Jensen, S. Koseki, N. Matsunaga, K.A. Nguyen, S. Su, T.L. Windus, M. Dupuis, J.A. Montgomery, *J.Comput.Chem.*, **1993,** 14, 1347.

STUDIA UNIVERSITATIS BABES-BOLYAI, PHYSICA, XLIX, 3, 2004

SPECTRAL INVESTIGATIONS OF NANOSTRUCTURED ALUMINA HYDRATE FOR CATALITIC PURPOSES

ANA-MARIA KASZONI PRICOP[1,2], ELISABETH-JEANNE POPOVICI[1], VIORICA POP[1,2], LUMINIŢA SILAGHI-DUMITRESCU[2], RODICA GRECU[1] And EMIL INDREA[3]

[1] "Raluca- Ripan" Institute for Research in Chemistry, 30 Fântânele, 400294 Cluj-Napoca, ROMANIA
[2] Faculty of Chemistry and Chemical Engineering, Arany Janos"Babeş-Bolyai" University, 400028 Cluj-Napoca
[3] National Institute for R & D of Isotopic & Molecular Technology, Donath 30, 400295 Cluj-Napoca

ABSTRACT. Alumina monohydrate can be used as binder in the preparation of porous adsorbing layer for catalitic purposes. The paper presents some of our results referring to the characterisation of alumina hydrate samples obtained as nanostructured powders in different preparation conditions.

Key words: alumina hydrate, boehmite, catalysts.

1. INTRODUCTION

Alumina monohydrate known as boehmite ($Al_2O_3 \cdot H_2O$) is frequently used as binder for the manufacture of metallic and ceramic monolith catalysts [1].

Crystalline structure, particle size and chemical composition of alumina hydrate influence the quality of the support washcoating i.e. surface area, porosity and adherence to the metallic or ceramic substrate.

The paper presents some of our results refering to the synthesis of nano-structured alumina monohydrate that is to be used as binder for the manufacture of the absorbing layer on the metallic substrate.

2. Experimental part

Alumina hydrates [$Al_2O_3 \cdot xH_2O$] samples were prepared by adding nitric acid to sodium aluminate solution obtained from aluminium turnings and sodium hydroxide. The diluted HNO_3 solution was slowly added, under constant stirring, until the medium pH was 9. The separated gel was centrifuged, washed and dried at 110^0C for 24 hours. The as-obtained alumina hydrate samples were conditioned with specific solvents, dried, milled and sieved.

Alumina hydrate samples were investigated by thermal analysis (Paulik-Erdely OD-102 Derivatograff; heating rate = 6^0C/min), X-ray diffraction (DRON 3M Diffractometer; CuK_α radiation) and FT-IR spectroscopy (JASCO-610 Spectrophotometer; KBr disks). The micro-structural parameters were calculated by using the RXLINE program (Warren Averbach theory).

Correspondence: kaszoni@icrr.itim-cj.ro

3. RESULTS AND DISCUSSION

In order to prepare alumina monohydrate for catalytic purposes, sodium aluminate solution obtained from aluminium turnings and sodium hydroxide was treated with diluted nitric acid.

$$2Al + 2NaOH + 6H_2O \rightarrow 2Na[Al(OH)_4] + 3\ H_2\uparrow$$

$$Na[Al(OH)_4] + HNO_3 \xrightarrow{pH=9} Al_2O_3 \cdot xH_2O + NaNO_3$$

Taking into consideration that the quality of alumina hydrate is strongly influenced by the precipitation conditions [2] the effect of reagent concentration and ratio was studied (Table 1).

Table 1.

Preparation conditions of alumina hydrate samples

Samples	C_{Al2O3} (mol/l)	ν_{NO3}/ν_{Al2O3}	pH	*η (%)
B15.1	0.440	1.8	9.0	24.1
B15.2a	0.088	2.8		23.2
B15.2b	0.088	2.5		18.9
B15.3	0.044	1.8		24.5

**preparation yield (as Al_2O_3)*

Thermogravimetric (TG), differential thermogravimetric (DTG) and differential thermal analysis (DTA) as well as infrared absorption spectroscopy (FT-IR), and X-ray diffraction (XRD) were used to evaluate the quality of as prepared alumina hydrate samples.

The thermal behaviour of samples prepared by using various reagent concentration and ratio is different. The experimental thermal weight losse of all samples is quite equal and almost twice the theoretical value (15%) of the anhydrous boehmite AlO(OH). Every sample is characterised by a very strong endothermic effect (associated with the water removal process) whose position is very different. The dehydration process is very intense at about 315ºC for sample **B15.1** and at about 190ºC for sample **B15.3**.

TG-DTG-DTA curves suggest that, in our preparation conditions, two types of alumina hydrate are obtained possessing different hydratation degrees (table 2).

Table 2.

Thermal behaviour of the two-alumina hydrate series

Samples	Thermal analysis data				Alumina hydrate type
	Δw (%)	**T_{max} (ºC)	Effect	Estimated formula	
B15.1	33.1	140 315	Weak endo-effect Strong endo - effect	$Al_2O_3 \cdot 2.80\ H_2O$	$Al(OH)_3$
B15.2a	25.6	160 440	Strong endo-effect Weak endo - effect	$Al_2O_3 \cdot 1.95\ H_2O$	AlO(OH)
B15.2b	26.5	200 360	Strong endo-effect Weak endo - effect	$Al_2O_3 \cdot 2.04\ H_2O$	
B15.3	28.3	190 435	Strong endo-effect Weak endo - effect	$Al_2O_3 \cdot 2.16\ H_2O$	

*** from DTA curves*

The vibrational spectra and the XRD patterns evidenced the difference between the crystalline structures of alumina hydrate samples.

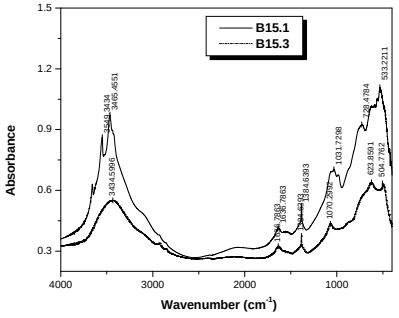

Figure 1. FTIR spectra of two types of alumina hydrate samples

Figure 1 suggests that the **B15.1** lattice is better organised than **B15.3** sample. The structure of the spectrum in the high frequencies domain suggests the simultaneous presence of adsorbed water, crystallisation water and free OH groups. For the **B15.1** sample, the pair of bands at 980 and 1032 cm^{-1} could be associated with the characteristic vibrations of the Al-OH bonding. The wide absorption band with maximum at 3465.45cm^{-1} is due to the vibration of H_2O molecules, hydrogen bonded to Al_2O_3 surface.

In the case of **B15.3** sample, an intense broad band at 3434.59 cm^{-1} ($\nu_{H\text{-}O\text{-}H}$) was observed. This suggests a high content of unstable H_2O. The specific absorption bands of the boehmite prepared with nitric acid are noticed at 1060-1080 cm^{-1} ($\nu_{Al\text{-}OH}$); ~1385 cm^{-1} (ν_{NO2}); ~ 1650 cm^{-1} ($\nu_{H\text{-}O\text{-}H}$); ~ 3200-3700 cm^{-1} ($\nu_{Al\text{-}OH}$).

FTIR analysis proved the existence of two types of alumina hydrates, namely with $Al(OH)_3$ composition (**B15.1** sample) and with boehmite AlO(OH) structure (**B15.3** sample).

XRD patterns confirmed this supposition (figure 2). Sample **B15.1** corresponds to monoclinic aluminium hydroxide with bayerite structure and possesses high cristallinity degree. Sample **B15.3** can be associated with orthorhombic aluminium oxy-hydroxide with boehmite-pseudoboehmite structure and show relatively low cristallinity.

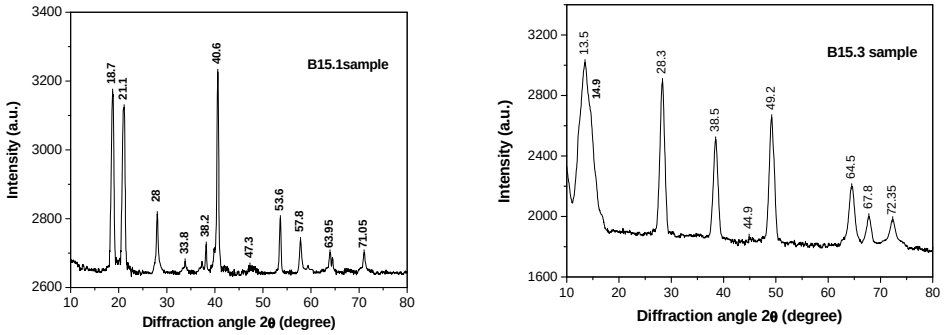

Figure 2. XRD patterns of two type of alumina hydrate samples

The calculated micro-structural parameters illustrate that boehmite samples are nanostructured, with medium crystallite size of 50-65 Å (figure 3). The two boehmite samples possess different lattice strain distribution.

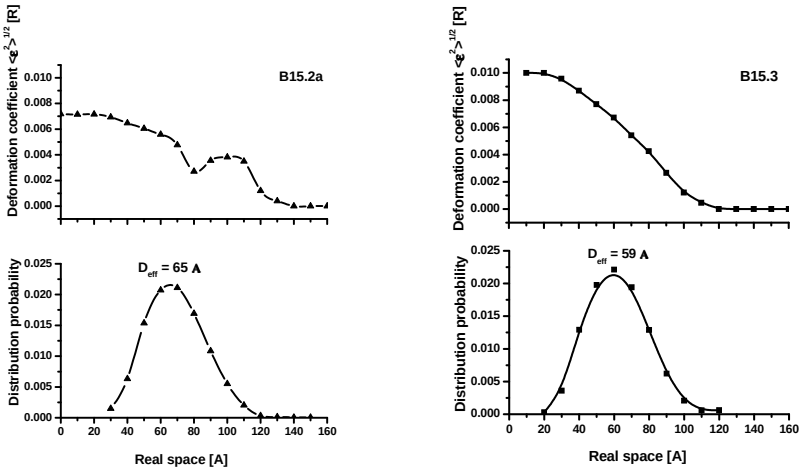

Figure 3. Deformation coefficient distribution (up) and crystallite size distribution (down) of two sortiments of boehmite samples

4. CONCLUSIONS

Infrared absorption spectroscopy, X-ray diffraction and thermal analysis put in evidence that, in our experimental conditions, two different types of alumina hydrate were obtained: *type I* - containing mostly aluminium hydroxide i.e. alumina trihydrate $Al_2O_3 \cdot 3H_2O \Leftrightarrow Al(OH)_3$ and *type II*, consisting mainly in nanostructured boehmite i.e. alumina monohydrate $Al_2O_3 \cdot H_2O \Leftrightarrow AlO(OH)$. The reagent concentration and ratio determine the composition and the crystalline structure of alumina hydrate obtained and its binding ability.

Acknowledgements:

The work was supported by Romanian Research Program MATNANTECH, under contract no. 109/2002.

REFERENCES

1. W.P.Addiego, C.S.Magee,*"Alumina-bound high strength ceramic honeycombs",* US 6,677,261, 2004.
2. A.M. Kaszoni Pricop, E.J. Popovici, D. Roiban, T. Ursaleş, R. Grecu, E. Indrea, *"Multifunctional skeletal catalytic support. 1. Alumina-based composition for porous adsorbing layer"*, Journal of Optoelectronics and Advanced Materials, 6(1), 2004, p. 219-224.